Electrochemical reduction of carbon dioxide to liquid fuels: Conversion of a thermal catalyst to an electrocatalyst

by

Kayode Adesina Adegoke

Submitted in fulfilment of the requirements for the degree

Doctor of Philosophy (Chemistry)

In the Faculty of Natural & Agricultural Sciences

University of Pretoria

Pretoria, South Africa

April 2020

Supervisor: Prof. Emil Roduner

Co-supervisor: Dr. Shankara G. Radhakrishnan

DECLARATION

I, Adegoke, Adesina Kayode, declare that the thesis, which I hereby submit for the degree of Doctor of Philosophy at the University of Pretoria, is my own work and has not previously been submitted by me for a degree at this or any other tertiary institution.

SIGNATURE: 

DATE: 10th April 2020.

DEDICATION

This thesis is dedicated to my:

Beloved mother: Mrs. Rachel Adegoke for her determination, encouragement and self-sacrifice to raise me after the death of my loving and caring father.

Wife: Rhoda Oyeladun; the love of my life.

Children: Toluwanimi and Temiloluwa; my precious gifts.

Siblings: my kindhearted people.

ACKNOWLEDGMENTS

I am privileged to express my unending gratitude to my God; Jesus Christ for the protection, guidance, inspiration and wisdom received to complete this Ph. D degree. My sincere respect and appreciation to all who inspired, guided and motivated me towards the completion of this Ph. D journey. Undertaking this degree inculcated strong research senses within me, and I also came about knowing many new things.

Firstly, I acknowledge and extend my profound gratefulness to my supervisor: Prof. Emil Roduner and co-supervisor: Dr. Shankara G. Radhakrishnan; for their exemplary guidance and constructive criticism throughout this research; I appreciate all your valuable guidance, direction and intent supervision at every stage of research work. The thesis would not have been completed without their constant guidance and help at every stage of the work. These two personalities have been a constant source of inspiration and help; they are cardinal to my success. They are role models; God will continue to lift them up.

I also would like to express my unending gratitude to the National Research Foundation and the World Academy of Sciences (NRF-TWAS) for the prestigious Doctoral Scholarship award (UID: 105453 & Reference: SFH160618172220 and UID: 121108, & Reference: MND190603441389). Also, I am grateful to the South Africa/France Science and Technology Research Collaboration (PROTEA) for the opportunity given to me to conduct part of my research at the Laboratoire IC2MP, UMR-CNRS, Université de Poitiers, France. I am grateful to Prof. B. Kokoh, Prof. C. Comminges, Prof. C. Morais and Paul, for their assistance during my stay in France.

My sincere appreciation to the Head of Department: Prof. Vinesh Maharaj and staff of the Chemistry Department for their unrelenting efforts in one area or the other. I also appreciate the help with and access to experimental techniques like XRD, SEM, and FTIR. I cannot forget

the efforts of my research group members: Prof. E.R. Rohwer, Dr. Sieglinde Bauermeister, Dr. Basia, Clarissa, Simphiwe and Mokgadi, for the wonderful role played, you are the best!

My special thanks to my wife Rhoda Oyeladun and my wonderful children: Toluwanimi and Temiloluwa for overwhelming me with their love, encouragement, support and understanding. Thank you “Nkem”, I love you and God bless you abundantly. I wish to immensely thank my mother; Mrs. Rachel Adegoke and in-law; Rev’d and Mrs. Oyewole, mentor; Prof. O. S. Bello, brothers: Solomon, Elijah, Sunday, Samson, Ademola, Akinloye, Oyedeji, Dr. Aderogba; sisters: Esther, Dorcas, Foyeke, Oyebimpe, Oyenike, Kemi, Grace, and my Cousins for their prayers and support. I cannot forget the kindness of my sister-in-law: Mrs. Oyeronke Olorode; of blessed memory!

I also acknowledge Rev’d Dr. & Mrs. Lekan Ajao, Rev’d Dr. & Mrs. Ajibade, Pastor & Mrs. Adelowo, Pastor Kemi Amuda, Rev’d Dr. & Mrs. Julius Mbu, Pastor & Mrs. Bamigbohun, Pastor Wole Daniel, Dn. Adetayo, Prof. Adedosu, Prof. & Dr. (Mrs) Ogunleye, Mr. & Mrs. Olaniyan, Mr. Afolabi, Mr. Kolapo, John, Dr. Oluwole, Kayode, Ezekiel, Olagoke, Justina, Chidinma, Tola, Tosin, Rasheed, Dr. Giwa, Church members and all who have contributed in one way or the other to this achievement, I appreciate you so much, God will enrich you tremendously.

TABLE OF CONTENTS

List of Figures

List of Tables

ABBREVIATIONS AND SYMBOLS

Ag/AgCl	Silver/silver chloride reference electrode
CA	Chronoamperometry
CCS	CO_2 capture and storage
CL	Catalyst layer
CO_2RR	Carbon dioxide reduction reaction
CV	Cyclic voltammetry
E^{θ}	Standard redox potential
$E^{\theta'}$	Formal potential
E_A	Activation energy
EIS	Electrochemical Impedance Spectroscopy
EtOH	Ethanol
EU	European Union
F	Faraday's constant
FA	Formic acid
FARR	Formic acid reduction reaction
FAOR	Formic acid oxidation reaction
FE	Faraday efficiency
FFP	Flow field plate
FID	Flame ionization detector
FTIR	Fourier Transform Infrared
FWHM	Full width at half maximum
GC	Gas chromatography
GCE	Glassy carbon electrode
GDE	Gas diffusion electrode

GDL	Gas diffusion layer
GHG	Greenhouse gases
ΔG^0	Standard Gibbs energy change
ΔH^0	Enthalpy change
λ	Wavelength
$\hbar$	Planck constant
HPLC	High performance liquid chromatograph
In_2O_3	Indium oxide
j	Current density
IPCC	Intergovernmental Panel on Climate Change
iPrOH	Isopropanol
IrO_2	Iridium oxide
IUPAC	International Union of Pure and Applied Chemistry
k	Equilibrium constant
k_B	Boltzmann constants
LSV	Linear Sweep Voltammetry
MEA	Membrane electrode assembly
MeOH	Methanol
mm	Millimeter
mmol	Millimol
mA/cm^2	Milliampere per square centimeter
mV/s	Millivolts per second
µL	Microliter
MPL	Microporous layer
NHE	Normal hydrogen electrode

NP	Nanoparticle
OECD	Organization for Economic Co-operation and Development
OCV	Open circuit voltage
ORR	Oxygen reduction reaction
PCET	Proton Coupled Electron Transfer
PEFCs	Polymer Electrolyte Fuel Cells
PEM	Proton conducting membrane
PEMFC	Proton exchange membrane fuel cell
PXRD	Powder X-ray diffraction spectroscopy
θ	Angle of diffraction
R	Molar gas constant
RCP	Representative concentration pathway
RHE	Reversible hydrogen electrode
ΔS^0	Entropy change
S	Surface area of electrode.
SCE	Saturated calomel electrode
SHE	Standard hydrogen electrode
STY	Space-time yield
T	Temperature
TaC	Tantalum carbide
TCD	Thermal conductivity detector
PTFE	Polytetrafluoroethylene
US-DoE	United States Department of Energy
WE	Water electrolysis
wt%	Weight percent

SUMMARY

Having been a hot topic for some time, the interest in recycling carbon dioxide to renewable liquid fuels or other valuable chemicals has rocketed since the adoption of the Paris Agreement on Climate Change. This is due to the EU ruling that from 2020, a considerable fraction of renewable fuel of non-biological origin has to be added to gasoline and the commitment of large air carriers like UA to go 50% carbon neutral by 2050. The primary novelty of this thesis was the development and conversion of the thermal catalyst indium oxide to an electrocatalyst that could do the conversion of formic acid and CO_2 at ambient conditions with water as the only hydrogen source and the second starting compound. Here, the synthesis of indium oxide (In_2O_3) and supported iridium oxide (IrO_2) electrocatalysts were done in-house. The crystallinities and average particle size characterizations were examined via powder X-ray diffraction. Scanning electron microscopy was used to study the surface morphologies of both electrocatalysts. Three different anodic electrocatalysts including 60:40 wt% IrO_2:TaC, 70:30 wt% IrO_2:TaC and 100:00 wt% IrO_2:TaC were fabricated and employed for water electrolysis, with 70:30 wt% IrO_2:TaC demonstrated to be of superior electrochemical activity and further employed for subsequent studies.

Currently, In_2O_3 is the best thermal catalyst for methanol formation from CO_2 [1]. Here, the as-synthesized thermal catalyst was converted to a cathodic electrocatalyst by firstly making electroconductive material in a nanosize form with very small crystallite grains, which contain numerous defects near the surface; thus, making it more conductive. This was used to prepare high-performance membrane electrode assemblies (MEAs). The reaction cell containing the MEA that was set up by spray-coating the respective catalyst inks onto either Nafion® or a carbon gas diffusion cloth. The PEM electrolysis cell configuration with Nafion® as the polymer electrolyte was used. It minimizes Ohmic losses, and a standard TaC-supported IrO_2 water-splitting catalyst served as the anode, titanium mesh served as anodic gas diffusion

layer, and the experiments were conducted at ambient temperature. The cathode consisted of In_2O_3 spray-coated on carbon paper which acts as a gas diffusion layer and titanium mesh current collector. The cathode electrocatalyst was enhanced by the addition of a small amount of polytetrafluoroethylene to the nanosized In_2O_3 to facilitate diffusion of FA and CO_2. The electrochemical characteristics were examined via cyclic voltammetry, linear sweep voltammetry and chronoamperometric methods. The infrared spectroelectrochemical cell was also used because it permits *in-situ* analysis of the change of reactant concentrations and ideally the identification of intermediates

Addition of PTFE to the In_2O_3 electrocatalyst layer for FARR has led to significant improvement in current density from 1.94 mA/cm^2 (without PTFE) to 66.0 mA/cm^2 (with 0.15 wt% PTFE) and 70.3 mA/cm^2 (with 0.30 wt% PTFE) which is a factor of ca. 34 and ca. 36 respectively at 2.4 V cell voltage. This further reduces the onset potential of the electroreduction by 0.4 V and notably, the cell Ohmic resistance was reduced by a factor of 15, implying that the activation energy of the electrode and the transport resistance in the porous structure are significantly reduced. This is due to the increase in the hydrophobicity in the porous electrocatalyst layer. The Tafel slope was also used to investigate the electrochemical reaction of water splitting, co-electrolysis of 4.30 M formic acid and water on In_2O_3 and PTFE-In_2O_3 cathodes. Tafel values of all the samples over the respective number of LSV cycles were consistent with each other. Tafel analysis of the PTFE-In_2O_3 electrode improves significantly with the lower Tafel slope in comparison with the PTFE-free In_2O_3 electrode.

The steady-state current density experiment in the absence of any flow showed excellent stability over the investigation period. A current density observed to be limited to ca. 26 mA/cm^2 in the absence of any flow over 24 h from the initial current density of 70.3 mA/cm^2, the limitation is a result of FA transport across the diffusion layers in the electrocatalyst surface. This behavior was further investigated using the Cottrell equation and

this was observed to qualitatively reproduce the experimental behavior, thereby confirming a diffusion layer that builds up, resulting in a reactant depletion near the electrode surface. For a long time, it was thought that formic acid is a dead-end that does not lead to larger product molecules. For the first time, the co-electrolysis of water and aqueous 4.30 M formic acid, the first stable intermediate of CO_2 electroreduction, results in a mixture of methanol, ethanol and isopropanol with a maximum combined Faraday efficiency of 82.6% at 3.5 V and a space-time-yield of $0.431\,g_{alcohol}h^{-1}g_{cat}^{-1}$ that compares well with results from heterogeneous catalysis. It was further discovered here that high Faraday efficiency of the alcohols and current density can be achieved under a relatively low overpotential by tuning the amount of PTFE used.

FTIR spectroelectrochemistry was used to monitor the disappearance of FA and the formation or disappearance of CO_2 reaction intermediates as a function of time and potentials. The consumption of FA propelled significant decreasing of absorption of up to 6 vibrational modes in the observation window including bands: at 3670 cm^{-1} belonging to the O–H stretching vibration, 3037 cm^{-1} assigned to the C–H stretching mode, 2120 cm^{-1} attributed to the C=O stretching mode, a double band near 1667/1589 cm^{-1}, assigned to the vibrational modes with major FA C–O stretching character, and finally one at 1225 cm^{-1} which are somewhat higher than corresponding literature values, suggesting interactions with the catalyst and the presence of the aqueous environment. In the experiment performed with CO_2 catholyte on PTFE-In_2O_3 (in the absence of FA), the CO_2 band disappears as expected with no FA build-up, suggesting that formic acid is bypassed as an intermediate. An additional convincing difference was that while R/R_0 is >1 dominated by the FA disappearance and CO_2 formation in FA catholyte, it is <1 in CO_2 catholyte, and the spectra revealed the CO_2 disappearance with the formation of intermediates and products; seen as a broad structured background. The CO_2

band changes in the positive direction, demonstrating that CO_2 is used up with the applied potential going more negative.

The CV experiments further established a cross-over oxidation peak which indicates multiple redox species or a multi-step parallel or consecutive mechanism with the PTFE-In_2O_3 cathode. This was due to the slow formation of redox-active intermediates and slow follow-up reactions occurring in the diffusion layer on the surface of the electrode. This further indicates that the appropriate amount of PTFE in the In_2O_3 catalyst layer would enhance the adhesion properties of the In_2O_3 catalyst layer on the carbon paper and create the hydrophobic channels in the catalytic layers. Finally, in agreement with the cyclic voltammetry, spectroelectrochemistry and electrolysis experiments, a plausible reaction mechanism for FA reduction to methanol on In_2O_3 cathode was proposed while the higher alcohols (i.e. C_2 and C_3 alcohols) may be formed through the same stepwise reduction pattern involving the different intermediate species formed. Therefore, this study established that the In_2O_3 electrocatalyst could do the conversion of formic acid (HCOOH) and CO_2 at room temperature and with water in place of hydrogen as the second starting material in contrast to the known methods which were achieved at elevated temperatures. Importantly, the addition of PTFE facilitated FA and CO_2 diffusion and enhanced the electrochemical performance of the In_2O_3 electrocatalyst.

Chapter 1

INTRODUCTION

1.1 Background of the study

The undeniable emission of anthropogenic greenhouse gases (GHGs) into the atmosphere remains a foremost cause of global climate change threatening global peace [2–6]. In fact, the issues of climate change have nowadays become a complex phenomenon. Atmospheric concentrations of carbon dioxide (CO_2) have been considered to be harmful and notorious pollutants and the significant contributor of GHGs. It increases yearly by approximately 2 ppm and thereby continues and has passed 400 ppm [2,3,6]. The fossil fuel combustion contributes about three-fourths of the atmospheric CO_2 increase [7]. In spite of the definitive goals of some nations to phase out fossil fuel in their power generations and also transportation sectors, this switch to the energy of renewable sources remains slow and dawdling, thus making the prediction futile and unproductive. As such, the world energy demands would still be largely fossil-fuels dependent in the coming years [8,9].

Up till now, the CO_2 capture and storage (CCS) technology has been given much attention over the years by various researchers worldwide, and very recently industrial-scale demonstrations of CCS were firstly commissioned owing to high carbon resources in CO_2 and its potential opportunities to be converted to high value-added products [10,11]. Based on this, lots of approaches for CO_2 reductions and mitigation of climate change have been considered: improvements of energy efficiency, reduction of economy carbon intensity, capturing CO_2 from flue gas and its consequent long-term storage following isolation from the atmosphere [4,6,12–14] are receiving considerable attention till date.

South Africa is a heavy carbon dioxide emitter to the atmosphere, to about 2/3 from point sources. Ca. 50% of it is due to electricity production from coal, another ca. 16% arises from Sasol's Fischer-Tropsch process in the production of gasoline and commodity chemicals

from coal. The most straightforward way of reducing CO_2 emission consists of replacing coal-fired electricity generation by renewable energy, in particular solar (SA has one of the highest solar irradiances, on par with Australia) and wind. Besides this, recycling CO_2 using renewable energy sources offers an ideal way of reducing its climatic consequences. Liquid fuels from recycled CO_2 allow for a sustainable way of maintaining the mobility of our society. They are easy to transport over large distances using existing infrastructure, *i.e.* pipelines, trucks, and ships [15,16]. Also, they are efficient for storing larger amounts of energy in chemical form, much better than batteries or other means of energy storage, and thus even be lucrative for export. They can also be admixed in high fractions to gasoline and used in combustion engines. Alternatively, hydrogen can be produced on-board of automobiles via electro-reforming of methanol (CH_3OH) for use in hydrogen fuel cells [3], or it can be converted straightforwardly to dimethylether or to gasoline under doubling of its energy density.

To avoid extra emissions of CO_2, the electrochemical conversion of CO_2 to value-added chemicals remains a viable method to be employed, owing to its ability to use electricity from renewable energy sources (e. g. solar energy, wind energy and hydropower) [14,17–19]. In this manner, the anthropogenic carbon cycles would be closed through the conversion of CO_2 to liquid fuel materials and some other valuable chemicals (Fig. 1). The crucial technological challenges to achieve this are developing cheap and more importantly earth-abundant catalytic materials capable of reducing CO_2 electrochemically such that cost-effective processes with higher efficiency, controllable selectivity, and long-term stability are achieved [3,12,19–24].

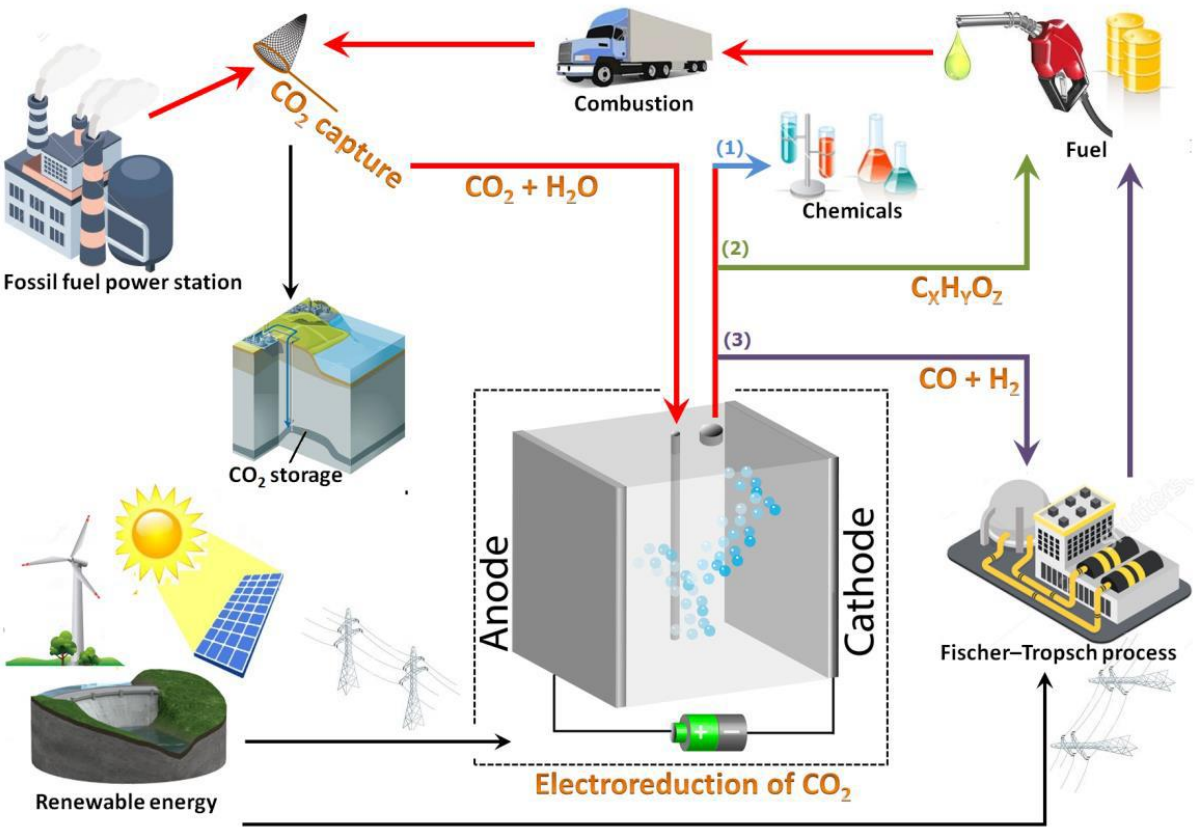

Fig. 1.1: Production of carbon-neutral fuels via reduction of CO_2 by electrochemical methods powered by renewable energy sources. (Adapted from reference 25).

The cathodic CO_2 reduction reaction (CO_2RR) has engrossed a significant consideration recently, especially as an alternative to photosynthesis for the production of organic raw materials or fuels. The major reaction product in aqueous solutions is formic acid (or the formate ion), with Faraday efficiency (FE) over 90% on Sn and In metal electrodes [26]. However, the reduction of formic acid is more difficult and has been thought to be a dead-end over the years. The best electrocatalyst materials are metals with high hydrogen overpotential (e.g. Pb, Sn, In) and low point of zero charges [26,27]. This latter condition is related to the adsorption and desorption of reaction intermediates. Formic acid has limited uses and hence its conversion to liquid fuels is of crucial importance for the efficient recycling of CO_2 [28,29]. Electroreduction of CO_2 involves $6e^-$ to methanol during which formic acid is realized as an intermediate. Thus, this study has adapted to formic acid electroreduction in order to confirm the reaction mechanism of CO_2 reduction. It investigated the synthesis and study of indium

oxide for the electrocatalytic CO_2 reduction. We started this by first understanding the concept through the process of water electrolysis and formic acid reduction (FARR) to fuels prior to CO_2 reduction.

In a search of a suitable catalyst we ventured into studying a simpler indium oxide (In_2O_3) system. In_2O_3 is an n-type semiconductor having a wide bandgap of about 3.6 eV at room temperature. It is a reducible oxide that is frequently employed together with tin oxide (SnO_2) and widely used in optoelectronics, photocatalysts, lithium-ion battery, solar cell, biosensor, sensors, electro-optic modulators and field-emission display [1,30–32]. Its superior activity and selectivity in numerous CO_2 catalytic transformations including a photocatalytic reduction to CO [33], methanol steam reforming [34,35] and electrochemical conversion to formic acid [36]. The latter gives us insight into its ability to reduce formic acid to more valuable fuels. The density functional theory (DFT) investigations on both defective [37] and non-defective [38] CO_2 hydrogenation also show that methanol formation is the most favorable product with the reaction mechanism observed to follow cyclic creation and annihilation of oxygen vacancies. Investigations using impedance and IR spectroscopies revealed an enhanced conductivity for In_2O_3 when exposed to H_2 at mild temperature [39], which suggests that vacancies could be present at the relevant conditions for methanol formation. However, subsequent analysis on commercial In_2O_3 in CO_2 hydrogenation suggested a rate of reaction comparable to the Cu-ZnO system but only a moderate methanol selectivity of about 55% [40] against the DFT predictions [37]. Very recently, an In_2O_3/ZrO_2 catalyst was reported for 100% methanol yield with a remarkable selectivity and stability over 1000 h on stream using operating conditions for industrial methanol synthesis while a conventional $Cu/ZnO/Al_2O_3$ catalyst suffered a rapid deactivation under the same conditions [1]. Lately, formation of CH_3OH was reported with selectivity exceeding 80% for PdIn intermetallic nanoparticles [41]. All these are thermal catalysts with the conversion to fuels carried out at a higher temperature. Nevertheless, indium

oxide (In_2O_3) as bulk is an insulator and the best thermal catalyst for methanol production [1]. However, we need electroconductive material with very small crystallite size (powder) having nanosized grains, which near the surface is richer in defects, thus making it more conductive. This project attempts to convert this thermal catalyst to an electrocatalyst. Here, In_2O_3 was synthesized by simple chemical routes, converting this thermal catalyst to an electrocatalyst using it to prepare membrane electrode assemblies (MEAs) and demonstrating its electrochemical selectivity to produce C_1 to C_3 alcohols from formic acid at room temperature. This fabrication method involves the preparation of a series of catalyst inks for spraying to carbon paper (Torrey) supported electrodes to produce an electrolytic membrane. In this way, high-performance electrocatalyst MEAs could be prepared by improving the contact between the catalyst layer and the electrolyte. This preparation method is cheap, efficient and allows lowering the catalyst loading to achieve a high utilization efficiency [42–44].

1.2 Rationale and Motivation

Carbon dioxide is a linear molecule and non-polar. It represents carbon in its highest oxidation state and is thermodynamically extremely stable. The reaction of CO_2 to produce target products, e.g. fuel, involves substantial input of energy to break the inherent thermodynamic barrier which mainly accompanies the water oxidation half-reactions. Moreover, the kinetic barrier necessitates catalyst utilization for limiting the over-potentials, thereby promoting the product selectivity. To achieve this, the necessary energy required for CO_2 conversion must come from a sustainable source. Intermittent electrical energy supplied from wind turbines, tidal or solar irradiance sources could successfully be put in storage as fuel derived from CO_2. The CO_2 reduction via a single electron to form the $CO_2^{\bullet-}$ encompasses substantial energy penalties considering the reduction potential (–1.9 V *vs.* NHE) coupled with a re-arrangement from a linear structure of CO_2 to form bent structures. On the contrary, the

CO_2 electrochemical reduction in the presence of proton sources have the ability to sustain significantly lower energy costs, thereby producing more desirable and appropriate products like alcohols, formic acid, etc. While Proton Coupled Electron Transfer (PCET) allows the transformation to be more electrochemically favorable, it introduces additional complexities having the requirements of the catalytic systems for managing multi-proton or multi-electron pathways. These facets are predominantly relevant to reaction selectivity in that CO_2 reductions could lead to the realization of preferred products without hydrogen formation.

However, the synthesis of organic /inorganic electrocatalyst for CO_2 reduction also remains challenging due to difficulties in controlling the composition and morphology. Despite the notable success in the existing methods employed for the reduction of CO_2 to a sustainable energy technology not only in emission control but also in the production of alternative fuels, a clear picture of the mechanism is still problematic in the synthesis of stable electrocatalysts. Furthermore, most of the reported methods are time-consuming; hence restricting their use in the conversion process and, thereby, making the synthesis difficult to scale-up from environmental and economical viewpoints. The conversion of CO_2 to value-added products (alcohols, formic acid, etc.) could be achieved in several ways. Thus, the energy required for conversion processes should emerge from processes that do not emit more GHGs directly into the atmosphere. The current technologies available for the conversion of CO_2 do not fall within these criteria. To overcome the limitations, there is a need to develop a process that is not only green but also able to address most of these challenges; the energy required for the reduction process preferably must be supplied from renewable and/or alternative sources. Thus, to draw attention to unresolved or unaddressed issues, it is particularly interesting to study the mechanistic aspects of electrocatalytic CO_2 reduction for energy storage over In_2O_3 electrodes by firstly converting a thermal catalyst to an electrocatalyst with a well-defined structure. Over the years, it has been noted that existing techniques involved some toxic organic chemicals that

are hazardous to the environment. To the best of my knowledge, there is no report on indium oxide electrocatalyst with formic acid as the starting material while only very limited studies are available on some indium compounds for conventional CO_2 reduction, and until now the reduction mechanism is not clearly understood. However, the preparation or system design for In_2O_3 electrocatalysts with well-defined structure and morphology and their application in the electrochemical reduction of CO_2 or formic acid to valuable chemicals is a hot topic of recent times.

A number of thermal catalysts are available that can convert carbon dioxide to methanol with reasonable yield and selectivity at significantly elevated temperature and pressure, using gaseous molecular hydrogen. Hydrogen has to be produced first in a separate step, and renewable energy is available primarily in the form of electricity instead of by thermal energy. Furthermore, most previous electrochemical attempts have used aqueous solutions of CO_2. Partly for reasons of poor solubility and mass transport limitation, these have shown poor current densities. In contrast to thermal reactions, which are reversible, the energy landscape of electrochemical reactions can be changed massively by application of a forward bias voltage. Since the reaction of CO_2 with water to methanol is endergonic by $\Delta G° = 700$ kJ mol^{-1}, this is impossible to do in a thermal reaction. A forward bias of 1.21 V, slightly less than that for water electrolysis, offsets this energy so that the hydrogenation reaction can basically occur at a considerably lower temperature than thermal hydrogenation with H_2. The liquid products condense from the product mixture, which favors their formation against the gaseous products (principle of Le-Chatelier and Braun).

Moreover, as opposed to most electrochemical work in literature, which uses aqueous solutions, CO_2 will be provided from the gas phase so as to facilitate transport. In order to minimize Ohmic losses, it is essential to use a membrane setup with short transport distances between the electrodes. Here, both electrodes need to be equipped with gas diffusion layers to

avoid flooding of the active sites and permit the CO_2 or formic acid reactant to access the cathode and the product O_2 to leave the anode. The focus is entirely on the cathode catalyst. A high density of active centers is necessary to achieve high current densities; ideally about 1 A cm^{-2} is common for water electrolysis.

1.3 Information on aim and objectives

This thesis aims at the development and conversion of the thermal catalyst indium oxide to an electrocatalyst that can do the CO_2 conversion near room temperature and with water electrolysis giving hydrogen as the second starting compound.

Research objectives

(i). Synthesis and preparation of standard anodic electrocatalytic powder and membrane electrode assembly for water electrolysis.

(ii). Synthesis and preparation of indium oxide cathode and membrane electrode assembly for HCOOH and CO_2 reductions.

(iii). Characterization of anodic and cathodic powder using different characterization techniques.

(iv). Potentiostatic electrochemical measurements with HCOOH and CO_2 at ambient temperature and 1 bar CO_2 pressure.

(v). Establishment of product analysis and determination of product selectivity and Faraday efficiency.

(vi). Dynamic electrochemical measurements with HCOOH and CO_2 using cyclic voltammetry.

(vii). *In-situ* FTIR spectroelectrochemical measurement with HCOOH and CO_2.

(viii). Scientific evaluation of the mechanisms of the reaction for the electrocatalytic conversion of HCOOH and CO_2 to fuels and writing of global conclusions.

Chapter 2

LITERATURE REVIEW

2.1 Rising CO_2 levels and the necessity for clean power technologies

Humanity faces the challenges of a transition to an energy economy based on fossil fuels-free origin [9,45,46]. Many scientific proofs have linked the increasing level of CO_2 to urbanization and industrialization [47] which has drastic consequences on the rising of sea levels and the average temperature [48]. It has been reported recently that the energy consumption worldwide (Fig. 2.1a) is expected to reach 736 quadrillion Btu (quads) in 2040 from 575 quads in 2015, an increase of 28%, (though this depends on the scenario). The atmospheric concentration of CO_2 worldwide has risen from ~330 ppm in 1981 to ~ 412 ppm in December 2019 (www.CO2now.org) and is projected to continue increasing with a similar trend [49,50].

Globally since the mid-1700s, fossil fuels (the major cause of GHG) represented the principal energy resource for the growing economy [9]. Currently, we are facing the results or penalties of two centuries of dramatic economic growth driven by these fossil fuels including energy security, degradation of the environment, climate change, etc., with the outlook that fossil depletion might occur in 50-100 years [9]. Above all, energy is indispensable for all facets of life in this contemporary world. The global emission of CO_2 from burning fossil fuels for the year 2017 reached 33 gigatons, which is twice the amount in which CO_2 is naturally absorbed back into the environment through land and ocean carbon sinks. CO_2 has been projected to not only contribute to climate change in the next few decades but also major soil, water, air pollution, which is already affecting many cities today, especially in developing countries. Fig. 2.1b presents a global utilization of fossil fuels and currently, about 35 gigatons of CO_2 are emitted yearly. The predicted cumulative emission of CO_2 of the "business-as-usual" and the "liquid sunshine" cases (Fig. 2.1b) fit within the predicted emission of CO_2 of

the IPCC demonstrative concentration pathways (RCP)8.5 and RCP4.5 scenarios[51]. The emission of CO_2 of OECD countries continues to decline since around 2010 [52], which is projected to be continued. By comparison, emission of CO_2 among the non-OECD countries is expected to significantly upsurge during the next decades.

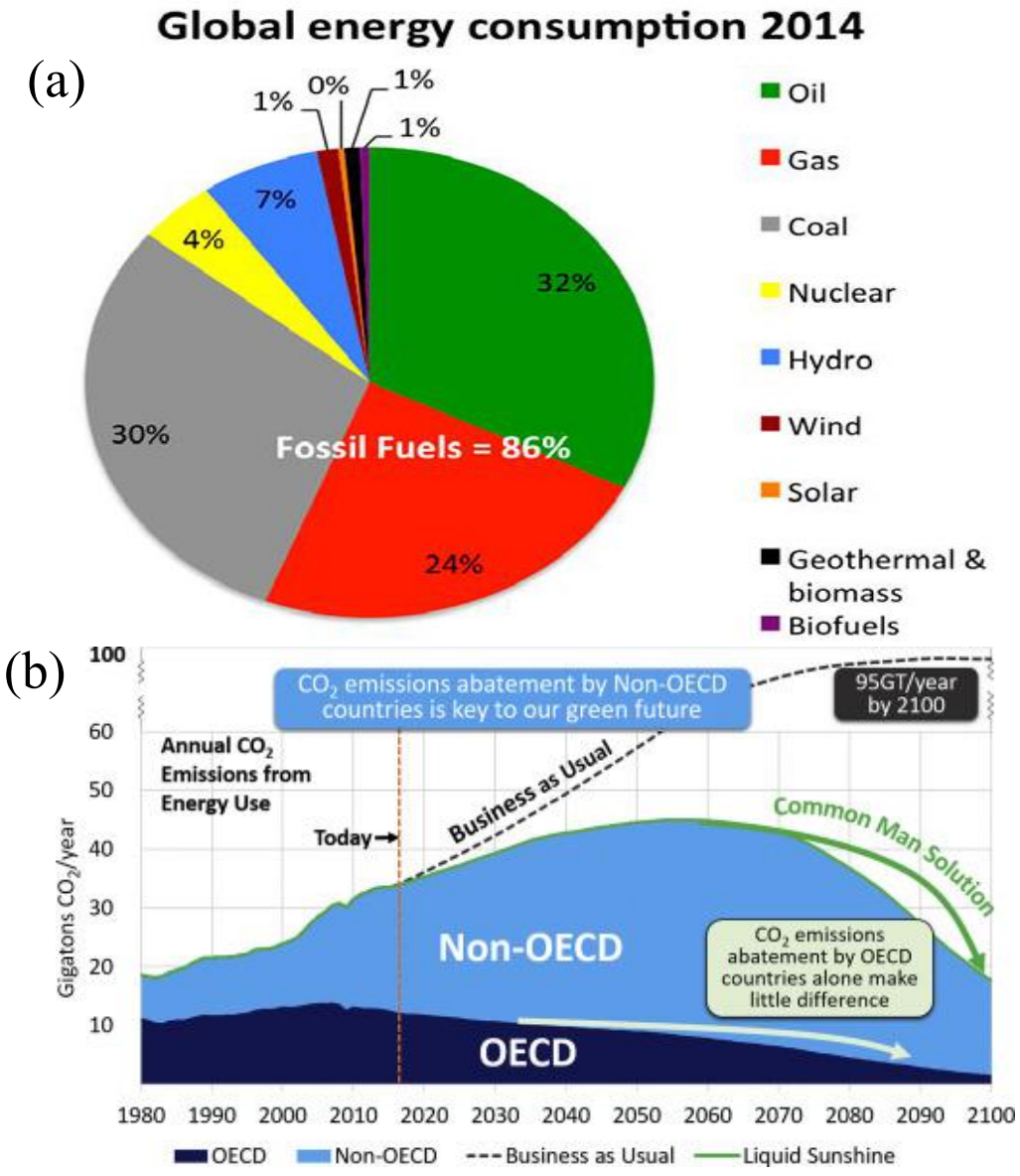

Fig. 2.1: (a) 2014 global energy consumptions revealing a dependency on fossil fuels [79] and (b) Emission of CO_2 from OECD and Non-OECD Countries. Under the business-as-usual scenario, CO_2 emissions in 2100 will triple today's emissions. (Reprinted from reference 9 with permission from Elsevier).

Nonetheless, developing an innovative process to recycle the captured CO_2 is becoming an attractive prospect owing to its ability to allow CO_2 valorization. In this way, CO_2 is converted to valuable or useful products including fuels and other hydrocarbons. It should be noted that only an effective chemical conversion of CO_2 to some liquid fuels of high importance such as dimethylether, methanol, ethanol, would allow its recycling and the re-use to important fuels. This approach is believed to offer a feasible solution to the increasing environmental problem of CO_2 in the atmosphere and its associated global warming, while at same time, it renders renewable fuels environmentally carbon-neutral [12,17,53]. Such an approach would be considered as a potential candidate having the ability to offer solutions to the environmental crisis resulting from increasing atmospheric CO_2 and associated global warming.

Recently, the production of carbon-neutral renewable fuels or materials by chemical recycling of CO_2 has proven to be a feasible and powerful fresh approach having gradual and practical implementations [18,54]. As comprehensive in whole reviews on the valorization of CO_2 (for instance, [3,19–22]), diverse groups of conversions of CO_2 are eminent, including inorganic, biological, chemical, electrochemical and photochemical method. In the last few years, the electrochemical CO_2 valorization approach remains promising with wider and important attention. An advantage of electrochemical CO_2 reduction is that; unlike many other hydrocarbons' transformations, it can easily be performed under ambient conditions. However, being at the experimental level there is still considerable work to be done to bring the process up to a commercial level. The typical current density has been on the order of milliamp per square centimeter (mA/cm^2) of the electrode surface, whereas industrial water electrolyzers operate at up to 2 A/cm^2 [23,55]. This current state can be improved as it has been for water electrolysis by improving cell design and electrode configuration. However, this still has to be demonstrated in the literature. For this analysis, it has been assumed that the reduction cell can operate at the same level as typical water electrolyzers.

Numerous works have revised diverse investigations in the studies of electroreduction of CO_2 and many mechanistic aspects coupled with reaction pathways have been extensively discussed [23,55–61]. Therefore, the CO_2 conversion by electrochemical reduction to liquid products remains a hot topic. It simply involves the supply of electrical energy for establishing a potential between two electrodes so as to allow the transformation of CO_2 into its reduced forms. Many researchers have proposed that CO_2 capture from point sources (e.g power plants), followed by its conversion into fuels or chemical feedstocks, can be practically feasible [62–65]. This makes the CO_2 conversion by electrochemical techniques elegant long-term solutions, owing to their mild mode of operation for the conversion, and also the valuable products can be produced selectively [18,66,67]. In this manner, the electrochemical method has been highlighted to be a future sustainable approach to produce liquid fuels if the CO_2 reduction to liquid chemical products were made with high efficiency. [18,57].

Several factors are responsible for the type and yield of CO_2 conversion products using electrochemical reduction. Such factors are forms and nature of materials employed as the cathode, the reaction medium, as well as temperature and pressure conditions. At ambient conditions in aqueous media, the major products obtained largely depend on the cathode used. The Cu electrodes are known for mixtures of hydrocarbon products, typically methane, ethylene, and alcohol; while metal electrodes such as Ag, Au, or Zn are known for producing CO as the main product. Other metals like In, Hg, Pb, or Sn are widely known for their selective productions of methanol, formic acid, etc [23,55,58,68]. Formic acid, and methanol are among the valuable chemicals obtained via electrochemical conversion of CO_2 and they appeared to possess the preeminent chance of having practical developments of economic and technically viable processes [69]. Many traditional industries employed these chemicals for a variety of purposes such as animal feed additives, silage preservations, textile finishing, chemical intermediates, and so on [70]. Principally, formic acid has a growing demand in many industrial

processes including pharmaceutical synthesis, pulp, and paper production [71]. Interestingly, formic acid has been singled out as a potential fuel candidate for fuel cells with lower temperatures [72]. As currently produced, formate/formic acid is somewhat costly [67] due to the negative environmental impacts of their manufacturing processes [73] which involved the hydrocarbon oxidation or thermochemical processes that centered on the carbonylation of methanol [70].

However, methanol remains one of the world's top ten petrochemicals [1,74]. Beside this, it is a promising bridging technology to replace fuels or serve as chemical feedstock besides oil, because syn-gas, that is required for producing methanol, is available from many sources, such as coal or biomass [75]. In addition, the synthesis of methanol offers currently the sole opportunity of employing CO_2 emissions on a large scale [76]. Moreover, methanol is an important starting material for the synthesis of many products of technical importance. Large efforts worldwide indicate the urgent nature of this substantial challenge, as evidenced by a large number of recent reviews [37,54,85,77–84]. These efforts also included detailed quantum-chemical calculations for both, thermal heterogeneous and electrocatalysis [59]. Nevertheless, the subject is still awaiting a real breakthrough, in particular; as regards selectivity to the desired liquid fuel product and its yield.

Currently, the conception of the "hydrogen economy" is one of the approaches which offer reliable promises of meeting energy demands (Fig. 2.2). In this way, hydrogen could be stored in larger amounts and used as an energy carrier and chemical energy when needed in mobile and/or stationary applications and transportation [86–88]. However, industrial production of hydrogen is mainly by methane steam-reforming [89]. This has detrimental effects, because it contributes largely to emissions of GHG [90,91]. Nowadays, water electrolysis (WE) has been developed [91–93] which only accounts for about 4% of the total hydrogen produced (Fig. 2.2). The concept is that if the required energy input to generate hydrogen emanates from

renewable sources, zero-emission of GHG in the overall energy conversion cycles can be attained. Fuel cells are other crucial technologies for generating energy. Here, chemical energy is transformed into electrical energy through the electrochemical conversion [94–96].

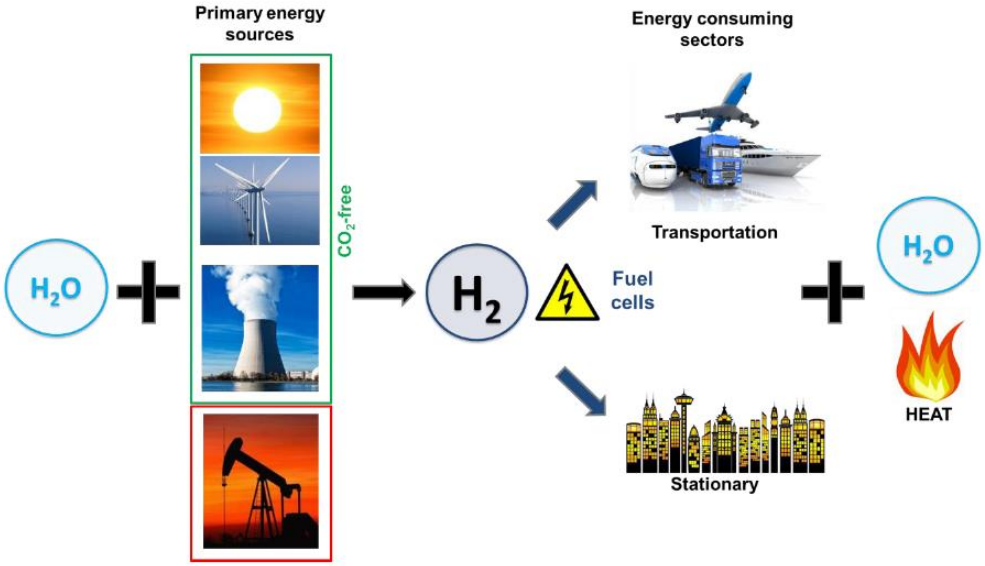

Fig. 2.2: Hydrogen economy-based cycle. (Adapted from reference 97)

2.2 Reduction of fuel cell costs

The Polymer Electrolyte Fuel Cells (PEFCs) have been arguably systems with most potential automotive applications. The US-DOE recently set strict cost targets for fuel cell technology to allow the prevalent integrations into the world market [93]. From 2006 to 2010, there was a drastic decrease in the cost estimate of PEFC systems (Fig. 2.3) which continued to decrease in the following year upon further costs cut down till they became relatively insignificant. The annual estimated cost in 2015 was approximately $53 per kW (considering the high volume of manufacturing of about 500,000 units/year), while the system costs target by DoE for 2020 at a large production scale is $40 per kW [93].

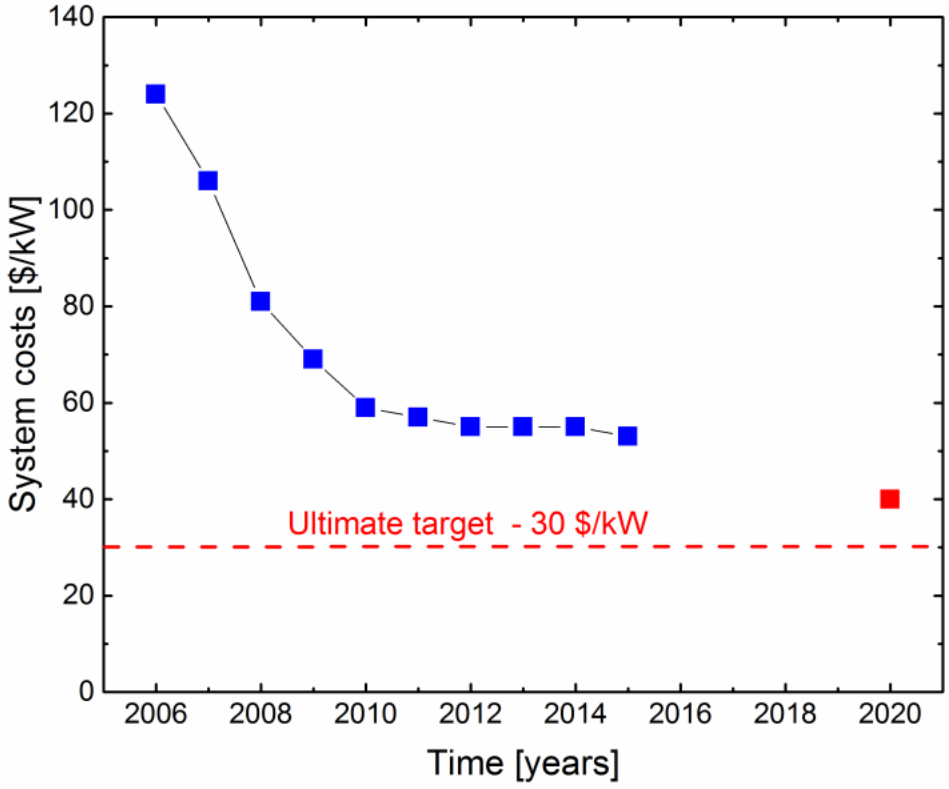

Fig. 2.3: Estimated targeted automotive costs for fuel cell systems from 2006 to 2020. (Adapted from reference 93).

2.3 The basic concept of CO_2 electrochemical reduction reaction

This section only discusses the basic principles behind the CO_2 electrochemical reduction. Numerous researchers have reported detailed information and also provided outstanding reviews on the subject of Carbon dioxide reduction reaction (CO_2RR) [20,58,105–110,88,98–104]. In CO_2RR, electricity is supplied into the electrochemical cell that contains aqueous solutions of dissolved CO_2. The CO_2 reduction takes place at the cathode and is balanced by the electrolytic dissociation of H_2O at the anode. This thereby supplies the necessary proton required for CO_2 hydrogenation via a proton exchange membrane. For example, Fig. 2.4, schematically illustrates the reduction of CO_2 to CO which is similar to the process in a PEM fuel cell [3,111–113].

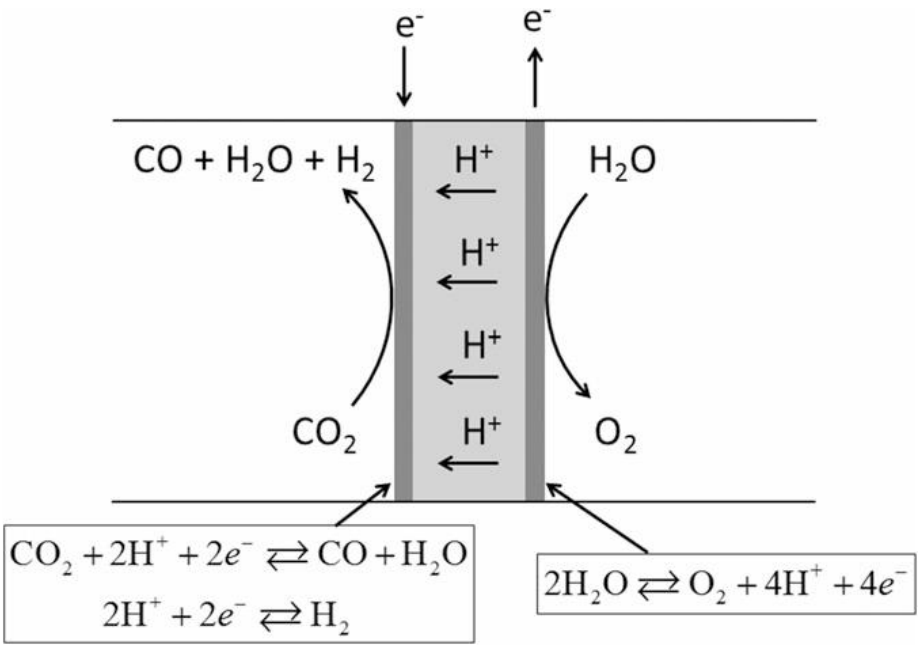

Fig. 2.4: Electrochemical cell design of CO_2 reduction to CO [111].

Looking at another example of the conversion of CO_2 to CH_3OH, it was found that oxidation and reduction occur at the anode and cathode, respectively [88,111]. The reactions in Scheme 2.3 show the overall chemical reaction and their respective potentials versus the saturated calomel electrodes (SCE) for the conversion of CO_2 to CH_3OH [88]. To speed-up reaction rates, the catalyst is typically deposited on the electrode surfaces.

Cathode: $CO_{2\,(aq)} + 6H^+ + 6e^- \rightarrow CH_3OH + H_2O$ $E^0 = -0.22$ V (Scheme 2.1)

Anode: $3H_2O \rightarrow \frac{3}{2}O_2 + 6H^+ + 6e^-$ $E^0 = +0.99$ V (Scheme 2.2)

Overall: $CO_{2\,(aq)} + 2H_2O \rightarrow CH_3OH + \frac{3}{2}O_2$ $E^0 = +1.21$ V (Scheme 2.3)

The CO_2RR is accomplished in an electrolysis cell, which consists of electrode pairs containing cathode and anode. The catalysts are coated on the electrode surfaces, and the electrolyte transfers ions through to the anodes and the cathodes. At the positively charged electrode (i.e. anode), oxidation products from reaction site are transported and discharged through its pores; at the negatively charged electrode (i.e. cathode, where electrons enter the substrate (i.e CO_2)), CO_2 passes through its surface to the reaction site and the electron is

transported from the current collector to the reaction site through the electron-conducting particles (Fig. 2.5) [114].

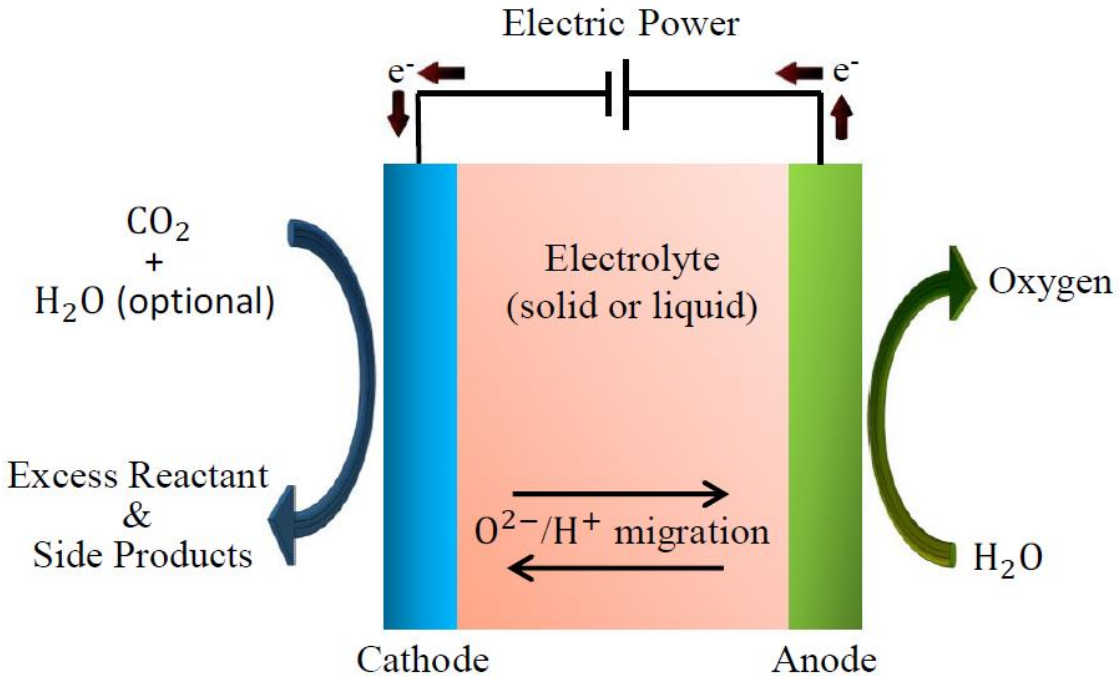

Fig. 2.5: Basic electrolytic cell design of electroreduction of CO_2 to liquid fuels [114].

Many researchers have suggested mechanisms involving CO_2 electroreduction [23,114–118], the one depicted in Fig 2.6 being the most widely accepted [23]. It illustrates that following the adsorption of gaseous CO_2 as $*CO_2$ (ad), it is (a) electronated to produce CO_2^-(ad). (b) Upon a subsequent reaction of $*CO_2^-$(ad) and H_2O, the formed OH^- ions are released and the adsorbed HCO_2 undergoes further electronation to produce (c) HCO_2^- (formate ions). (d) As electrons are paired after electronation, the HCO_2^- species are desorbed from the electrode surface [114]. There are several steps involved in the CO_2 electroreduction processes that occur at the cathode and adjacent active sites. They are (i) CO_2 adsorption, (ii) formation of three-phase interfaces, the reduction of CO_2, the evolution of HCOOH, etc. The anodic functions have an implementation similar to that of conventional hydrolysis cells (such as (i) catalytic oxidation reactions, (ii) product removal) [118–120].

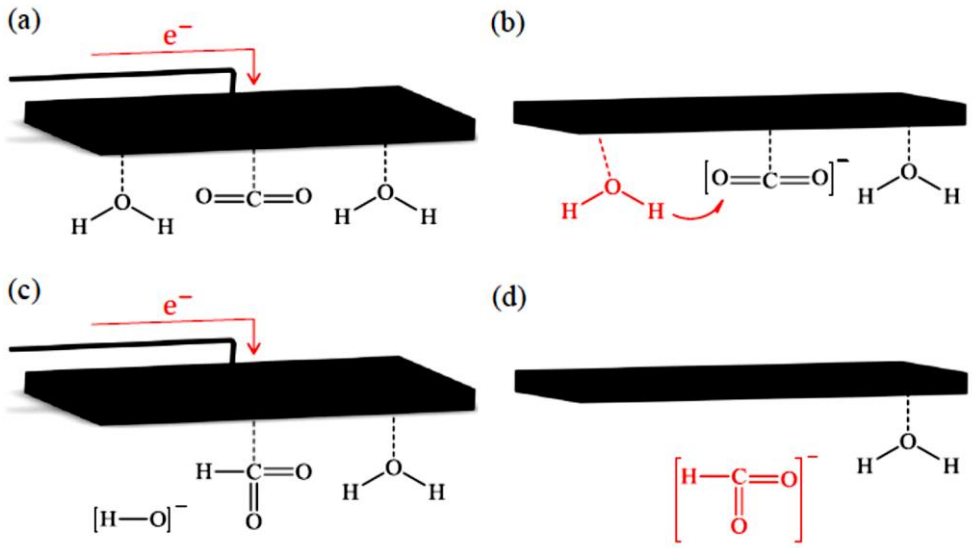

Fig. 2.6: Mechanism involved in CO_2 electroreduction in an electrolysis cell [114].

In this section, the focus is on the cathode side because this side is the limiting factor and a bottleneck in the performance of the electrochemical cell. To ensure a continuous supply of CO_2 to the electrochemical cell, it is basically bubbled through the solution until the reaction process is completed. Although, a significant challenge is a fact that the solubility of CO_2 is limited, thus, remains a serious burden that needs to be addressed.

2.4 Advantages of electrochemical approach over other methods of CO_2 conversion

Conversion of CO_2 to fuels can be achieved through photochemical, thermochemical, and electrochemical approaches. By way of required operational conditions, an electrochemical conversion could be achieved at ambient pressure and room temperature, thereby bringing greater feasibility for a reduction of atmospheric CO_2. Also, the conversion of CO_2 through the electrochemical method is known to have a highly controllable characteristic and also the potential for very high conversion efficiencies. Its industrial prospects and practicability provide the electrochemical approach with numerous advantages over other methods. The electrochemical method has a wide range of conversion products such as formic acid esters [121], formamides [122], carbon monoxide [123,124], methane [125–127], methanol [36,75,103,128–131], formic acid [114,132–135], dimethylcarbonate [136,137], alkylene carbonates [122],

carbamic acid esters [121], lactones [121], aliphatic polycarbonates [121] while photochemical conversion produces only limited products such as formate [101], formic acid [138], carbon monoxide [139–141] and methanol [138,142].

2.5 Proton conducting membranes

Proton conducting membranes or polymer electrolyte membranes (PEMs) are made of solid polymer electrolytes. They conduct protons effectively and block the electron and gas transports. The Nafion® membrane manufactured by DuPont® is currently the most promising material used by many researchers. PEMs are produced from perfluorosulfonic acid ionomers and comprise sulfonated-polytetrafluoroethylene (PTFE, Teflon) backbones with a thickness of about 15-30 µm. The anchor for conducting the proton in the hydrated membrane is the presence of sulfonic acid groups (consisting of SO_3^- + H_3O^+). Today, the Nafion® membrane has been widely reported for its immense contributions to the costs of fuel cells, thus providing a new research opportunity to searching new and low-cost membrane alternatives that have their root on different technologies, including hydrocarbon-based membranes [143] or radiation grafting [144].

2.6 Catalyst layer

A catalyst layer (CL) is a porous layer composed of: (i) catalyst particle, (ii) conductive supports (carbon), (iii) ionomers as a binder in the catalyst layer. CLs may be coated/deposited on either membrane or gas diffusion layers (GDLs) or microporous layers (MPLs). Typically, a CL is between 5 µm and 10 µm thick and coated on the membrane (or micro-porous inner side layer). Usually, the catalysts loadings ("mass of precious metal per geometric surface area") are lower at the anode side and higher at the cathode side so as to have an increased available specific surface area that would compensate the sluggish kinetics of the oxygen reduction reaction (ORR). The three-phase boundary in the catalyst layer plays

important roles. For a reaction to occur an interface must exist between the solid particles and the liquid and gas (hydrogen/oxygen).

2.7 Electrochemical cell designs, components, and configurations for the CO_2 reduction reaction

Numerous works reported on CO_2RR are on electrocatalysis with the main focus on catalytic electrode reactions. Numerous laboratory investigations were performed typically in a small batch electrochemical cell under a standard condition, but the practical applications were not captured or reflected. Their studies have vital significance for identifying the optimum catalytic system(s) and for gaining insight into mass-transport limitations occurring at the cathode. But it is also important to develop practical implementations as to designing scale-up continuous flow devices having industrial feasibility and applications [145].

Configurations of electrochemical cells have diverse conceptualizing options since ages [146] as shown in Fig. 2.7. Certain configurations or electrochemical cell designs have less or no suitability for the CO_2RR. For instance, the fuel cell-like configuration shown in Fig. 2.7a might possibly be unfavorable/suitable for the reduction of CO_2 owing to the competing hydrogen evolution reaction (HER). In another configuration (Fig 2.7b), pH buffer must be introduced to prevent the excess flux of protons to the cathode. However, in such cases, the cell resistances might be extremely high if the buffer layers are thick. The next alternative/option is the use of an anion exchange membrane (AEM) shown in Fig. 2.7c, thereby simplifying the buffer-layers-based systems. Nonetheless, another option is to use a Nafion® membrane in its K^+ form, thereby allowing the OER to be carried out in an alkaline condition with the CO_2 reduction occurring at the cathode, (Fig. 2.7d). Noteworthy success was the breakthrough in the implementations of gas diffusion electrodes (GDE) now having wide applications in electrochemical cells for electroreduction of CO_2 to liquid fuels and chemicals [147] (Fig. 2.8). The GDE currently remains the most promising for improving the

mass transfer characteristics. Nevertheless, a GDE has its associated drawback owing to its ability to accumulate the liquid phase product in the pores of the GDE, thereby resulting in blockage of flow channels or pore structures [148]. The presence of liquid water in the GDLs can only have a negative influence on performance. It blocks pores and therefore increases the resistance to diffusive transport.

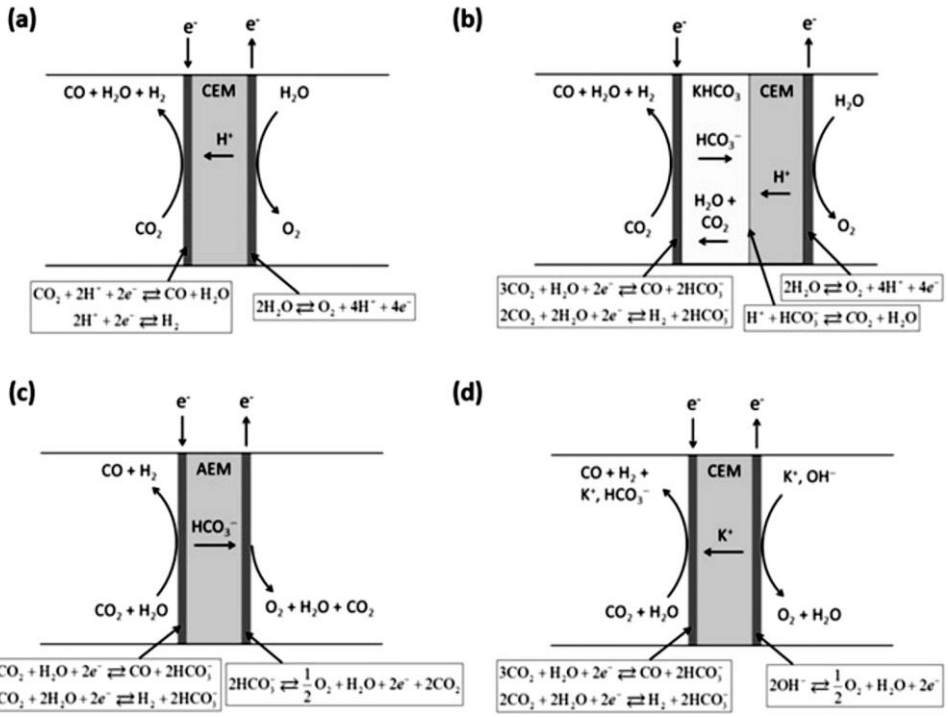

Fig. 2.7: Convectional electrochemical cell configurations: (a) cation exchange membrane as the electrolyte, (b) modified cell with pH buffer layers of $KHCO_3$ (aq), (c) anion exchange membrane as the electrolyte, (d) cation exchange (Nafion®) membrane in the K^+ form [146]. (© IOP Publishing. Reproduced with permission. All rights reserved).

The present-day cathode and anode of PEFCs are symmetrically constructed. Though, each corresponding layer may have certain characteristics that differ between the cathode and anode because individual layers are mirrored regarding the central components and the membranes. The individual layers are briefly described as follows:

2.8 Microporous layer

The microporous layer (MPL) is composed of a mixture of carbon particles (either carbon black or spherical carbon onion) and hydrophobic polymers (e.g. PTFE). Under a

particular humidity condition, the MPL is now accepted as a principal component to achieve a high power density [149]. The significant functionalities of an MPL are (i) the reduction of CL flooding, (ii) provision of water improvement managements especially when fully humidified gases are used, (iii) reduction in CL-MPL electrical constant resistance owing to their close contacts and decreased in roughness, and (iv) decrease in CL and membrane degradation due to smoother MPL surfaces [150–153].

2.9 Gas diffusion layers

In short, the thickness of a GDL is between 100 and 500 μm. Its porosity is about 0.7-0.9 with average pore diameter ranging from 10 μm to 40 μm. A GDL is stacked between the flow field plates and membranes (or MPL as the case may be). It conducts electrons and heat, provides mechanical supports for both membrane and CL, and also transports the reactant gas(es) while removing the liquid water produced electrochemically. In this project, the GDL is used owing to the aforementioned benefits (Fig. 2.8). The GDLs are three-dimensional porous materials composed of diverse arranged fashions of carbon fibers. Fig. 2.9 shows that the GDL has attracted enormous attention from researchers with more than 300 research articles published yearly between 2011 and 2016, altogether over 3500 publications are currently available. This shows a continuously growing interest in GDL usage owing to the crucial roles it plays in successful PEFC technologies (Fig. 2.8).

The flow field plates contain channels that ensure the gas distributions over the whole cell active areas. At the same time, the channels collect and remove the water, and electrons needed to be gathered by the plate. There are several types of flow field geometries including straight parallel, serpentine, or inter-digitated flow channels that can be used [154]. The variations of their design provide some possibilities of facilitating one mode of

transport over others (e.g. convection over diffusion in case of an inter-digitated flow-field) [97,155].

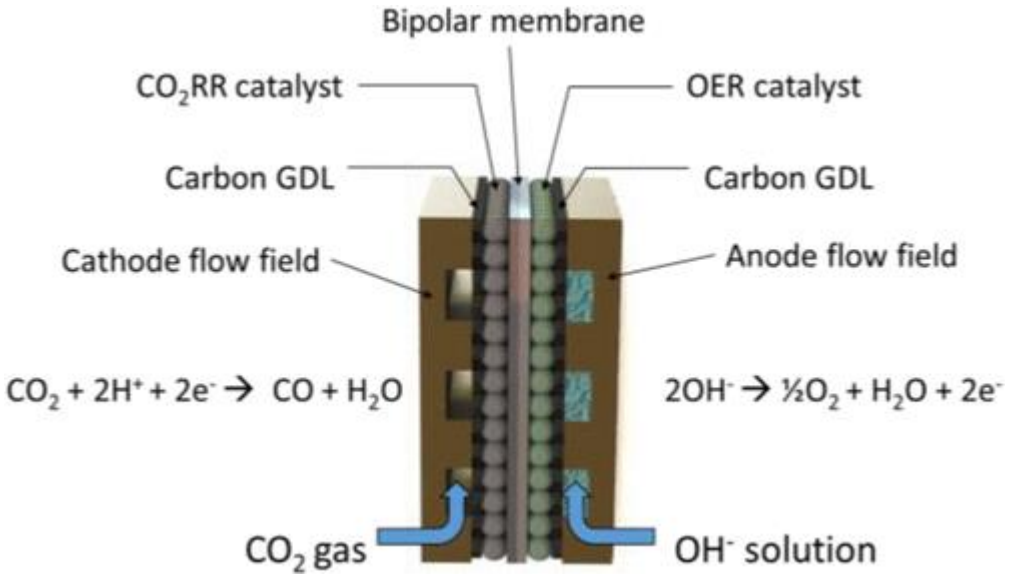

Fig. 2.8: Gas diffusion layer (GDL) electrochemical device for the reduction of CO_2. (Reprinted with permission from reference 147. Copyright © 2016, American Chemical Society)

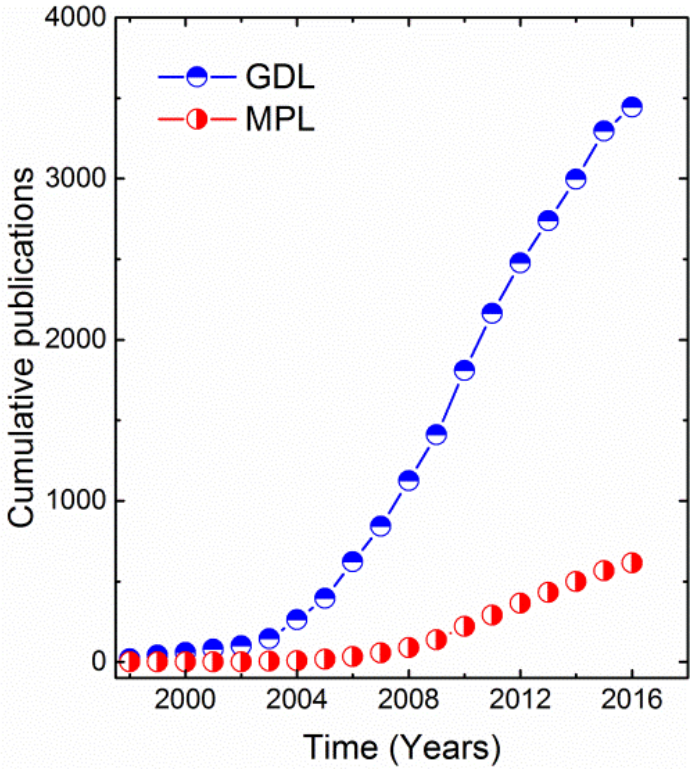

Fig. 2.9: Cumulative publication numbers on the usage of MPLs and GDLs since 1998. (Adapted from reference 97).

2.10 Electrode structure

Generally, in an electrolysis cell, the electrode encompasses the catalyst layer. The multifunction in electroreduction of CO_2 to liquid fuels, e.g. formic acid includes:

(i). Adsorption of CO_2 gas;

(ii). Transportation of CO_2 gas from substrates to the catalyst layers;

(iii). The creation of active reaction sites on the surfaces for the substrate to adhere to;

(iv). The distribution of HCOOH from the catalyst layer into the electrolyte;

(v). Conduction of proton and electron by low resistance.

The important effects of cathode structures on the operation of the cell with respect to the transport process of gaseous CO_2 cannot be overemphasized. From planar metals to mesh structures, followed by porous configurations, the performance, and improvement of the cell is largely dependent on the developments of electrode structures.

Numerous researches on the planar metal electrode have been ongoing since 1990 and a number of catalytic materials such In, Pb, Sn, Hg, Tl, Cd, etc. are proven to be competent with proper addition of modifier atom(s) [68]. However, several constraints have been noticed which limit their effectiveness. Such restrictions include small surface areas, limited current density, and low CO_2 solubility which in turn led to unsatisfactory concentrations of CO_2 at the electrodes. In attempts to curb these problems, the copper mesh was proposed as a working electrode, thereby maintaining high catalytic activity. Previous experiments have indicated that copper mesh electrodes have advantages over the planar types, showing that in acidic electrolytes, unwanted poisoning reactions can be greatly suppressed and three-phase interfaces can be formed [156–158]. A high CO_2 concentration is maintained throughout the electrolysis cell process [156,159].

In general, GDEs have been proven to be appropriate remedies for low transfer rates of CO_2 in the cathode surface(s). A GDE contains not only the conventional catalyst

layer(s), but also the gas diffusion layer(s) typically prepared from a dense array of porous carbon fibers[62,146]. There are woven carbon cloth fabrics and non-woven carbon paper. It also provides good mechanical support and protects from corrosion. Other multi-roles include:

(i). CO_2 pathway and diffusion of the electrolyte;

(ii). Intermediary between proton and electron transfer;

(iii). Channel for removal of products so as to prevent flooding of the cathode;

(iv). Heat transfer medium.

The GDE was proposed first in 1956. It has conductive granules positioned at the interior of the porous electrode body electrically connected with the current tap [160]. Recently, promoting the efficiency of the three-phase regions and the stability of the system became another focus of researchers. To address this, the numerical optimizations of GDEs design parameters were conducted. Such parameters include hydrophobicity, porosity, and permeability. These have been investigated by 1-D mathematical models and GDE geometric dimensions [161].

As mentioned earlier, one major competitive advantage of GDE is its very porous structure. Lately, the porosity has been further raised with the rapid development of nanotechnology. Via spectroscopic and electrochemical investigations, nanoporous globular, or irregular manganese dioxide particles have shown a higher degree of agglomeration, long-term stability and a more effective three-phase interface region in nanostructured GDEs than the traditional composite electrodes [162].

Furthermore, towards the end of the 20th century, extensive investigations on GDE materials were reported with amorphous carbon materials such as carbon-fiber and -black observed to possess high conductivity and chemical stability as well as a high diffusion rate [163]. Thus, highly porous carbon material was observed to profoundly increase the rate of mass

transfer of gaseous CO_2, thereby improving the ability of transmission of charges within the electrodes.

Moreover, the valuable effects of microporous layers (MPLs) have also been discovered as the added advantage to CL and GDL. MPLs are thin porous layers comprised of carbon NP mixed with hydrophobic materials. Modeling work demonstrated that MPL-insertion between CL and GDL during a lower temperature reaction involving electroreduction of CO_2 would have a great effect in decreasing water saturation for GDL to ca. 5% from ca. 25% [164] because MPL has a small porosity. This implies that MPL with small pores has the ability to suppress the formations and growth of interfacial droplets on the surface of CL[165]. It was experimentally proved that double-sides MPL cells would accomplish better performances than the so-called single side MPL cell under the same operating conditions, including cell voltage(s), reactor resistance and current density [166].

Although a GDE is known for its excellent performance, the role of binders cannot be overlooked. A binder highly influences the serviceability of the whole system. It does not only play a role in gaseous reactants and high charge transport rates but also for the satisfactory adhesion of catalysts to the surfaces. Several binders have been used over the years due to their excellent chemical stability, electrical conductivity, hydrophobicity and better adhesiveness. Binder allows the transfer of gaseous CO_2 to the electrolytes via the electrodes and blocks the electrolytes in the system pore layers. PTFE as a binder was reported as having good catalytic performances with the maximum current efficiency of 22% at –2.0 V vs. SCE for the conversion of CO_2 to HCOOH [167].

Besides PTFE, Su *et al.* have expanded the research of polymer binders to materials including conventional Nafion, polybenzimidazole and polyvinylidene difluoride blend, observing that PTFE and polyvinylidene difluoride performs better than Nafion and the polybenzimidazole polymer, whose maximum power density and maximum current density

were recorded to be 0.61 Wcm^{-2} and 0.52 Acm^{-2}, respectively [168]. Blending polymeric binder with other materials has been attempted and GDEs with catalytic composition were fabricated based on a mixture of silver/nickel and polymeric binder, showing better reactor stability and reactivity of gaseous reactants.

In addition to efforts made on inner structure optimization, coating technology has also brought progress to GDEs' development. Methods of preparing catalytic layer (e.g. airbrush, screen-print, or hand-paint) have been compared [169]. It was observed that the overall performance of the electrolytic cell is largely dependent on the catalyst uniform distributions and lesser particle agglomerations, which means that layers with uniform distributions and small agglomerations perform better. Depositing CLs using a fully-automated air-brushing technique was reported to lead to a 56% enhancement in electrode performance and drastic improvements in electrode-to-electrode (and cell-to-cell) reproducibility [169].

Particularly, Pb-coated GDEs for CO_2 conversion to HCOOH have been reported to show high reaction rates with current density and FE as high as 115 mA/cm^2 and ≈100%, respectively, at the applied potential of -1.8 V vs. SCE [170]. Another high-performance catalyst, Ru-Pd was also shown to exhibit high electrocatalytic performance with GDEs; the FE was 90% while the current density at −1.1 V vs. SCE was 80 mA/cm^2. A similar result was demonstrated when Zn- and Cu-based phthalocyanines were coated on GDEs to produce HCOOH with current densities as high as 100 mA/cm^2 [171].

Moreover, to achieve more efficient three-phase regions and high porosity, the incorporation of nanotechnology into GDE developments was tested based on investigating microporous and mesoporous materials, therefore new insight was developed from nanostructured carbons to develop electrodes for electrochemical reduction of CO_2. For instance, CNTs were tested by researchers which observed that a cylindrical nanostructure with a big length-to-diameter ratio, showed a high mass transfer rate, a more structured three-phase

boundary and better confinement effects [172,173]. Gangeri *et al.* also reported on Fe/CNT and Pt/carbon nanotube showing improved productivities and stabilities for CO_2 conversion to liquid fuels. Similar observations were reported by others [174,175]. It was concluded that CNT electrodes have a promising potential to advance CO_2 conversion to liquid fuels.

2.11 State-of-the-art IrO_2 electrocatalyst and supporting materials

Oxygen evolution remains a bottleneck in the water electrolysis. The energy losses at the anode in both PEM and alkaline electrolyzers owing to the higher overpotentials has been attributed to the sluggish kinetics of the OER. It has been established extensively that RuO_2 and IrO_2 are unique active electrocatalysts for OER during WE. However, RuO_2 is known to suffer from deactivation; due to dissolution in alkaline and acidic environments, whereas, IrO_2 shows the best trade-off between the stability and electrocatalytic activity in these media [176,177]. Iridium is among the least abundant earth elements, but the use of cheaper abundant materials is desirable. This has remained a major challenge in PEM electrolysis [176].

Since 1966, the unique activities of Ru and Ir have been investigated for WE in acidic media [178], while 10 years later, the electrocatalytic activities of the OER on various binary alloys and metals were compared in acidic media [179]. The primary investigations started from the catalyst in the metallic forms (oxide films) on the surface at higher anodic potentials during the OER [180]. In comparison with the others, Ir (IrO_2) and Ru (RuO_2) outperformed Au, Nb, Pd, Pt, and Rh for the OER in acidic media [178–181]. The lower activity of Pd and Pt was observed to cause by the high resistance of the oxide films formed on the metal surfaces. On the other hand, RuO_2 and IrO_2 exhibited higher electronic conductivities [182]. These were attributed to the metal-distances and radii of the cation that had values that allowed overlapping of the inner d-orbitals, that is in turn responsible for the electron conduction [183]. Comparing RuO_2 and IrO_2, while they both exhibited a similar activity for the OER, Ru has the advantage of high abundance in nature, but RuO_2 suffered from dissolution and/or corrosion during the OER in

an acidic environment to form RuO_4 [184]. Though IrO_2 experienced corrosion, but to a very much lesser extent [185,186], it was therefore considered more favorable than RuO_2 and others. Consequently, IrO_2 has been the focus of many researchers for PEMWE studies.

Unfortunately, iridium is both expensive (1085 $/troy ounce as of 1st December 2011) [187], and scarce (approximately 50 times less abundant than Pt [187,188]. The electrochemical industry accounted for about ¼ of its total demands in 2010 [187,189]. The imminent practical application of the process necessitates the reduction of IrO_2 at the anode of PEM water electrolyzers [190]. The search for more cost-affordable PEM electrolysis systems has led to numerous alternative electrocatalysts which are all based on the three main routes shown in Fig. 2.10. One major approach to achieve this is the use of electrocatalyst supports; non-reactive materials that are not only readily available but also inexpensive [191]. Examples of available supporting materials are titanium carbide [192], tantalum carbide [187], silicon carbide-silicon [193], indium tin oxide [194], and antimony doped tin oxide [195]. Among the above literature, tantalum carbide has been proven to be suitable as an anode electrocatalyst support since it is stable in the strongly reducing environment that is harsher than in a fuel cell [187,190]. The roles of electrocatalyst supports include: (i) they enable the synthesis of smaller crystallites of IrO_2 since they offer crystallization centers during the deposition of IrO_2 which at the same time reduce the probability of their agglomeration [187]. (ii) the unsupported particles are smaller than the supported particles which are beneficial during the preparation of the CL because; larger particles do not penetrate deeply into the layer but stay in good contact with the PEM [187]. This therefore favors the electrocatalyst used to achieve high efficiency. (iii) electrocatalyst interactions with the supports may influence the electrocatalytic property of the resulting material owing to the synergic effects [187].

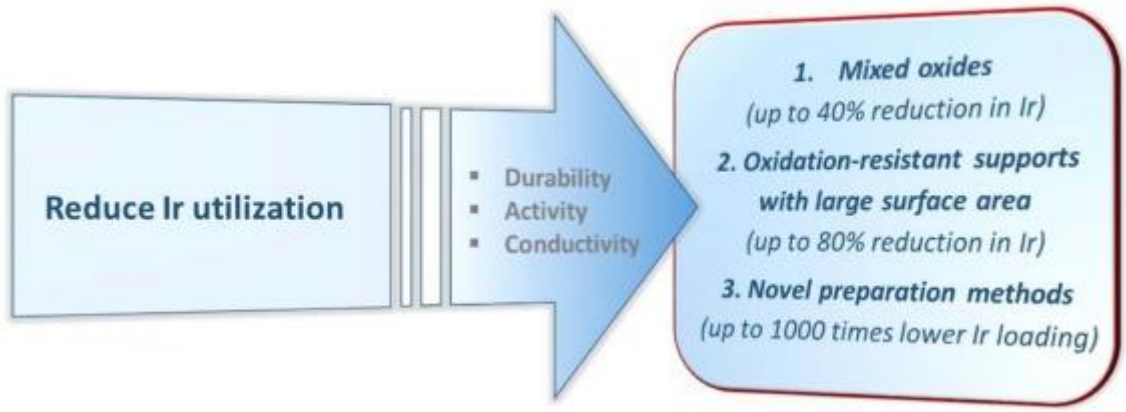

Fig. 2.10: Strategies for reducing noble metal utilization in PEM OER electrocatalysis. (Reprinted from reference from reference 176 with permission from Elsevier).

2.12 Recent literature surveyed on In_2O_3 electrocatalyst

In heterogeneous electrocatalysis, the use of metal electrodes or OD-metal electrodes that has an HER overpotential has been one of the common methods for improving the selectivity towards carbon products [196]. It has been of great interest to better understand the way of controlling the selectivity of carbon product obtained from the reduction of CO_2 and also to better design the electrocatalysts; in which the product selectivity could be finely tuned [197]. Indium is one of the least active metals for HER [196]. Detweiler *et al.* reported that In and In_2O_3 NPs could produce formate with high selectivity in an aqueous environment [36,198,199] and observed that a native surface oxide layer on an In metal electrode and In_2O_3 NP would be reduced electrochemically to In^0 in the absence of CO_2 [36,198,199]. However, in the presence of CO_2, indium oxide was not reduced to In^0, but an In-CO_3 surface adsorbed intermediate formed on the oxide layer. This was shown to be responsible for the formate formation via the two-electron, -proton reduction. Based on the key role of oxide layers in the mechanism for formate formation on the In-based electrocatalyst, they hypothesized that if electroreduction of CO_2 occurred directly on an In^0 surface, (for example by reducing the surface oxide layer to In^0 *in-situ* before exposure to CO_2), the selectivity of the product may change. Prior evidence showed

that an Indium based-electrocatalyst prepared through *in-situ* electrochemical deposition selectively reduced CO_2 to CO in an acetonitrile-containing-imidazolium ionic liquid [200].

Recently, a carbon-coated In_2O_3 nanobelt was demonstrated to convert CO_2 to CO and CH_4 [201]. Shaughnessy, *et al.* [196] showed that the selectivity of CO_2 electroreduction on an In-based electrocatalyst can be tuned to produce CO as against the earlier reports for formate production. They reported a lower onset potential of −1.0 V vs Ag/AgCl in the aqueous electrolytes. Formation of an In^0–In_2O_3 composite was first electrochemically observed by reducing In_2O_3 NP *in-situ* before exposure to CO_2. Whereas, upon exposure to CO_2, the In-based nanocatalyst electrochemically converted CO_2 to CO near a 100% selectivity. This was attributed to direct exposure of In^0 to CO_2 in solution, which did not exist owing to the native layer that formed on the In metal. Their study further showed that CO could be selectively collected *in-situ* by using the Pt Scanning Electrochemical Microscopy tip electrode during the voltammetry experiment as it was produced on the electrocatalyst electrode. This ensures the feasibility of obtaining accurate potential-dependent measurements for the production of CO [196]. In addition, the formation of syngas was boosted on supported Cu/In_2O_3 catalysts core/shell NPs by Xie *et al*. [202] and the mechanistic studies showed that the synergistic effects between the lattice compressions and doped Cu/In_2O_3 shell might enhance the binding of *COOH on Cu/In_2O_3 NP surfaces resulting in the generation of an enhanced CO relative to Cu and In_2O_3 electrocatalyst. Also, other studies have reported the production of CO, formic acid, or oxalic acid from various In-based electrocatalysts [59,170,203–210].

Chapter 3

THEORETICAL BACKGROUND

3.1 Electrochemical terminologies

3.1.1 Current density and exchange current density

The current density, *j*, remains a major parameter used to determine the performance of electrocatalysts. It can be defined as the current per unit of electrode geometric surface area. This is a vector quantity having a magnitude of electric current per cross-sectional area at given points and applied potentials. If the current density at a potential is high, then the reaction rate of electrochemical reactions would also be higher. Also, the lower the potentials (in absolute value terms), the lower the overpotentials of the reactions in such systems. Hence, the utmost desired electrocatalyst and reactor configuration should be able to produce high current density at a potential close to standard Nernst potentials (E^o) versus SHE (the condition of zero overpotential). In this work, the overall current density for the formic acid reduction was typically determined by dividing the current by the geometric surface area of the working electrode. As a measure of the reaction rate, this parameter is vital for practical applications, since it determines the electrolyzer size and the cost of the process [2].

The exchange current density (j_0) is defined as the forward current density when it equals the backward current density so that there is no net reaction. It is a good measure of the activity of a catalyst for a given reaction. It can be considered as background current to which the net current observed at various overpotentials is normalized. The transfer of electron process of redox reactions, written as a reduction in the equilibrium potential, continues at the electrode/solution interface in both directions, and the current density is, therefore, the electric current per unit area of the cross-section [211–213].

3.1.2 Determination of the onset potential and Ohmic resistance from the linear sweep voltammetry plots

Throughout this work, the onset potential was defined as the potential at which the electron transfer process for a specific redox reaction begins (i.e. on-) as indicated by rising in the current from zero as shown in Fig. 3.1. The Ohmic resistance is determined by taking the inverse of the slope of the Ohmic part of the linear sweep voltammetry (LSV) curves. From Fig. 3.1, two significant regions can be seen which are (i) the region in which there is an exponential increase in current density as electrode potential increases up to around –0.26 V and the charge transfer is the rate-limiting step. (ii) the second region is linear with predominant Ohmic resistance (around –0.011 to –0.260 V) with membranes as the major contributors owing to a linear current increase with potential. Ohmic resistances can therefore be determined by finding the inverse of the slope of the Ohmic region, the unit is Ωcm^2.

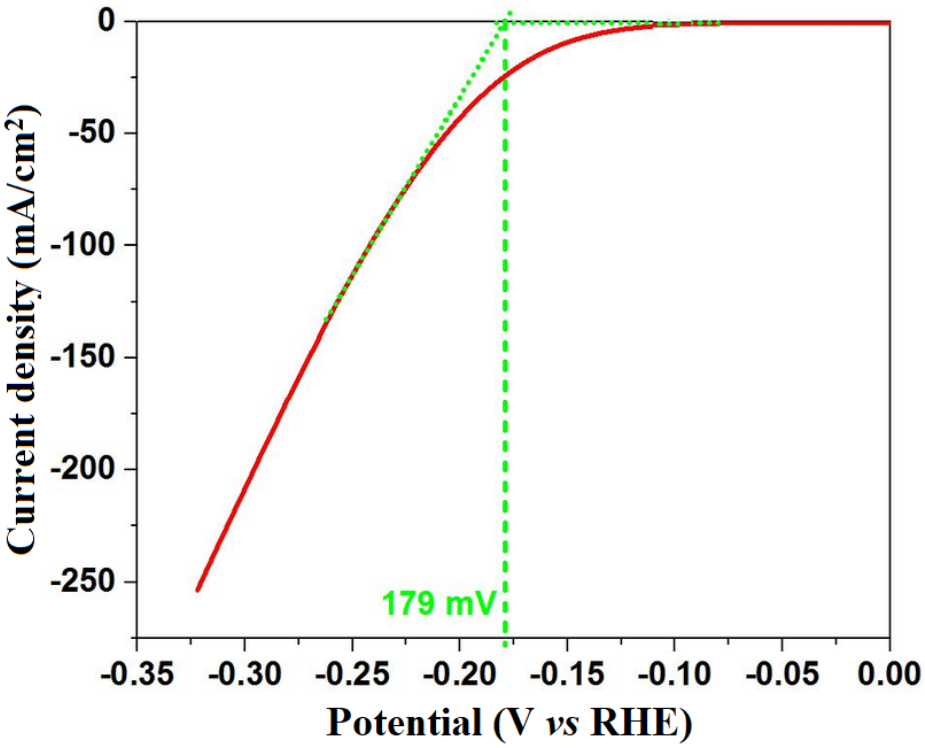

Fig. 3.1: Typical LSV curve showing the onset potential (0.1M KOH as electrolyte and Ag/AgCl as reference electrode).

3.2 Thermodynamic considerations

The thermodynamics aspect of possible products or substances from the conversion process of CO_2 is illustrated in Fig. 3.2 with their respective Gibbs free energy of formation for CO_2 reduction products. Obviously, CO_2 is a molecule with high stability and considerable energy input, optimized reaction condition and an active catalyst are needed for a CO_2 chemical conversion process into any carbonaceous fuel to take place. It must be noted that the chemical conversion reactions are largely determined by the difference in the Gibbs free energy (shown by the Gibbs Helmholtz relationships below) between the reactant and product under a certain condition of a chemical reaction.

$$\Delta G^0 = \Delta H^0 - T\Delta S^0 \qquad (3.1).$$

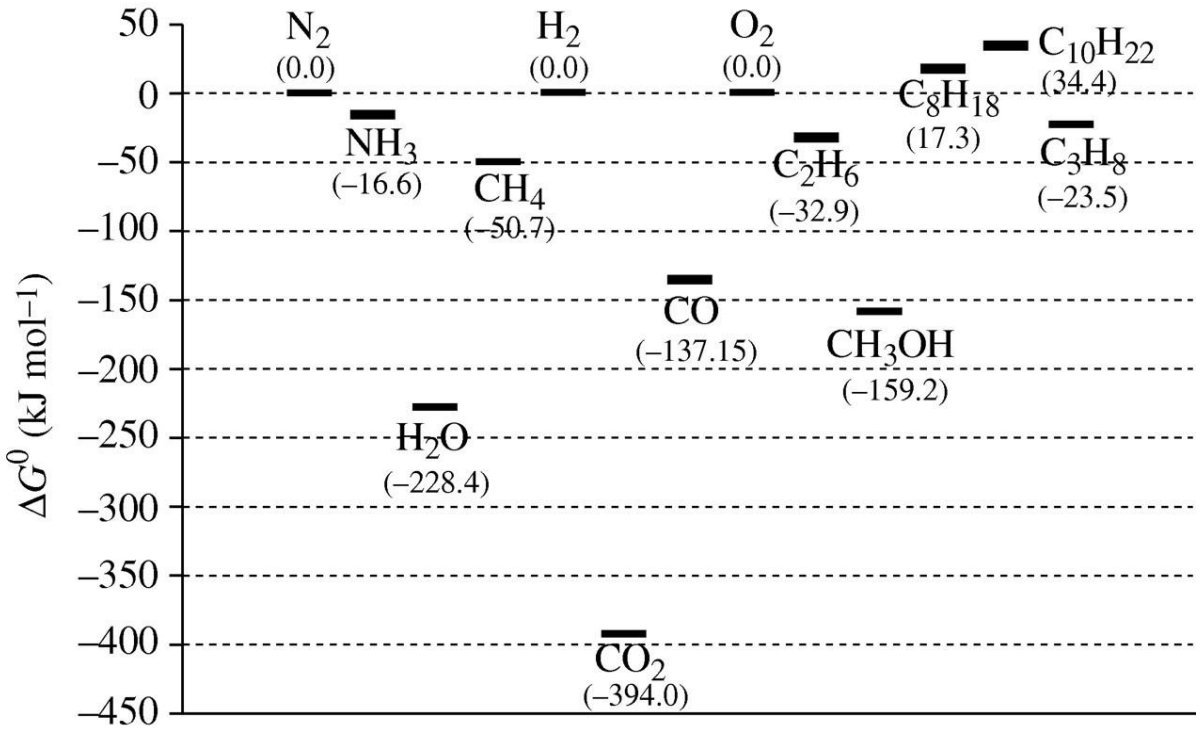

Fig. 3.2: Gibbs free energy of formation for some selected CO_2 reaction products with ΔG^0 taken as a reference point for the constituent materials [3]. Here, ΔG^0 for the constituent elements is taken as the reference point (Temperature is assumed to be 298.15 K).

Moreover, any further attempt for using CO_2 as chemical feed-stocks, the ultimate reaction products and their relative stability in comparison to the reactants must be taken into a cognitive account. Neither ΔH^0 nor $T\Delta S^0$ is favorable on the Gibbs free energy for conversion of CO_2 to fuels [113]. The bonds between carbon and oxygen are quite strong and require high energy input for reduction. Therefore, the enthalpy term ΔH^0 remains a noble initial guide to assess the thermodynamic feasibility and stability of converting CO_2 to fuels. In addition, CO_2 is chemically inert and among the most stable molecules having a linear geometry [113]. To break C=O bonds and to bend its linear molecular structure demands a huge energy input and suitable catalysts [106]. Again, the ΔG^0 for the transformation and conversion of just one molecule of H_2O to H_2 and $1/2O_2$ is 237.2 kJ mol^{-1} (under standard conditions) [108]. Conversely, the CO_2 reduction with H_2O into liquid fuels or oxygenates, e.g. ethanol, remains an uphill reaction having a high positive ΔG^0 of 818.3 $kJmol^{-1}$ and 702.2 $kJmol^{-1}$, respectively, thus making the reduction of CO_2 to fuels quite striking challenges [110].

Moreover, Freund *et al.* [113] observed that any remarkable progress in using CO_2 as a valuable reactant towards the synthesis of fuel would only arise from the judicious usage of novel and innovative catalytic chemistry, thus making the physicists, engineers and material chemists to have high potential impact. It was also noted that positive change in free energy is not sufficient evidence of not pursuing potential suitable CO_2 reactions. Thus, the relationship $\Delta G^0 = -RT \ln K$ gives information on product yields at equilibrium showing that a favorable reaction kinetics might be obtained. On this basis, given that kinetics is favorable, the reduction of CO_2 to CO might be possible at the surface of the metals and other catalytic materials such as nano-scale metal [174,214]. The Song group [105,106] noted that "*There appear to be some perceptions . . . that* CO_2 *conversion would be so endothermic that its conversion would not be feasible".* Obviously, large numbers of chemical and manufacturing industries are now operating globally on the basis of a strong and highly endothermic nature of the chemical

reaction (Scheme 3.1) such as syngas and hydrogen production from hydrocarbons steam-reforming, production of a high volume of "merchant hydrogen" in fertilizer, food and gas industries.

$$CH_4 + H_2O \rightarrow CO + 3H_2 \ (\Delta H^0 = +206.3 \text{ kJ mol}^{-1}) \qquad \text{(Scheme 3.1).}$$

Considering a general electrochemical reaction:

$$A \rightleftarrows B^{n+} + ne^- \qquad \text{(Scheme 3.2)}$$

where A and B are the oxidized and reduced species, respectively, and *n* symbolizes the number of electrons transferred in the reaction. When controlling the potential of a metallic electrode, the Fermi level will rise, provided negative potential is applied, which energetically favors the electron transfer from the metal to the substrate. As the electrons are transferred from electrode to the substrate, the energy level of the electrode will decrease, whereas, the energy level of the substrate will increase, until equilibrium is reached. This phenomenon can be illustrated diagrammatically as shown in Fig. 3.3.

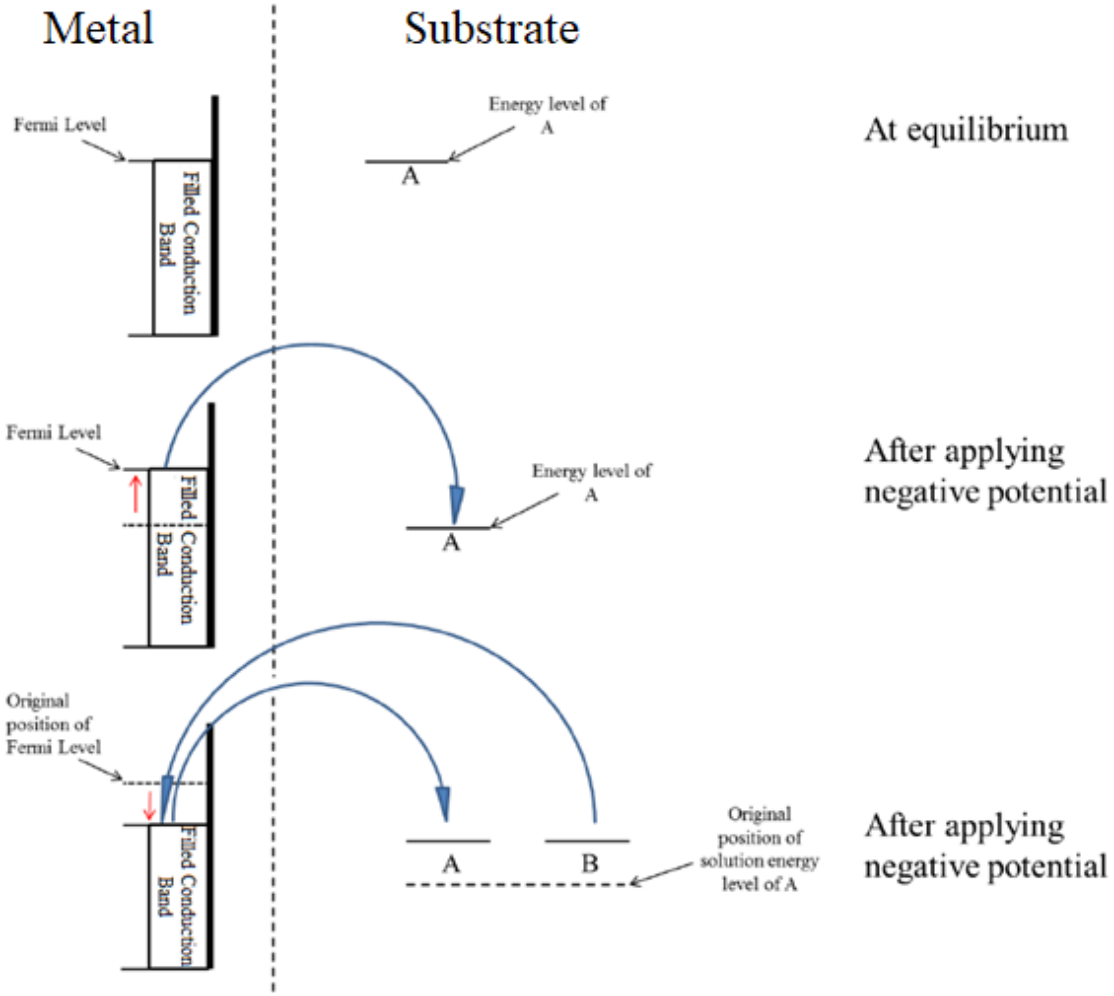

Fig. 3.3: Fermi energy change of electrode before and after applying an electric potential [215].

At equilibrium, there is no net current flow, because the rate of the forward reaction is equal to that of the backward reaction (*i.e.* A and B). Nernst described this relationship in terms of potential and gave an equation:

$$E = E^{\theta} + \frac{RT}{nF} ln \frac{a_A}{a_B} \qquad (3.2)$$

where E^{θ} = standard potential of the redox couple of A/B and a_i = activities of species *i*. It should be noted that it is challenging to determine the activities of higher concentrations, therefore the formal potential $E^{\theta\prime}$ is frequently employed. In order to substitute a standard potential with a formal potential, activity coefficients must be converted. Thermodynamically,

the activity of the solution can be written as dimensionless activity coefficients, γ, multiplied by the concentration ratio, c, over standard concentration, c^0, *viz.*, 1 mol L^{-1}.

Hence, the Nernst equation can be illustrated as:

$$E = E^{\theta} + \frac{RT}{nF} ln \frac{c_A}{c_B} + \frac{RT}{nF} ln \frac{\gamma_A}{\gamma_B} \qquad (3.3)$$

Since the formal potential is the sum of the standard potential and the terms involved in the activity coefficient in Eqn (3.2) with respect to the concentration, the Nernst equation can be approximated by the Eqn (3.4). In practice, the formal potential works only when the concentrations of each species are known.

$$E = E^{\theta\prime} + \frac{RT}{nF} ln \frac{c_A}{c_B} \qquad (3.4)$$

3.3 Kinetics considerations

Apart from the thermodynamic limitations, **kinetic limitations** are another elementary challenge needed to be considered in CO_2RR. Thermodynamics explains electrochemical reactions at equilibrium but information about the rate of the reaction was not provided. However, electrochemists are frequently interested in the reaction rates of electron or ion transfer. Consequently, kinetic investigations are necessary to understand the process of electrochemical reactions. Considering the simple and basic reaction:

$$A_{(aq)} \underset{k_b}{\overset{k_f}{\rightleftharpoons}} B_{(aq)} \qquad \text{(Scheme 3.3)}$$

Then the rate of the forward reaction could be written as:

$$V_f = k_f C_A \qquad (3.5)$$

and the rate of the backward reaction:

$$V_b = k_b C_B \qquad (3.6)$$

Therefore, the net rate would be:

$$V_{net} = k_f C_A - k_b C_B \qquad (3.7)$$

The net rate becomes zero at equilibrium, therefore the relation between the rate constant and concentration is written as:

$$K = \frac{k_f}{k_b} = \frac{C_B}{C_A} \qquad (3.8)$$

Since the rate constant changes with varying temperatures, the natural logarithm of the rate constant is linear with the inverse of temperature (1/*T*) as discovered first by van't Hoff [216] who expressed this isochore as:

$$\frac{\partial\, lnK}{\partial T} = \frac{\Delta H^{\theta}}{RT^2} \qquad (3.9)$$

where *K* = equilibrium constant, *T* = temperature, R = molar gas constant and ΔH^{θ} denotes the change in standard enthalpy.

Arrhenius [217] used the van't Hoff relationship for introducing an equation which explained the phenomenon of the temperature dependence of the constant rate of reaction:

$$k = Ae^{-E_A/RT} \qquad (3.10)$$

where "E_A = activation energy, and *A* = frequency and probability factor. As shown above, the exponential factor indicates that the activation energy can be surmounted by thermal energy, which relates thermodynamics to kinetics".

Fig. 3.4 shows the change in energy along the reaction coordinates. The potential energy of the system must be raised to the maximum level so as to form products from reactants. The energy requisite from reactant to E_A is depicted as E_f, while the energy required from the product back to the reactant is E_b.

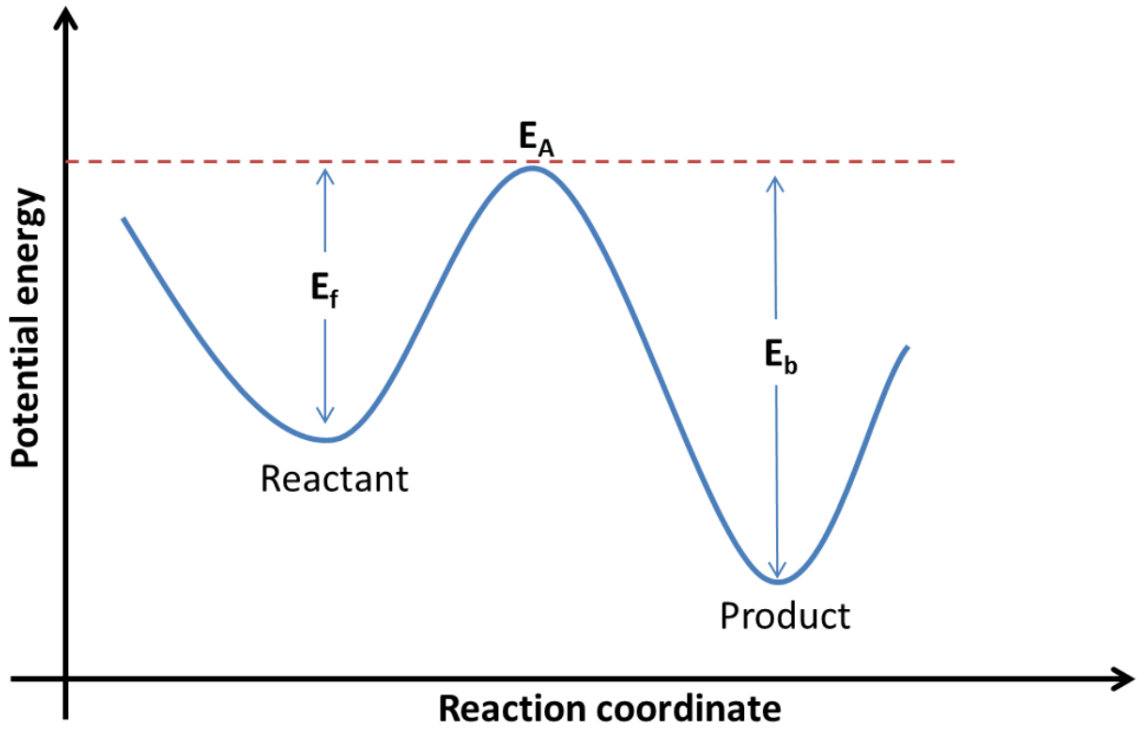

Fig. 3.4: The changes in potential energy during a reaction.

The two minimum levels are occupied depending on the energy of the reactant and product. This indicates the energetic stability of the reactants and the product. Transition state theory further explains that the reactants are combined to form an activation complex, meaning that the energy $\Delta E^{\ddagger}$ is required by the transition state. For a reaction involving the condensed phase, changes in pressure and volume can be neglected, so the standard enthalpy of activation ($\Delta H^{\ddagger}$) can be approximated to be $\Delta E^{\ddagger}$. So Eqn (3.11) can is written as:

$$k = Ae^{-\Delta H^{\ddagger}/RT} \qquad (3.11)$$

Thus, in terms of standard Gibbs energy (or standard free energy) of activation, the Eqn (3.11) can be illustrated as:

$$k = A'e^{-\Delta G^{\ddagger}/RT} \qquad (3.12)$$

Where "A" = $\exp(\Delta S^{\ddagger}/R)$, $\Delta S^{\ddagger}$ = standard activation entropy, and R = molar gas constant. Therefore, Fig. 3.4 can be explained by the standard free energy rather than the potential

energy. Introducing the Planck and Boltzmann constants ((h and k_B respectively), the Eqn (3.12) can be rearranged as:

$$k = K\frac{k_B T}{h}e^{-\Delta G^{\ddagger}/RT} \qquad (3.13)$$

Considering the electrochemical reaction:

$$A \underset{k_b}{\overset{k_f}{\rightleftharpoons}} B^{n+} + ne^{-} \qquad \text{(Scheme 3.4)}$$

At the cathode surface, the rate of the forward reaction is

$$V_f = k_f C_A = \frac{i_c}{nFS} \qquad (3.14)$$

while at the anode, the rate of the backward reaction is expressed as

$$V_f = k_b C_B = \frac{i_a}{nFS} \qquad (3.15)$$

where n = molar number of electrons transferred in the reaction, F = Faraday's constant and *S* = the surface area of electrodes.

Therefore, the net current at the electrode surface is expressed as:

$$i = i_c - i_a = nFS(k_f C_A - k_b C_B) \qquad (3.16)$$

By conventional means, IUPAC described the oxidation current by the positive sign and reduction current as a negative sign.

Noteworthy, conversion of CO_2 to most valuable organic products including HCOOH and CH_3OH is more tedious and challenging than the small molecules e.g. CO. The reason is that forming a complex molecule requires multiple proton-coupled electron transfers, thereby resulting in a more significant kinetic barrier, which consequently lowers conversion efficiencies. To find appropriate catalyst(s) having the ability to suppress the kinetic barrier thereby simultaneously promoting the formation of all intermediates and at the same time not catalyzing unwanted parasitic reactions remains a big challenge. Such catalyst(s) must have a low kinetic barrier (i.e. activation energy) for all desired reaction steps. Another choice

is the utilization of different catalysts to perform diverse reduction steps, though, from the practical viewpoint, it is essential to directly convert CO_2 to liquid products using a single or distinct electrochemical device. Further details about kinetic consideration are discussed below.

Some electrokinetic investigations have been reported for the electroreduction of CO_2. For instance, kinetics characterization and Tafel analysis with reaction-order dependency studies have been investigated for oxide derived (OD)-Au catalysts [218]. An intrinsically better performance has been reported for OD/Au catalysts for exhibiting Tafel slopes from 114 $mVdec^{-1}$ for polycrystalline Au catalyst to 56 $mVdec^{-1}$ for OD-Au catalysts. The authors observed that provided the reaction intermediates coverage is negligible, the Tafel slope for polycrystalline Au would indicate a rate-determining initial electron transfer process while that of OD-Au would be revealing initial electron preequilibrium which occurs before the rate-determining step. This suggested an improvement that OD/Au is a promising candidate having a better ability to stabilize CO_2 with resulting intermediates from electron transfer than the polycrystalline Au. In correlation with reported studies [209,219], the first-order dependence on both HCO_3^- and CO_2 concentrations, proposed a possible mechanism of reaction for both OD/Au and polycrystalline Au and pointed out that HCO_3^- exists as the CO_2RR proton donor.

The kinetic behavior of a glassy carbon-supported copper-NP electrode for CO_2 reduction to CH_4 was studied [220]. The study showed that the Tafel slope changed from 86 mV dec^{-1} for polycrystalline Cu foil to 60 mV dec^{-1} for n-Cu/C. This indicated a fast electron transfer process prior to a rate-limiting nonelectrochemical step with the assumption that coverage of reaction intermediates was minor.

Rosen *et al.* carried out comprehensive investigations on Ag nanostructured catalysts. They observed that the order of reaction can be influenced by changing the pH of the electrolytes as a result of different concentrations of both HCO_3^- and CO_2 [221]. It was also suggested that instead of constant potentials (with respect to reference electrodes), such a

study should be performed at constant overpotentials (with respect to RHE scales). Through this, H^+ concentrations which are significant CO_2RR reactants could be kept constant, thus leaving the concentration of either HCO_3^- or CO_2 as the only variable.

Electrokinetic studies remain definite and powerful tools for probing reaction mechanism of CO_2RR, though, in reality, performing well-defined electrokinetic studies become tricky [222]. Therefore, a useful indicator for the rate-limiting step of a reaction that involves the transfer of the electron is the Tafel analysis. Tafel slopes depend on several factors [222], including the existence of adsorbate owing to the CO_2RR complex nature and the effects of mass transport in complicated electrode structures. Likewise, in studying fixed overpotentials or driving forces, concentrations of reactant and/or product deviating from the standard condition can alter the equilibrium potentials from the predicted thermodynamic values.

Furthermore, a **high cathodic over-potential** is another fundamental challenge in the CO_2 electroreduction. The overpotential is defined as the "difference between the applied electrode potential at a given current and the thermodynamic potential". It comprises of three main components: Ohmic overpotentials, activation overpotentials and concentration overpotentials. The Ohmic losses are attributable to electrode and electrolyte resistances. Activation overpotentials reflect the kinetic barriers (required energy for maintaining the electrode reactions to a significant extent). It must be noted here that adsorption of reaction intermediates can cause poisoning and thereby lead to the deactivation of electrode surfaces. Hence, the selection of appropriate electrode materials is vital. The concentration overpotentials develop because of the mass-transfer limitations caused by the reactant and product diffusions to/from the electrode surfaces. Thus, CO_2 electroreduction occurs in an aqueous medium at a quite low temperature, the diffusion also becomes relatively slow. The limiting currents are always reached when the maximum rate of CO_2 consumptions at the surface

of the electrode significantly exceeds the CO_2 rate of diffusion to the electrodes. Hence, the morphology of the electrode turns out to be a very essential factor governing the performance of the electrochemical cell. To achieve practical implementations, the CO_2 mass transfer limitations towards the cathodic surfaces must be properly addressed.

The **low solubility of CO_2**, especially in H_2O is a major intrinsic and inherent limitation. The solubility of CO_2 in H_2O exposed to pure CO_2 is about 30 mmol/L at 293 K and 101 kPa. Meanwhile, in aqueous electrolyte used in electroreduction, the CO_2 solubility is much lower, owing to higher ionic strength; up to 10 M [111]. Providing a pure stream of CO_2, preconcentrations of the CO_2-containing feedstocks is necessary, which could be achieved by "pressure-swing adsorption" and "membrane separation", however, the running costs (operating and capital costs) are significantly high, and this will eventually end up in increased overall production costs. Therefore, direct usage of diluted CO_2 streams without prior upstream preconcentration is the only preferred alternative. Though, the low content of CO_2 (between 10 and 15 mol%) in fossil fuels combustion flue gas would produce lower concentrations of dissolved CO_2. The ultimate undesirable outcome of the lower solubility of CO_2 in water as well as lower concentrations of aqueous CO_2 are the limiting current densities (eqn. 3.17) [99].

$$j_L = nFk_mC_b \qquad (3.17)$$

Where "*n* is the electron stoichiometry coefficient (*n* = 2), *F* is the Faraday constant (96485 C mol^{-1}), k_m is the mass transfer coefficient (10^{-5} m s^{-1}), and C_b is the bulk concentration of CO_2 (0.03 kmol m^{-3} for pure CO_2 at 101 kPa and 293 K)". Simple computation shows that the limiting current density is j_L = 6 mA/cm^2. For diluted CO_2 containing streams, this limiting current will be further decreased. Such geometric current densities, below 10 mA/cm^2, are considered as insufficient for typical industrial applications involving electrochemical processes. The economics dictate that geometric

current densities above 100 mA/cm^2 with current efficiencies of at least 50% are usually required to make the technology profitable [111,145]. The reason is that the rate of an electrochemical reaction per electrode area (r, mol/(m^2 s) is directly proportional to the current density via Faraday's law (FE is Faraday efficiency, also called current efficiency):

$$r = \frac{1}{\mathrm{A}}\mathrm{R} = \frac{j}{\mathrm{nF}}\,\mathrm{FE} \qquad (3.18)$$

$$\mathrm{A} = \frac{\mathrm{RnF}}{j\mathrm{FE}} \qquad (3.19)$$

where "A" denotes a total area of the electrode and gives a required area of electrode dependent on the rate of production ("R", mol s^{-1}) and "j" is the current density. The equations above basically dictate that the required "area of the electrode is inversely proportional to the current density (j)". Consequently, a lower current density requires a larger electrode surface, thereby resulting in larger electrochemical device sizes and, of course, higher costs of operation and capital investment. Currently, typical industrial electrochemical reactors are about $10000 per square meter of anodic or cathodic area [111]. Minimizing such huge capital investment is crucial. Therefore; the electrochemical process is mostly operated at a current density of about 100 mA/cm^2 or greater, and Faraday efficiency higher than 50%. Conversely, industrial space velocity for gaseous feeds must be greater than 100 per hour, preferably, in the order of magnitudes of 1000 per hour (contact times of seconds) [111]. These restrictions pose great challenges to the kind of requirements for designing electrochemical devices that are economically viable for the conversion of CO_2 to valuable chemicals and liquid fuels.

3.4 Butler-Volmer Kinetics

The Butler-Volmer kinetics describes a relationship between the applied potential and the rate of transfer of electrons across the electrolyte-electrode interface. If we consider the reaction in Scheme 2.5 and assume a single electron transfer process, then the change in standard free energy *via* a reaction coordinate presented in Fig. 3.5.

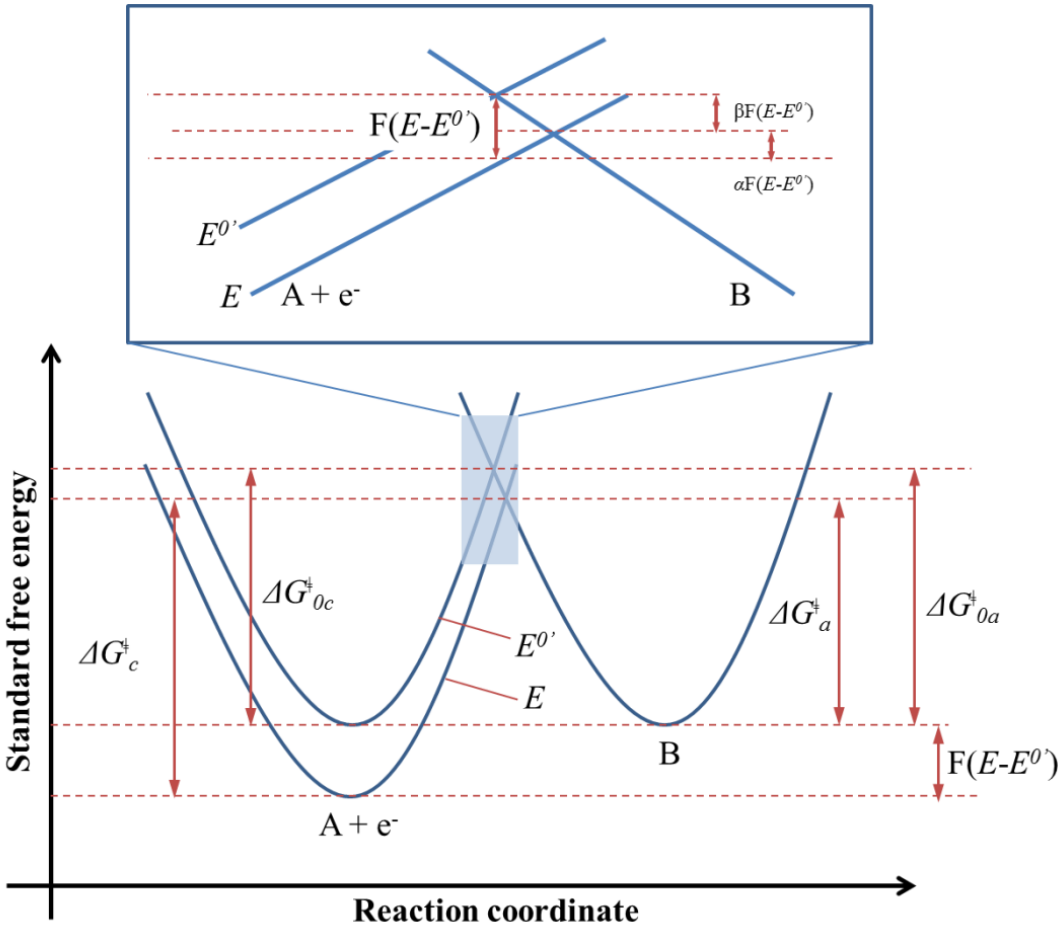

Fig. 3.5: Typical diagram of Butler-Volmer kinetics [215].

According to the Fig. 3.5 the electrode potential starts at the reference curve, $E^{0'}$, and the oxidation potential is denoted as E, the change in energy of electron would then be expressed as $-F(E-E^{0'})$. It should be noted that the change in transition state energy is smaller than $-F(E-E^{0'})$, therefore, it can be expressed as a fraction of $-F(E-E^{0'})$, which is defined as $\beta F(E-E^{0'})$, where $\beta=(1-\alpha)$, and α is called transfer coefficient which essentially indicates the symmetry of the energy barrier. Therefore, the Gibbs free energy change can be expressed as:

$$\Delta G_a^{\ddagger} = \Delta G_{0a}^{\ddagger} - \beta F(E - E^{o\prime}) \qquad (3.20)$$

and

$$\Delta G_c^{\ddagger} = \Delta G_{0c}^{\ddagger} - \alpha F(E - E^{o\prime}) \qquad (3.21)$$

Where $\Delta G^{\ddagger}_{0a}$ and $\Delta G^{\ddagger}_{0b}$ are anodic and cathodic Gibbs free energy changes.

By applying the Arrhenius equation, the respective rate constants of the forward (Eqn 3.22) and backward (Eqn 3.23) reactions can be expressed as:

$$k_f = A_f e^{-\Delta G_{0c}^{\ddagger}/RT} e^{-\alpha f(E-E^{o\prime})} \qquad (3.22)$$

and

$$k_b = A_b e^{-\Delta G_{0a}^{\ddagger}/RT} e^{-\beta f(E-E^{o\prime})} \qquad (3.23)$$

Where f = F/RT. At equilibrium, $\Delta G^{\ddagger}_{0a}$=$\Delta G^{\ddagger}_{0c}$, and the term $A_f e^{-\Delta G_{0c}^{\ddagger}/RT}$ equals $A_b e^{-\Delta G_{0a}^{\ddagger}/RT}$ and can be substituted by k^0. Thus, combined with Eqn. 3.21, the relationship between current (i) (other terms have been defined above) and potential is rewritten as:

$$i = FAk^0\{c_A \exp[-\alpha f(E - E^{o\prime})] - c_B \exp[\beta f(E - E^{o\prime})]\} \qquad (3.24)$$

3.5 Tafel law

For a process involving electrochemical reactions, Scheme 2.3 according to Butler-Volmer kinetics, the net rate (or reaction flux), j, can be given as:

$$j = k_f^0 exp\left[\frac{-\alpha F(E - E_f^o)}{RT}\right] C_A - k_b^0 exp\left[\frac{\beta F(E - E_f^o)}{RT}\right] C_B \qquad (3.25)$$

where the standard rate constants for the forward and backward reactions are k_f^0 and k_b^0, and the transfer coefficients are represented by α and β, respectively, with α+β =1. The electrode potential is denoted by E, whereas E_f^0 is the standard potential for A/B couple with c_A and c_B being the concentrations of A and B in bulk solution. Note that j = 0 at equilibrium. Nevertheless, at an extreme potential (either oxidation or reduction), such that $E \gg E_f^0$ or $E \ll E_f^0$, then it is possible to neglect one term or another in the Eqn. 3.25.

Thus, for an oxidation process:

$$j = k_b^0 exp\left[\frac{\beta F(E - E_f^o)}{RT}\right] C_B \qquad (3.26)$$

and for a reduction process:

$$j = k_f^0 exp\left[\frac{-\alpha F\left(E - E_f^o\right)}{RT}\right] C_A \qquad (3.27)$$

as $E_f^0$is a fixed number, the overpotential, η (where η = $E - E_f^0$) is the function of change in potential, S is the surface area of the electrode, then Eqns. (3.26) and (3.27) can be rewritten as:

$$ln|j_{red}| = \frac{-\alpha F\eta}{RT} + ln\left(FSk_f^0 C_A\right) \qquad (3.28)$$

and

$$ln|j_{ox}| = \frac{\beta F\eta}{RT} + ln(FSk_b^0 C_B) \qquad (3.29)$$

The term on the right-hand side of the equations can be abbreviated by a constant. Therefore, according to Eqns. 3.25 and 3.26, a plot of $|lnj|\ vs.$ E can provide information about the electron transfer coefficient, α. This plot is known as a Tafel plot as represented in Fig. 3.6. The transfer coefficient could be determined from a slope of the linear region of the graph. From Fig. 3.6, j_0 denotes the exchange current (see Butler-Volmer kinetics). The value of the slope is unaltered by the formal potential since the slope signifies a ratio rather than the precise number. In the equilibrium region, the current tends to be small, while the logarithm of current tends to infinity.

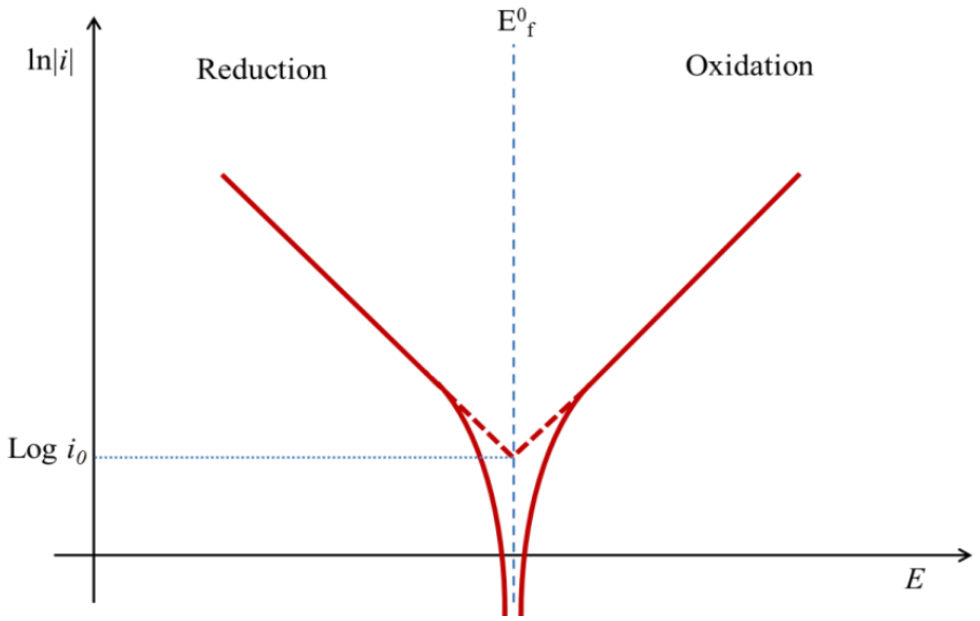

Fig. 3.6: Representation of Tafel plots [223].

3.5.1 Determination of the Tafel slope and exchange current density from the linear sweep voltammetry plots

The Tafel equation is the high overpotential limiting case of the Butler-Volmer equation: b log(j)+ a = η. The Tafel plot connects the overpotential with the logarithm of the current density, j_o, which is very useful in evaluating the electrocatalysts' performance. The Tafel parameters are the intercept, a, which is actually the log (j_o), and the slope, b. These are evaluated such that the Tafel plot representation of current vs. voltage data is easier to read for linear sweep (one segment) current vs. voltage data. In this thesis, the linear scan voltammogram generated during the LSV measurement (Fig. 3.7a) is replotted in the form of the overpotential, η, vs. log(j) (Fig. 3.7b). The resulting graph is known as a Tafel plot, and Tafel parameters can be determined by fitting the linear portion of the plot. The intercept is then used to determine j_o. In general, a smaller Tafel slope indicates better catalytic performance. In the case of CO_2 and formic acid electroreduction, the Tafel slope is often used to investigate the mechanism of the reaction [224].

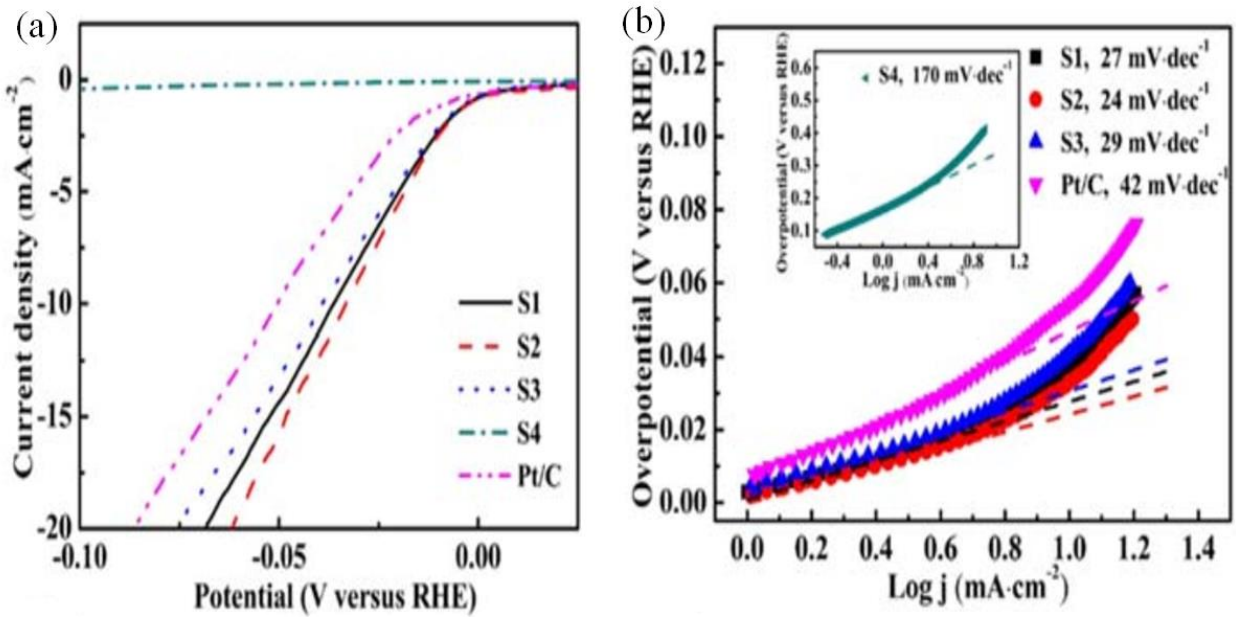

Fig. 3.7: Typical (a) Linear polarization curves and (b) Tafel slope in 1 M KOH respectively. (Reprinted from reference 225 with permission from Elsevier).

3.6 Scherrer equation

The Scherrer equation was used in this study to determine the crystallite sizes of particles of crystals of the anodic and cathodic electrocatalysts powders. In X-ray diffraction and crystallography, the Scherrer equation remains a useful formula that relates the size of crystallite particles in a solid to the broadening of a peak in a diffraction pattern. This equation was named after Paul Scherrer [226,227].

The Scherrer equation can be written as:

$$d = \frac{0.89\lambda}{\beta\, Cos\theta} \qquad (3.30)$$

where θ is the diffraction angle, β is the line broadening at full width at half maximum (FWHM) intensity, after subtracting the instrumental line broadening, in radians. λ is the wavelength (in nanometer) of the X-ray radiation, K is a constant taken as 0.89. d is the crystallite size measured in the nanometer. It is important to realize that the Scherrer formula provides a lower bound on the particle size. This is because a variety of factors contributes to

the width of diffraction peaks besides instrumental effects and crystallite size; the most important of these are usually inhomogeneous strain and crystal lattice imperfections.

3.7 The gas diffusion layer and membrane electrode assembly used in this work

The membrane electrode assembly is the core of all electrochemical systems. It is a place where the electrochemical reactions occur; either to generate electrical power in a proton exchange membrane fuel cell (PEMFC) or to carry out reactions by application of power in the solid polymer electrolyte membrane reactor. Typically, a MEA comprises of two GDLs, two dispersed electrocatalyst layers, and the membrane. The unique role of the GDL used in this work was to uniformly distribute the reactant(s) from flow channels along the electrocatalyst active surface layers. Additionally, the GDL guarantees adequate transport of liquid products, electrons, and heat. The GDL assists in managing formic acid by allowing proper amounts of formic acid to reach the electrocatalytic layer and while the water that forms would repel easily from the electrocatalyst surfaces to prevent flooding. If water collects near, or in the electrocatalyst layer, larger fractions of the electrocatalyst will not be utilized. Typically, PTFE is applied through several approaches to the GDL in order to manage formic acid (or CO_2) at the cathode side. PTFE is not an electric conductor and when GDL is treated with PTFE which generally renders it hydrophobic, therefore, it reduces water saturation and helps in water transport [228,229]. Thus, care must be taken to use the appropriate amount of PTFE [228,230]. The GDL provides the electrical contact between the current collector bipolar plates and the electrocatalyst layers. So, a thin GDL with high conductivity is desired for electrical efficiency. Furthermore, the GDL used in this experiment serves as the base substrate for depositing/coating the cathode electrocatalysts, thereby forming protective layers over the very thin layer of the electrocatalysts. The construction of GDLs is frequently from porous carbon paper with a thickness in the range of 110-370 μm. The in-plane and the through-plane

resistivities of the commercial GDLs are in the range of 25-100 mΩ/cm^2 and 6-20 mΩ/cm^2, respectively [58]. The in-plane and the through-plane resistances depend on the microstructure of the GDL. The in-plane resistance affects the uniformity of the reaction while the through-plane resistance dictates the cell resistance. To improve mass transport, GDLs can be made more porous at the cost of increased electrical resistance. The performance of the GDLs can be affected by numerous parameters including the PTFE content, thickness, pore size distribution, and microstructure. The MEA performances are governed by the activities of the anode and cathode electrocatalysts. The procedures and methods of preparation and/or deposition of the MEA play significant roles in the distribution, efficiency and electrocatalytic activity of the electrocatalysts. In summary, the GDL used in this work in combination with an optimized MEA and cathode catalytic layer loading methods leads to a significant enhancement in the FARR performance. This electrode structure, together with the PTFE utilization, have solved certain problems associated with the use of liquid phases in the FA electroreduction with an improved mass transfer of FA diffusion.

3.8 Electrolytes

Numerous electrolytes ranging from acidic to basic have been investigated [209,231]. Aqueous electrolytes comprise of cationic alkalis such as K^+, Na^+, several anions including hydroxide, bicarbonate (HCO_3^-), halide anions, etc. have been employed in the electrochemical reduction of CO_2 owing to their higher water conductivity which can, of course, be a good source of proton exchange [62,211]. Therefore, the use of electrolyte plays a vital role in product formation and selectivity. This makes the selection of electrolytes have a significant impact on the current density and selectivity of CO_2 electroreduction products. Based on this, the use of Na_2SO_4 was used as an electrolyte since it is free of any CO_2 precursor. This only applied to the cyclic voltammetry experiments of chapter 6 and the voltammetry and FTIR spectroelectrochemical experiments (chapter 7)

3.9 Cyclic voltammetry

This is a common voltammetry type where the measurements of the electrode current response to the linear increase or decrease of the potential cycles are performed [232]. Fig. 3.8 is a typical example of the resulting cyclic voltammetry (CV) scan against time. This example describes a reversible electron transfer with diffusion control. The potential of the working electrode is measured against a reference electrode which maintains a constant potential, and the resulting cell voltage produces an excitation signal such as that of Fig. 3.8. Usually, the experiment is started at a voltage where there is no electrode process (0.2 V in the plot), and the voltage is scanned at a constant rate to the switching voltage (0.7 V in the plot). In the presence of the electrochemically active compounds in the solution phase, the anode peaks at the potential (E_{pa}) are detected with the peak current (I_{pa}). During the reverse scans, further current peaks at a potential (E_{pc}) may be noticed with the corresponding cathode peak current (I_{pc}).

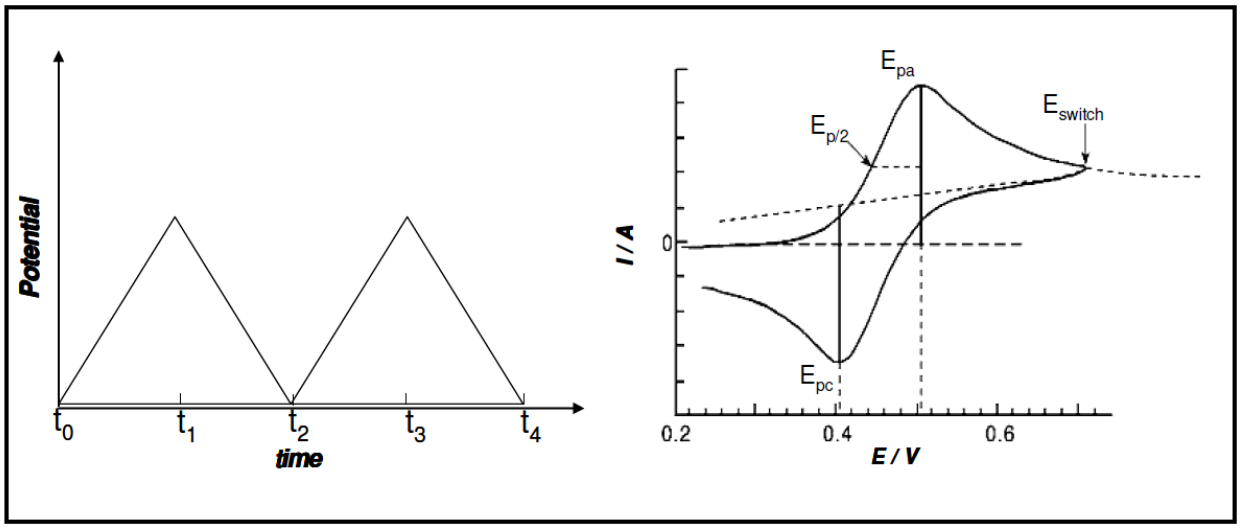

Fig. 3.8: The potential-time waveform and a typical cyclic voltammogram for a reversible redox process [233].

3.10 *In-situ* Fourier-transform infrared spectroelectrochemistry

The *in-situ* Fourier-transform infrared (FTIR) spectroelectrochemistry was pioneered in the early 1980s by Bewick *et al.* [234,235]. It is used for acquiring molecular information

involving the ionic and neutral adsorbates at electrodes along with other species in the solution involving the electrochemical reaction. Numerous studies have reported the use of this technique from static to dynamic environments, rough to smooth surfaces, and aqueous to non-aqueous media. The valuable data obtained can provide molecular pictures of the electrochemical double-layers and further augment the detailed understanding of the reactions or processes at the interfacial surfaces.

Implementing FTIR spectroelectrochemistry on the solid and liquid interfaces require that certain obstacles associated with the increased signal to noise ratios (S/N) must be overcome. This includes (i) the IR beam is required to be strongly absorbed by the electrolyte solution species; (ii) the IR energy is lost partially during the reflections at the surface of the electrode; (iii) the IR-signal from adsorbate (sub)monolayers (in the order of 10^{15} molecules cm^{-1}) on the surface of the electrode is very weak. In addition to the utilization of extremely reflective electrodes, the use of weak signal determination approaches e.g. polarization or potential modulation can advance the S/N of recorded *in-situ* FTIR spectra. Also, the accessories of the IR reflection can ensure the optimum incident angle and the IR electrochemical cells remains a key factor for carrying out a successful *in-situ* FTIR investigation

There are two main approaches for designing the *in-situ* FTIRS cell to minimize the strong IR absorption by electrolyte species. They are external and internal reflection configurations as schematically presented in Fig. 3.11. For the external reflection configurations, the electrode should be placed in close contact with the light-guiding prism to form a thin layer (1–10 mm thick) of electrolyte and a very short path length is ensured through the liquid and the electrode maximum IR illumination. This external configuration has the advantage of using a wider range of electrode materials, such as nanomaterial, single metal crystal, oxide materials carbon materials, etc. and can simultaneously determine both solution

species and adsorbates present in the electrochemical reaction processes. Mass transport may to a large extent be limited in the thin-layer configurations existing between the thin-layer and the bulk solutions. To overcome such a limitation, a microelectrode may be used coupled with certain precautions in designing the cell [236]. The internal reflection configuration makes use of attenuated total reflection (ATR) mode. This consists of a thin-film metal deposited on the IR transparent prism of higher refractive index which therefore uses a working electrode [237,238]. When the IR beam is focused at the interface from the back of the electrode (through the prism) and the reflected radiation is detected, a thick solution layer can be used, and this allows a free-mass transport. However, the electrode materials for internal reflection configurations are limited to <100 nm thin film on the IR window prism that is not electrically conductive and also limited to only a few metals (Au, Pt, Pd, etc.) by sputtering or electroless deposition [239–241]. The IR ATR mode is also applied to characterize the Pt/Nafion membrane interface in oxygen reduction reaction [242].

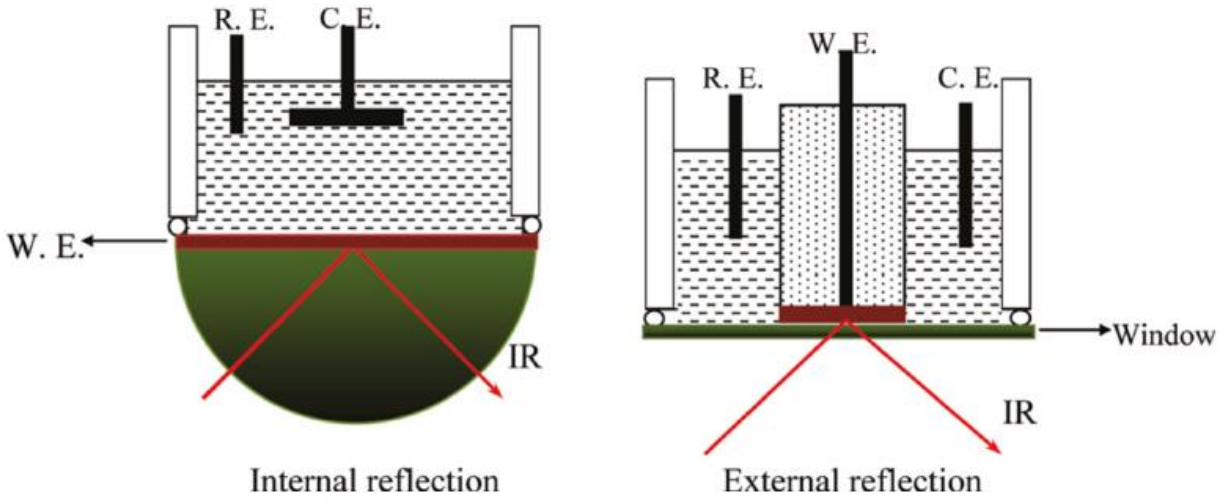

Fig. 3.9: Schematic presentations of *in-situ* FTIR cells with internal and external reflection configurations. (Reprinted from reference 235 with permission from Elsevier).

The difference technique is frequently used in the *in-situ* FTIR to increase the S/N due to absorption of IR light by the species in the thin-layer solutions and the environmental impurities in the IR beam by subtracting a strong background spectrum. The spectra are

acquired at two potentials, E_1 and E_2, at otherwise identical experimental conditions. The single-beam reflection spectrum at potential E_1 ($R(E_1)$ is then subtracted from the spectrum recorded at potential E_2 ($R(E_2)$. The difference between the two single-beam spectra is then divided by $R(E_1)$, and the final spectrum is reported as a relative change in electrode reflectivity. When the IR window is transparent, e.g. in case of a CaF_2 window, the resulting spectrum can be calculated as

$$\frac{\Delta R}{R} = \frac{R(E_1) - R(E_2)}{R(E_1)} \qquad (3.31)$$

However, when IR reflection by the IR window could not be neglected, such as in case of ZnSe, Si, and KRS5 (a mixture of 42% TlBr and 58% TlI) windows, the relative change of the electrode reflectivity should be expressed as

$$\frac{\Delta R}{R} = \frac{R(E_1) - R(E_2)}{R(E_1) - R_W} \qquad (3.32)$$

where R_w is the single-beam reflection spectrum recorded with the IR window alone (that is, with the electrode moved away from the IR window).

The geometry of the IR window is also a significant factor that governs the *in-situ* FTIR performances. In most cases, a flat window is convenient for varying the incident angle of the IR beam, and it can yield sufficient S/N, especially for nanomaterial electrodes and the CaF_2 window which are transparent. Nevertheless, the IR energy loss due to reflection is often observed with a flat window. The loss may become important when opaque windows such as Si, ZnSe, and KRS5 are employed. This problem may be overcome when a prism or a hemispherical window is used. Faguy and Fawcett gave a comprehensive discussion of the relative performance of the flat, prism, and hemispherical windows [235,243]. In addition, to eliminate the IR energy loss due to IR beam reflection by the window, the prismatic and hemispherical geometries are designed to optimize the field strength of the photon at the

electrode/solution interface. Therefore, spectra of adsorbed species with much better S/N could be obtained.

The FTIR instrument is required in subtractively normalized interfacial Fourier transform infrared spectroscopy (SNIFTIR) [244,245] and related techniques, such as single-potential alteration IR spectroscopy (SPAIR) [246] and multistep IR spectroscopy (MSIR) [247]. The interferograms are collected at a reference potential (E_1) and sample potential (E_2), respectively. Usually, E_1 is chosen as the potential at which the adsorbates are stable, or no reaction occurs, and E_2 is the potential at which oxidation/reduction of adsorbates or reagents takes place. To improve the S/N, which is proportional to the square root of the number (n) of interferograms collected, i.e. $S/N \propto \sqrt{n}$, many interferograms are collected and coadded at each of the two potentials. The Fourier transform of the coadded interferogram yields the single-beam spectrum at E_1 ($R(E_1)$) or E_2(($R(E_2)$. Finally, the resulting spectrum is then calculated using Eqn.3.31 and Eqn.3.32.

3.11 Linear Sweep Voltammetry

Linear sweep voltammetry (LSV) is an electrochemical technique where the current at the working electrode is measured while the potential between the working electrode and a reference electrode is swept linearly in time [248]. In LSV, a specified voltage range is scanned from a lower limit to an upper limit. By changing the scan rate, we can alter the time taken to sweep the range. The characteristics of a linear sweep voltammogram can be influenced by several factors which include chemical reactivity of electroactive species, the rate of electron transfer reactions and the voltage scan rate. Fig. 3.10 shows a typical LSV plot scanned from 0.0 V to 1.9 V. the blue arrow at 1.6 V indicates the onset potential (as previously defined in section 3.1.2). The green dotted lines have the same meaning as in Fig. 3.1. The scan begins from the left-hand side of the current/voltage plot. As the voltage begins to increase from left to right the current also increases. In reactions where the electron transfer rate is faster

relative to the voltage sweep rate, equilibrium is established at the electrode surface and for the reactions where the electron transfer process is slow relative to the voltage scan rate, they are called irreversible electron transfer reactions. This happens when the kinetics of the reactions are slow and current takes more time to react to the applied voltage, equilibria cannot be established rapidly. In this situation, the shape of the voltammogram recorded would be to the one in Fig. 3.10 but the position of peak current shifts depending on the reduction rate constant.

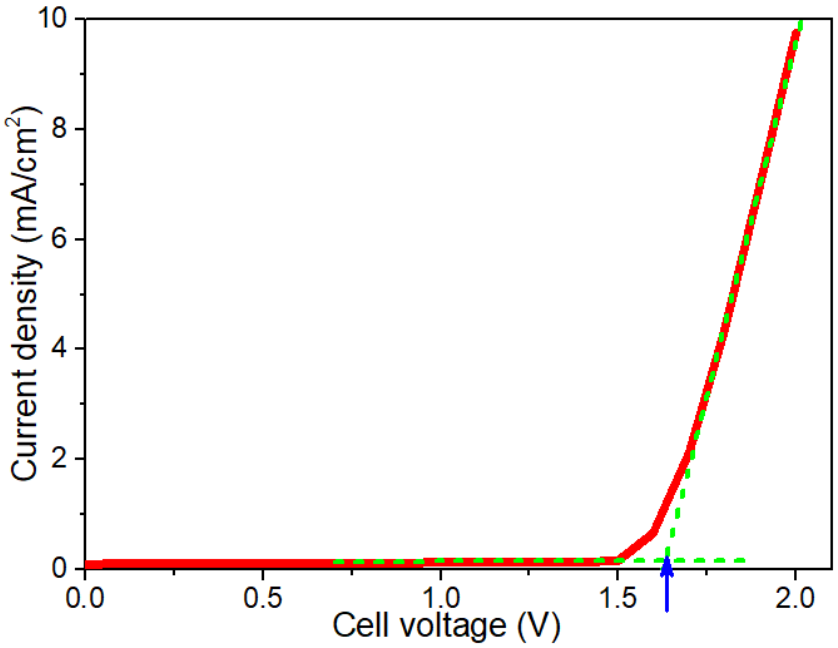

Fig. 3.10: Measurement using linear sweep voltammetry in a two-electrode set-up (scan rate of 0.001 V/s and potential steps of 0.1 V).

3.12 Chronoamperometry

Chronoamperometry (CA) is a technique used to investigate the time behavior of reaction kinetics, diffusion and adsorption processes. This technique measures the current as a function of time by keeping the cell voltage constant. The cell voltage versus time profile in Fig. 3.11a is the input given to the system where E_i is the initial voltage where there is no electron transfer (i.e. current = 0) and E_1 is the final voltage where the transfer of electrons occurs and usually, the reaction is under mass transfer control). At time t=0, the voltage

spontaneously rises from E_i to the final value. The current (i) versus time (t) profile in Fig. 3. 11b is obtained as an output for the given input. Such a plot is called chronoamperogram. For reactions that are under diffusion control, the current decay follows the Cottrell equation (Cottrell describes the change in electric current with respect to time). In this thesis, the voltage between the two electrodes was held at a fixed value and the current response was recorded.

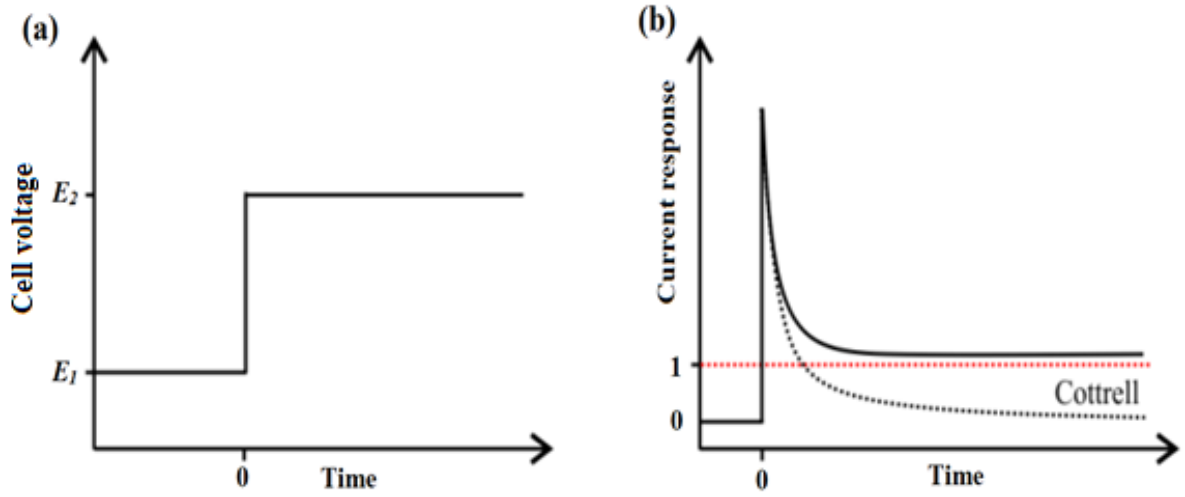

Fig. 3.11: (a) Voltage and (b) Current profiles using the chronoamperometry technique [233]. (Cottrell describes the change in current with respect to time).

3.13 Faraday's Law

Electrochemical cells consist of three different types: (a) galvanic cell (Fig. 3.12), (b) electrolytic cell (Fig. 3.12b), and (c) "supergalvanic" cells. In a galvanic cell (also called a primary cell), the potential can be autonomously generated, thereby allowing the flow of current whereas, in the electrolytic cell, an external force is required for the flow of current. The "supergalvanic" cell is usually used for Joule's heating through electrical discharges in the supergalvanic regions where i^2R_i loss is employed for heating the systems.

The electrolytic cell can be operated such that the current is allowed to flow from one electrode to another. The reduction occurs at the cathode and oxidation at the anode. However, in a

galvanic cell, the reduction happens at an anode or *vice versa*, this is because the reduction of the species takes an electron from the electrode causing it to become more positive. The extent of electrolysis is related to the charge that is passed through the electrodes. Since the charge carried by each electron is known as -1.602×10^{-19} Coulomb, the passage of one mole of electrons (i.e. 6.022×10^{23} electrons), flowing into a cathode can be determined to be 96485 Coulomb, which is called the "Faraday constant". The Faraday law can be illustrated using:

$$Q = nMF \qquad (3.33)$$

Where Q =charge (in Coulomb (C)), n =number of mole of electrons, M =number of moles of molecule(s) reacted and F = Faraday constant.

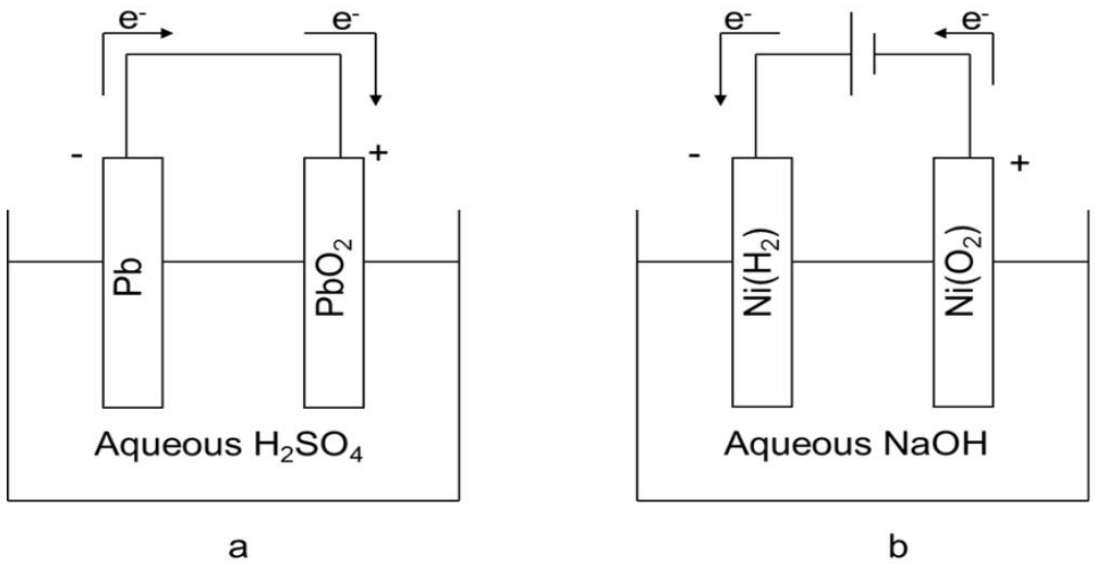

Fig. 3.12: Typical diagram of: (a) galvanic cell and (b) electrolytic cell.

3.13.1 Determination of the Faraday efficiency

It is quite usual to obtain various CO_2 electroreduction products (e.g. CO, CH_4, CH_3OH, etc.) and side products (e.g. H_2). Thus, in order to obtain knowledge about the selectivity of a catalyst, it is essential to quantify the relative formation of e.g. CO with respect to all the products. The product yield generated electrochemically can be expressed in terms of the Faradaic efficiency (FE), which is the commonly employed parameter to describe the product

selectivity and occurrence of product crossover of an electrochemical reaction [211]. Therefore, the FE used throughout the work was defined as the ratio of the number of Coulombs required in forming a certain amount of product (which is determined by chemical analysis) to the total charge over a specific interval of time. The FE for product formation in this research work was calculated using:

$$\mathrm{FE} = \frac{\mathrm{e^-_{output}}}{\mathrm{e^-_{input}}} \qquad (3.34)$$

where

$\mathrm{e^-_{output}} = \text{mole of the product} \times \text{number of electrons required to form 1 mol of the product}$

and

$$\mathrm{e^-_{input}} = \frac{\mathrm{Q}}{\mathrm{F}} = \frac{\mathrm{I} \times \mathrm{t}}{\mathrm{F}} \qquad (3.35)$$

where F is the Faraday constant (96485.33 s A/mol), Q is the measured charge (C), I is the current (A), t is the duration of the experiment (s), and F is Faraday's constant (C/mol). Normally, the summation of FEs of all products should be 100 % to achieve a Faraday balance. The achievement of this balance is the first step in any kinetic study of reactions in an electrochemical system.

3.13.2 Energy efficiency (EE) for co-electrolysis

This can be estimated from the product of Nernst potential ($\Delta E°$) and Faraday efficiency divided by cell voltage (U).

$$\frac{\Delta E° \text{ x FE}}{U} \qquad (3.36)$$

3.14 Determination of the space-time yield and percentage depletion

The space-time yield (STY) of the cathode electrocatalyst and its percentage depletion are determined using the relation below:

$$STY_{alcohol} = \frac{g_{alcohol}}{t(h) \times g_{cat}} \quad (3.37)$$

Where $g_{alcohol}$ is the mass (in g) of the alcohol produced, t = duration (h) and g_{cat} is the mass (in g) of the electrocatalyst.

Once the number of moles of carbon in the products is known, the percentage depletion can be calculated as follows:

$$\%\, depletion = \frac{number\ of\ mole\ of\ the\ products\ formed}{initial\ number\ of\ mole\ of\ FA} \times 100 \quad (3.38)$$

where the concentration of 15%FA, [FA] = 4.30 M, volume of FA in the tank = 0.02 dm^3. Number of moles of FA = [FA] x V_{FA} = 4.30 M x 0.02 dm^3 = 0.086 mol.

Number of mole of products formed ($n_{products}$) = $n(_{MeOH}) + 2(n_{EtOH}) + 3(n_{iPrOH})$.

Chapter 4

EXPERIMENTAL

4.1 Materials and reagents

Materials used are Nafion® 117 membranes (Fuel cell store, USA), Kimwipes* (Kimtech Science*brand delicate task wipes), Scotch tape (Scotch TM Magic Tape) Silicone rubber (JTR-S-0.5, 0.5 mm thick/13 cm x 18 cm), airbrush (Conrad Electronic Airbrush-Pistole AB-200), Titanium mesh (Fuel Cell Store, product number 592782), carbon paper (Toray-H-060, wet proofed). The reagent used includes hexachloroiridic acid ($H_2IrCl_6 \cdot 4H_2O$, Alfa Aesar, 99%, Ir 38-42%), tantalum carbide (TaC, Aldrich, ≥5 μm, 99%), isopropanol (Sigma-Aldrich, HPLC 99.9%), methanol, ethanol (Sigma-Aldrich, HPLC 99.9%), $NaNO_3$ (Sigma-Aldrich, ≥99%), $In(NO_3)_3.9H_2O$ and NH_4OH, Na_2SO_4, Nafion® perfluorinated resin solution (Aldrich, 5 wt% in lower aliphatic alcohols and water), polytetrafluoroethylene (60 wt.% dispersion in H_2O, 0.05-0.5 μm), H_2O_2, H_2SO_4, MilliQ water which was purified by the Millipore® water purification system. All chemicals were analytical grade and used without further treatment. Devices used include a furnace (Carbolite), Millipore® Sterifil® filtration, gas chromatography (Agilent G1530A 6890), syringe (Hamilton-Bonaduz, MICROLITER® #7002).

4.2 Synthesis of IrO_2 electrocatalyst

The Adams fusion method [249] employed in this study involves the fusion of the metal chloride precursor with $NaNO_3$ at high temperatures. The method has been used over the past years to prepare various noble metal oxides [187,250–253]. In this study, iridic acid ($H_2IrCl_6 \cdot 4H_2O$, Alfa Aesar, 99%, Ir 38-42 %) was used as the metal precursor and tantalum carbide (TaC, Aldrich, ≥5 μm, 99%) as the supporting material. Since iridium is not only expensive but also scarce, the imminent practical applications of the process necessitate the reduction of IrO_2 loading on the anode of PEM water electrolyzers. Therefore, among the literature reviewed,

TaC has been proven to be suitable electrocatalyst support since it is stable under the accelerated stability conditions owing to its electrical conductivity and stability in the harsh environments which are harsher than the condition in PEMFC. The catalyst support increases the dispersion of metal catalysts in addition to surface exposure and establishes significant electronic interactions between the catalysts and the support materials, which lead to a significant increase in catalyst utilizations [187,254,255].

In this study, a predetermined amount of iridic acid was weighed into a crucible, followed by the addition of a predetermined amount of TaC which was transferred quantitatively from the glass weighing funnel using 10 mL isopropanol (Sigma-Aldrich, HPLC 99.9 %) as shown in Table 1. This was then magnetically stirred for 1 h. Thereafter, $NaNO_3$ was added to the mixture in an approximate ratio of 16.7:1 of $NaNO_3$: Ir, and further stirred for 30 minutes and heated to 70°C using a digital thermometer until a sludge formed. The stirrer bar was then removed, and the crucible placed in the furnace (Carbolite) which was heated to 500°C at 250°C/h, left to dwell at 500°C for 1 hour and then allowed to cool to room temperature overnight. The resulting dark grey powder was scraped from the crucible into the centrifuge tube filled with 6 mL deionized water and then centrifuged four times. The powder was then washed and filtered to remove the excess $NaNO_3$. The paste formed was then allowed to dry overnight. Electrocatalysts were prepared with concentrations of 60, 70, and 100 wt.% IrO_2. No additional annealing step followed to limit the sintering of the nanosized particles.

Table 4.1: Preparation procedure of anodic electrocatalyst powders

Ratio (wt %)	$H_2IrCl_2.xH_2O$ (mg)	TaC (mg)	$NaNO_3$ (mg)	Isopropanol (mL)
60:40	50	0.0054	0.0592	10.00
70:30	50	0.0035	0.0592	10.00
100:00	50	0. 000	0.0592	10.00

4.3 Synthesis of In_2O_3 electrocatalyst

The starting materials were $In(NO_3)_3.9H_2O$ and NH_4OH. These were used without further purification. 2.0 g of $In(NO_3)_3.9H_2O$ was dissolved in 8.0 mL deionized (DI) water and 23.3 mL ethanol [1,32]. The solution was then stirred at room temperature for 0.5 h. 6.0 mL NH_4OH was added slowly into the solution under stirring until pH 9 was reached. The slurry formed was then aged for 10 mins at 80^{o}C. The white precipitate formed was collected by filtration using a Millipore® Sterifil® filtration system with 0.4 μm diameter HTTP type filter paper and then washed with DI water. The resulting precipitates were transferred into the crucible and placed into the furnace (Carbolite) to dry for 12 h at 65^{o}C and then calcined at 300^{o}C for 3 h to form the yellow solid called indium oxide (In_2O_3) [1,32].

4.4 Physical characterization of the electrocatalysts

4.4.1 X-Ray Diffraction

X-ray diffraction (XRD) remains a popular technique for materials characterization. This technique is non-destructive and reveals information about the crystalline phase and chemical composition of synthesized materials. In XRD analysis, the crystallinity of the materials signifies the high active surface area which enhances the activity of the catalyst. The 2-theta (2θ) scanning diffractometer remains a powerful tool to obtain the XRD patterns, it usually scans from 4 to 80 degrees, and the patterns are usually compared with the pattern of the Joint Committee on Powder Diffraction Standards (JCPDS). To measure the XRD pattern of both catalysts, fine-powdered materials are usually spread onto a glass slide with the use of double sticky tape. The crystallinities and average particle size characterization of the powdered samples were examined via powder X-ray diffraction (PXRD) using a Bruker D2 Phaser powder diffractometer at room temperature. CuK-α radiation was generated at 30 kV and 10 mA with a wavelength, λ = 1.542 Å. Patterns were collected in a range from 5 – 45° 2θ

in steps of 0.05° and a counting time of 2 s/step. The crystallite sizes (d) measured are generally calculated using the Scherrer equation (3.30).

4.4.2 Scanning Electron Microscopy

The scanning electron microscopy (SEM) is one of the prevailing visualization tools used to investigate the morphology of catalysts such as pore and particle sizes, surface characteristics, structures and dispersion of impregnated metals on the catalytic supports. In this study, the physical properties and surface morphologies of both anode and cathode catalysts were investigated using the scanning electron microscope (JEOL JSM-6460LV) operated at 20 kV.

4.5 Manufacturing of gas diffusion electrodes

A GDE consists of a GDL on which a catalytic layer is deposited. For both anodic (IrO_2) and cathodic (In_2O_3) electrocatalyst, the inks were formulated using the Sun *et al.* (2008) method [42]. A carefully weighed electrocatalytic powder and predetermined amount (details are shown in Tables 4.2 and 5.2 & 5.4 in the next chapter) of Nafion® perfluorinated resin solution (Aldrich, 5 wt% in lower aliphatic alcohols and water) was added, this was stirred for 1 h. 1 mL of isopropanol was then added, stirred for 15 min and sonicated for 1 h. Thereafter, 72 mL of ethylene glycol (Sigma-Aldrich, spectrophotometric grade ≥99%) were also added and sonicated for another 1 h. The resultant inks were left on continuous stirring till used to ensure homogenous suspension.

For the anodic catalyst, the Nafion® 117 membranes (Fuel cell store, USA) produced by DuPont® were used as proton exchange membrane (PEM) electrolyzers. Prior to catalytic loading, the 4 x 4 cm Nafion® membrane was cut and pre-treated with 10% H_2O_2 for 1 h at 80^{o}C, then rinsed with DI water, followed by 2 h light boiling in DI-water at 80^{o}C and 1 h light boiling in 0.5 M H_2SO_4 at 110 ^{o}C, and finally rinsed four times in light boiling DI-water. The

cleaned membrane was then stored in DI-water until use. For catalyst loading, the stored membrane was removed from the DI-water and dried with Kimwipes* (Kimtech Science*brand delicate task wipes). This was taped on a cleaned glass with Scotch tape (Scotch TM Magic Tape) to reveal only 2 x 2 cm surface area for catalytic spraying. A 4 x 4 cm silicone rubber with only 2 x 2 cm area cut out of it and placed over the membrane as the mask to ensure adequate fastening to the glass board with tape and to ensure that only a 2 x 2 cm surface area was spray-coated. The airbrush (Conrad Electronic Airbrush-Pistole AB-200) was used to load the catalytic ink onto the membrane with N_2 pressure. In cases where membranes swelling was observed, these membranes were allowed to first return to normal flat shape before resuming with the ink spraying. In all cases, the entire ink suspension was used for each membrane. Both anode and cathode electrocatalysts were coated by the spraying method as shown in Fig. 4.1 and the membranes were left at least for 24 h to completely dry before proceeding to the electrochemical experiment. The detailed catalyst loadings and preparation procedure for various wt% IrO_2 used for water electrolysis are presented in Table 4.2. For the cathode, carbon cloths with 40% Pt/C were used during the water electrolysis experiments.

For FARR and CO_2RR, In_2O_3 was used as the cathode electrocatalyst. Initially, during the FARR experiment, the In_2O_3 inks were sprayed on the other side of the Nafion® membrane before electrochemical testing. During the membrane activation for electrochemical experiments, it was discovered that In_2O_3 (i.e. the cathode) coated on the membrane got dissolved when the membrane was activated in 0.5 M H_2SO_4 at 80^oC prior to the electrochemical experiment. In order to resolve the issue, In_2O_3 ink was coated on carbon paper instead of coating directly onto the Nafion membrane. Before the spray-coating of the cathode ink, the carbon paper was first immersed in an acetone solution under mild sonication to remove the associated impurities on the surface of carbon papers. Then the cleaned carbon paper was rinsed many times with MilliQ water, and in the oven-dried at 90^oC. The inks were sprayed

layer by layer and allowed to dry at room temperature until a catalyst loading of 7.2 mg/cm^2 was obtained. Since In_2O_3 ink was discovered not to dry easily on carbon paper after weeks, the coated GDL was rather dried in the microwave oven at 90^{o}C till the desired loading was obtained. The total catalyst loading was either 7.2 mg/cm^2 or 7.5 mg/cm^2 on 4 cm^2 geometric active surface area of the cathode. Then, after the completion of the loading, the resulting electrocatalysts were allowed to remain in the oven at the same temperature for 24 h to ensure complete removal of any water residue and evaporation of isopropanol. Care must be taken in loading the catalyst such that a uniform loading is achieved. Loading too much catalyst onto carbon paper each time may lead to the inks being clogged onto a spot of surface thereby preventing the homogenous or uniform distribution of the ink across the targeted surface. Therefore, it must be ensured that each layer is dried each time before continuing with the remains. Later, the cathodic electrocatalyst was modified by adding 0.15 wt% or 0.30 wt % PTFE suspension into the In_2O_3 catalyst layer to facilitate diffusion of formic acid during the electrochemical experiment. Nafion was used as the binder since it can enhance proton conduction whereas PTFE cannot conduct protons [256–258].

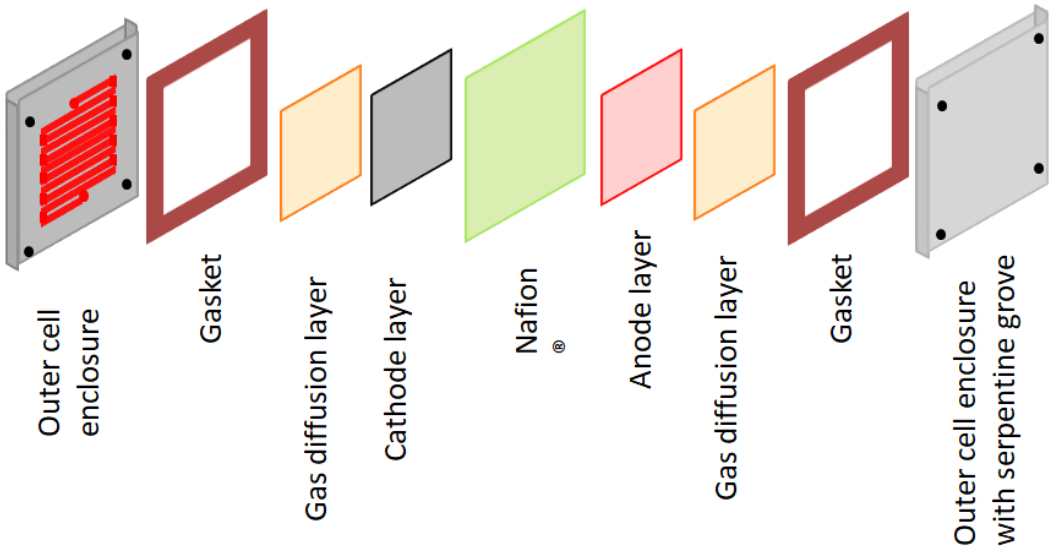

Fig. 4.1: Manufacturing of gas diffusion electrodes (GDE)/MEA.

Table 4.2: Catalyst preparation and loading for water electrolysis

Ratio (wt % IrO_2: TaC)	Anode	Catalyst loading (mg/cm^2)
60:40	14.4 mg 70:30 wt% IrO_2: TaC + 86 µL Nafion solution + 72 µL ethylene glycol; coated on a 2 x 2 cm active area Nafion membrane	3.6
70:30	14.4 mg 70:30 wt% IrO_2: TaC + 86 µL Nafion solution + 72 µL ethylene glycol; coated on a 2 x 2 cm active area Nafion membrane	3.6
100:00	14.4 mg 70:30 wt% IrO_2: TaC + 86 µL Nafion solution + 72 µL ethylene glycol; coated on a 2 x 2 cm active area Nafion membrane	3.6

4.6 The membrane electrode assembly

4.6.1 Water electrolysis electrode assembly

The cell body was made up of a titanium mesh, cut into 2 x 2 cm surface area. Titanium mesh was used on the anode side. The as-prepared MEA was sandwiched between the current collectors and silicone gasket. On the cathode side, a cut of 2 x 2 cm platinum-coated-carbon cloth was used as the GDL, followed by the current collector. The outer casing had a serpentine groove containing both inlet and outlet points to storage tanks. A silicone gasket was used to ensure leak proofing the anode and cathode compartments. The set-up was carefully assembled, including tubing. About 30 cm^3 DI-water was filled into each storage tank and allowed to sit for at least 30 min to allow good saturation and to ensure non-leakage. The anode and cathode electrocatalytic layers were ensured to have good electrical contact with the current collectors, which are critical components in achieving high performance in the PEM WE. The set-up is shown in Fig. 4.2.

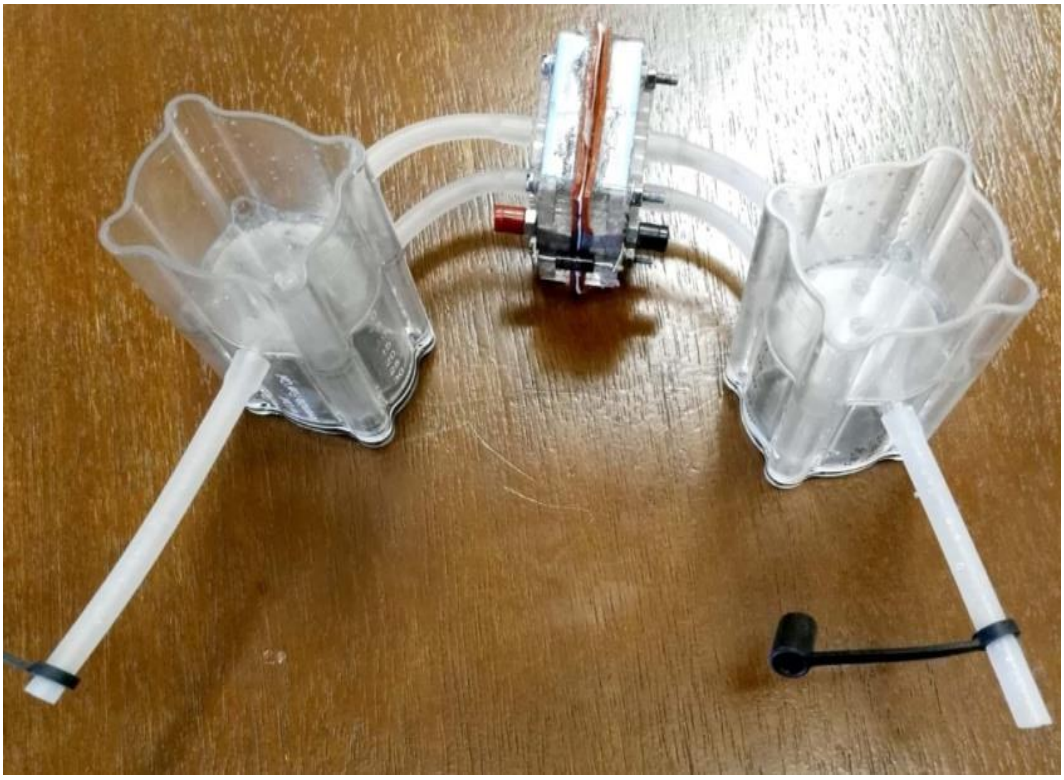

Fig. 4.2: Cell set-up including the MEA for water electrolysis**.**

4.6.2 FARR electrode assemblage

Initially, the double-sided membrane was sandwiched between the Ti mesh (anode GDL) and carbon paper (cathode GDL). A silicone gasket was used to ensure adequate sealing of anode and cathode compartments. This was then followed by current collectors and finally the outer cell casings. The anode was then connected to a storage tank tubing and filled with DI-water while the cathode was connected to a glass cylinder with an open top and filled with 4.30 M formic acid. After discovering that In_2O_3 dissolved during membrane activation, In_2O_3 ink was sprayed on the cathode GDL (carbon paper) as explained in section 4.5. The set-up is shown in Fig. 4.3.

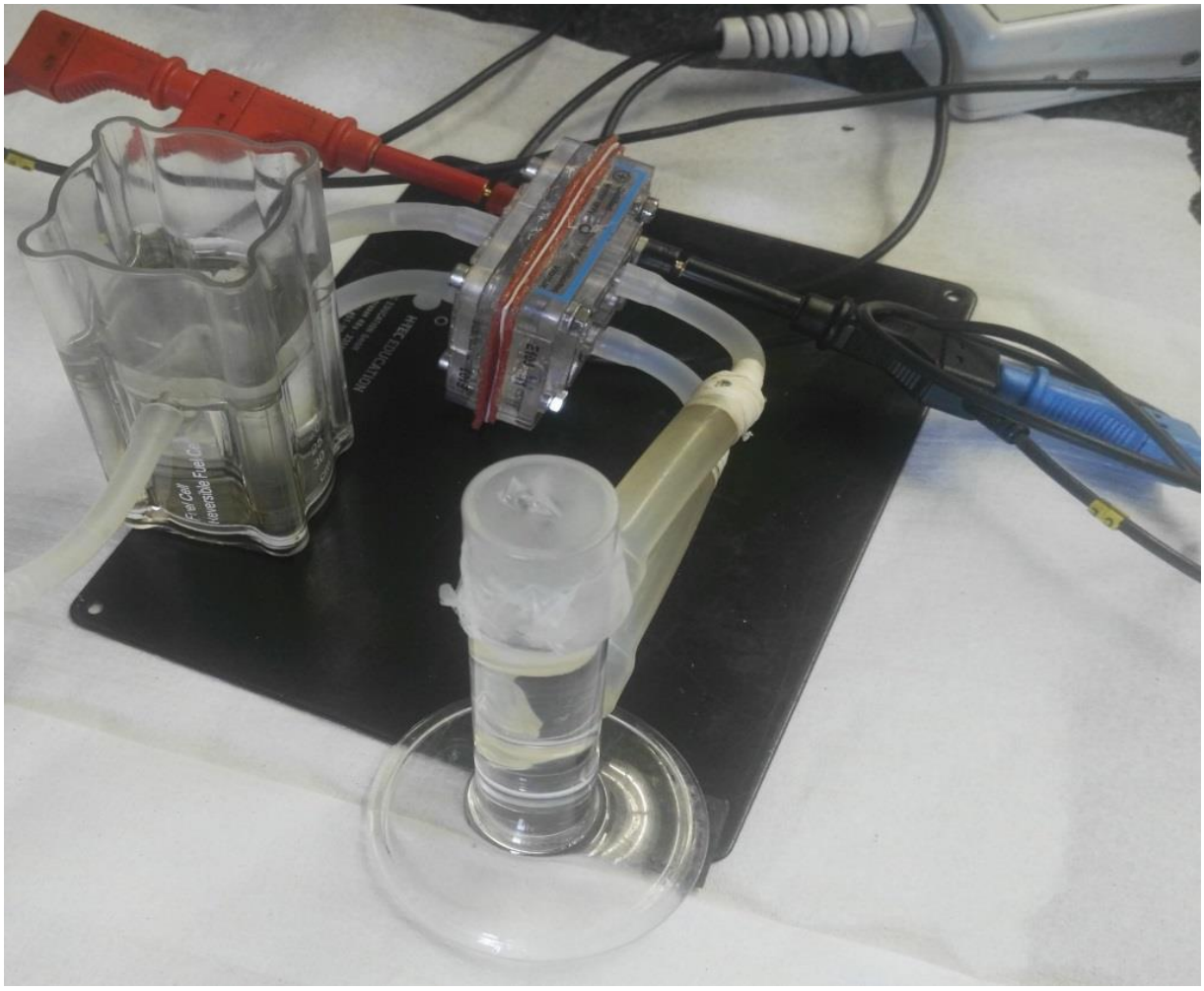

Fig. 4.3: Cell set-up including the MEA for the FARR.

4.7 Potentiometric measurement (electrochemical characterization)

4.7.1 Cyclic voltammetry

Cyclic voltammetry is an excellent technique used to survey the reactivity of new materials or compounds and provides information about the potential at which oxidation or reduction processes occur. CV experiments were carried out using a PGStat (Autolab, AUT87766) controlled by Nova® 1.0 software in a standard three-electrode electrochemical cell with a carbon plate counter electrode and a saturated calomel reference electrode. The working electrode was a 5 mm diameter glassy carbon electrode which was carefully polished on a polishing cloth for 1 min using an aqueous suspension of alumina with 0.05 μm mesh size. The residual alumina particles were then removed by sonication in distilled water for 2 min.

Thereafter, the electrode was air-dried, and the deposition of In_2O_3/PTFE ink was done by depositing 7 µL of the ink and then dried under nitrogen for about 20 mins before use. Ohmic drop was compensated using the positive feedback compensation implemented in the instrument. All experiments were carried out after bubbling the solution at room temperature (22 ± 2 °C) for about 30 min with N_2 gas for FARR or with CO_2 for CO_2RR. Briefly, for ink preparation, a 25 mg In_2O_3 powder was carefully weighed into a glass vial and 100 µL of Nafion solution was added, ultrasonicated for 30 min, followed by the addition of 0.15wt% PTFE and then ultrasonicated for 30 min. Then 1 mL of iPrOH was added to the solution and shake for another 30 min. The as-prepared ink was then used without additional treatment.

4.7.2 Linear sweep voltammetry and chronoamperometry

Electrocatalytic activities of the as-prepared catalysts were determined by linear sweep voltammetric and chronoamperometric methods. Electrochemical studies were conducted on the assembled cell using a PStat (Autolab, AUT72638) controlled by Nova® 2.1 software. The LSV was carried out at room temperature with a scan rate of 0.001 V/s in steps of 0.1 V. For FARR, the scan rate and voltage range differed for some experiments. The CA studies were performed at a cell voltage of 1.9 V for 12 h for water electrolysis. These conditions were varied with respect to cell voltage and time for FARR experiments. Before and at the end of an electrochemical reduction (ECR) experiment, the liquid products were pipetted out, volumetrically measured, and then analyzed using gas chromatography (GC). For chapter 6, the reference electrode was Ag/AgCl, but for comparability, the absolute potentials were all converted to values against the SHE (Eqn. 4.1):

$$|E_x|(\text{V vs SHE}) = E\ (\text{V vs Ag/AgCl}) - 0.197\ \text{V} \qquad (4.1)$$

4.8 Fourier-transform infrared spectroscopy measurements coupled with electrochemical experiments

The FTIR measurements were carried out in a Bruker IFS 66v spectrometer which was modified for beam reflection on the electrode surface at a 65° incident angle. As described previously [259], a 10^{-6} bar vacuum was used in order to remove interferences from atmospheric water and CO_2. The detector was an MCT (HgCdTe) type which was beforehand cooled with liquid nitrogen. The spectral resolution was 4 cm^{-1} and the FTIR spectra were recorded in the wavenumber range between 1000 and 4000 cm^{-1}. A homemade three-electrode spectroelectrochemical cell (Fig. 4.4), fitted on the bottom with a MIR transparent window (CaF_2) and a Metrohm AUTOLAB potentiostat (model PGSTAT101 AUT40888) were used. A carbon plate served as a counter electrode and the reference electrode was an SCE, but for convenience and comparability, all potentials were converted to SHE (Eqn. 4.2). The working electrode was a 7 mm diameter glassy carbon upon which In_2O_3 with or without PTFE was deposited. To minimize the absorption of the infrared beam by the solution, the working electrode was pressed against the window and a thin layer of electrolytic solution was obtained. The methods used were Single Potential Alteration IR Spectroscopy (SPAIRS), and Chronoamperometry/FTIRS coupling. In the SPAIRS method, the electrode reflectivity *R*Ei was recorded at different potentials Ei, each separated by 0.05 V during the anodic scan at a sweep rate of 1 mV s^{-1}. In the other spectro-electrochemical methods, the potential was maintained at a fixed value, and spectra were recorded every 180 s. IR spectra were calculated for each potential value (or time) as changes in the reflectivity (R) relative to a reference single-beam spectrum (R_{ref}) as $R = R_i / R_{ref}$. Upward and downward going absorption bands represent, respectively, the decrease and increase of corresponding species.

$$|E_x|(\text{V vs SHE}) = E\ (\text{V vs SCE}) - 0.241\ \text{V} \qquad (4.2)$$

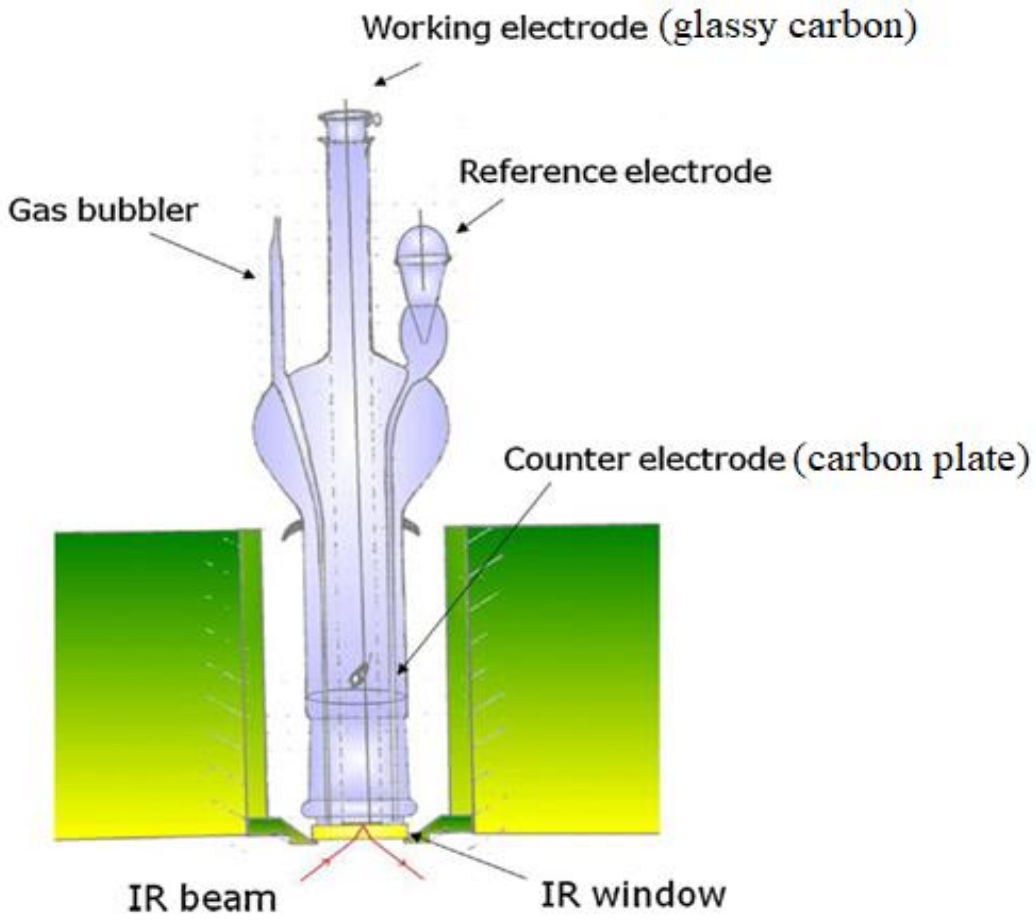

Fig. 4.4: Infrared spectroelectrochemical cell [190].

4.9 Product detection and analysis

4.9.1 Liquid-phase analysis using gas chromatography

Gas chromatography (GC) analysis was performed using a GC-Flame ionization detector (FID) (Agilent G1530A 6890) with a split injection port controlled by a two-position actuator module - VICI (Valco Instruments Co. Inc.). Helium gas was used as the carrier gas. For FARR, a clean syringe (Hamilton-Bonaduz, MICROLITER® #7002) was used to inject the samples into the front inlet. The details about the GC set-up are presented in Table 2. Figs. 4.5 and SI 9 present the calibration curves of MeOH, EtOH and iPrOH. Fig. SI 9 was done due to the change of system software and upgrading of the GC which affected the retention time of the three alcohols in chapter 6.

Table 4.3: GC set-up and conditions

Column 1	Zebron 7HG-G007 -11 ZB-WAX column
Nominal length	30.0 m
Nominal diameter	250 µm
Nominal film thickness	0.25 µm
Mode	Constant flow
Initial flow	1.2 mL/min
Nominal init. Pressure	91.7 kpa
Average velocity	40 cm/s
Outlet pressure	Ambient
Front Inlet	
Pressure	91.7 kPa
Split ratio	50.1
Initial temp	250°C 9 (on)
Total flow	64.0 mL/min
Detector	Flame ionization detector fitted with a methaniser (nickel catalyst)
Temperature	250°C (on)
Air flow	450 mL/min (on)
Hydrogen flow	50.0 mL/min (on)
Electrometer	On
Lit offset	2.0
Column 2	
Model number	Combi combi
Capillary column	Carboxen -1006 +molsieve5A
Nominal length	40.0 m
Nominal diameter	530 µm
Nominal film thickness	20 µm
Nominal init pressure	116. 0 kpa
Mode	Constant flow
Initial flow	18.3 mL/min
Average velocity	104 cm/s
Back Inlet	
Pressure	116 kPa (on)
Initial temp	200°C (on)
Total flow	112 mL/min
Detector	An analogue input board (AIB) was used to connect a pulsed discharge ionization detector (PDHID)
Oven	
Initial	40°C for 7 min
Ramp	230°C at 20°C/min
Maximum temperature	240°C
Equilibration time	0.50 min
Run time	25.00 min

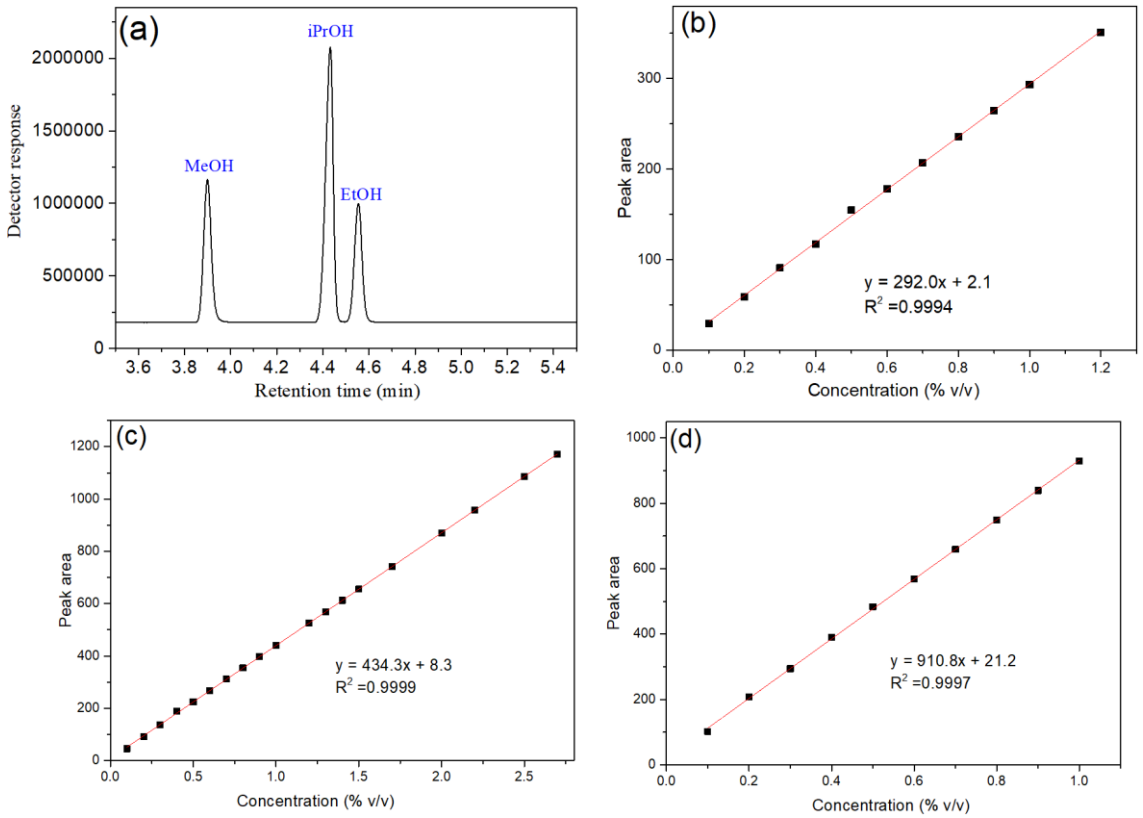

Fig. 4.5: (a) Liquid injected GC-FID chromatogram of the standard and GC-FID Calibration curves of (b) MeOH, (c) EtOH and (d) iPrOH, demonstrating good reproducibility with negligible scatter.

4.9.2 Gas phase analysis

Gas products were quantified with online gas chromatography (Agilent Technologies, 490 µGC). The residual reactant and/or product gases from the outlet of the cathodic compartment were vented manually using a 10 mL syringe into the gas-sampling loop of the gas chromatograph (µGC), equipped with a thermal conductivity detector (TCD) that possesses three channels calibrated at different temperatures. The first one was equipped with a packed M5A^{H}BF column at 80^{o}C for H_2 detection. The second channel contained a packed PPQ^{H} column at 60^{o}C for hydrocarbon (C_xH_y) detection, and the third one was equipped with a packed COX^{H}BF column at 120^{o}C for CO_2 and CO detection. Argon (Airgas, 99.999%) and helium (Airgas, 99.999%) were used as the carrier gases to quantify hydrogen and CO concentrations, respectively.

Chapter 5

PHYSICAL CHARACTERIZATION AND ELECTROCHEMICAL PROPERTIES OF IrO_2:TaC FOR WATER ELECTROLYSIS AND In_2O_3 FOR FORMIC ACID REDUCTION IN THE TWO-ELECTRODE SET-UP

5.1 Physical characterization

5.1.1 Powder x-ray diffraction

Fig. 5.1 shows the powder X-ray diffractogram (PXRD) of the synthesized IrO_2:TaC (Fig. 5.1a) and In_2O_3 (Fig. 5.1b) electrocatalysts at different compositions.

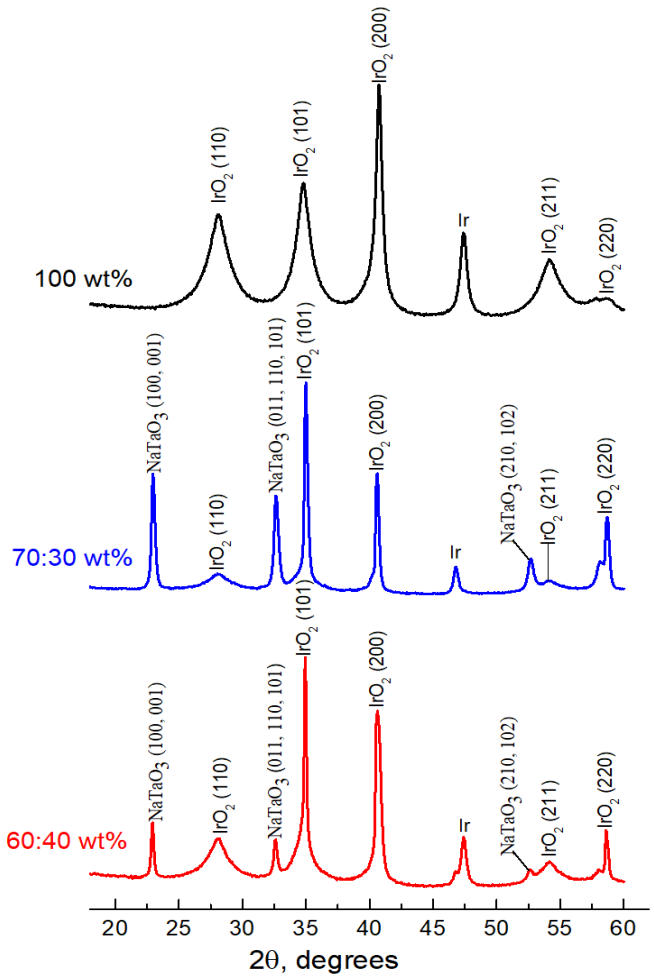

Fig. 5.1a: Powder X-ray diffractogram of the synthesized IrO_2:TaC.

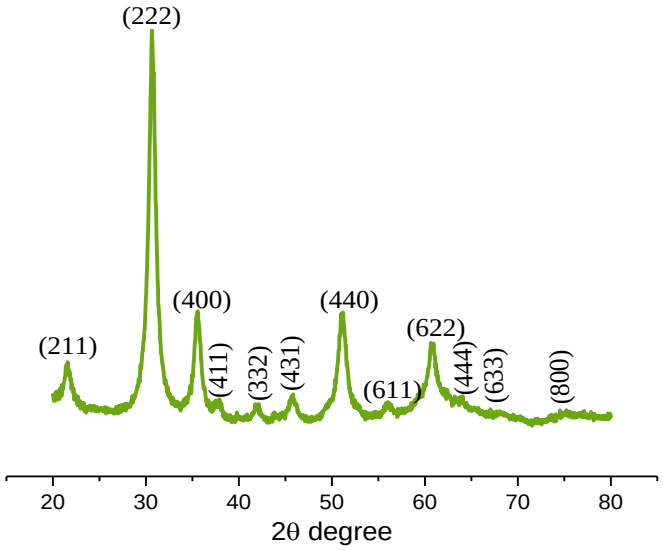

Fig. 5.1b: Powder X-ray diffractogram of the synthesized indium oxide (In_2O_3).

As shown in Fig. 5.1a, all diffractograms showed well-defined lines of IrO_2 and TaC (except IrO_2 100, i.e. pure IrO_2). IrO_2 and TaC have the same reflection at $2\theta = 40.68^o$ (200) and therefore seen as one peak (overlapped with each other). However, there is an additional component that is identified as $NaTaO_3$ at $2\theta = 22.92^o$, 35.50^o and 52.90^o, respectively, observed in the diffraction spectra of the supported electrocatalysts: IrO_2:TaC 70:30 and 60:40. This originated from the oxidation of the TaC support by $NaNO_3$ during the Adams fusion process. The calculated crystallite size (D) using the Scherrer equation for IrO_2 at $2\theta = 28°$ is 4.6 nm while the full width at half maximum is 1.74 rad. This observation is in good agreement with Polonsky *et al.* (2012) and Felix *et al.* (2012). [260,261].

For In_2O_3 (Fig. 5.1b), all of the detectable peaks were indexed as the In_2O_3 cubic structure. The average crystallite size estimated for the most intense In_2O_3 (222) reflection is 8.7 nm at $2\theta = 32^o$ with FWHM of 0.99 rad, evidencing the formation of In_2O_3 nanoparticles. The observation agreed with Chandradass *et al.* (2011) [32] and Al-Resheedi *et al.* (2014) [262].

5.1.2 Scanning electron microscopy (SEM)

The Figs. 5.2-5.4 present the SEM images of the synthesized different anodic (wt% IrO_2: TaC) electrocatalysts while Fig. 5.5 shows the cathode (In_2O_3) electrocatalyst.

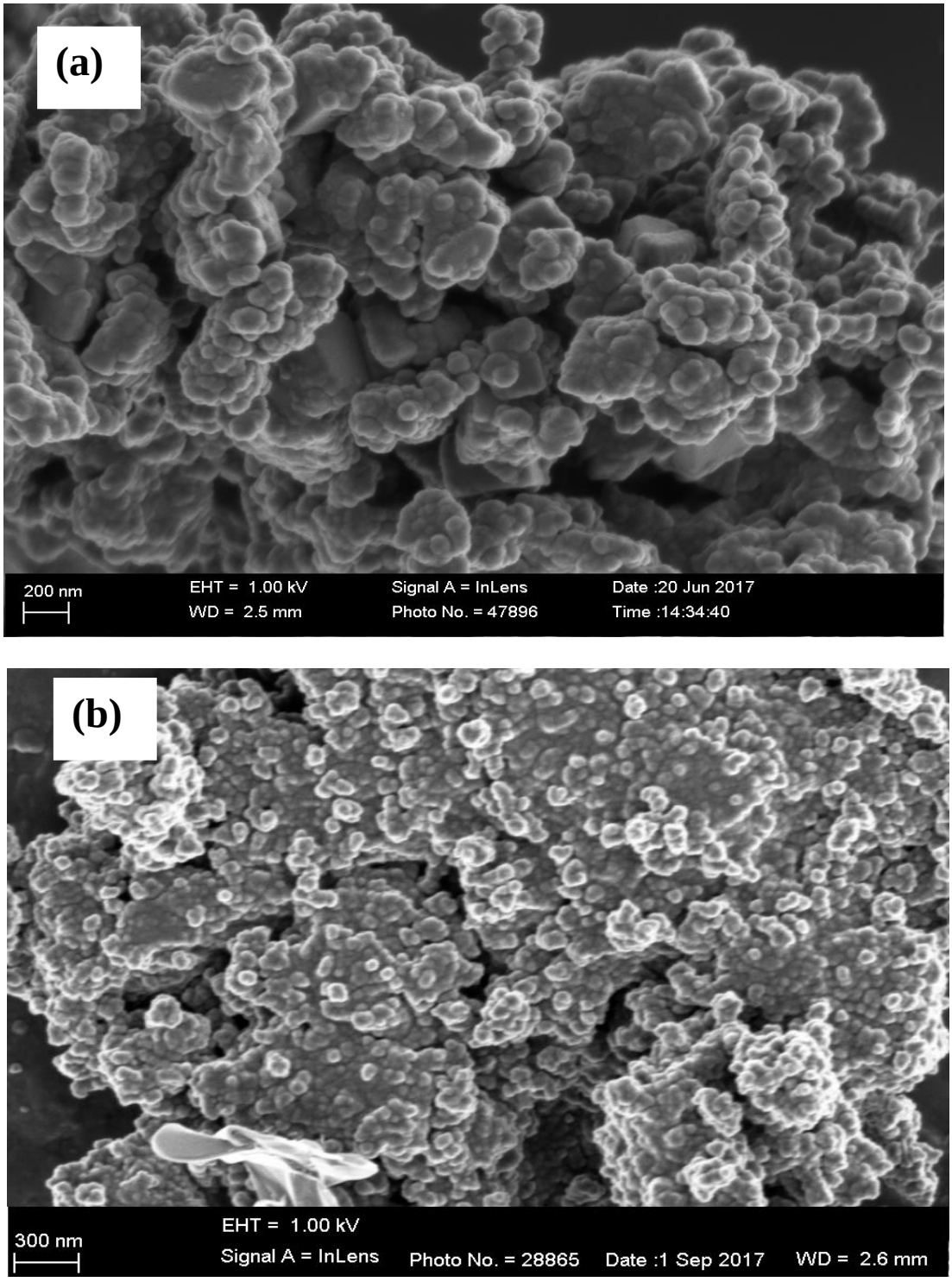

Fig. 5.2: SEM images of 100:00 wt% IrO_2:TaC(a) before WE (b) after WE.

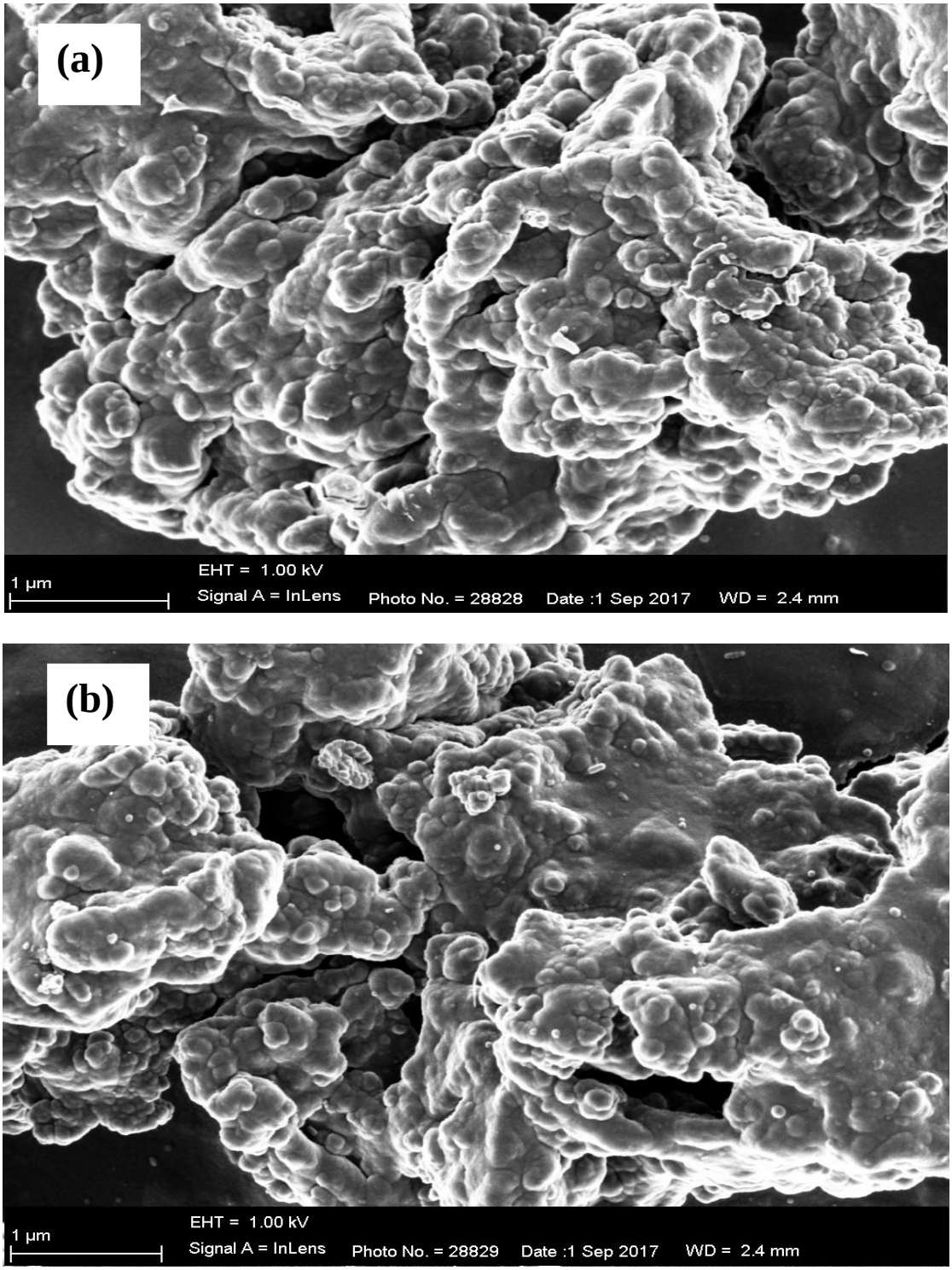

Fig. 5.3: SEM images of 60:40 wt% IrO_2:TaC (a) before WE and (b) after WE.

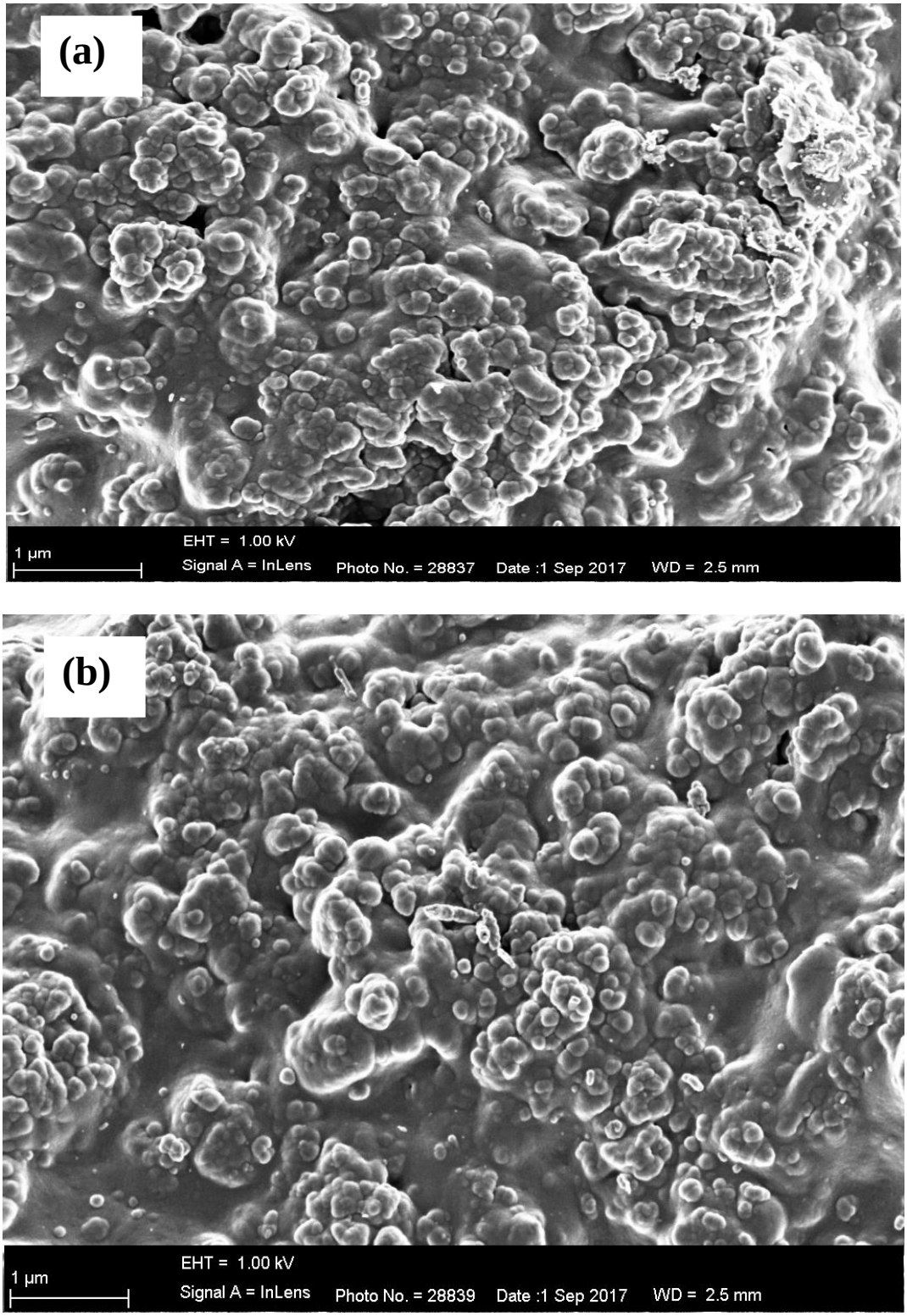

Fig. 5.4: SEM images of 70:30 wt% IrO_2:TaC (a) before WE and (b) after WE.

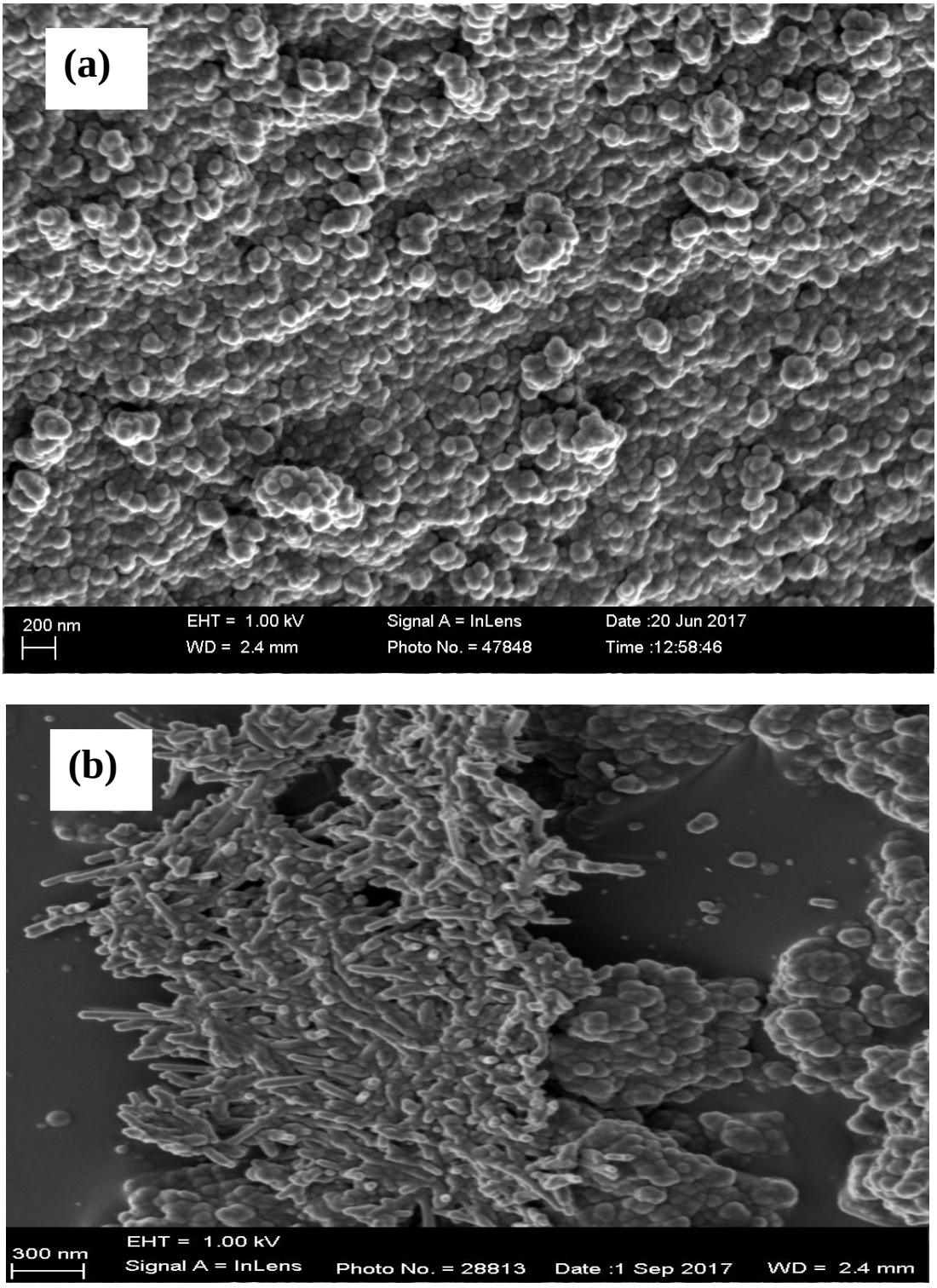

Fig. 5.5: SEM images of In_2O_3.

The SEM images of both 100% IrO_2 (Fig. 5.2), 60:40 wt% IrO_2:TaC (Fig. 5.3) and 70:30 wt% IrO_2:TaC (Fig. 5.4) reveal similarities with the presence of IrO_2 agglomeration with rounded/spherical shapes at the nanometer (100% IrO_2) and micrometer (70:30 and 60:40 wt%

IrO_2:TaC) scales. Fig. 5.2-5.4 shows the agglomerated area with a high concentration of particles with rounded shapes. The agglomerated rounded shape is an indication that the catalysts have the ability to promote electrocatalytic activity [187,261]. After water electrolysis (WE), the SEM images of the IrO_2:TaC in Figs. 5.2b, 5.3b & 5.4b reveal only minor changes in the morphology of the IrO_2:TaC supported by the membrane, but there were minor cracks and very little destruction of the membrane surface when compared with pure IrO_2 (100%) before (water electrolysis). This disruption at the particle–water interface modifies the surface properties, leading to a minor change in particle morphology. Another interesting observation is the influence of TaC: the sample morphology without TaC (100:00 wt.% IrO_2:TaC) is more roughened after WE as compared to 70:30 and 60:40 wt.% IrO_2:TaC samples. This is a clear indication of the catalytic support (TaC) showing a great influence on these two samples thus making the IrO_2 remain in good contact with the membrane even after the WE. This thus implies that as the WE duration increases, the surface and IrO_2 contact with the membrane for 100:00 wt.% IrO_2:TaC sample tends to decrease, which may influence its electrocatalytic activity in comparison with 70:30 and 60:40 wt.% IrO_2:TaC samples.

Fig. 5.5 reveals the SEM images of In_2O_3 captured at different positions. They show agglomeration, and the nanosized distribution is not uniform, thereby revealing aggregates of different shapes and sizes. In addition, nanorod morphologies (Fig. 5.5b) agglomerated into different sizes and shapes were also noticed.

5.2 Water electrolysis using the IrO_2:TaC electrocatalyst in the two-electrode set-up

Fig. 5.6a, 5.7a & 5.8a present the LSV plots of the different wt% IrO_2:TaC samples randomly selected over 40 cycles in the cell voltage range of 0 to +1.9 V. LSV results containing the current density of each selected cycle, onset potential and Ohmic resistance of each cycle are presented in Table 5.1. Under this scenario, the current densities at 1.9 V and Ohmic resistance of 2nd cycle for 60:40, 70:30 and 100:00 wt% IrO_2:TaC samples were 1.4 mA/cm^2 and 183.2 Ωcm^2; 5.1 mA/cm^2 and 44.7 Ωcm^2 and 0.7 mA/cm^2 and 701 Ωcm^2 respectively with 70:30 wt% IrO_2:TaC having the least Ohmic resistance. As seen in Table 5.1, the current density decreased with increasing Ohmic resistance over the 20th and 40th cycles. Decreasing current densities among the three samples were observed over the 40 cycles. However, the 70:30 wt% IrO_2:TaC surface is more active and conductive than the other two compositions and also more stable.

The current density obtained from the LSV curves of 70:30 wt.% IrO_2:TaC was further compared with LSV curves of 60:40 and 100:00 wt.% IrO_2:TaC samples (Fig. 5.9). At 1.5 V, they were 0.6 mA/cm^2, 5.9 mA/cm^2 and 1.3 mA/cm^2 for 100:00, 70:30 and 60:40 wt% IrO_2:TaC, respectively, thus, signifying that 70:30 wt.% IrO_2:TaC exhibited a higher current density than the others (Figs. 5.7 and 5.8). Comparing with the theoretical onset potential of the WE, the current study shows an overpotential of 0.32 V for the 70:30 wt.% IrO_2:TaC. The LSV and CA measurements were done back-to-back on a single cell for a time-period of 72 hours lead to electrode degradation (Figs. 5.8-5.10), which is responsible for the reduction in current density. Nevertheless, the onset voltage remains largely unaltered, revealing that no electrocatalyst poisoning takes place. However, from Fig. 5.6a, 5.7a, 5.8a & 5.10a, two regions were evident from the curves, which are first; the region in which there is an exponential increase in current density as the cell voltage increases up to 1.55 V and the charge transfer is the rate-limiting step. The second region is linear with predominant Ohmic resistances (1.55 V

to 2.0 V) with membranes as the major contributors owing to a linear increase with cell voltage. It is believed that the PEMWE is supposed to operate in the industry in this region [254]. It is evident from Fig. 5.6 and 5.10 that 70:30 wt.% IrO_2:TaC achieved the best current density. No visible change in the electrode was observed in the voltage range used in the experiment, showing that the TaC was a good support material and that it is stable under the experimental testing condition. Since 70:30 wt.% IrO_2:TaC gave the best performance, this ratio was further employed to prepare the subsequent anodic electrocatalyst for other experiments.

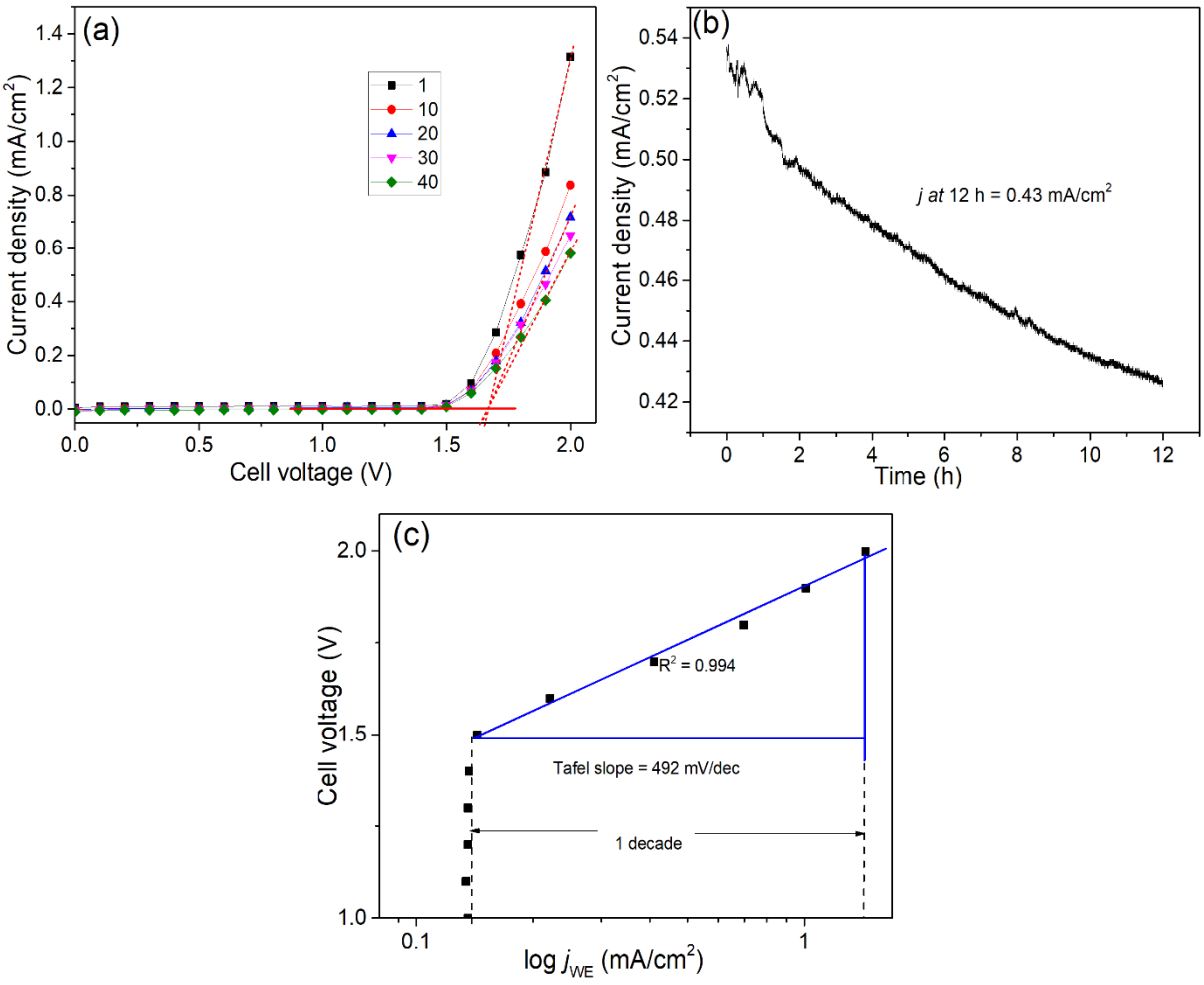

Fig. 5.6: (a) LSV for WE, (b) chronoamperometry of 60:40 wt% IrO_2:TaC at 1.9 V, and (c) Tafel plot.

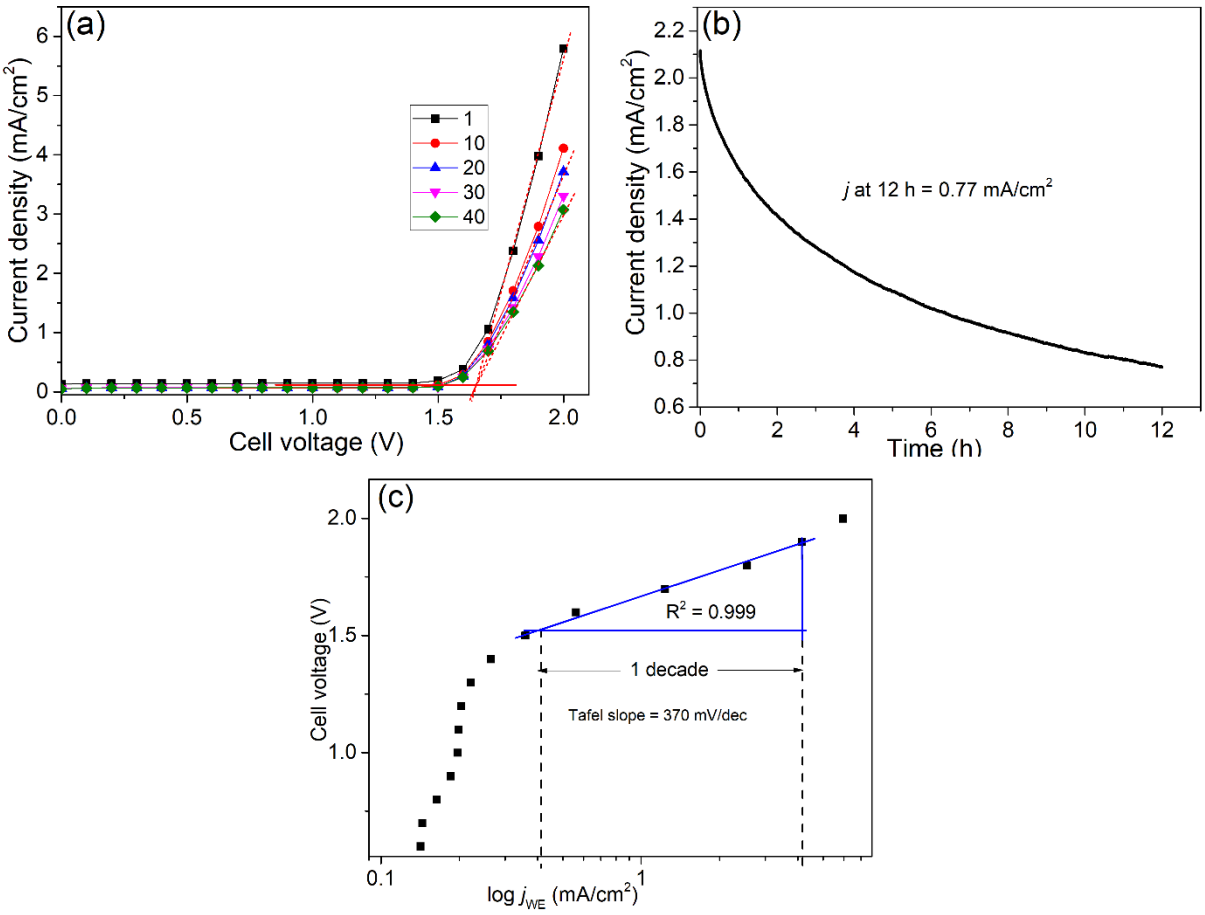

Fig. 5.7: (a) LSV for WE, (b) chronoamperometry of 70:30 wt% IrO_2:TaC at 1.9 V, and (c) Tafel plot.

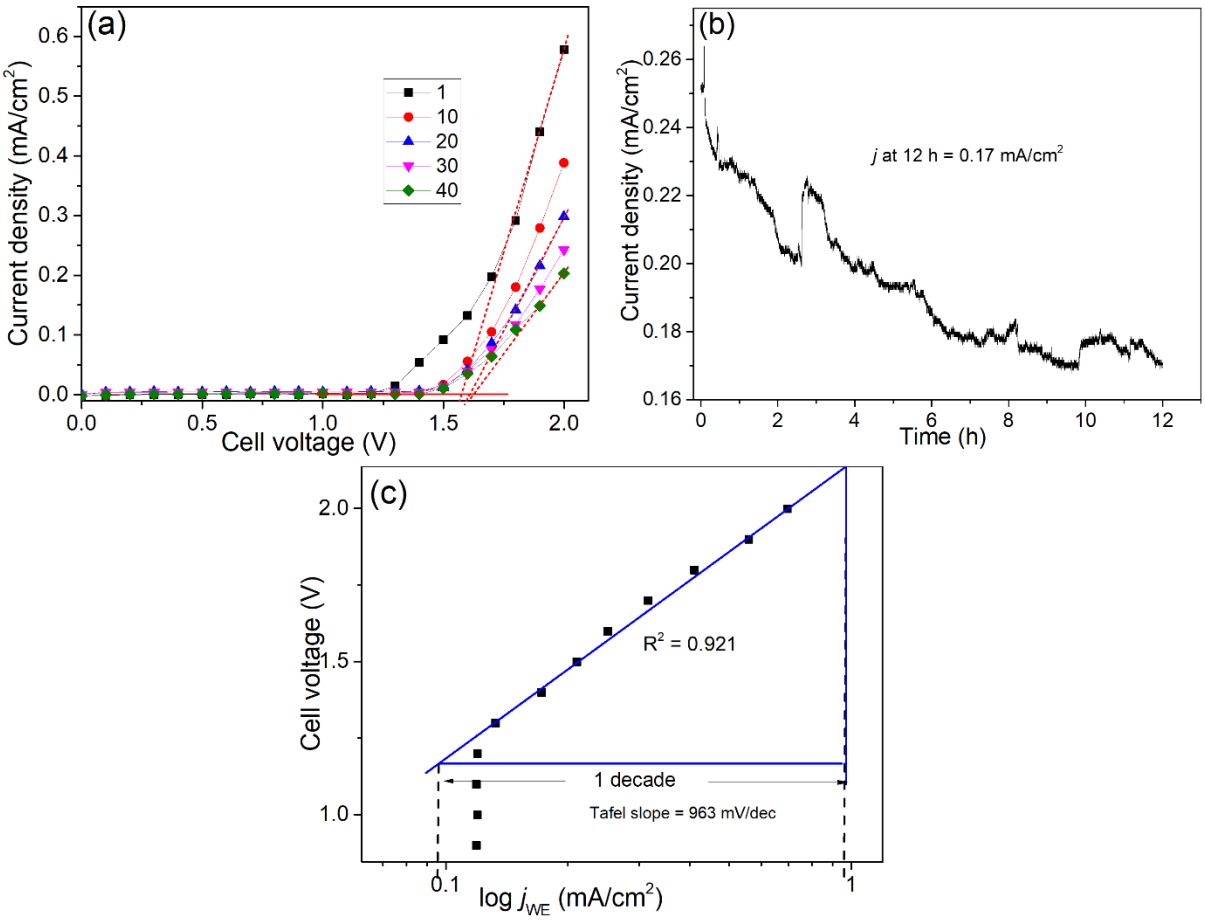

Fig. 5.8: (a) LSV for WE, (b) chronoamperometry of 100:00 wt% IrO_2:TaC at 1.9 V, and (c) Tafel plot.

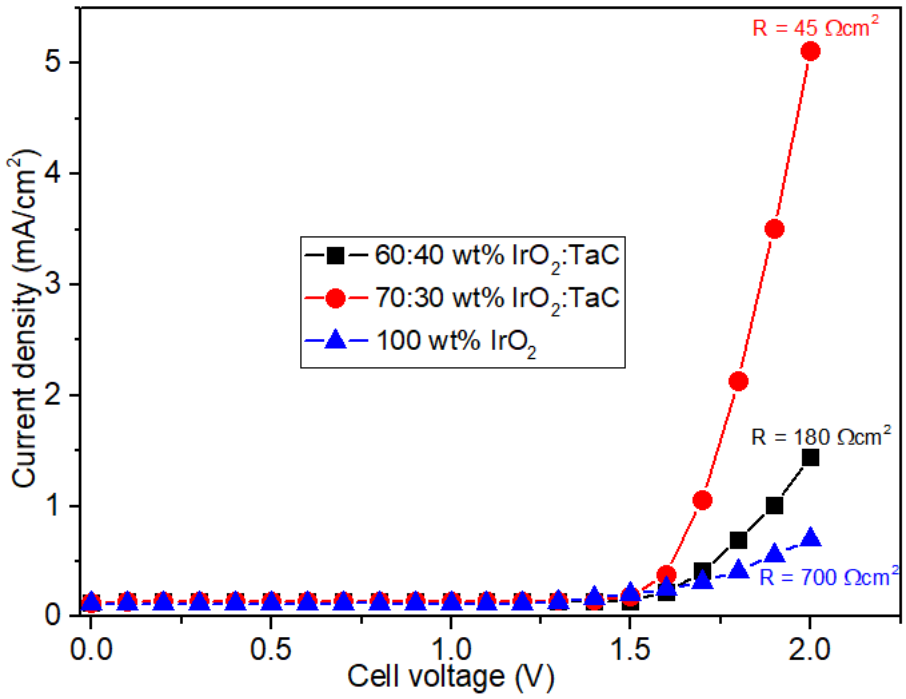

Fig. 5.9: LSV of WE; comparing the current density as a function of different electrocatalytic ratios.

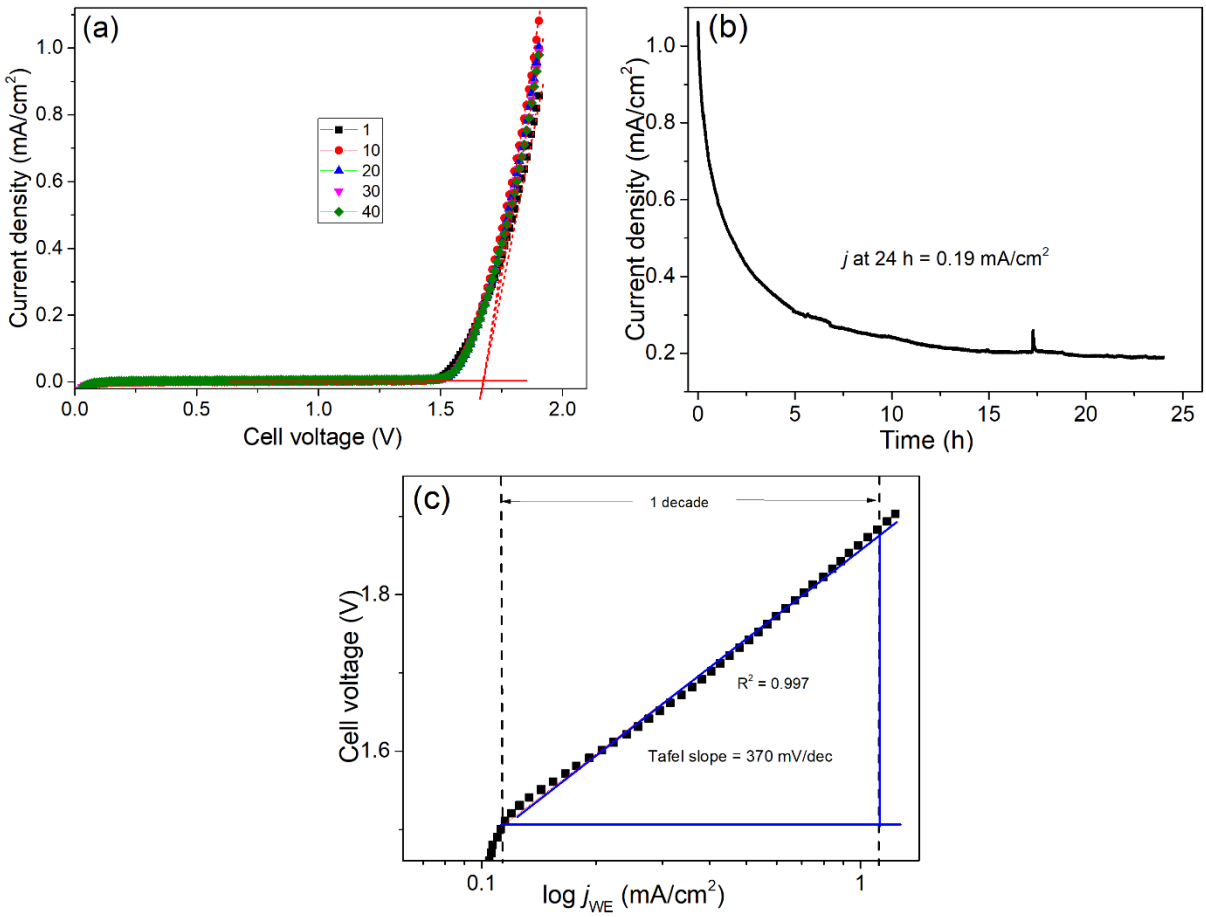

Fig. 5.10: (a) LSV for WE of 70:30 wt% IrO_2:TaC, (b) chronoamperometry at 1.9 V, and (c) Tafel plot.

Table 5.1: LSV results obtained from WE samples and the parameters obtained from the corresponding Tafel plots.

Wt% IrO_2:TaC	Current density at 1.9 V (mA/cm^2)			Onset potential (V)			Ohmic resistance (Ωcm^2)			CA at 1.9 V (mA/cm^2)	Fitting of equations	b (mV/dec)	j_o (A/cm^2)
	2^{st}	20^{th}	40^{th}	2^{st}	20^{th}	40^{th}	2^{st}	20^{th}	40^{th}				
60:40	1.44	0.85	0.71	1.66	1.66	1.66	183	333	413	0.43	y = 0.45x + 1.88	492	1.3×10^{-2}
70:30	5.11	3.79	3.18	1.64	1.64	1.64	45	70	84	0.77	y = 0.30x + 1.67	370	2.1×10^{-2}
70:30	0.96	1.10	1.08	1.69	1.69	1.69	237	267	275	0.19*	y = 0.37x + 1.86	370	1.4×10^{-2}
100:00	0.69	0.42	0.32	1.59	1.64	1.67	700	1198	1597	0.17	y = 1.24x + 2.27	963	5.4×10^{-3}

CA = Chronoamperometry performed for 12 h and * at 24 h, b = Tafel slope, j_o = exchange current density, 1^{st}, 20^{th} and 40^{th} are number of cycles.

Tafel plots were used in this study to evaluate the performance of each catalyst. A lower Tafel slope reveals a better performance. As shown in the Figs. 5.6c, 5.7c and 5.8c, the Tafel slope of 60:40, 70:30 and 100:00 wt.% IrO_2:TaC samples are 492, 370, and 963 mV/dec respectively. The 70:30 wt.% IrO_2:TaC sample gave the lowest Tafel slope, thus signifying its better activity than 60:40 and 100:00 wt.% IrO_2:TaC counterparts.

Chronoamperometry analysis (Figs. 5.6b, 5.7b and 5.8b) was used to evaluate the activity of the synthesized IrO_2 electrocatalysts towards the (OER). The initial quick decrease at the beginning of the run may be due to the charging current. As the running duration was increased from 0–12 h, the current densities decrease, and electrodes were stable under longer experimental running time. A constant current density plateau was not quickly obtained in the CA curves of 60:40 and 100:00 wt.% IrO_2:TaC samples while the 70:30 wt.% IrO_2:TaC sample (Figs. 5.7 & 5.10) maintained a constant current density during the 12 h CA runs. The current decay with time observed in CAs somehow obeyed the Cottrell behavior [190] (article from this work), i.e. diffusion limitation, but this may probably, not play a major role since both anolyte and catholyte are only H_2O, though, the within the catalyst pores there may be some gradient building up [190] which may be small to notice (thus negligible). This indicates good stability after the 12 h period would be achieved and ability of 70:30 wt.% IrO_2:TaC sample able to proceed beyond 12 h runs. In order to ascertain this, a new sample of 70:30 wt.% IrO_2:TaC (Fig. 5.10) was prepared and allowed to run for 24 h, thus confirming the stability of 70:30 wt.% IrO_2:TaC catalyst after 12 h. The two MEA containing 70:30 wt.% IrO_2:TaC electrocatalyst display the same Tafel slope of 370 mV/dec, which indicates the same electrocatalytic activity. The significant difference in their Ohmic resistance is an indication that MEA preparation and cell assembly seem to be the limiting factor of the setup.

This result is compared with those of the Polonsky group [254,263] which reported very high current densities in the range of 1.00 to 1.50 A/cm^2 at a cell voltage of 1.4 V to 1.8 V. The current density of this study showed a significant deviation which could be a result of the loading of the catalytic ink on the Nafion 117 membrane used in this experiment, while the Polonsky group loaded the catalyst directly onto the GDL. More so, the electrochemical experiments of the Polonsky group were carried out at elevated temperature (90^{o}C, 110^{o}C, 120^{o}C and 130^{o}C) while the present study was performed at room temperature (between 22°C and 24^{o}C). Furthermore, many authors applied significantly elevated temperature and pressure on their electrocatalytic compartment [187,254,261,263,264] to enhance the electrode reaction kinetics and increase the Nafion conductivity. This may significantly improve the current density by suppressing the bubble formation, thereby allowing the free movement of water and also ensuring its staying as liquid (with stirring). But in the present study, all experiments were carried out at ambient pressure and temperature, thus resulting in hydrogen bubble formation. Therefore, as long as there was bubble formation in the serpentine tubing; the reaction may be prevented from occurring at higher efficiency, thereby lowering the current densities and variation in current densities over the 40 cycles of runs. However, despite these difficulties, our catalyst indicated a good promise for WE, and the experiments were successfully carried out at room temperature and pressure conditions, thereby paving the way for lower cost of the experiment and also for modification in the near future.

5.3 Electrochemical reduction of FA on the In_2O_3 cathode in the two-electrode set-up

The only binder used in this section was Nafion solution (5% w/w in water and 1-propanol) owing to its ability to enhance proton conduction in the catalytic layer. The polymer electrolyte membrane used was the Nafion 117 membrane, while ethylene glycol which is a viscous liquid was used in the fabrication of MEAs to suppress the problem of swelling/wrinkling associated with the Nafion membrane, which is of great significance to achieve high-quality catalyst-coated membranes. IrO_2 was used as the anodic electrocatalyst whereas In_2O_3 was used as the cathodic electrocatalyst and carbon paper as the GDL upon which the In_2O_3 was sprayed. Table 5.2 presents the detailed preparation and catalyst loading for different samples.

Table 5.2: Catalyst loading of anode and cathode powders of samples A-E.

Anode	Catalyst loading (mg/cm^2)	Cathode	Catalyst loading (mg/cm^2)
14.4 mg 70:30 % wt IrO_2: TaC + 86 µL Nafion solution + 72 µL ethylene glycol; coated on 2 x 2 cm active area Nafion membrane	3.6	28.8 mg In_2O_3 powder + 172 µL Nafion solution + 100 µL ethylene glycol; coated on 4 x 4 cm active area carbon paper	7.2

5.3.1 Presentation of results of the In_2O_3 cathode in the two-electrode set-up

The results of electrocatalyst samples A-E presented in this section were to show how the electrocatalyst preparations were improved and to also check the reproducibility of these as-prepared electrocatalysts. This helped to further established the influence of electrocatalyst preparations on the electrochemical performance and to know whether the electrocatalysts that were dried naturally (electrocatalyst samples A-C and E) or dried using a microwave oven (electrocatalyst sample D) would perform better electrochemically at the same cell voltage.

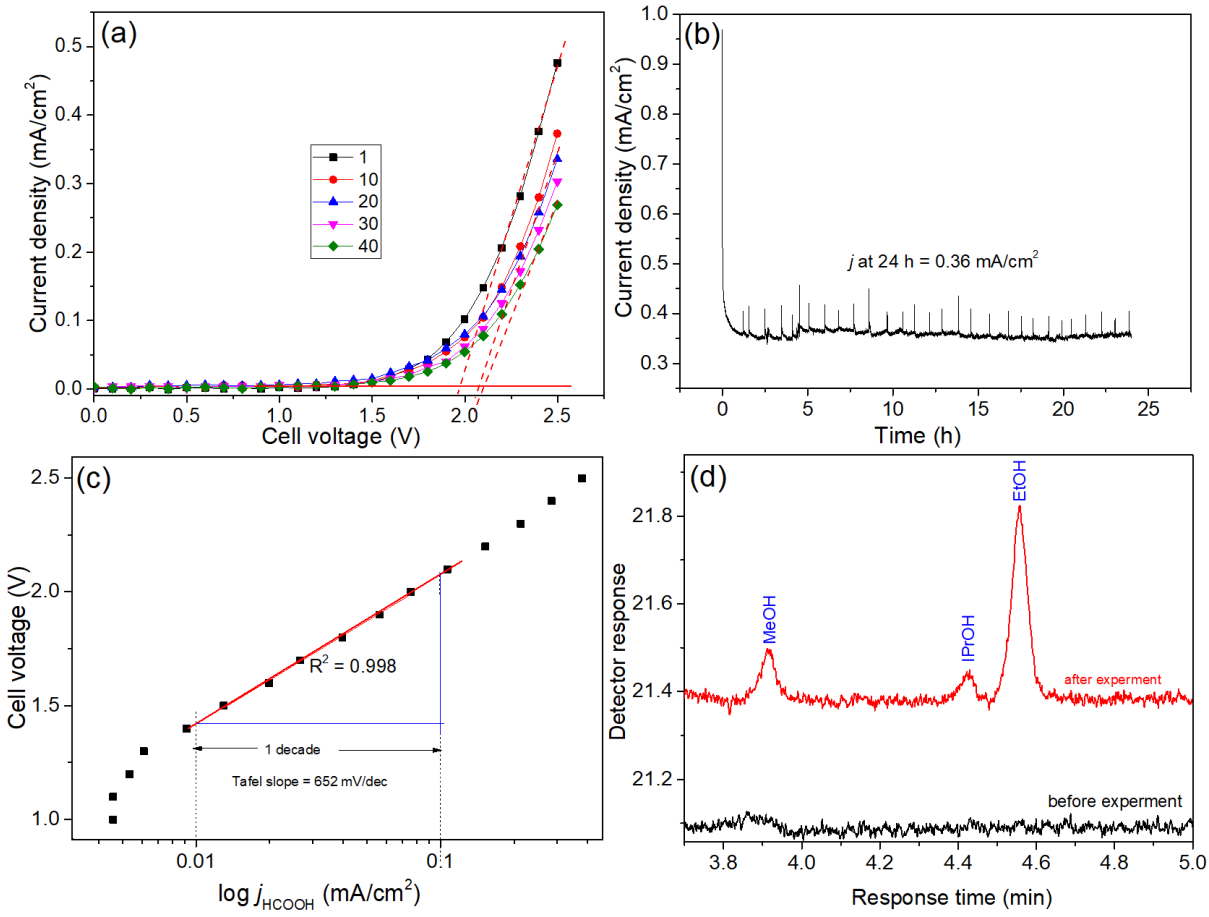

Fig. 5.11: LSV of FA reduction on In_2O_3 cathode (anode: 70:30 wt% IrO_2:TaC) for sample A: (a) Current density picked at random cycles, the red dotted lines are for the determination of the onset potential, (b) chronoamperometry at 2.4 V in the absence of any flow, (c) Tafel plot, and (d) liquid injected GC-FID chromatogram.

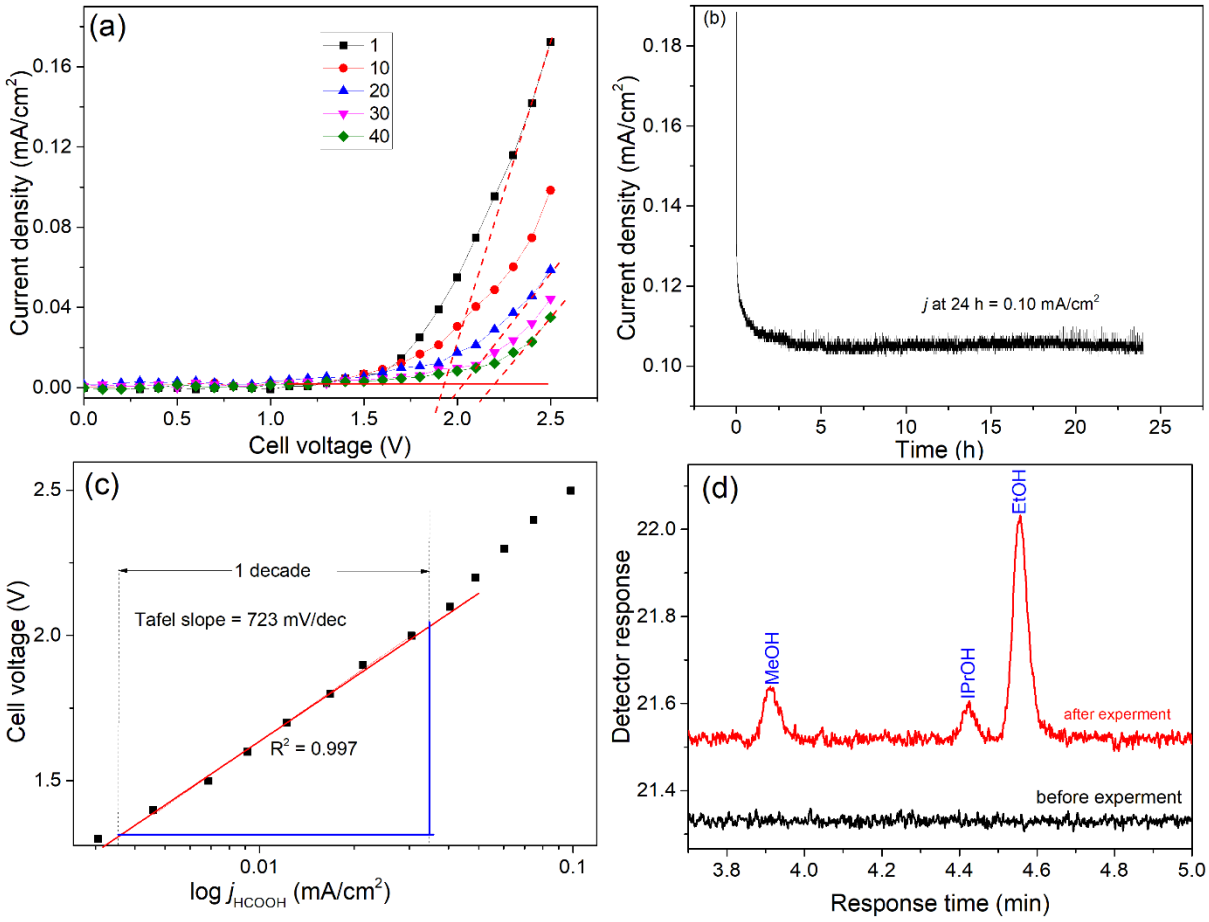

Fig. 5.12: LSV of FA reduction on In_2O_3 cathode (anode: 70:30 wt% IrO_2:TaC) for sample B: (a) Current density picked at random cycles, the red dotted lines are for the determination of the onset potential, (b) chronoamperometry at 2.4 V in the absence of any flow, (c) Tafel plot and (d) liquid injected GC-FID chromatogram.

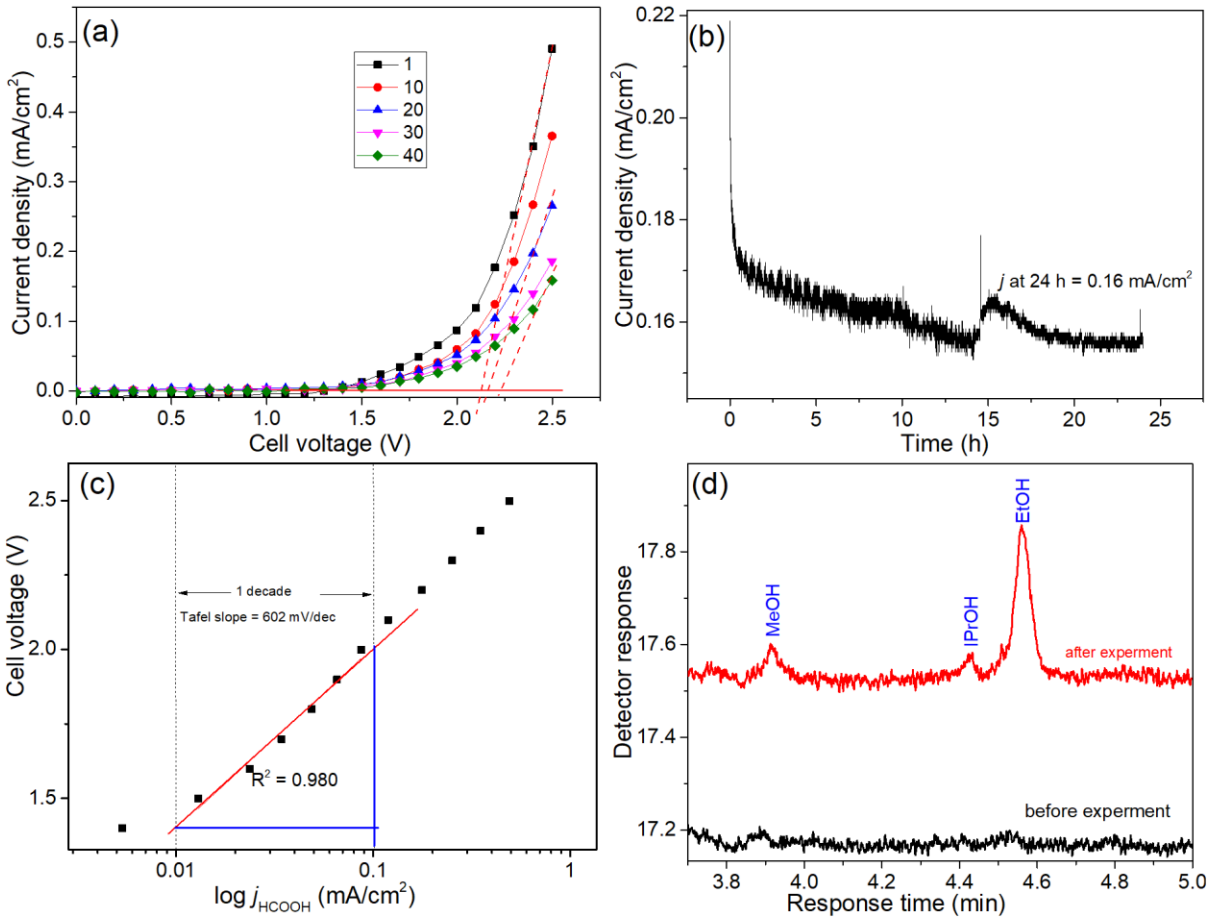

Fig. 5.13: LSV of FA reduction on In_2O_3 cathode (anode: 70:30 wt% IrO_2:TaC) for sample C: (a) Current density picked at random, the red dotted lines are for the determination of the onset potential, (b) chronoamperometry at 2.4 V in the absence of any flow, (c) Tafel plot, and (d) liquid injected GC-FID chromatogram.

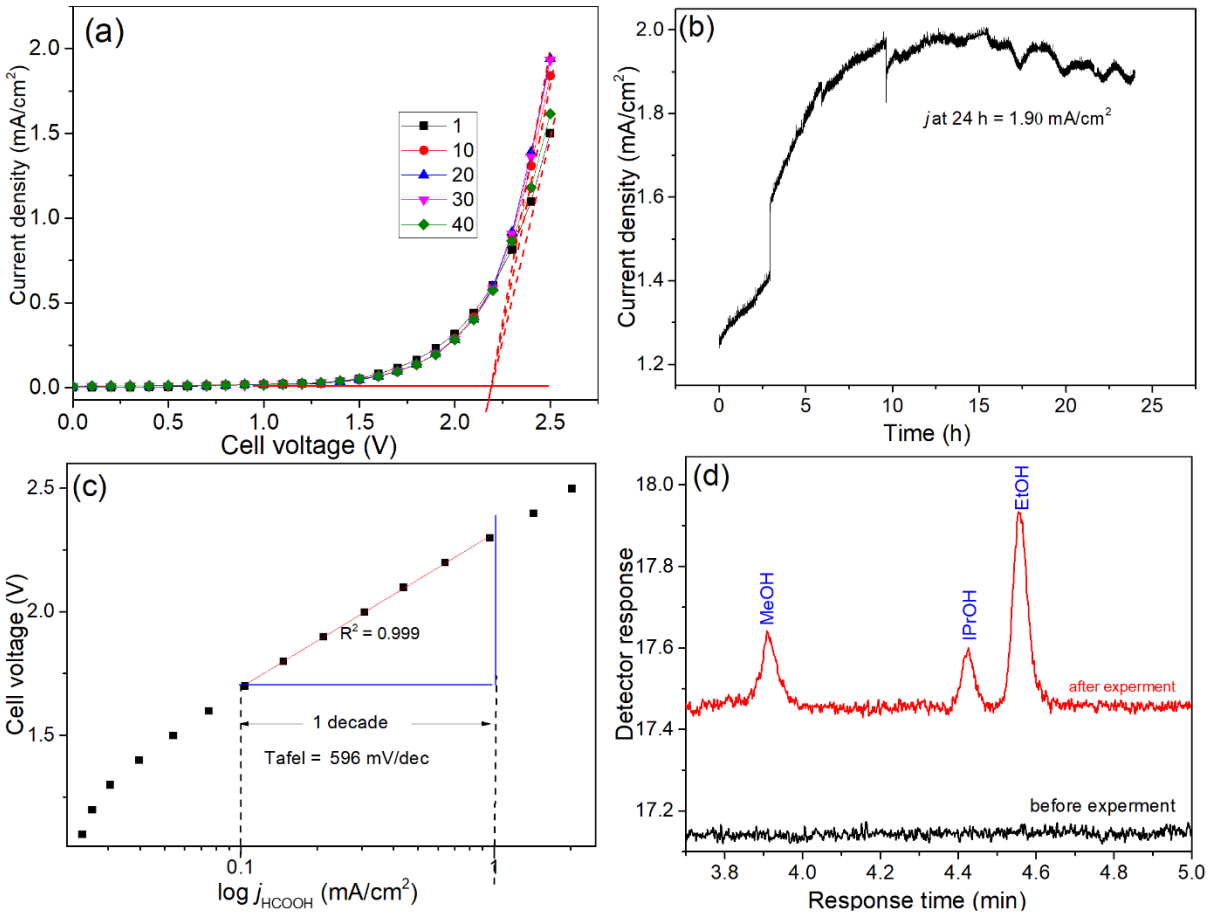

Fig. 5.14: LSV of FA reduction on In_2O_3 cathode (anode: 70:30 wt% IrO_2:TaC) for sample D: (a) Current density picked at random cycle, the red dotted lines indicate the onset potential, (b) chronoamperometry at 2.4 V in the absence of any flow, (c) Tafel plot, (d) liquid injected GC-FID chromatogram.

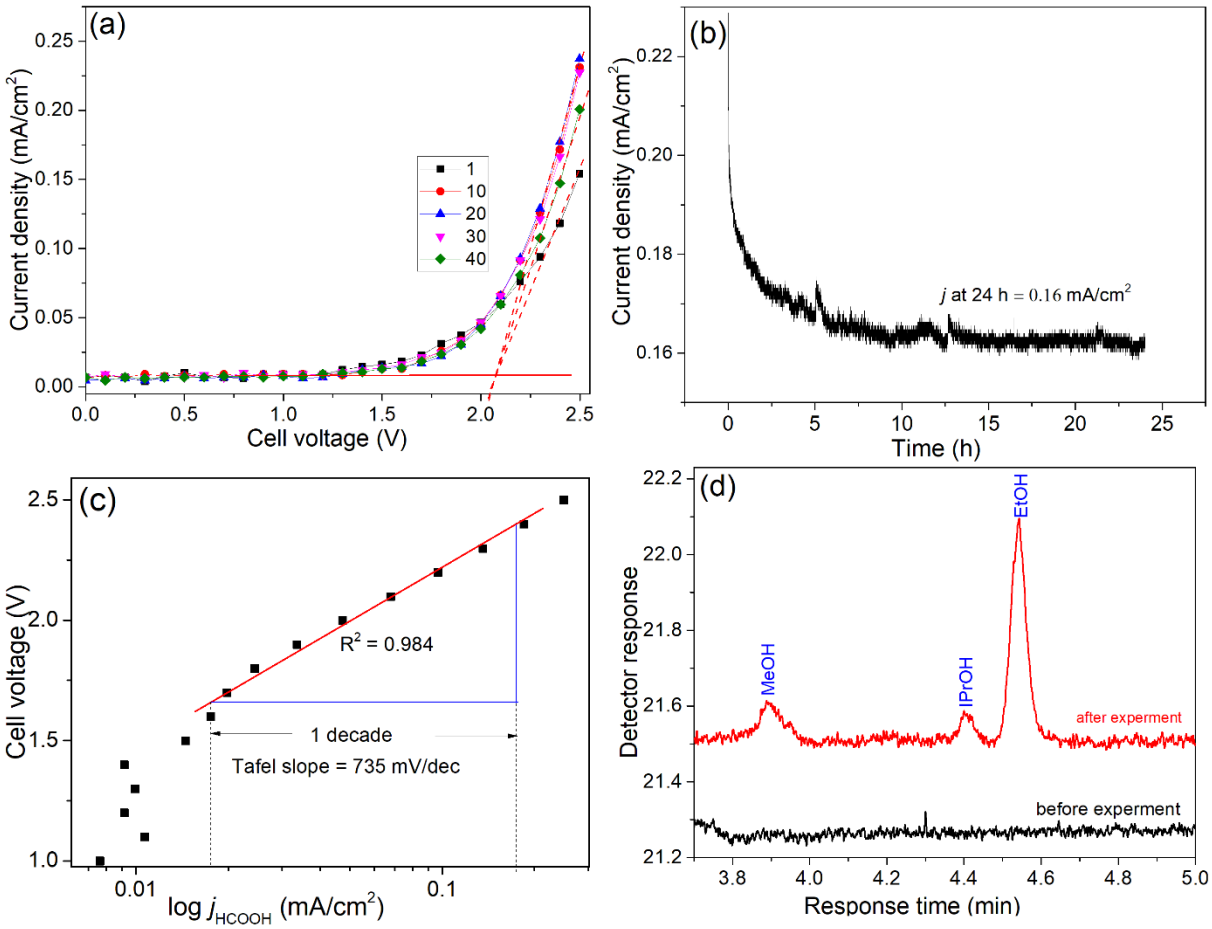

Fig. 5.15: LSV of FA reduction on In_2O_3 cathode (anode: 70:30 wt% IrO_2:TaC) for sample E: (a) Current density picked at random cycle, the red dotted lines are for the determination of the onset potential, (b) chronoamperometry at 2.4 V in the absence of any flow, (c) Tafel plot, and (d) liquid injected GC-FID chromatogram.

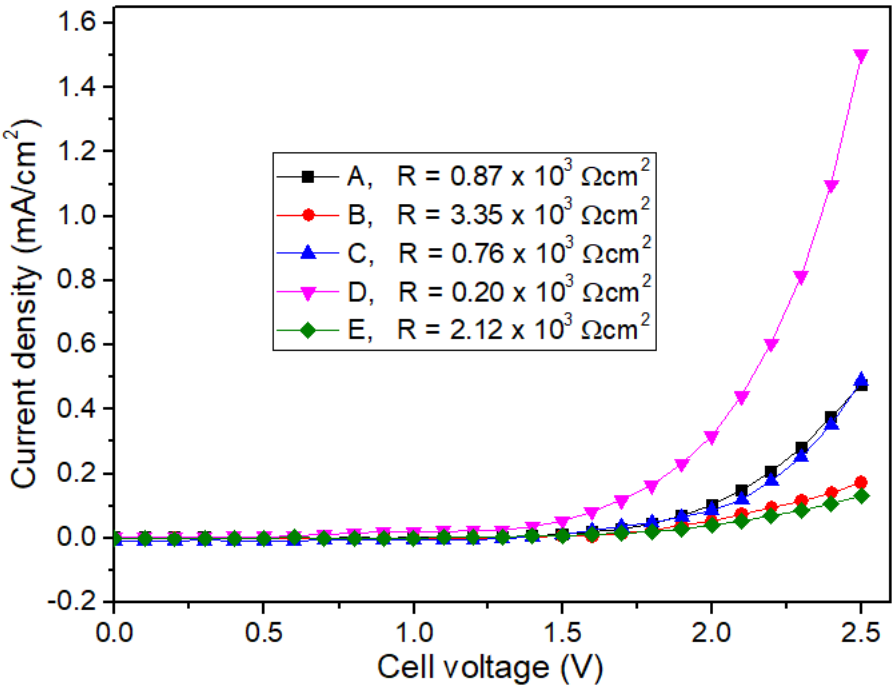

Fig. 5.16: LSV curves comparison of current densities of electrocatalyst samples A, B, C, D and E.

Table 5.3: LSV results obtained from samples A-E and the parameters obtained from the corresponding Tafel plots.

Sample	Current density at 2.4 V (mA/cm^2)			Onset potential (V)			Ohmic resistance x 10^3 (Ωcm^2)			CA at 2.4 V (mA/cm^2)		Fitting of equations	b (mV/dec)	j_o (A/cm^2)
	1^{st}	20^{th}	40^{th}	1^{st}	20^{th}	40^{th}	1^{st}	20^{th}	40^{th}	1^{st}	2^{nd}			
A	0.48	0.34	0.27	2.09	2.15	2.19	0.87	1.06	1.13	0.36	0.24	y = 0.7x+2.7	652	1.9×10^{-3}
B	0.17	0.06	0.04	1.93	2.12	2.29	3.35	6.49	0.61	0.10	0.10	y = 0.8x+3.1	723	7.4×10^{-4}
C	0.49	0.27	0.16	2.13	2.20	2.28	0.76	1.10	1.27	0.17	0.16	y = 0.6x+2.6	602	2.4×10^{-3}
D	1.50	1.94	1.62	2.19	2.19	2.19	0.20	0.16	0.19	1.90	-	y = 0.6x+2.3	596	4.8×10^{-3}
E	0.15	0.24	0.20	2.19	2.19	2.19	2.23	1.35	1.61	0.17	0.16	y = 0.7 + 3.0	735	1.1×10^{-3}

*CA = Chronoamperometry, b = Tafel slope, j_o = exchange current density, 1^{st}, 20^{th} and 40^{th} are cycle numbers.

5.3.2 Discussion of results of the In_2O_3 cathode in the two-electrode set-up

Using a GDE for FARR, both FA, electrons and protons came through the GDL, the CL and the electrolyte-catalytic layer interfaces. It should be noted that transferring electron and proton and FA diffusion must be sufficient to achieve efficient FARR. In this section, Nafion solution was used as the binder, while the cathodic GDE consists of carbon paper upon which the cathode electrocatalyst was sprayed.

Linear sweep voltammetry was employed to monitor the reduction on the In_2O_3 layers in the GDEs. The electrochemical FARR reduction was performed at 2.4 V cell voltage. The polarization curves revealed a shift in voltage towards more negative voltage which is obvious in samples A–C; as shown in Figs. 5.11a, 5.12a, and 5.13a. In samples D and E, the current density increases from run 1 to run 30 and is more stable from cycle 10 to 30. The instability of the runs 1 to 10 could be attributed to electrode conditioning whereas between run 10 and run 30, the electrode is approaching an equilibrium state while after the 30th run, it began to decline. However, considering their random selection over the 40 cycles, sample D (Fig. 5.14a and Table 5.3) exhibited an increased current density, (j) from 1.50 mA/cm^2 (1st cycle) to 1.94 mA/cm^2 (20th cycle) at 2.19 V but afterward started fluctuating. Sample E (Fig. 5.15a and Table 5.3) also showed the same trend: j = 0.15 mA/cm^2 (1st cycle) to 0.24 mA/cm^2 (20th cycle). The degradation in sample D and E after 30 runs could be attributed to the electrode achieving its complete stability state (or reached equilibrium) and afterward started to degrade as noticed in runs 30–40. Comparing the current density for sample D and E, sample D was more than 8 times higher than E, and sample E was also approximately 9 times more resistant than sample D; this was attributed to the better drying/preparation procedure. It was discovered during spray-coating that In_2O_3 inks had trouble drying (whether ethylene glycol was used in the In_2O_3 ink preparations or not) at room temperature, thereby resulting in some ink wastage during the long sitting period of drying which may take at least one week, and even at this time, the

complete drying is not guaranteed. Having discovered this, the spraying of In_2O_3 ink on carbon paper for sample D was aided by microwave drying to facilitate the complete drying of the coated GDL.

Conversely, the sample A to C (Figs. 5.11a, 5.12a and 5.13a) showed gradual degradation of the electrode from runs 1–40 (and Table 5.3), they followed similar trends and no perfect stability was observed throughout the whole 40 runs. This is also obvious in their polarization curves (Figs. 5.11a, 5.12a and 5.13a) which degraded with an increase in cell voltage. The instability of the electrode cannot be attributed to the electrode conditioning, but degradation effects which could be due to the preparation method of the electrode. This shows that the efficiency of sample B – C decreases over time, as observed in their 1^{st} to 40^{th} cycle. Sample B (Fig. 5.12a) degraded from 0.49 mA/cm^2 at 2.13 V (onset potential) to 0.16 mA/cm^2 at 2.28 V (onset potential), while sample C (Fig. 5.13a) showed a degraded current density from 0.17 mA/cm^2 at 1.93 V to 0.04 mA/cm^2 at 2.29 V, whereas, sample A (Fig. 5.11a) observed a similar trend from 0.48 mA/cm^2 to 0.27 at the same cell voltage of 2.4 V. Nevertheless, a fair amount of stability was observed in sample A between 9 and 16 cycles, therefore the cycles 11 to 20 were considered meaningful to average the curves (Fig. SI 4 in the appendix) with current density and Ohmic resistance of 0.36 ± 0.02 mA/cm^2 at 2.4 V and 122 Ωcm^2 respectively. It is evident from LSV runs that sample A was more stable than B and C, revealing that the preparation method for sample A was much better than that of B and C.

Overall, sample D performed much better than E and others (Fig 5.16). This is evident in their respective LSV as shown in Figs. 5.14a & 5.15a; implying that the preparation procedure for samples D and E was improved on; in comparison with samples A – C catalysts. This observation may be due to the catalyst peeling off from the GDL after this period. This is consistent with previous works [265–268] and the solid electrode results reported [269,270]. The possibility of gradually peeled-off catalysts from the carbon paper (GDL) has been reported by

various authors as a common phenomenon observed in GDE systems, thereby resulting in a rapid decrease in the FARR performance [265–268,271,272]. The variation in the current density may be due to the preparation method and drying procedure. Because, ordinarily, the ink took longer to completely dry on carbon paper; sometimes the drying was aided by oven drying which could have a positive effect on the performance of the electrode. Nonetheless, the entire LSV curves (Figs. 5.11a, 5.12a, 5.13a, 5.14a & 5.15a) exhibited two distinct regions. The region 1 could be attributed to a charge transfer (the rate-limiting steps) region where there is an exponential increase in current density as the cell voltage increases up to around 1.4 V and becomes almost linear afterward. The region 2 can be attributed to the dominance of the Ohmic resistance of the system.

Considering the fact that the FARR under study is a complex reaction that involves three different reactions occurring at the same time in a single cell (formic acid reduction, HER and OER), it is very difficult or even impossible to know which one of the reactions contributed most and this may affect the current density variations. It should be noted that Nafion played a dual role in FARR: it enhanced the proton transfer and allowed the integration of the catalytic layer which may favor FARR. But Nafion cannot conduct electrons and hinders the electron transfer between the gas diffusion layer and catalyst layers and also electron transfer within the catalytic layer. This would decrease the FARR. Similar findings have been reported in the literature [256,273,274].

The chronoamperometry (CA) experiments for FARR were carried out for 24 h at a cell voltage of 2.4 V (Figs. 5.11b, 5.12b, 5.13b, 5.14b & 5.15b). The current densities (j) of samples A, B, C, D and E are 0.36, 0.10, 0.17, 1.90 and 0.17 mA/cm^2, respectively. Sample D exhibited the highest current density (Fig. 5.14b). From the individual CA, certain drops in initial currents were seen which are probably just of capacitive (not Faradaic) nature and electrochemical change in the surface: for A (Fig. 5.11b) 0 – 1.6 h and reached plateaus at 1.6 – 24 h; for B

(Fig. 5.12b): 0 – 3 h, and reached plateaus at 3 – 24 h. Sample C (Fig. 5.13b) was 0 –16 h and observed plateaus at 16 – 24 h; for sample D (Fig. 5.14b) from 0 – 10 h and reached plateaus at 10 – 24 h; whereas, E (Fig. 5.15b) was from 0 –8 h, and exhibited its plateaus at 8 – 24 h. The jumps experienced with sample C (Fig. 5.13b) between 14 and 17 h could be attributed to bubble formation occurring during the investigation. It is evident that all CAs experienced pulses before stabilizing/leveling and achieved a plateau. During this period methanol (MeOH), isopropanol (iPrOH) and ethanol (EtOH) were formed as shown in their respective chromatogram (Figs. 5.11d, 5.12d, 5.13d, 5.14d & 5.15d). The retention time in comparison with the standard observed for MeOH, iPrOH and EtOH were 3.92, 4.43 and 4.55 min, respectively, as shown in their respective chromatograms.

Tafel plots were employed to assess the electrochemical reaction of FARR to products. Parameters obtained from Tafel plots are presented in Table 5.3. They were obtained according to the respective voltammograms of samples A, B, C, D and E and are presented in Figs. 5.11c, 5.12c, 5.13c, 5.14c & 5.15c. The Tafel equation obeyed a linear region of the plot, related to the overpotential (η) and the exchange current density (j_o) [233]. As shown in Table 5.3, slopes ranging from 596 mV/dec to 735 mV/dec were obtained from the corresponding Tafel plots (Figs. 5.11c, 5.12c, 5.13c, 5.14c & 5.15c.). The relevant comments on Tafel analysis are given in page 121. Though, the obtained values were somewhat high but still similar to some works reported [133,275–277], showing that we carried out a complex reaction in a single system.

5.4 Enhancing the formic acid diffusion by adding polytetrafluoroethylene into the catalyst layer of the In_2O_3 in the two-electrode set-up

A GDE consists of GDL, CL and current collector. The CL consists of the binder and catalysts. The FA diffusion, proton and electron conductions in the CL are crucial to achieving an effective electrochemical reaction. However, it was noticed that the FA diffusion in the CL is insufficient since Nafion is unable to provide enough channels as observed in the low current densities of the samples with only Nafion solution as the binder. Here, in this section, polytetrafluoroethylene (PTFE) was added to the In_2O_3 CL to facilitate diffusion. Nafion solution was used as the binder owing to its ability to enhance proton conduction while PTFE cannot conduct protons [256–258,265]. Therefore, hydrophilic Nafion solution and hydrophobic PTFE are the primary binders used in this section. The optimum mixture creates a hydrophobicity that prevents the pores from getting flooded by the liquid and thus facilitates the transport of the gases. The difference in the preparation procedure and catalyst loadings are presented in Table 5.4.

Table 5.4: Detail of catalysts loading of anode and cathode powders for H, I, K and L.

Sample	Anode	Catalyst loading (mg/cm^2)	Cathode	Catalyst loading (mg/cm^2)
H	14.4 mg 70:30 % wt IrO_2: TaC + 86 µL Nafion solution + 72 µL ethylene glycol; coated on 2 x 2 cm active area Nafion membrane	3.6	28.8 mg In_2O_3 + 172 µL Nafion solution + 0.15 wt% PTFE; coated on 4 x 4 cm active area carbon paper	7.2
I	14.4 mg 70:30 %wt IrO_2: TaC + 86 µL Nafion solution + 72 µL ethylene glycol; coated on 2 x 2 cm active area Nafion membrane	3.6	28.8 mg In_2O_3 + 172 µL Nafion solution +0.15 wt% PTFE; coated on 4 x 4 cm active area PTFE treated carbon paper at 110 ^oC for 30 min	7.2
K	14.4 mg 60:40 % wt IrO_2: TaC+ 86 µL Nafion solution + 72 µL ethylene glycol; coated on 2 x 2 cm	3.6	28.8 mg In_2O_3 + 172 µL Nafion solution + 0.15 wt% PTFE; coated on 4 x 4 cm active area carbon paper	7.2

	active area Nafion membrane			
L	14.4 mg 60:40 %wt IrO_2: TaC + 86 µL Nafion solution + 72 µL ethylene glycol; coated on 2 x 2 cm active area Nafion membrane	3.6	28.8 mg In_2O_3 + 172 µL Nafion solution +0.15 wt% PTFE; coated on 4 x 4 cm active area PTFE-treated carbon paper at 110 °C for 30 min	7.2

5.4.1 Presentation of results of the PTFE-In_2O_3 cathode in the two-electrode set-up

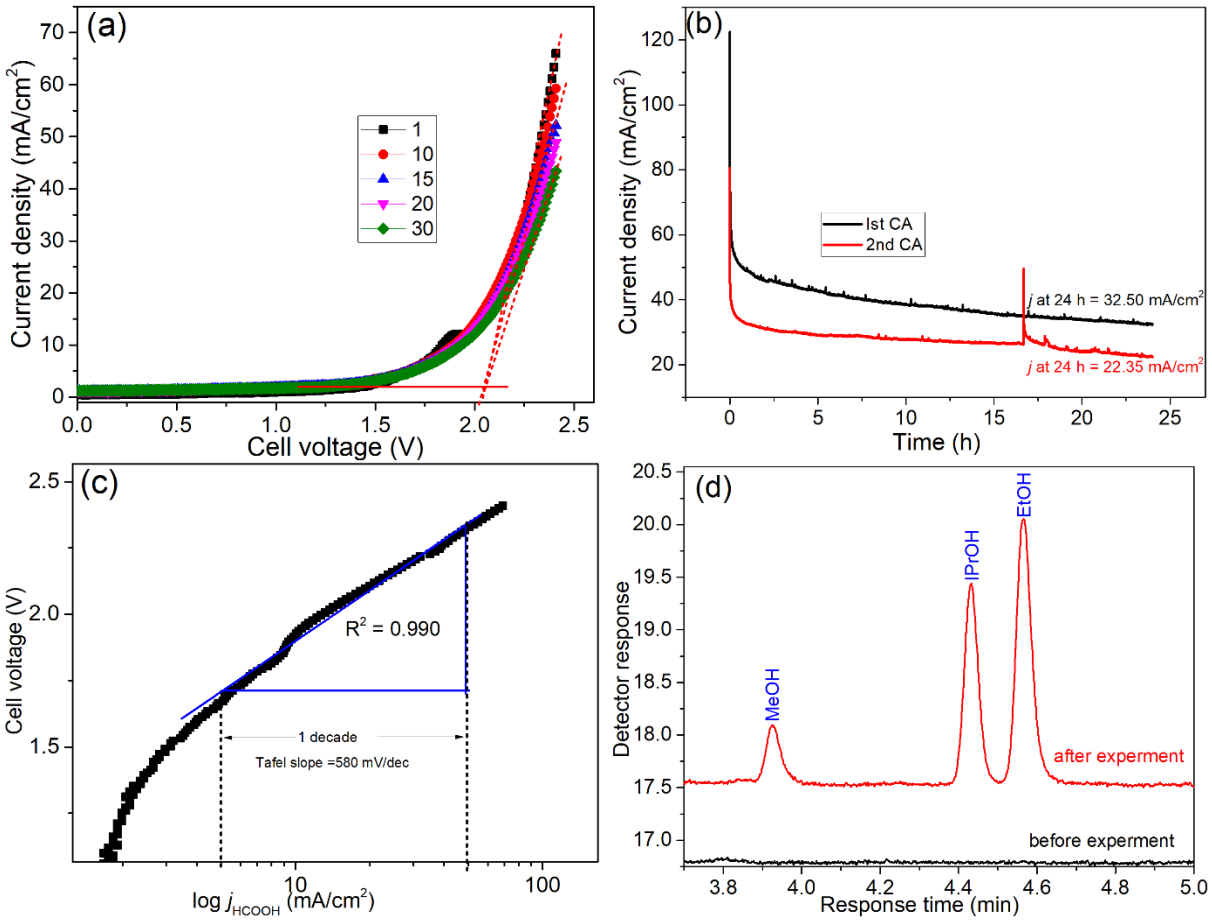

Fig. 5.17: LSV of FA reduction on 0.15 wt% PTFE-In_2O_3 cathode (anode: 70:30 wt% IrO_2:TaC) for Sample H: (a) Current density picked at random cycles, the red dotted lines are for the determination of onset potential, (b) chronoamperometry at 2.4 V in the absence of any flow, (c) Tafel plot, and (d) liquid injected GC-FID chromatogram.

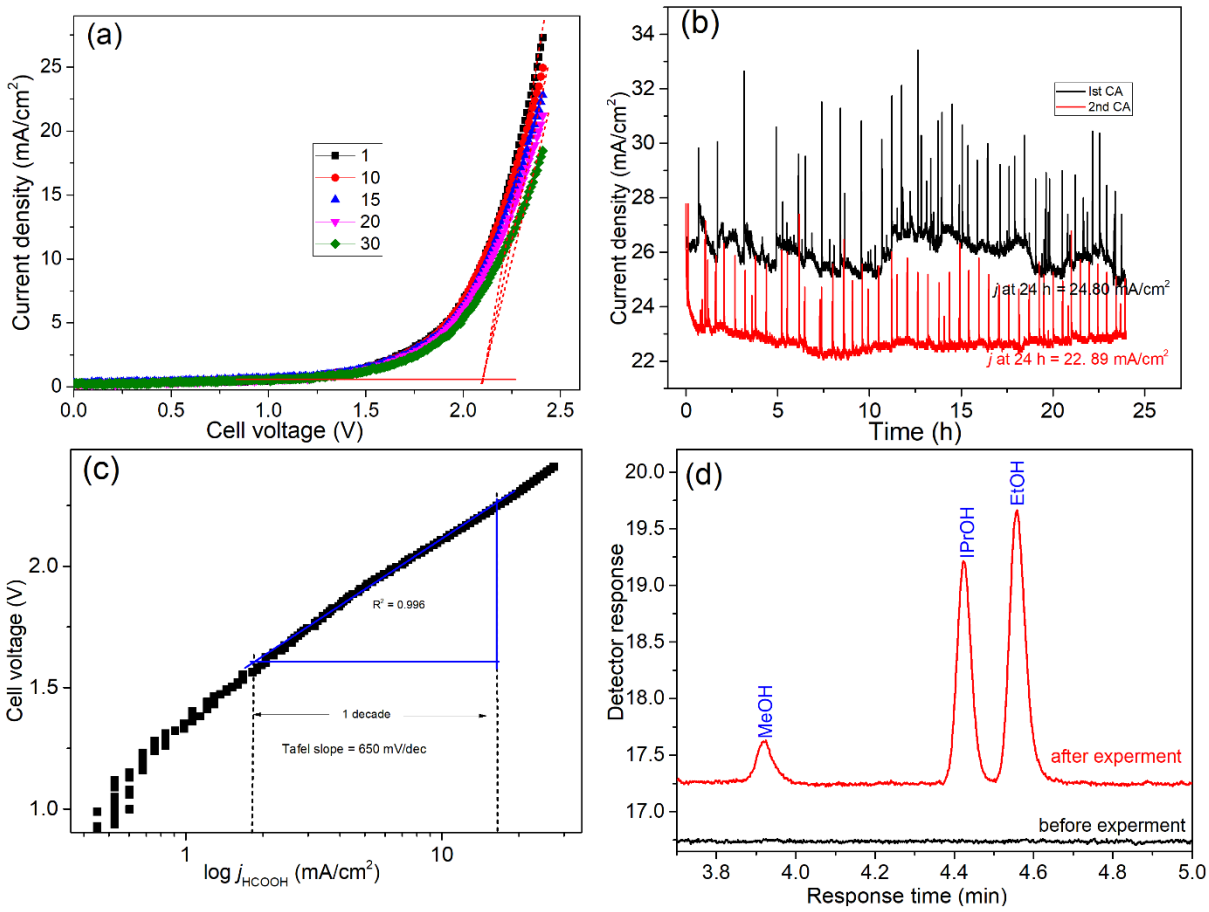

Fig. 5.18: LSV of FA reduction on heat-treated carbon paper 0.15 wt% PTFE-In_2O_3 cathode (anode: 70:30 wt% IrO_2:TaC) for Sample I: (a) Current density picked at random cycles, the red dotted lines are for the determination of onset potential, (b) chronoamperometry at 2.4 V in the absence of any flow, (c) Tafel plot, and (d) liquid injected GC-FID chromatogram.

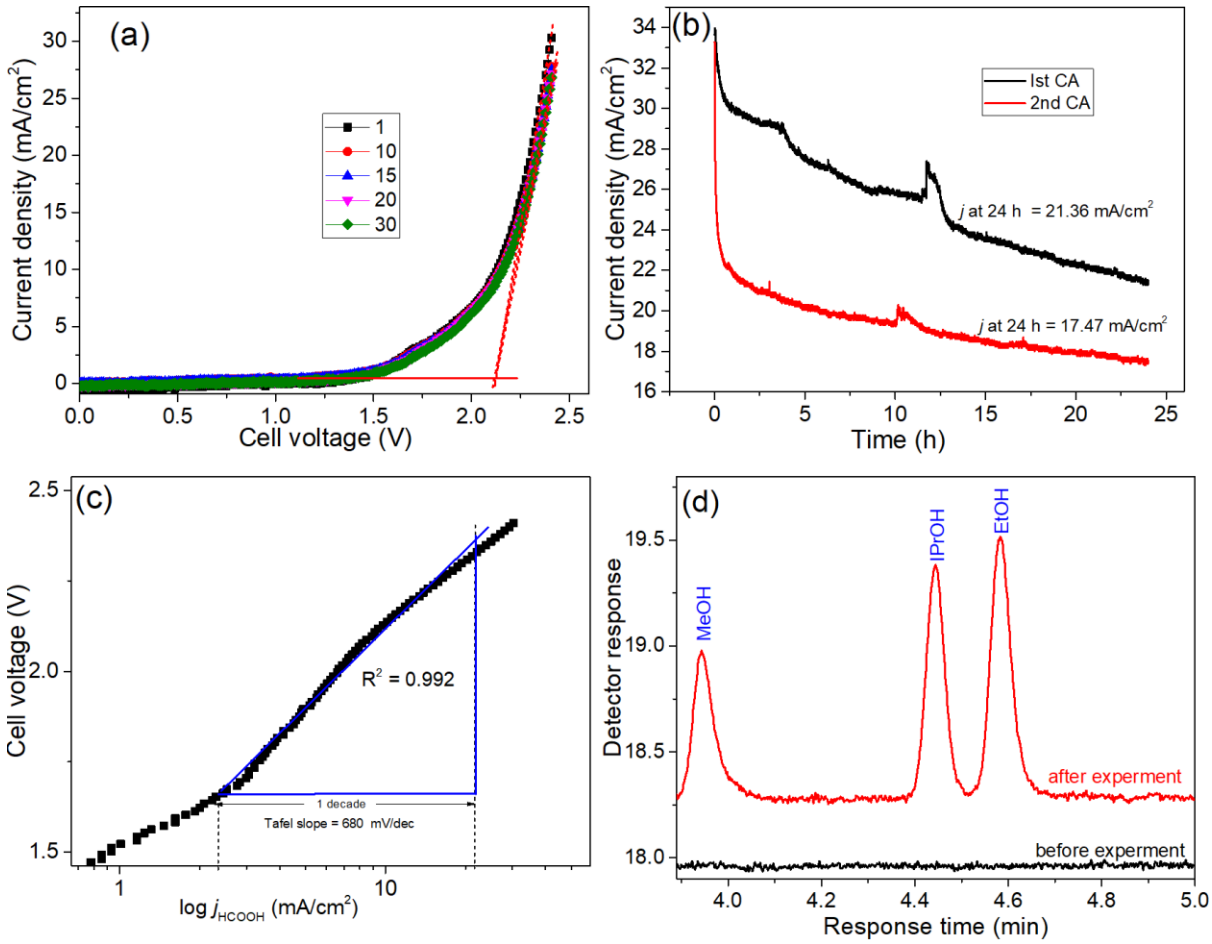

Fig. 5.19: LSV of FA reduction on 0.15 wt% PTFE-In_2O_3 cathode (anode: 60:40 wt% IrO_2:TaC) for sample K: (a) Current density picked at random cycles, the red dotted lines are for the determination of onset potential, (b) chronoamperometry at 2.4 V in the absence of any flow, (c) Tafel plot, and (d) liquid injected GC-FID chromatogram.

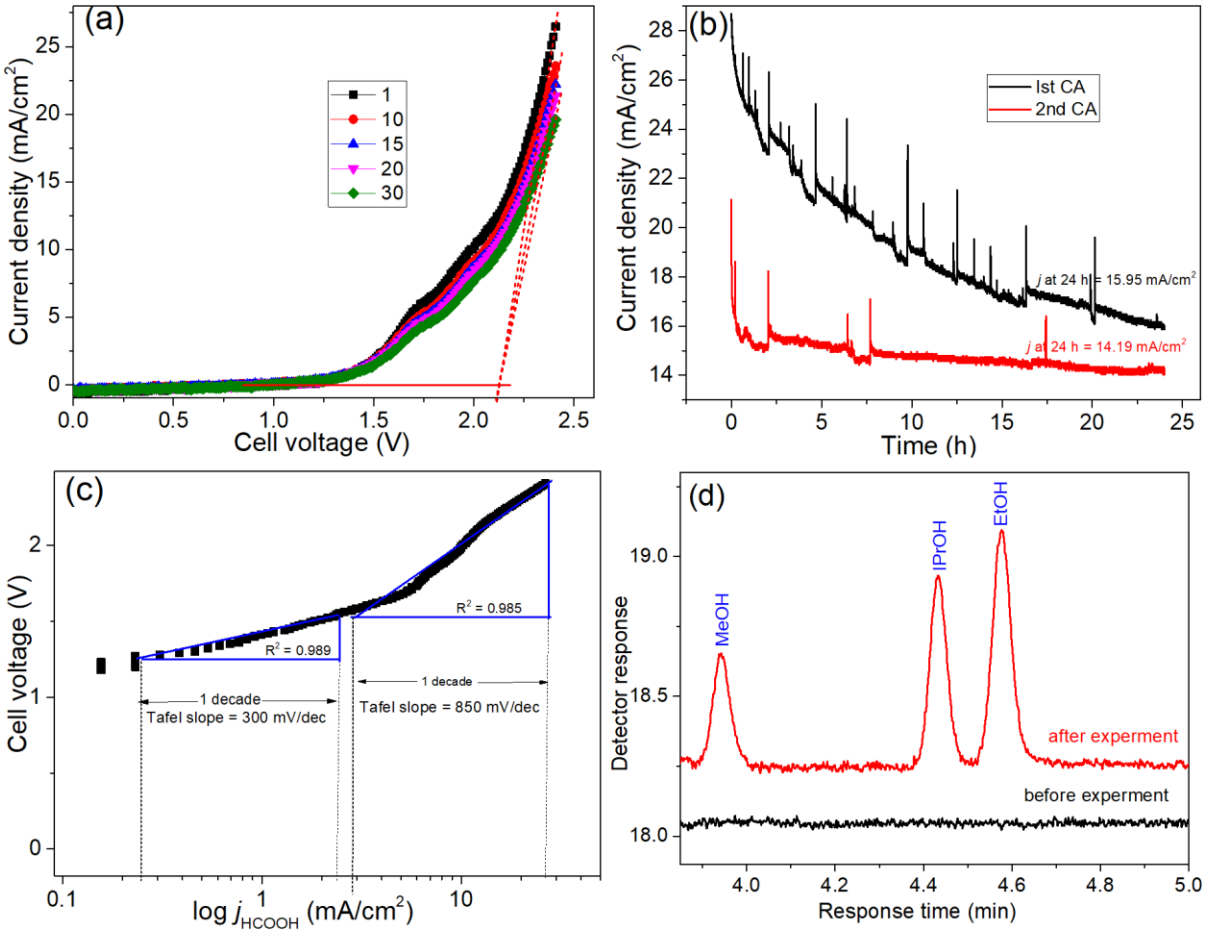

Fig. 5.20: LSV of FA reduction on heat-treated carbon paper 0.15 wt% PTFE-In_2O_3 cathode (anode: 60:40 wt% IrO_2:TaC) for sample L: (a) Current density picked at random cycles, the red dotted lines are for the determination of onset potential, (b) chronoamperometry at 2.4 V in the absence of any flow, (c) Tafel plot, and (d) liquid injected GC-FID chromatogram.

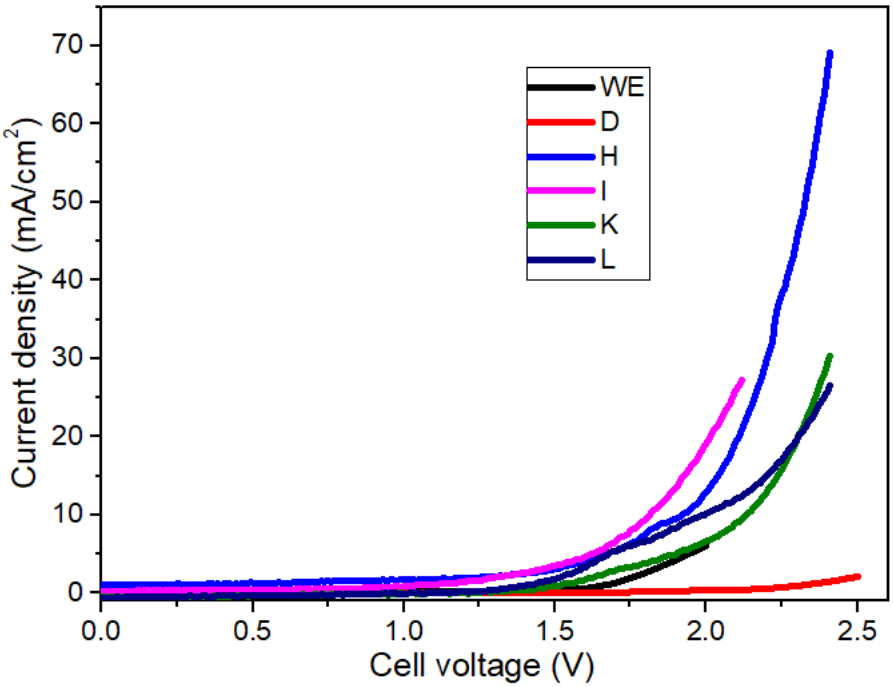

Fig. 5.21: LSV curves showing the comparison of current densities of WE with samples D, H, I, K, and L.

(**Curves I, K, and L were corrected by a constant small offset in the current values**).

Table 5.5: LSV results obtained from samples H, I, K, and L and the parameters obtained from the corresponding Tafel plots.

Sample	Current density at 2.4 V (mA/cm^2)			Onset potential (V)			Ohmic resistance (Ωcm^2)			CA (mA/cm^2) at 2.4 V		Fitting of equations	b (mV/dec)	j_o (A/cm^2)
	1^{st}	15^{th}	30^{th}	1^{st}	15^{th}	30^{th}	1^{st}	15^{th}	30^{th}	1^{st}	2^{nd}			
H	65.99	52.19	43.41	2.06	2.06	2.06	5.45	6.93	8.39	32.50	22.35	y = 0.65x + 1.25	580	0.06
I	27.39	22.89	18.50	2.10	2.10	2.10	11.66	14.04	17.52	24.80	22.89	y = 0.68x + 1.43	690	0.04
K	30.64	27.95	26.85	2.12	2.12	2.12	9.64	10.58	10.98	21.36	17.47	y = 0.74x + 1.38	680	0.04
L	26.48	22.39	19.61	2.13	2. 13	2. 13	10.68	12.65	14.40	15.95	14.19	y = 0.83x + 1.17	300 & 850	0.07

Where H is 0.15 wt% PTFE-In_2O_3 cathode (anode: 70:30 wt% IrO_2:TaC), I is heat-treated carbon paper 0.15 wt% PTFE-In_2O_3 cathode (anode: 70:30 wt% IrO_2:TaC), K is 0.15 wt% PTFE-In_2O_3 cathode (anode: 60:40 wt% IrO_2:TaC) and L is on heat-treated carbon paper 0.15 wt% PTFE-In_2O_3 cathode (anode: 60:40 wt% IrO_2:TaC). CA is chronoamperometry

1^{st}, 15^{th} and 30^{th} are the number of cycles.

5.4.2 Discussion of results of the PTFE-In_2O_3 cathode in the two-electrode set-up

LSV was employed in monitoring the FARR on the PTFE-In_2O_3 layer in the GDE from 0 to 2.4 V and each CA was performed at 2.4 V for 24 h. The Figs. 5.17a, 5.18a, 5.19a, and 5.20a represent the LSV curves selected randomly over the 30 cycles of EC runs while Table 5.5 presents the LSV results obtained from samples H, I, K and L. For sample H (Fig. 5.17a) the recipe consists of 70:30 wt% IrO_2:TaC (anode) and 0.15 wt% PTFE added to the CL of the In_2O_3 cathode, respectively. The current density curves were selected over a period of 30 cycles. A higher current density of 66 mA/cm^2 (with Ohmic resistance, R = 5.45 Ωcm^2) was observed in sample H at 2.06 V in the 1st run. As the number of cycles proceeds, a decrease in current density was observed at 2.06 V in the 15th (j= 52.2 mA/cm^2 and R= 6.93 Ωcm^2) and 30th (j= 43.4 mA/cm^2 and R = 8.39 Ωcm^2) cycles, respectively, showing that the efficiency of this electrode decreases over the 30 cycles because of the increased Ohmic resistance. Fig. 5.18a (sample I) presents the result of PTFE-treated carbon paper for 30 min at 80^{o}C, a lower current density of 27.4 mA/cm^2, 22.9 mA/cm^2, and 18.5 mA/cm^2 at higher onset potential of 2.10 V and high Ohmic resistances (11.7 Ωcm^2, 14.0 Ωcm^2 and 17.5 Ωcm^2) were obtained in the 1st, 15th and 30th cycles respectively in comparison with sample H (Fig. 5.17a). This implies that sample H was approximately 2 times more effective for FARR than the sample I (Fig. 5.18a). The reduction in current density of sample I (treated carbon paper in PTFE at 80^{o}C for 30 min) could be attributed to the fact that the addition of PTFE is excessive, which may cause some of the catalyst grains to be electrically isolated, giving a reduction in the catalysts active surface areas. This means that the efficiency of FARR may be reduced by insufficient electrical contact with the catalyst.

In order to establish the results of sample H and I, samples K (Fig. 5.19a) and L (Fig. 5.20a) containing the anode recipe of 60:40 wt% IrO_2:TaC was prepared and the In_2O_3 cathodes

were subjected to the same condition used in electrocatalyst samples H and I respectively. As expected, similar trends as observed with samples H and I were noticed in samples K and L, as shown in Figs. 5.19a and 5.20a, respectively. While sample K exhibited a stable electrode even at the randomly selected cycle number (Fig. 5.19a) with current density and Ohmic resistance of 30.6 mA/cm^2 and 9.6 Ωcm^2, 28.0 mA/cm^2 and 10.6 Ωcm^2, and 26.9 mA/cm^2 and 11.0 Ωcm^2 (for 1^{st}, 15^{th} and 30^{th}) respectively. Fig. 5.21 presents polarization curves showing the comparison of current densities of electrocatalyst samples H, I, K, and L. Overall, there was a decrease in the current densities with the increasing cycle number of the sample H, I, K, and L, thereby resulting in an increased resistance over the 30 cycles (Table 5.5). On the other hand, the decrease in performance of FARR can also be ascribed to factors, such as the loss of the coated/sprayed catalyst particles on the membranes, the competing hydrogen evolution reaction and the deactivation of the catalyst upon prolonged exposure to FAs as it is already known; acid dissolves In_2O_3. The onset potential in terms of PTFE-treated carbon paper catalysts is higher than that obtained for PTFE-In_2O_3 catalysts. Moreover, the PTFE-In_2O_3 cathode electrocatalysts of both anodic recipes revealed a lower resistance than PTFE-treated carbon paper electrocatalysts treated at 80^oC. This further explains the best performance of the PTFE-In_2O_3 catalyst in particular with higher current densities.

From the result of the samples H, I, K and L shown above, the current densities increase with increasing cell voltage. The increased current densities were achieved for membrane loadings of In_2O_3 with both Nafion and PTFE for the entire voltage range. As explained in section 5.3.2, two important regions can be distinguished on the LSV curves (Figs. 5.17a, 5.18a, 5.19a and 5.20a): firstly, there is an exponential increase in current density as the cell voltage increases to 2.06 V, 2.10 V, 2.12 V and 2.13 V for sample H, I, K and L respectively, after which the increase

becomes linear. In these regions, the rate-limiting step is the charge transfer, i.e., the kinetics of the electrode reactions. However, in the second region, the systems' Ohmic resistances become predominant (around 1.7 V, 1.56 V, 1.7 V and 1.34 V for H, I, K and L, respectively); with the membrane as the major contributor. The predominance of Ohmic resistances at cell voltage greater than 1.6 V has been reported previously on PEMWE and solid polymer electrolyte (SPE) [254,263,278,279]. Similar behavior was observed on other cathodes for FARR and CO_2 reduction such as Cu-Sn-Pb [28], GDE-In/C [280], In, $In(OH)_3$, and In_2O_3 NPs [199], In-wire [281], Cu [282], Cu-MOF [283] Sn [258,273,284], Sn-Pb alloy [285] and Ag [286].

Comparing the onset potential of In_2O_3 cathodes (with and without PTFE (section 5.3.2)), the onset potentials of the In_2O_3-containing PTFE samples were lower, and the current densities were significantly improved unlike when only Nafion is used as seen in the Fig. 5.21. This implies that the presence of PTFE in that catalytic layer of the In_2O_3 did not only increase the current densities but also decreases the overpotential (which is current-dependent) in comparing with sample D in section 5.3 which has a higher overpotential for the product formation. PTFE is added to the catalyst layer in association with Nafion binder to facilitate FA diffusion, thus giving a higher current density than with Nafion alone. The changes in electrochemical reactions of individual electrodes were also revealed by lower onset potentials. This means that the PTFE used to support the Nafion solution has effectively different catalytic properties than the one without PTFE, which agrees with Wang *et al.* (2015) [258]. Therefore, supporting Nafion solution with PTFE on the In_2O_3 catalytic layer increases the active surface areas and enhances the approachability of the reactant to the active site in the pore, implying that addition of PTFE into the In_2O_3 CL is thought to show effects on both FARR and HER. It could promote FARR by enhancing the FA

diffusion and possibly reduce electron conduction since PTFE cannot conduct protons and electrons [258].

CA was carried out for a period of 24 h at a cell voltage of 2.4 V (Figs. 5.17b, 5.18b, 5.19b and 5.20b). The corresponding *j* values are presented in Table 5.5 for each sample. Sample H and I exhibited a constant current density at 2.4 V after 3 h with sample H showing a current density of 32.5 mA/cm^2 (1st CA) and 22.4 mA/cm^2 (2nd CA) while sample I current densities at 2.4 V were 24.8 mA/cm^2 (1st CA) and 22.9 mA/cm^2 (2nd CA). This is a clear indication of a stable behavior of the samples H and I electrocatalysts. The reactant depletions (Eqn. 3.38) of H and I over 24 h were calculated to be 32.8% and 17.3% respectively. However, as seen in the samples K and L (Figs. 5.19b and 5.20b), certain constraints were observed for the electrocatalysts to observe a perfect plateau, especially the 1st CA of both K (Fig. 5.19b) and L (Fig. 5.20b). The 2nd CAs (i.e. CA2) of both samples were more constant and reached their plateau earlier than the 1st CA (i.e. CA1). This implies that the recovery of the diffusion gradient – Cottrell behavior has taken place during the 6 minutes rest after the completion of the CA1, thus leading to CA2 somewhat more constant than CA1. This implies that more than a 24 h period will be needed for samples K and L to reach a complete plateau and their reactant depletions over 24 h were 21.0% and 13.6% respectively. Nevertheless, the partial plateau of CA1 is more obvious in 60:40 wt% IrO_2:TaC (anode), so it is not just FARR, WE is affected as well, hence confirming the observation reported for the WE experiment and the reason why the 70:30 wt% IrO_2:TaC performed better than 60:40 and 100:00 wt% IrO_2:TaC samples. It should be emphasized here also that LSV and CA were done back-to-back in a single cell, thus giving no chance for the catalyst to rest before starting the catalytic stability test which continued for another 24 h for each CA. Conversely, the continuous jump in CA signals of both samples I and L were assumed to be a result of bubble formation and electrical

isolation of catalysts owing to excessive PTFE during immersion and treatment of carbon paper. It should be noted that a predetermined amount of PTFE was also added to the CL of In_2O_3 cathode during ink preparation, thereby contributing to those that have already penetrated the carbon paper surface in 30 min treatment at 80^oC even before catalyst loading. Nonetheless, one can partly conclude that the chronoamperometric curves in all the experiments are stable, which implied good stabilities and stable behavior of the electrocatalysts which are also confirmed by the second chronoamperometric runs.

Three products including methanol, isopropanol and ethanol were detected as shown by the respective chromatograms (Figs. 5.17d, 5.18d, 5.19d and 5.20d). The retention time in comparison with the standard observed for methanol (MeOH), isopropanol (iPrOH) and ethanol (EtOH) for sample H and I were 3.92, 4.43 and 4.55 min respectively, while the retention time for sample K and L were MeOH (3.94 min), iPrOH (4.44 min) and EtOH (4.58 min) respectively. It was observed that the methanol, isopropanol and ethanol peaks observed with Nafion+PTFE samples were sharper and better visible than when only the Nafion solution was used. The presence of the PTFE shows different catalyst properties than in absence of PTFE, thereby increasing the FA conversion rate to more methanol, ethanol and isopropanol as indicated in the GC chromatograms where the yields are higher than with Nafion alone. The quantification of the products for H, I, K and L electrocatalysts revealed FEs of 7%, 8%, 13% and 14% for MeOH; 25%, 35%, 29% and 23% iPrOH; and 33%, 42%, 25% and 14% EtOH respectively as presented in the Fig. 5.22. It was observed that the %FE of the products followed similar trends for both samples (Fig. 5.22). It is remarkable to note that the number of moles of alcohol yields (Fig. 5.22c-d) increased from iPrOH to MeOH and EtOH with EtOH showing the highest millimole yields.

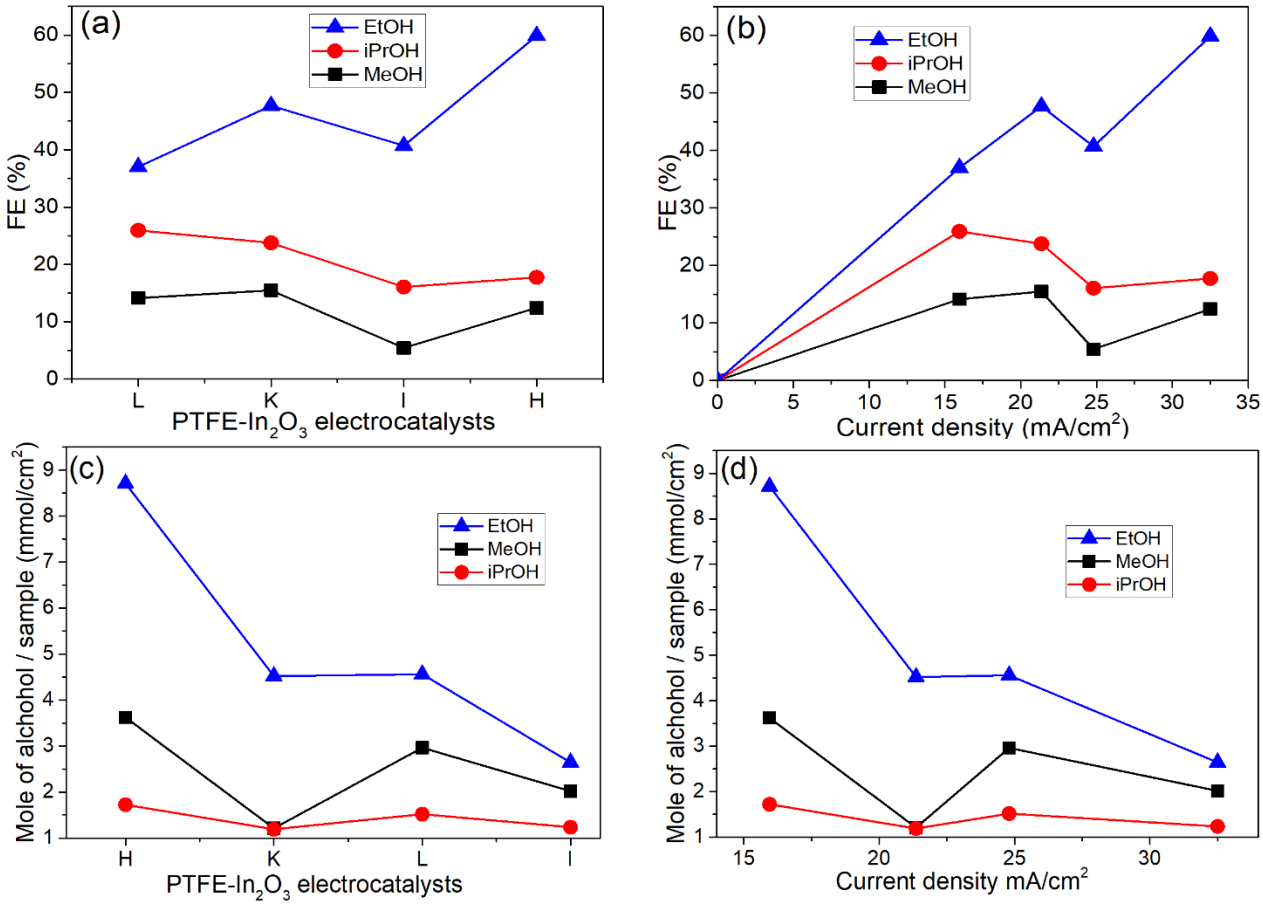

Fig. 5.22: Faraday efficiency of FARR on 0.15 wt% PTFE-In_2O_3: (a) with respect to different electrocatalyst conditions, (b) with respect to steady-state current density. Mole of alcohol yield per sample (c) with respect to different electrocatalyst conditions, (d) with respect to steady-state current density.

To investigate the mechanism of electrochemical FARR, Tafel plots were employed; which is a plot of overpotential against the log of the partial current density for the FARR products as shown in Figs. 5.17c, 5.18c, 5.19c and 5.20c. The reduction of FA shows slopes (b, mV/dec) values of 580 mV/dec at 1.72 to 2.30 V and 690 mV/dec at 1.57 to 2.26 V observed for H (Fig. 5.17c) and I (Fig. 5.18c), respectively. Whereas for samples K (Fig. 5.19c) and L (Fig. 5.20c), the corresponding slopes of 680 mV/dec at 1.65 to 2.33 V and 300 & 850 mV/dec at 1.26 to 1.56 V &1.55 to 2.40 V were obtained, respectively. The lower the Tafel slope, the more efficient the

electrolyzer. In the literature, a wide range of Tafel slopes from 53 mV/dec to 585 mV/dec has been reported on various systems such as N-doped graphene quantum dots [287], Cu-MOF [283], Sn-loading-GDE [275], polycrystalline Ag [288], polycrystalline Au [218], electrodeposited rhenium [289], Sn-coated Nafion electrode [133], nano-FeTSPc [84], Cu foil [290] and some other Sn-electrodes [284,291–293]. In this study, the Tafel slope observed for H is similar to 585 mV/dec on the ultrafine nanoporous palladium for formic acid electrooxidation [294], 575 mV/dec for the catalytic properties of freestanding palladium nanosheet [295], and 542 mV/dec obtained for CO_2 reduction over Sn-GDE [275], but slightly higher than 458 mV/dec for CO_2 reduction over Sn-Nafion® coated electrode [133]. This indicates that our Tafel slope is not bad, though a close comparison with the same reaction is difficult to establish since formic acid electroreduction has been often thought to be dead-end of CO_2 reduction to hydrocarbons or alcohols containing more than one carbon atom and are very scanty to be found in the literature.

Tafel analysis should in principle provide mechanistic information about the rate-determining step, for example, whether it involves a single or double electron transfer [190]. However, the entire Figs. 5.11c, 5.12c, 5.13c, 5.14c, 5.15c, 5.17c, 5.18c, 5.19c and 5.20c were measured in a two-electrode setup and are therefore given as a function of the cell voltage. This involves the water oxidation reaction at the anode and the formation of a mixture of methanol, ethanol, isopropanol and hydrogen, and it can be complicated further by the extent of coverage of the electrodes by adsorbed reactants [190,296]. Tafel plots of the same experiment obtained for the cathode reaction with a three-electrode setup against a reference electrode are shown in the next chapter (Fig. 6.4). Comparing with the best sample when only Nafion was used in section 5.3 (i.e. sample D), sample H demonstrates a better Tafel slope, which is also evident in its higher current density and lower Ohmic resistance, approximately 36 times lower than sample D (Fig. 5.14 and

Table 5.3) and also better than all samples in this section (as shown in Table 5.5 and Fig. 5.21). In this study, however, water is suggested to be involved in the initial step. The participation of water in the first step has been reported [297]. Table 5.5 presents the parameters obtained from corresponding Tafel plots.

However, the effective stability of the GDL is of crucial importance in the FARR as the catalyst may be peeling off gradually from the carbon paper. Therefore, to ensure the stability of In_2O_3-PTFE, different LSV cycles and 7 chronoamperometric studies were performed on a fresh and single PTFE-In_2O_3 electrode. The first successive LSV was performed before and after 2.0 V chronoamperometry experiments (Fig. 5.23a-b), followed by further CA tests at cell voltage of 2.5 V, 3.0 V, 3.5 V, 4.0 V, 4.5 V and 5.0 V (Fig. 5.23f) with another LSV curve after the 5.0 V chronoamperometry test (Fig. 5.23c). Very little degradation can be observed as the number of runs increases. This is evident in both the LSV (Fig. 5.23a-d) and the Tafel plots (Fig. 5.23e, have the same interpretation as with other In_2O_3-PTFE samples). The degradation is expected to be a result of FA depletion after a long CA at high cell voltage (as seen in Fig. 5.23d). The loss of catalyst particles which is a common phenomenon [265,266,268,271,272] is not obvious in the GDL. The current density also showed an increasing behavior as the voltage increases, while the CAs (the steady-state current densities) are stable at each cell voltage (Fig. 5.23f). The product analysis showed the formation of MeOH, iPrOH and EtOH for all cell voltage (the respective chromatograms are shown in Appendix (Fig. SI 7)). The corresponding FE and current densities at each cell voltage are presented in Table 5.6 and Fig. 5.24a&b. It was observed that the total FE (Fig. 5.24a and Table 5.6) increases with cell voltage up to 3.5 V; where it started to decrease gradually. In general, the number of moles of C_1-C_3 alcohol yields per sample (Fig. 5.24c-d) increased from C_3 to C_1 and to C_2 with C_2 alcohol demonstrating the highest molar yields.

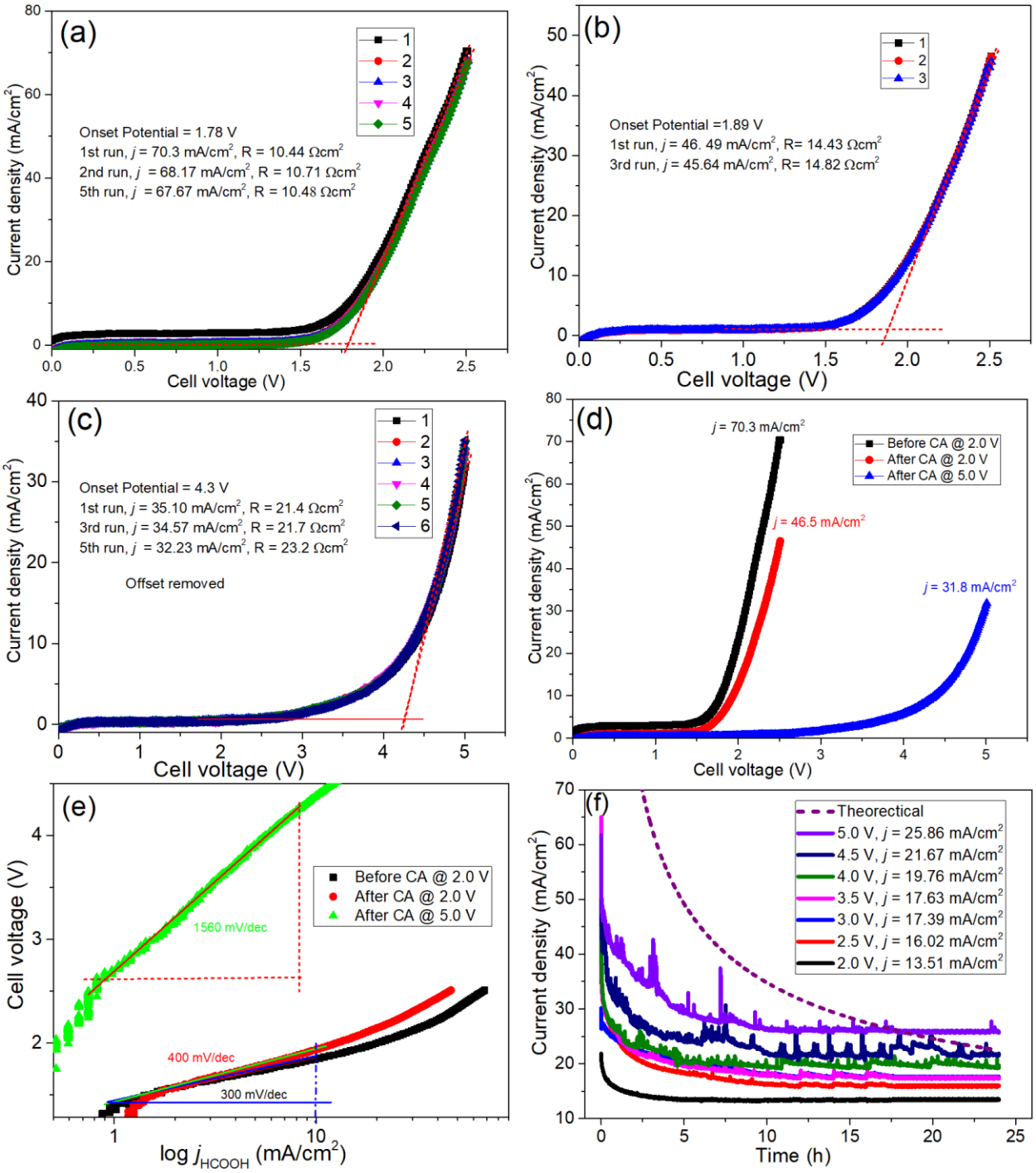

Fig. 5.23: LSV cycles run for FARR on 0.30 wt% PTFE-In_2O_3 (anode: 70:30 wt% IrO_2:TaC): (a) before 2.0 V CA, (b) after 2.0 V CA, and (c) after 5.0 V CA, (d) comparison of LSV runs showing FA depletion after a long CA run, (e) Tafel plot and (f) CA curves at different cell voltage saturate at the current densities given in the inset. The theoretical curve gives the Cottrell behavior for diffusion-controlled reactions [190].

Table 5.6: Faraday and energy efficiency (%) for co-electrolysis of 4.30 M formic and water as a function of cell voltage.

Cell	j	Faraday efficiency (%FE)				Energy efficiency (%)			
voltage (V)	(mA/cm^2)	MeOH	EtOH	iPrOH	Total	MeOH	EtOH	iPrOH	Total
2.0	13.51	7.07	27.75	8.85	43.67	3.96	14.15	4.38	22.49
2.5	16.02	10.33	35.77	11.99	58.09	4.63	14.59	4.75	23.97
3.0	17.40	11.18	52.69	12.55	76.42	4.17	17.91	4.14	26.23
3.5	17.63	11.94	55.70	14.93	82.57	3.82	16.23	4.22	24.28
4.0	19.76	9.06	40.20	11.37	60.63	2.54	10.25	2.81	15.60
4.5	21.67	7.79	21.51	9.85	39.15	1.94	4.88	2.17	8.98
5.0	25.86	0.69	3.03	2.09	5.81	0.15	0.62	0.41	1.19

From Fig. 5.23a, the slope of LSV curves in linear asymptote of the high cell voltage region in the early cycles (that is; in the absence of transport resistance) owing to depletion near the electrode was attributed to the Ohmic resistance of the membrane-electrode unit. Therefore, extrapolating this to zero current gave an onset potential of 1.76 V when the PTFE content admixed with catalyst was 0.30 wt% (Fig. 5.23a). Fig. 5.24 presents a close comparison of this with the 0.15 wt% PTFE content which has the onset potential of 2.07 V (Fig. 5.24, the arrows indicate the onset potentials), whereas, for a fresh sample in the absence of PTFE, it was 2.20 V (Figs. 5.14 and 5.24). Interestingly, one of the unique roles of PTFE noticed here is the reduction of activation polarization of the electrode reactions by up to ca. 0.41 V; thus revealing direct PTFE interactions with the electrocatalyst surface. Addition of PTFE to the catalyst leads to a significant improvement in the current density by a factor of >30 at a cell voltage of 2.4 V and onset potential by ca. 0.4 V. Similarly, the addition of 0.30 wt% PTFE considerably reduced the Ohmic resistance

of the MEA from ca. 155 Ω cm^2 to 10 Ω cm^2 (j= 70 mA/cm^2) by about a factor of 15 correspondings to a voltage drop of 700 mV.

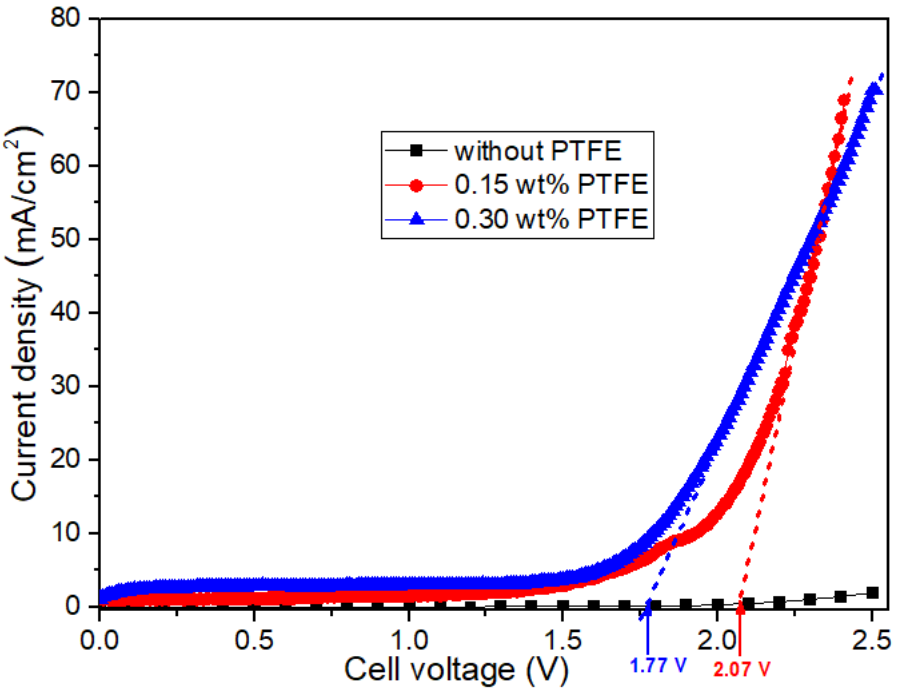

Fig. 5.24: LSV plot of: plain In_2O_3 cathode catalyst (black), In_2O_3 intermixed with 0.15 wt% PTFE (red) and In_2O_3 intermixed with 0.30 wt% PTFE (blue) [190].

It should be mentioned that MeOH, EtOH and iPrOH exhibited a maximum FE at 3.5 V with EtOH exhibiting the highest FE value (Fig. 5.25a&b). To achieve this, it is believed that the intermediates of these molecules derived from FA must have recombined efficiently. This suggests that they are either mobile on the electrocatalyst surfaces or formed in proximity. Though, an understanding of the reaction mechanism has not been attempted, but it could be recalled based on the previous literature that the bixbyite structure of In_2O_3 contains regular structural oxygen vacancies [298] which possibly bind both CO_2 or FA through their carbonyl oxygen. As presented in Fig. 5.25, the grey shaded area shows a suggested binding site for FA before (c) and after 2-

electron-proton reductions (d). Fig. 5.25e&f present the bixbyite structure of crystalline In_2O_3 with In ions (green), oxide ions (blue) and structural oxide vacancies (open circles) (adapted from ref. [298]). The grey shaded area shows a suggested binding site for formic acid before (e) and after 2-electro-proton reduction (f). Thus, upon the preparation of the electrocatalyst with the addition of 0.15 wt% or 0.30 wt% PTFE, the indium oxide surface might be hydroxylated at reductive voltage, such that PTFE allows the accessibility of the reactant into the electrocatalyst and permits surface hydroxylation (though oxide surfaces are normally hydroxylated in humid environments [299–302] (further investigation may be needed in the future to ascertain this), that further improved the HCOOH turnover by a factor of ca. >30. Surface oxygen vacancies were projected to be significant in heterogeneously catalyzed CO_2 hydrogenation on In_2O_3 [37].

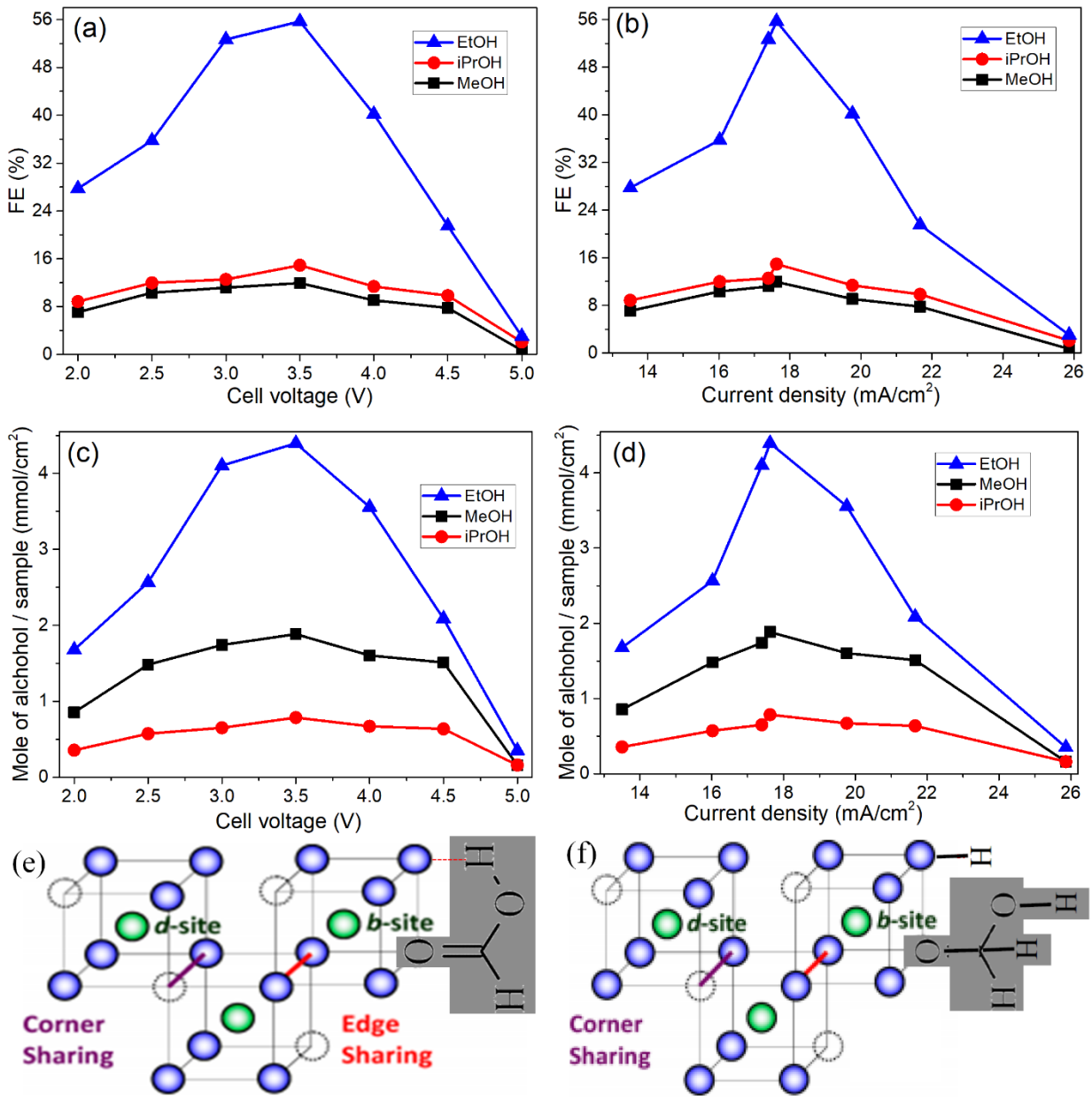

Fig. 5.25: Faraday efficiency of FARR on 0.30 wt% PTFE-In_2O_3: (a) with respect to **cell voltage**, (b) with respect to current density. Moles of alcohol yield per sample with respect to (c) cell voltage and (d) current density. (e, f) bixbyite structure of crystalline In_2O_3 with In ions (green), oxide ions (blue) and structural oxide vacancies (open circles) (adapted from ref. [298]). The grey shaded area shows a suggested binding site for formic acid before (e) and after (f) 2-electro-proton reduction [190].

The thermodynamic electrochemical standard voltage ($\Delta E°$) for a reaction involving FA and water to produce MeOH, EtOH, and iPrOH is 1.12 V, 1.02 V and 0.99 V respectively. The standard free enthalpy of reaction $\Delta G°$ of formic acid to alcohol can be defined as $\Delta G° = -nF\Delta E°$.

Where n is the number of electrons transferred for the formation of alcohol. Therefore, $\Delta G°$ for the formation of MeOH, EtOH, and iPrOH equivalent to +432.1 kJ/mol, +785.0 kJ/mol and +1141.0 kJ/mol respectively. The offset of the effective experimental onset potential of $\approx$ 1.8 V from these values could be further translated into effective activation energies for the electrode reaction of 66 kJ/mol for MeOH, 75 kJ/mol for EtOH, and 78 kJ/mol for iPrOH. The decrease beyond the 3.5 V cell voltage is likely due to reactant depletion occurring at the cathode (Table 5.7). Evidently, critical observation of CA experimental interpretations shows a sharp drop from 70.3 mA/cm^2 to less than half of this value and lastly over hours, the current densities reached plateaus (i.e.steady state) as shown in the Fig. 5.23f. The gradual decrease in current density beyond 10 h implies the excellent stability of the PTFE-In_2O_3 electrode. In fact, at 3.5 V, a decrease of 16% over 24 h is related to bulk reactant depletion due to consumed FA, the rest to electrode stability.

The decrease of FE with cell voltage beyond its maximum at 3.5 V (Fig. 5.25a&b) can be better understood based on the chronoamperometric curves presented in Fig. 5.23f. The curves start at current density values near 70 mA/cm^2 but drop rapidly to reach voltage-dependent plateau values beyond ca. 10 h. The Cottrell equation [303]

$$j = nFc_0\sqrt{D/\pi t} \qquad (5.1)$$

describes the time-dependence of the current density of a convection-free, diffusion-controlled (non-activated) reaction near a planar electrode. Where j is the current density (in A/cm^2) which is defined as $\mathrm{current/area}$, n is the number of electrons required to reduce FA, F the Faraday constant, c_0 the initial concentration of the reactant, D the diffusion coefficient in cm^2/s, and t the time in s [303]. The theoretical curve according to Eqn. (5.1) using n= 8 for ethanol (which has the highest FE) and D = 14.1×10^{-6} cm^2/s for FA is plotted in Fig. 5.23f. It qualitatively reproduces the

experimental behavior, thus, confirming a diffusion layer which builds up, resulting in reactant depletion near the electrode's surface [190]. Lower current densities at short times and the offsets with increasing cell voltage are because the electrode reaction is activated (Eqn. 5.1 does not contain the cell voltage). Higher current densities at long times may indicate the effect of stirring by convection, enhanced by bubble formation of gaseous products as indicated by the spikes at higher current densities (Fig. 5.23f). Depletion in the stationary FA solution near the cathode will likely lead to more H_2 formation, since the organic reactant is not available, which is in agreement with the decrease of the FE beyond 3.5 V as seen in Fig. 5.25a. The amplification of this competing reaction has been observed previously [28].

The electrical work spent per transferred electron amounts to ηF, where η is the cell polarisation. It contains mainly three contributions, the activation energy of the two electrode reactions, i.e. the oxygen evolution at the anode and the formic acid, CO_2 or proton reduction at the cathode, the Ohmic resistance of formic acid transport in solution, plus the Ohmic heat dissipated in the membrane-electrode unit.

Table 5.6 presents the percentage energy efficiency for co-electrolysis of 4.30 M formic and water as a function of cell voltage. A decrease in energy efficiency was observed from 3.5 V cell voltage since the offset represents a loss due to non-equilibrium. This was estimated from the product of thermodynamic voltage and FE divided by cell voltage (Eqn. 3.36). These values, tabulated in Table 5.6, are approximate since the conditions at the electrode surfaces do not exactly correspond to standard conditions. They decrease only slowly at low cell voltage since the effect of the offset from equilibrium is partly compensated by the increasing FE.

The space-time yield (STY) is presented in Table 5.7 (Eqn. 3.37). An increase in STY was observed from 2.0 V up to 3.5 V and thereafter a continuous decrease was maintained. At 2.0 V

and room temperature, the total STY of the three alcohols was calculated to be 0.175 g as a sum of the of MeOH, EtOH and iPrOH per h and per g In_2O_3 which increases to 0.431 $g_{alcohol}h^{-1}g_{cat}^{-1}$ at 3.5 V and decreases to 0.043 $g_{alcohol}h^{-1}g_{cat}^{-1}$ at 5.0 V. In comparison with literature, the total STY value at 3.5 V is only about a factor of 2.2 less than the most recent value reported by Frei *et al.* [41] using heterogeneous thermal catalysis with specifically engineered Pd-promoted In_2O_3 at 553 K and a hydrogen pressure of 50 MPa, but about double the value for plain In_2O_3 [41]. It should be noted that the values are not exactly comparable since our experiment has HCOOH and water as reactants, whereas the literature experiment starts with H_2 and CO_2.

Table 5.7: Assessment of percentage depletion and space-time yield in FARR over PTFE-In_2O_3.

Applied Potential (V)	% depletion	Space-time yield (STY) in ($g_{alcohol}h^{-1}g_{cat}^{-1}$)			
		MeOH	EtOH	iPrOH	Total
2.0	6.64	0.038	0.107	0.030	0.175
2.5	10.47	0.066	0.164	0.048	0.278
3.0	14.95	0.077	0.263	0.054	0.394
3.5	16.37	0.084	0.281	0.066	0.431
4.0	13.48	0.071	0.228	0.056	0.355
4.5	9.54	0.067	0.134	0.053	0.254
5.0	1.69	0.007	0.022	0.013	0.043

To further understand the superior electrocatalytic performance and behavior of the In_2O_3-PTFE electrode, the surface morphologies of the In_2O_3-PTFE coated on carbon paper were investigated before and after co-electrolysis of 4.30 M formic acid and water. Fig. 5.26 presents the SEM image of the In_2O_3-PTFE electrode recorded at different scanning scales/positions. The presence of PTFE on the In_2O_3 before the co-electrolysis created distinct porous morphologies

emerging on the surface of the In_2O_3 particles such that PTFE adsorbed on the In_2O_3 surface, hydrophobized it; so that it is better accessible for the formic acid to easily diffuse in, as compared to without PTFE (Fig. 5.5). The presence of the additional porosity on the whole In_2O_3 particles is expected to promote the accessibility of FA reacting species. However, some chemically cross-linked porous network morphologies can also be noticed at 20 µm and 200 nm scales. In the catalytic layer, there is the existence of numerous pores on the PTFE In_2O_3 particles. These are not present in the sample without PTFE (Fig. 5.5). The SEM after the electrolysis experiment exhibit more abundant, evenly and pore structure which might have been occupied by FA molecules, thereby showing shiny In_2O_3 particle distributions with some rod-like shapes (especially at 20 µm) which vary in length, thickness, and width. However, some morphologies show shiny flake-like shape orientations which are densely packed after the electrolysis. More so, the closures of exposed porous sizes were predominant after FARR. It can be said here that the better performance of the PTFE-In_2O_3 electrode can be attributed to the availability of electrons with surface-bound protons which in turn resulted in a higher FARR. The pore structures as a result of the addition of PTFE was beneficial in transporting FA and thus preventing the flooding.

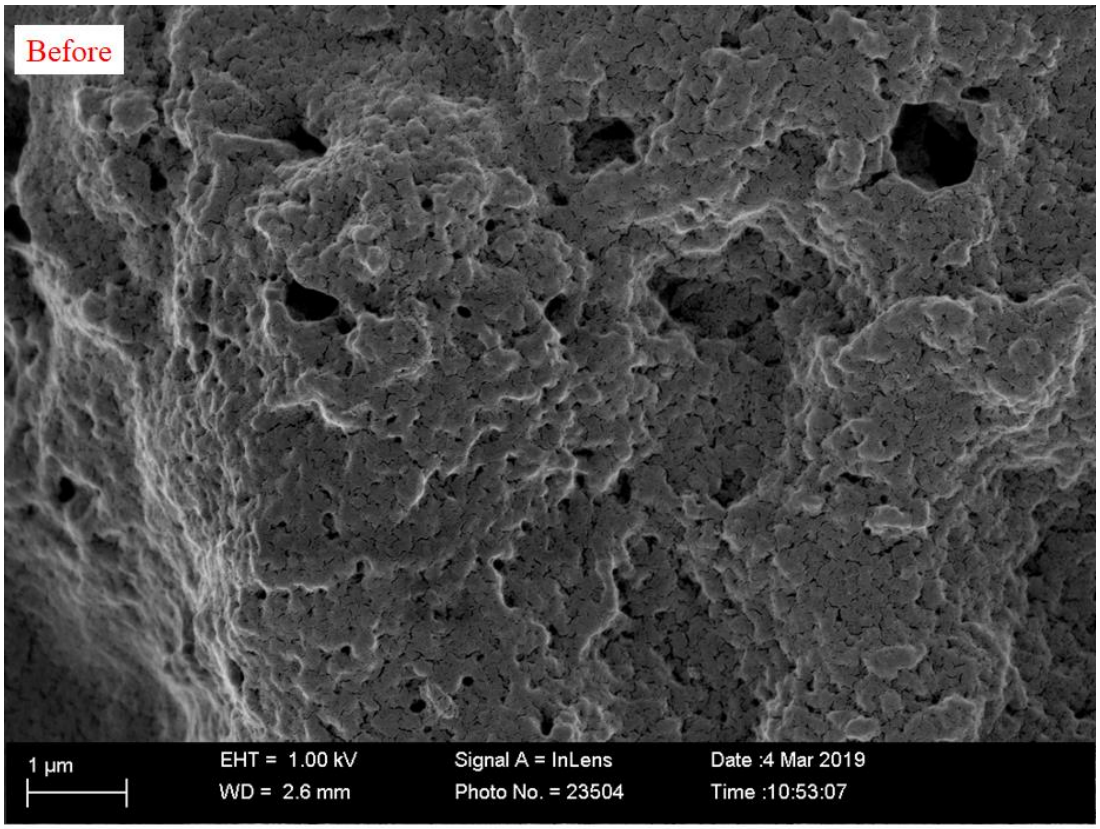
Before
1 µm
EHT = 1.00 kV
WD = 2.6 mm
Signal A = InLens
Photo No. = 23504
Date :4 Mar 2019
Time :10:53:07

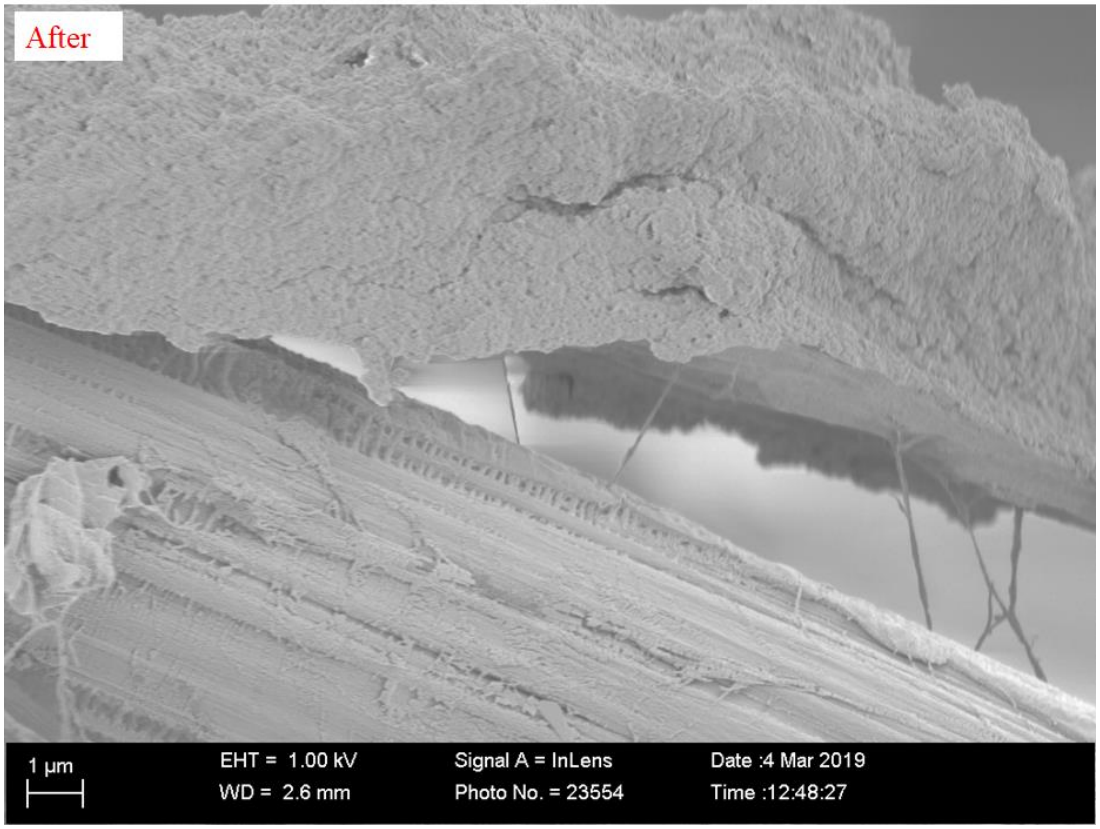
After
1 µm
EHT = 1.00 kV
WD = 2.6 mm
Signal A = InLens
Photo No. = 23554
Date :4 Mar 2019
Time :12:48:27

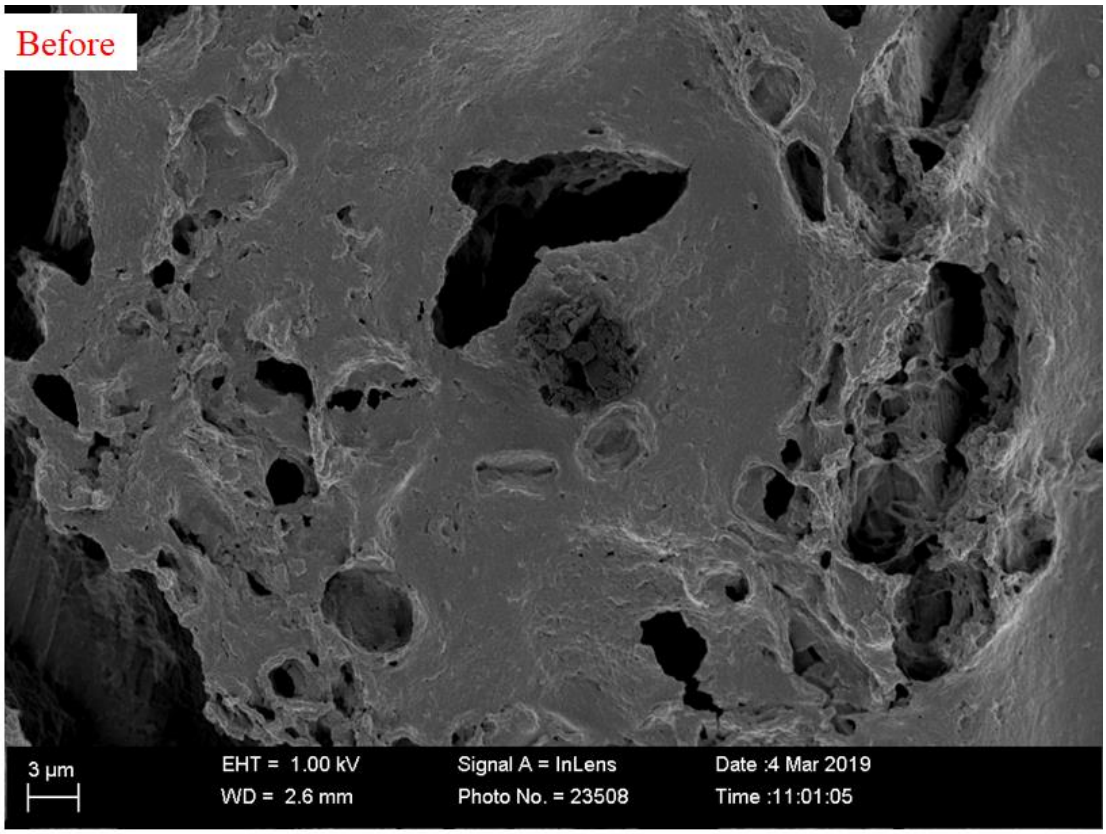
Before
3 µm
EHT = 1.00 kV
WD = 2.6 mm
Signal A = InLens
Photo No. = 23508
Date :4 Mar 2019
Time :11:01:05

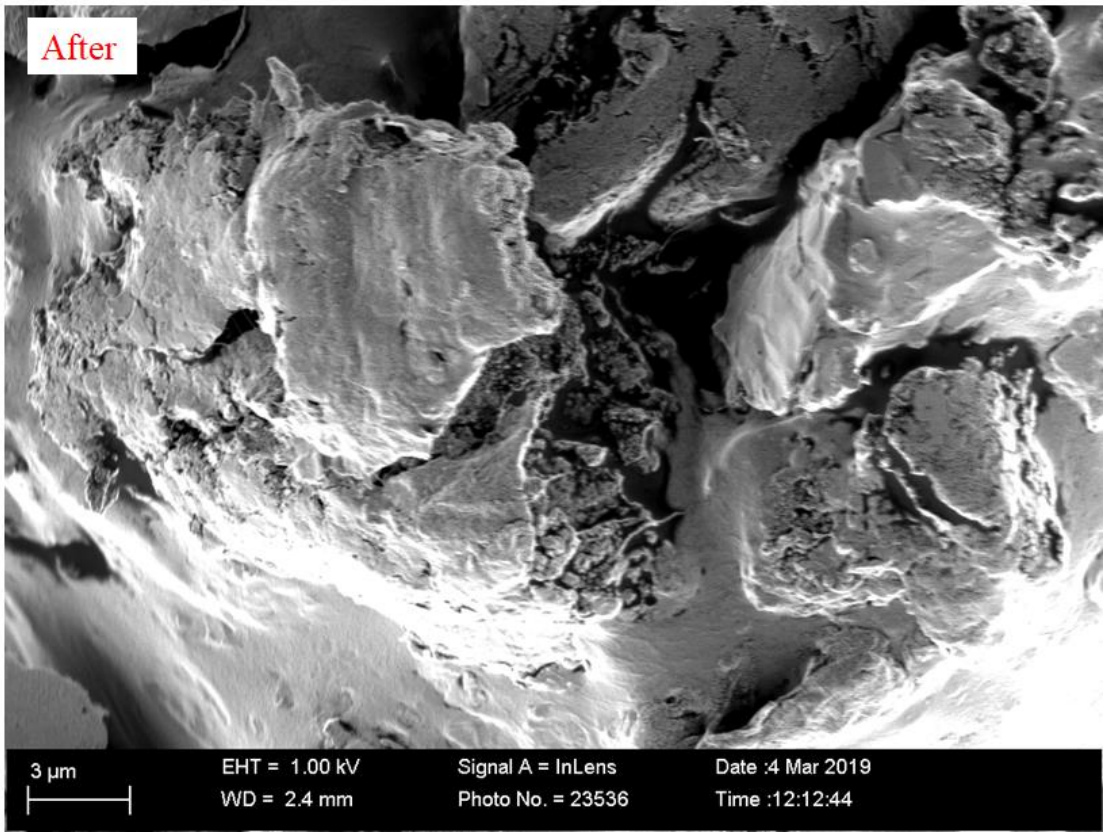
After
3 µm
EHT = 1.00 kV
WD = 2.4 mm
Signal A = InLens
Photo No. = 23536
Date :4 Mar 2019
Time :12:12:44

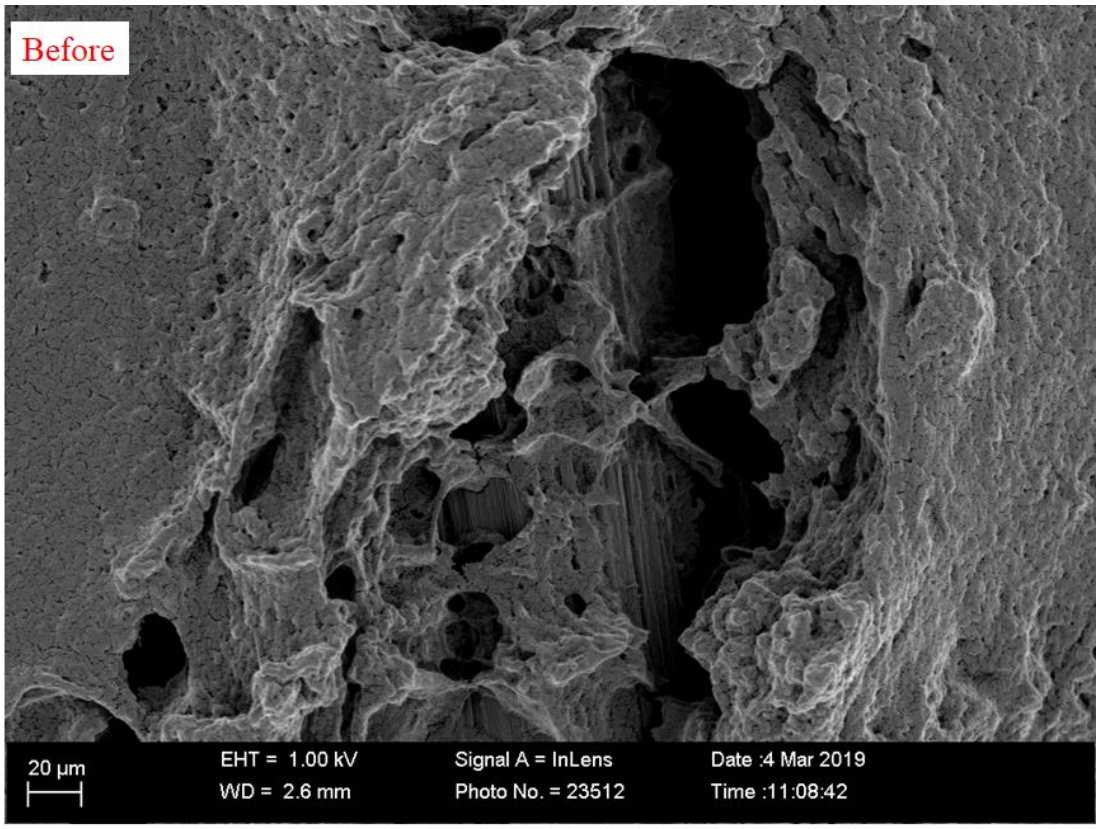
Before
20 µm
EHT = 1.00 kV
WD = 2.6 mm
Signal A = InLens
Photo No. = 23512
Date :4 Mar 2019
Time :11:08:42

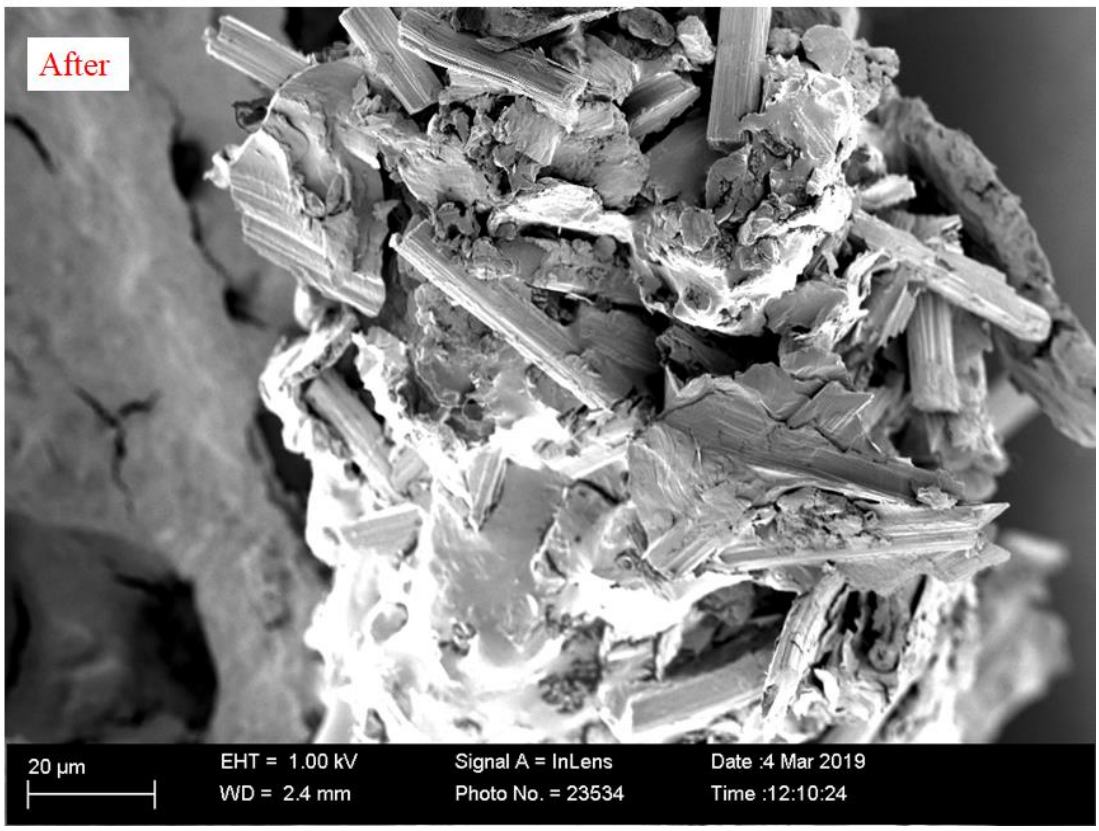
After
20 µm
EHT = 1.00 kV
WD = 2.4 mm
Signal A = InLens
Photo No. = 23534
Date :4 Mar 2019
Time :12:10:24

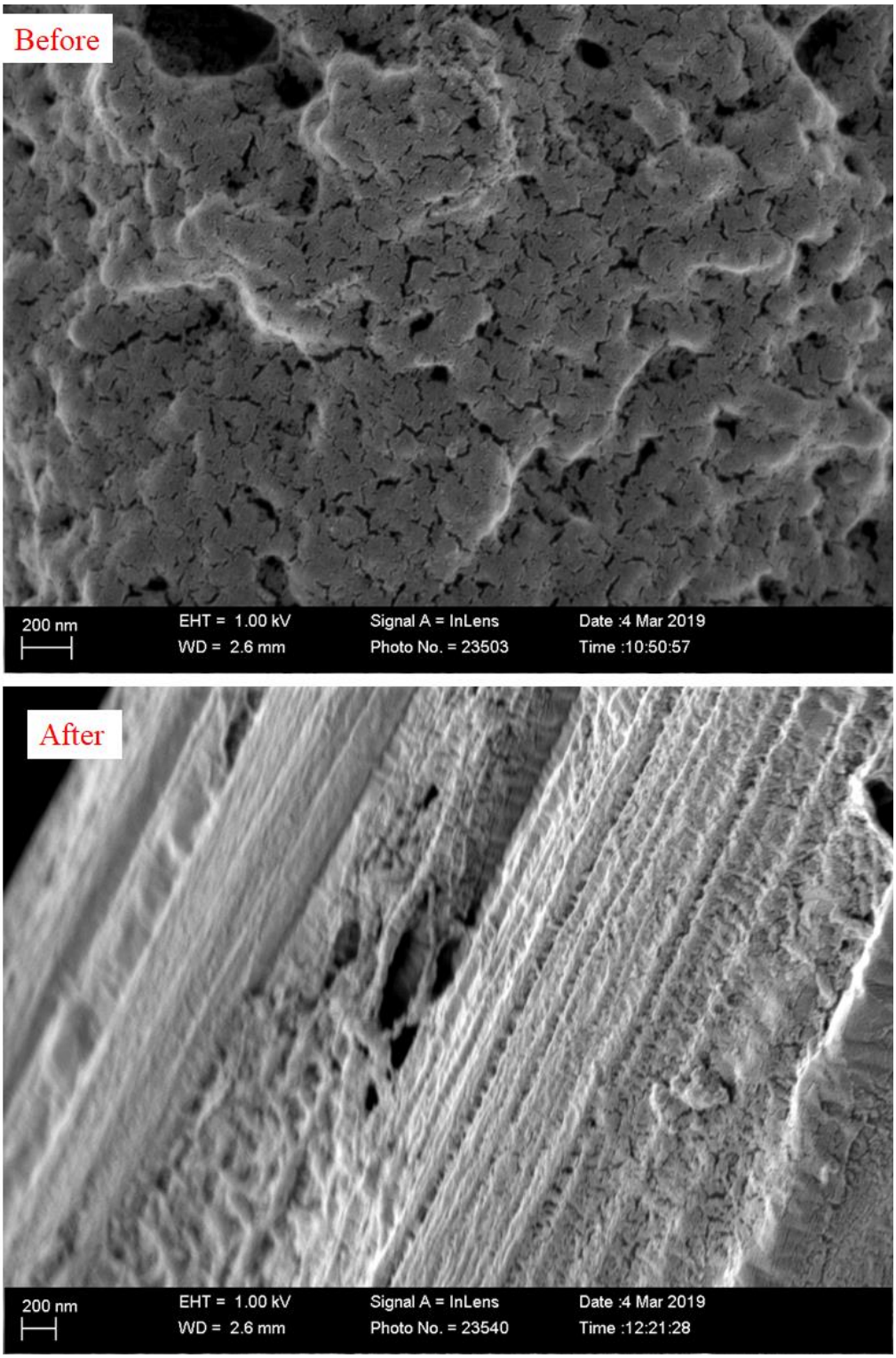

Fig. 5.26: SEM images of PTFE-In_2O_3 before and after FARR.

Chapter 6

ELECTROCATALYTIC PROPERTIES OF In_2O_3 AND PTFE-In_2O_3 ELECTRODES IN THE THREE-ELECTRODE SET-UP

The electrocatalytic information of In_2O_3 and PTFE-In_2O_3 electrodes were obtained using cyclic voltammetry (CV), linear sweep voltammetry (LSV), chronoamperometry (CA) measurements.

6.1 Cyclic voltammetry experiments

The CV experiments were carried out in a standard three-electrode electrochemical cell with a carbon plate counter electrode and a saturated calomel reference electrode but for comparability, the absolute potentials were all converted to values against the SHE (Eqns. 4.1 and 4.2). The working electrode was a 5 mm diameter glassy carbon electrode which was carefully polished on a polishing cloth for 1 min using an aqueous suspension of alumina with 0.05 μm mesh size.

Fig. 6.1 represents CV curves of 0.15 wt% PTFE-In_2O_3 ink with 8 mg catalytic powder used for ink formulation and 7 μL deposition on glassy carbon electrodes. The electrolyte used was 0.100 M Na_2SO_4 solution. In the presence of N_2, FA and CO_2 at a scan rate of 0.05 V/s and different potentials, no clear oxidation/reduction peaks in the CV curves in any potential range were observed. This implies that this catalyst was not conductive enough to establish the redox reaction in the electrolyte and ink formulation under consideration, thus, suggesting that the redox process may be mainly governed by the intercalation and deintercalation of the cations into the mesoporous PTFE-In_2O_3 matrixes [304]. Conversely, these CV curves resembled mirror images with respect to zero-current lines [305–307] owing to the small amount of catalyst powder used. This of course gave insight into increasing the amount of catalytic powder used in preparing the ink to 25

mg. Therefore, fresh ink was prepared, the deposition and the CV experiment were carried out under the same condition.

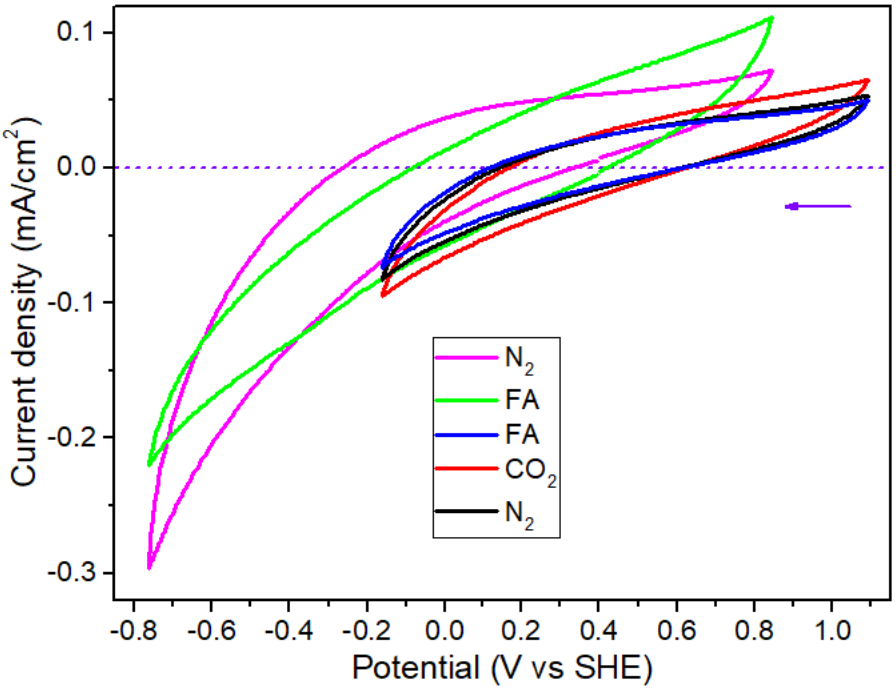

Fig. 6.1: CV plots showing the electrochemical performance of 8 mg PTFE-In_2O_3 powder on glassy carbon electrode (5 mm diameter) in the presence of 0.100 M Na_2SO_4, recorded at 0.05 V/s scan rates.

Fig. 6.2 presents the cyclic voltammetry plots on 25 mg electrocatalyst powder for the deposition on the glassy carbon (5 mm diameter) for FA electrochemical reaction in the presence of 0.100 M Na_2SO_4 at the different potential. In Fig. 6.2a, at a scan rate of 0.05 V/s the cathodic current follows an exponentially rising behavior in all cases. A clear oxidation peak (positive current density) is observed after the return potential was reached; however, there is no significant reduction peak (at the negative current density), clearly indicating that FA reduction did not take place at that potential window even though the switching potentials move progressively further in the negative direction. These features are common for all CVs shown in Fig. 6.2a. These plots,

therefore, present characteristic differences (apart from the charge involved in the polarization process), which are visible at the two extreme returning potentials measured: At the most negative potentials, the return current line presents a certain inclination until it achieves the anodic peak, while at the less cathodic return voltage from this plot, Fig. 6.2a, these lines seem to be vertical [308]. In the presence of N_2, no clear reductive current is seen in the potential range. When we compare CO_2 and FA with the N_2 voltammogram, the disappearance of the broad peak at around +0.3 V to –0.3 V vs SHE in the presence of CO_2 could be attributed to its reduction while the broad peak that appeared in the presence of FA indicating the onset potential for the FA reduction reaction.

As presented in Fig. 6.2b, the effects of changing the return potentials were evident by showing significant anodic peaks (between the potential of –0.35 V and –0.22 V and cathodic peaks (from –0.5 V vs SHE) in the presence of FA. In addition, it is believed in accord with the literature, that maximum reduction peak positions were not dependent on the scan rate [309,310]. This shows that the electron transfer kinetics is fast with respect to the cycling time scales, thus suggesting a Nernstian behavior [310,311].

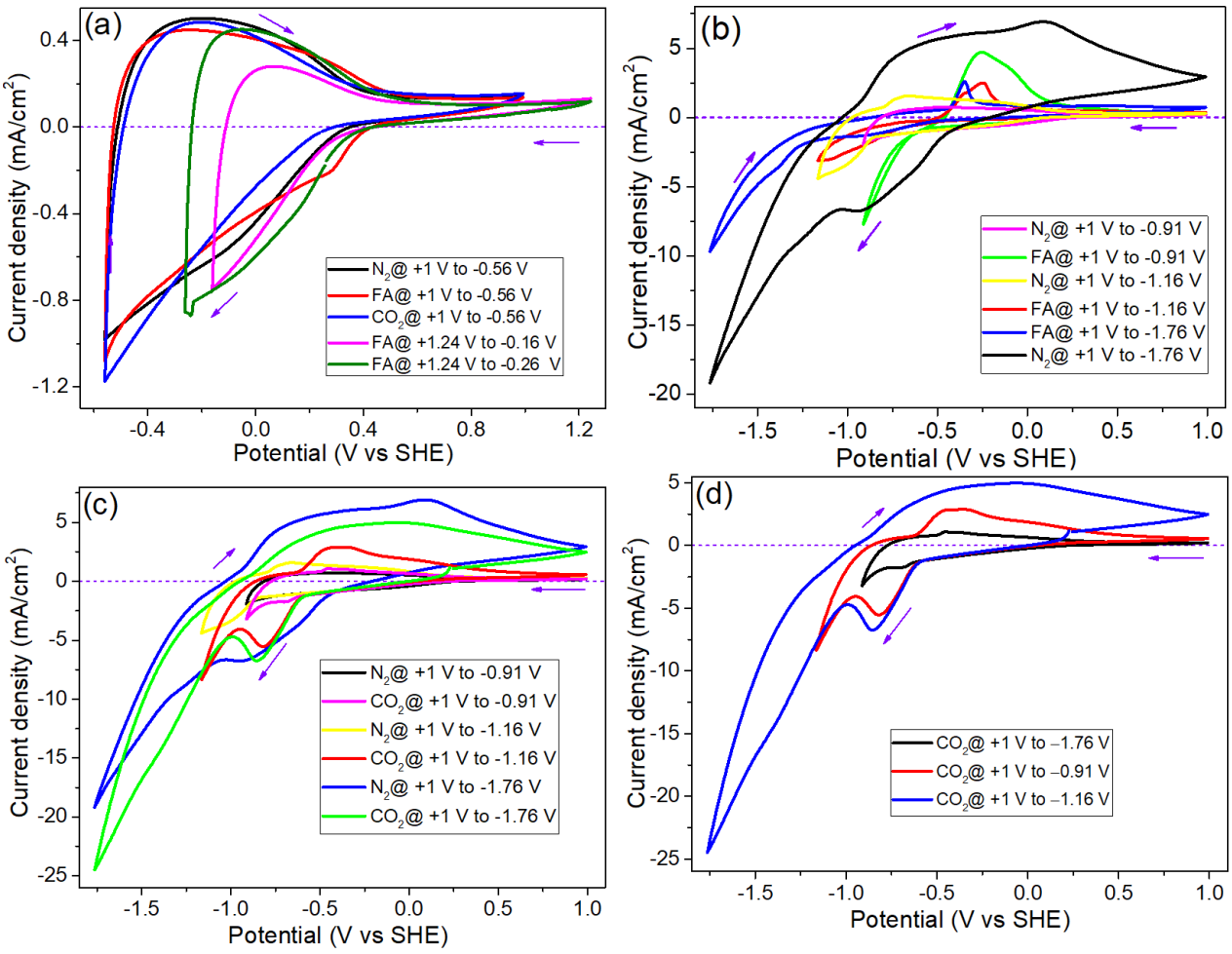

Fig. 6.2: Cyclic voltammetry plots of 0.15 wt% PTFE-In_2O_3 on a glassy carbon electrode (5 mm diameter) in the presence of 0.100 M Na_2SO_4, recorded at 0.05 V/s at varying potentials (in the absence of stirring) showing the comparison of: (a) FA and CO_2 with N_2 at low negative potentials, (b) FA with N_2 at high negative potentials, (c)) CO_2 with N_2 at high negative potentials and (d) CO_2 at different potentials.

Fig. 6.2c shows the CV of the CO_2RR at a more negative potential. In comparison with the CO_2RR in Fig. 6.2a, the reduction and oxidation peaks are clearly visible under this condition. It is clear under this condition that CO_2RR is favored when the electrode potential is more cathodic, which might further enhance the direct or continuous feed of CO_2 into the PTFE-In_2O_3. The appearance of a significant peak at around –0.58 V to –0.86 V in the presence of CO_2 (Fig. 6.2c) indicates the onset potential for the CO_2 reduction reaction while at more cathodic potentials,

reduction of the electrolyte to H_2 may become dominant (HER). Similar behavior has been reported on other cathodes including Pt, Sn [26], and Ag, TiO_2, Ti, In [312]. The appearance of a significant broad peak in the positive currents could be attributed to the oxidation of indium [313].

For a detailed understanding of the electrochemical performance of the electrode, Fig. 6.2 was critically looked into by specifically plotting separate graphs showing the relation between the 0.15 wt% PTFE deposited onto a glassy carbon electrode in 0.100 M aqueous Na_2SO_4 solution as presented in Fig. 6.3: (a) saturated with N_2 (black), CO_2 (red), and (b) 4.30 M aqueous FA solution in 0.100 M Na_2SO_4 saturated with N_2. The CV of the In_2O_3 electrode (Fig. 6.3a) in Na_2SO_4 electrolyte displays the characteristic redox couple In_2O_3/In both under N_2 (black trace) and CO_2 (red trace) atmospheres with a cathodic peak (c_1) at −0.8 V *vs*. SHE and anodic peak (a_1) at −0.34 V *vs.* SHE in the presence of CO_2 when compared with N_2. In the presence of FA as shown in Fig. 6.3b, the cyclic voltammogram is significantly modified [196]. The c_1 wave related to In^{III} reduction is cathodically shifted to a value of −0.98 V *vs*. SHE, suggesting that In_2O_3 reduction is more difficult in the presence of FA than CO_2. This can be explained by strong adsorption of FA on the oxide [196]. A second reduction peak (c_2) is observed at −1.38 V *vs*. SHE. At more cathodic potential, hydrogen evolution reaction (HER) becomes dominant (c_3 wave). On the anodic scan, a sharp oxidation peak (a_1) is observed at −0.35 V *vs*. SHE. Its full width at half maximum of 67 mV is characteristic of a bielectronic electron transfer occurring on an immobilized species with a transfer coefficient $\alpha = 0.5$ and a low rate constant [314]. As the stable oxidation state of In above a_1 peak is +3 and as the a_1 oxidation is a bielectronic wave, this means that an In^{I} species is oxidized on the anodic scan. Integration of the a_1 and c_1 peaks shows that the coulometry of the c_1 peak is twice that of a_1, suggesting that 4 electrons are transferred on the c_1 reduction peak. As the reduction of In^{III} to In^0 implies 3 electrons, another electrochemical process must be involved. It

can be envisioned that a proton undergoes a one-electron reduction to form an activated adsorbed hydrogen in the form In-H^*_{ads} [190]. This reaction occurs as soon as In^0 is formed, as recently suggested for gas phase catalytic hydrogenation of CO_2 on indium oxide [315] where a surface hydride was observed. This surface adsorbed hydrogen In-H^*_{ads}. can then reduce FA stepwise to alcohols by transferring 2 electrons, thus, producing In^I as a transient species that is readily reduced to In^0 at c_1 potential, or reoxidized to In^{III} at a_1 potential as a bielectronic wave [190].

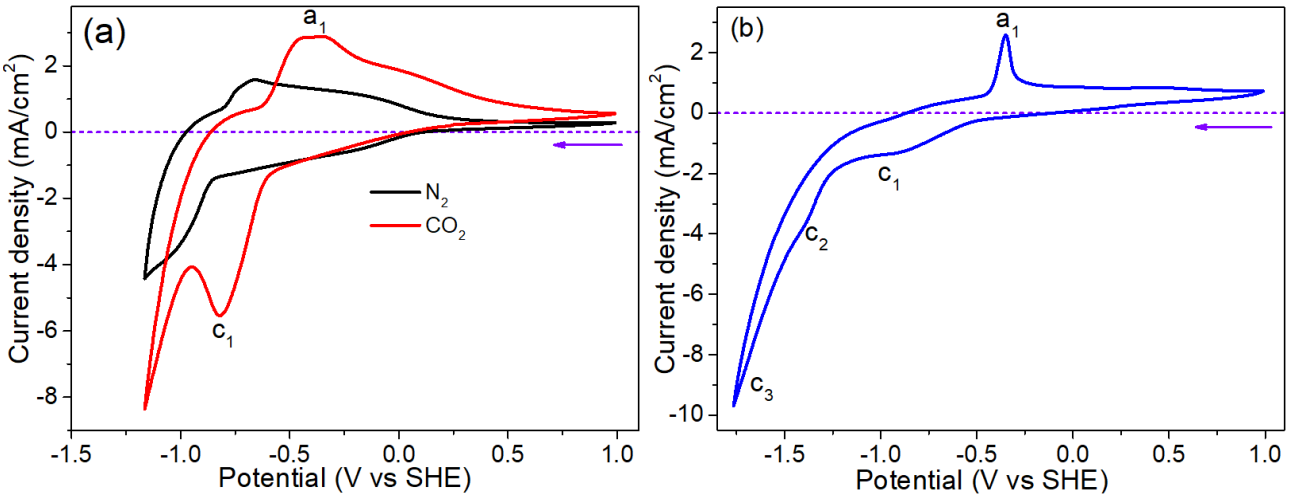

Fig. 6.3: Cyclic voltammogram of In_2O_3 with 0.15 wt% PTFE deposited onto a glassy carbon electrode in 0.100 M aqueous Na_2SO_4 solution, a) saturated with N_2 (black), CO_2 (red), and b) 4.30 M aqueous FA solution in 0.100 M Na_2SO_4 saturated with N_2 (blue). Scan rate: 0.05 V/s.

Nevertheless, a rigorous comparison between an In_2O_3 electrode (with or without PTFE) and a GDE is difficult to obtain by comparing different literature data since very scant work is available on the FARR to any product using electrochemical techniques, and more so, this work uses water and HCOOH as reactants whereas the literature experiments start with H_2 and CO_2. Moreover, many factors can affect the selectivity and the current density of the electroreduction (FARR in our case), for example, well-known factors including the nature, concentration and pH of the electrolyte can greatly affect the reaction [316]. In addition to that, the electrochemical cell

design is another important factor that must be considered as it can affect both the current density and FE of the products [280].

6.2 Linear sweep voltammetry experiments

The catalytic activities of the electrocatalysts towards 4.30 M FA electroreduction on 0.30 wt% PTFE-In_2O_3 were evaluated using the LSV techniques. In contrast to earlier experiments in the previous chapter, the catalyst loading of this present electrode was 12.5 mg/cm^2, spray-coated on carbon paper. The reference electrode was Ag/AgCl, but for comparability, the absolute potentials were all converted to values against the SHE. Fig. 6.4 presents a preliminary evaluation of the electrochemical performances of the samples with and without PTFE.

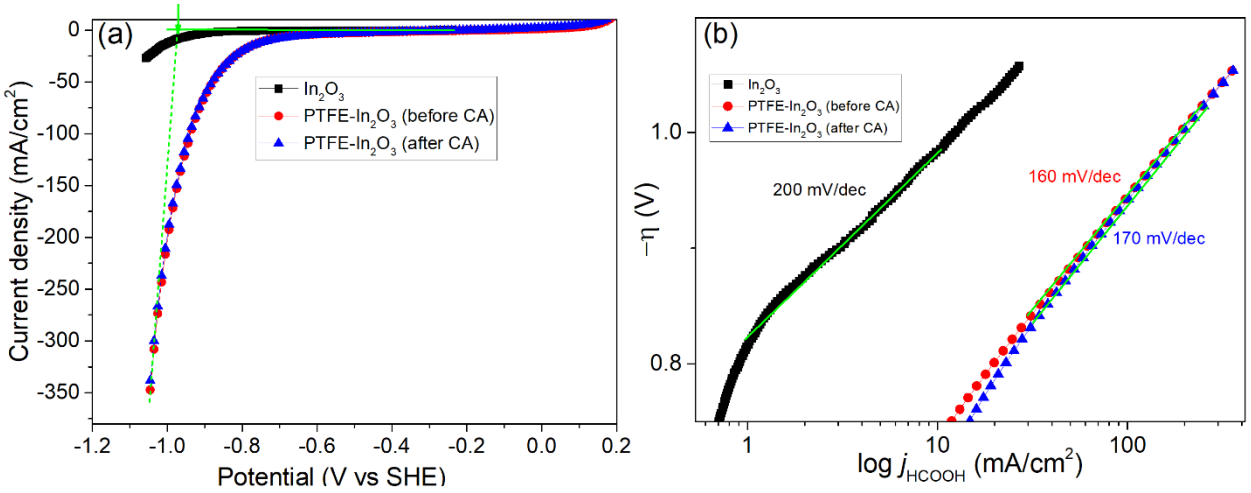

Fig. 6.4: (a) LSV plot of FARR on 0.30 wt% PTFE-In_2O_3 and PTFE-free In_2O_3 and (b) Tafel plot. (in the presence of 4.30 M aqueous FA solution, pH = 1.8, scan rate of 0.001 V/s, and absence of flow or in 0.100 M Na_2SO_4).

From the individual LSV curve, two domains can be noticed; the first domain is the region with an exponential increase in current density as the potential increases after which the increase becomes linear. This domain can be attributed to a rate-limiting step which is the charge transfer, i.e., the kinetics of the electrode reactions. Whereas, in the second domain, the systems Ohmic

resistances become predominant. It can be noticed in the second domain that when the potential was more negative than ca. −0.98 V (green dotted line with arrow), the PTFE-In_2O_3 has the maximum reduction current density of −360 mA/cm^2, while the In_2O_3 (without PTFE) has a maximum current density of −27 mA/cm^2 which is factor ~13 times less than the 0.30 wt% PTFE-In_2O_3 electrode. Why did PTFE increase current density so much? The lower Ohmic resistance and an enhanced current density of both with and without PTFE in comparison with the previous chapter could be attributed to the influence of catalyst loading [313] such that more active sites were present, providing better probability for catalyst activity [317]. The higher value of R obtained for PTFE-free In_2O_3 indicates that FA diffusion and its electroreduction reaction were limited. This suggested that an appropriate amount of PTFE promoted the electroreduction reaction by reducing the transport resistance in the porous structure. This means that the incorporation of PTFE into the catalyst layer exhibited better cell performances when compared with the MEA without PTFE, thus demonstrating higher intrinsic activities for FA electroreduction on 0.30 wt% PTFE-In_2O_3 than with pristine In_2O_3 catalyst. This is due to the improvement of FA ion diffusion. The final LSV as indicated in Fig. 6.4 was run after four chronoamperometry experiments performed at the different potential to investigate the behavior of this 0.30 wt% PTFE-In_2O_3. It is believed here that the role of PTFE in the In_2O_3 ink layer was to locally modify the property of active surface areas by creating electroactive porosity on the PTFE-In_2O_3 particles that can easily be accessible by the FA species. This is in agreement with the uniform and shining or well-polished 0.15 wt% PTFE-In_2O_3 sprayed samples as revealed by the SEM images shown in Fig. 5.26.

Typically, since our work based on the liquid (15% FA, which is 4.30 M) and water, one of the paramount issues is endowing the cathode catalytic layers with appropriate structures and hydrophobicity. The enhancement of the PTFE-In_2O_3 sample could be attributed to the addition of

the right amount of PTFE onto the catalyst layers which are thereby believed to discharge the generated water or FA more effectively, particularly at the higher current density [318,319], reduce flooding and enhance the FARR performances. So, the reactant can diffuse smoothly to the catalyst layer, then keep the activity and utilization of the In_2O_3. In agreement with the literature, the hydrophobic-hydrophilic balance of the cathode catalyst layer was reported to influence the performance of the PEM fuel cell. It was found that tuning the amount of PTFE promotes the hydrophobic-hydrophilic balance of the cathode catalyst layer, thereby significantly enhancing the performance of the MEA [229]. Fluorinated ethylene propylene (FEP) nanoparticle [320] was added to the cathode catalysts layer (CCL) to facilitate the removal of the excess liquid (e.g. water), as high hydrophobicity of the CCL with adding FEP could mitigate flooding of the MEA. A dual CCL was designed by Xiong *et al.* [321] using Nafion as a catalyst binder to form a thin inner hydrophilic layer and using the mixture of Nafion and PTFE as the binder to form a thin outside hydrophobic layer for an air-breathing PEMFC. They found that MEAs-based on dual CCLs showed excellent performance due to their improved water management ability. Li *et al.* (2010) added hydrophobic dimethyl silicone oil into the CCL to increase its hydrophobicity and prevent the cathode flooding at high current density, leading to a better MEA performance [322].

Also, the Choun group fabricated a hydrophobic CCL by adding polydimethylsiloxane that has the ability to decline the degradation performance and increase the durability of a fuel cell because of leveraging mass transfer and preventing carbon corrosion with the improvement of the water management in the CCL [323]. Thus, modifying the hydrophobic and hydrophilic properties of the cathodic GDL is a novel method to improve the liquid management such as 4.30 M formic acid in our own case and the performance of the MEA. A GDL with hydrophilic and hydrophobic double microporous layer was prepared by Kitahara *et al.* [319] to increase the discharge of excess

water from the catalyst layer, thereby enhancing the performance of the PEMFC. Öztürk *et al*. fashioned hydrophobic microporous layers with different hydrophobic polymers to reduce flooding phenomena [324] while the water management was reported to be improved by fabricating double-layer gas diffusion media, which therefore produced higher limiting current density and more stable performance [325].

The kinetic performance of the In_2O_3 with or without PTFE in the electrodes was measured using Tafel analysis. As shown in the plot in Fig. 6.4b, the Tafel slope of 160 mV/dec (before the co-electrolysis) and 170 mV/dec (after the co-electrolysis of water and aqueous formic acid) were obtained for the 70:30 wt% Ir_2O_3:TaC anode and 0.30 wt% PTFE-In_2O_3 cathode. The kinetic performance of 0.30 wt% PTFE-In_2O_3 electrode improves significantly, evidencing from its lower Tafel slope, whereas the Tafel slope for 70:30 wt% Ir_2O_3:TaC anode and In_2O_3 cathode without PTFE was 200 mV/dec which is higher than any of the 0.30 wt% PTFE-In_2O_3. A lower Tafel slope reveals a better performance of the electrode, thus revealing a better activity of 0.30 wt% PTFE-In_2O_3 than of a PTFE-free In_2O_3 cathode. As expected, the slight increase in the Tafel slope after CA (Fig. 6.4b) was a result of changes in the 0.30 wt% PTFE-In_2O_3 surface after several CA experiments. Conclusively, the separate Tafel analyses of the cathode reflect the grossly enhanced current densities resulting from the addition of PTFE to the cathode catalyst that is already obvious from the LSV curves [190]. The plots are of good linearity in the relevant range, leaving no possibility to discriminate between different products; perhaps the rate-determining step of the multi-electron transfer in the formation of the three alcohols (but quite likely not of hydrogen) is the same. The Tafel slopes are significantly enhanced over the value of 120 mV/dec that is normally expected for single electron transfer or of 60 mV/dec for double electron transfer [190].

6.3 Chronoamperometry (stability) tests

The chronoamperometry technique was used to investigate the stability of both cathodes; with or without PTFE at the different constant potentials. Fig 6.5 presents the chronoamperometry plots of In_2O_3 and 0.30 wt% PTFE-In_2O_3 electrodes in the absence of any flow.

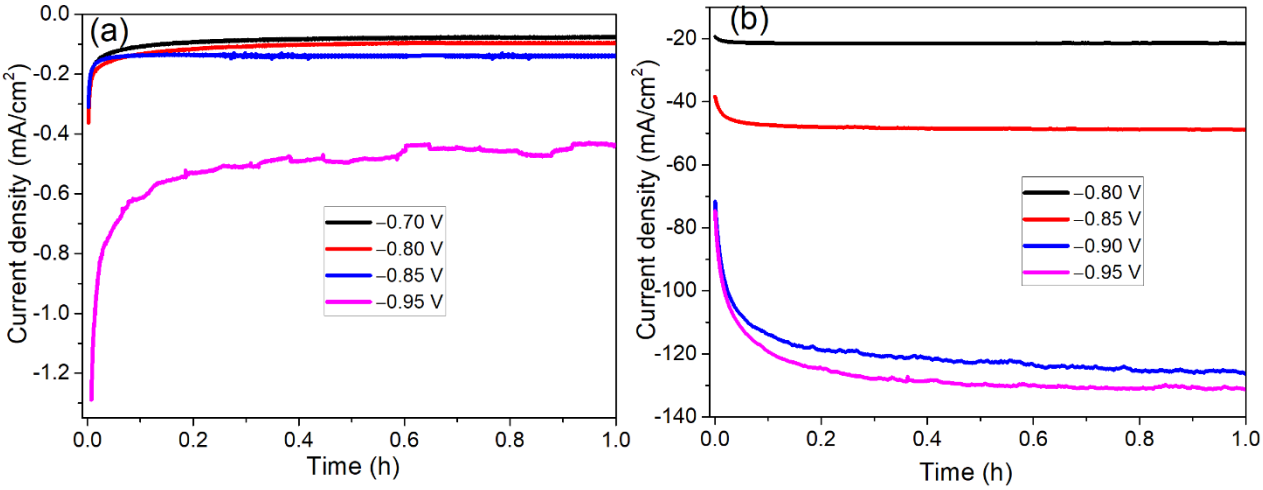

Fig. 6.5: Chronoamperometry plot of (a) In_2O_3 and (b) 0.30 wt% PTFE-In_2O_3 in the presence of 4.30 M aqueous FA solution, pH = 1.8, and absence of any flow. All potentials are relative to SHE.

As seen in Fig. 6.5a&b, at all potentials, the two electrodes behaved differently. With 0.30 wt% PTFE, the current density increased significantly with time while a decrease is observed in the PTFE-free sample (Fig. 6.5a) due to the diffusion limitation. Whereas, for Fig. 6.5b, the reason behind the remarkable increase is not fully known, but partly, it was attributed to the electrode surface been modified, thus leading to current enhancement [326]. In addition, the morphology of the catalyst can directly affect the activity of the catalyst with respect to the size of the catalyst grains and the number of surface sites available at the catalyst surface [327–329] Also, the increase in current over time in 0.30 wt% PTFE-In_2O_3 (Fig. 6.5b) could potentially arise from slight increases in the temperature of the cell at the highest current densities [326]. However, the cathode with PTFE gave

a very high current density and showed excellent stability performance in comparison with the one without PTFE. We believe that even though both samples are stable at their respective constant potentials, the addition of PTFE to the catalytic layer makes the difference in the In_2O_3 layers and more so, simultaneously promotes the FA conversion to products which are highly useful in the electrochemical recycling not only of aqueous formic acid, but also CO_2. This could be one of the first steps towards obtaining selective, efficient and cheap electrocatalysts in the near future. It is able to improve the FA management within the cell and quickly remove the associated liquid such as water from the cathodic catalyst layers such that the catalyst would not be flooded, thus keeping better catalytic activities [330]. For each potential, the cell was allowed to reach a steady state, after which the liquid product streams were analyzed using GC-FID. Interestingly, from the GC-FID analysis, three liquid products were produced from FARR including MeOH at a retention time of 2.34 min, iPrOH at a retention time of 2.67 min and EtOH at a retention time of 2.75 min with combined FE (for 0.30 wt% PTFE-In_2O_3) of 35.73%, 26.56%, 16.05% and 5.64% for –0.80 V, –0.85 V, –0.90 V and –0.95 V (vs SHE) respectively (Fig. 6.6). The remaining FE could be gaseous products (we could not analyze the gaseous product with our GC) but it is believed that these products could be the same as products obtained in IC2MP - Université de Poitiers using micro GC (μGC) which showed two unknown peaks; one at a retention time of 68.88 s (in column 2) and another at 164 s (in column 3) with 14% FE of hydrogen.

Fig.6.6 presents the corresponding FE as a function of potential (Fig. 6.6a) and current density (Fig. 6.6b) while the respective chromatograms are presented in the Appendix (Fig. SI 8). A decrease in total FE (Fig 6.6 and Table 6.1) and energy efficiency (Table 6.1) was observed at a more negative potential which indicates a loss due to non-equilibrium. However, Table 6.2 presents the STY and percentage depletion of the 0.30 wt% PTFE-In_2O_3 electrode which shows a

continuous increase in STY and % depletion observed from –0.80 V till –0.90 V and a sharp declined was noticed in –0.95 V. It worth mentioning that EtOH achieved the highest FE (same meaning as explained in the previous chapter). Considering the decrease in the FE and the STY of the alcohols, it can be inferred that H_2 formation increases and boosts up the current density.

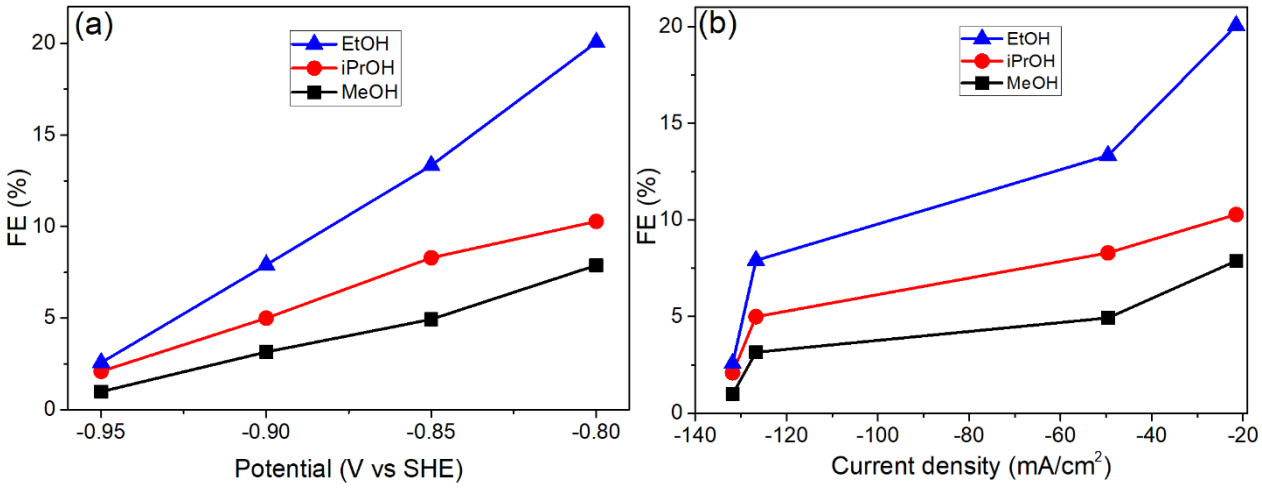

Fig. 6.6: FE of 0.30 wt% PTFE-In_2O_3: (a) with respect to potential, (b) with respect to current density.

Table 6.1: Faraday and energy efficiency (%) of 0.30 wt% PTFE-In_2O_3 for co-electrolysis of 4.30 M formic and water as a function of cell potential.

Potential (V vs SHE)	*j* (mA/cm^2)	Faraday efficiency (%FE)				Energy efficiency (%)			
		MeOH	EtOH	iPrOH	Total	MeOH	EtOH	iPrOH	Total
–0.80	-21.53	7.88	20.06	10.28	38.22	5.63	6.18	16.21	28.02
–0.85	-49.60	4.93	13.33	8.29	26.56	3.74	4.11	11.45	19.30
–0.90	-126.72	3.15	7.91	4.99	16.05	2.53	2.78	7.19	12.50
–0.95	-131.84	0.98	2.57	2.09	5.64	0.83	0.91	2.46	4.21

Table 6.2: Assessment of percent depletion and space-time yield in FARR over 0.30 wt% PTFE-In_2O_3.

Potential (V vs SHE)	% depletion	Space-time yield (STY) in ($g_{alcohol}h^{-1}g_{cat}^{-1}$)			
		MeOH	iPrOH	EtOH	Total
–0.80	9.26	0.04	0.03	0.07	0.15
–0.85	14.81	0.06	0.06	0.11	0.23
–0.90	22.89	0.10	0.09	0.17	0.36
–0.95	8.36	0.03	0.04	0.06	0.13

Chapter 7

VOLTAMMETRIC AND FTIR SPECTROELECTROCHEMICAL EXPERIMENTS OF In_2O_3 AND PTFE-In_2O_3 ELECTRODES

7.1 Introduction

The combustion of organic molecules produces CO_2 as the final carbon products, which is linear and stable from the thermodynamic point of view. The CO_2 reduction to the final product(s) is usually determined by the cathode electrocatalysts used in the electrochemical reactions. Generally, it is a multistep reaction process which involves adsorption of CO_2 onto the electrocatalyst surface, transfer of protons and electrons, and desorption of CO_2 from the surface of the electrocatalyst. It has been suggested [209,219,331–335] that the first step towards the final product(s) is $CO_2^{\bullet-}$ formation on the metal surfaces both in aqueous (Ag, Au, Cu and Zn) and non-aqueous (Ag, Au, In, Cd, Cu, Sn and Zn) media. $COOH^{\bullet}$ intermediates appear to be more favorable on the Cd, Hg, In, Pb, Tl and Sn surfaces. Since CO_2 reduction occurs through proton-coupled electron transfer process, electrocatalysts can electrochemically reduce CO_2 at room temperature because the energy required to overcome the activation barrier can be supplied in the form of an electrical energy [196,336].

The *in-situ* Fourier transform infrared spectroscopy combined with the electrochemical technique was first reported in the 1980s [234,235,337]. It is useful in acquiring information of the molecules including neutral and ionic adsorbates in the electrodes and solution species that are involved in electrochemical reactions. Numerous studies have extended the application of the *in-situ* FTIR from static to dynamic systems, smooth to rough surfaces, and aqueous to non-aqueous conditions. Data can provide the valuable molecular picture of the electrochemical double layers and further give insight into a detailed understanding of reactions involving the

electrocatalytic processes at the charged interfaces [235,338] since the interfaces between the electrodes and electrolytes are the vital parts in any electrochemical system. This indeed determines the behavior of the electrodes and whole cell performances. Therefore, understanding such interfacial processes and structures requires the implementation of the *in-situ* spectroscopic technique in combination with the electrochemical methods. Here, the *in-situ* FTIR spectroelectrochemical evidence of electroreduction of CO_2 but more importantly of formic acid, the first stable intermediate of CO_2 reduction, are presented. All experiments in this chapter were conducted on a homemade three-electrode spectroelectrochemical cell (Fig. 4.4). Glassy carbon (with 7 mm diameter) was used as the working electrode upon which In_2O_3 with or without PTFE was deposited. A carbon plate served as a counter electrode and the reference electrode was an SCE, but for convenience and comparability, all potentials were converted to SHE.

7.2 Voltammetric studies on In_2O_3 (without PTFE)

Fig. 7.1a shows the LSV plot of FA, CO_2 and N_2 redox reactions (Fig. 7.1a &c are just for more visibility). It can be seen that FA oxidation to CO_2 as the product was predominating between +0.74 V and –0.03 V. The double maximum may be due to the occurrence of more than one adsorption sites of FA (-OH groups). The FA and CO_2 reduction waves set in at approximately –0.14 V. For N_2, no redox reaction of In_2O_3 occurs in this potential range. The reduction currents obtained for both FA (7.1b) and CO_2 (Fig. 7.1c) confirm the presence of the adsorbed species occurring in FARR and CO_2RR. At more negative potential, the current density increases with FARR and CO_2RR, thereby demonstrating the significant active nature of In_2O_3 to reduce FA and CO_2 but not H_2O. For the FA, a large reductive current occurred at –0.36 V (Fig. 7.1a-b), in contrast to a flat background in N_2, whereas for CO_2, a significant reductive current occurred at

approximately –0.15 V (in the absence of flow or stirring). However, for the CO_2 experiment (red line in Fig. 7.1a&c), the absence of oxidation peaks between +0.74 V and –0.03 V noticed in contrast to FA (blue line in Fig. 7.1a&b), implying that CO_2 interacts with the oxides. The reduction around –0.43 V in the presence of N_2 (Fig. 7.1a-c) could be attributed to the HER, while in the presence of FA and CO_2, it could be attributed to both HER and FARR, or HER and CO_2RR, respectively.

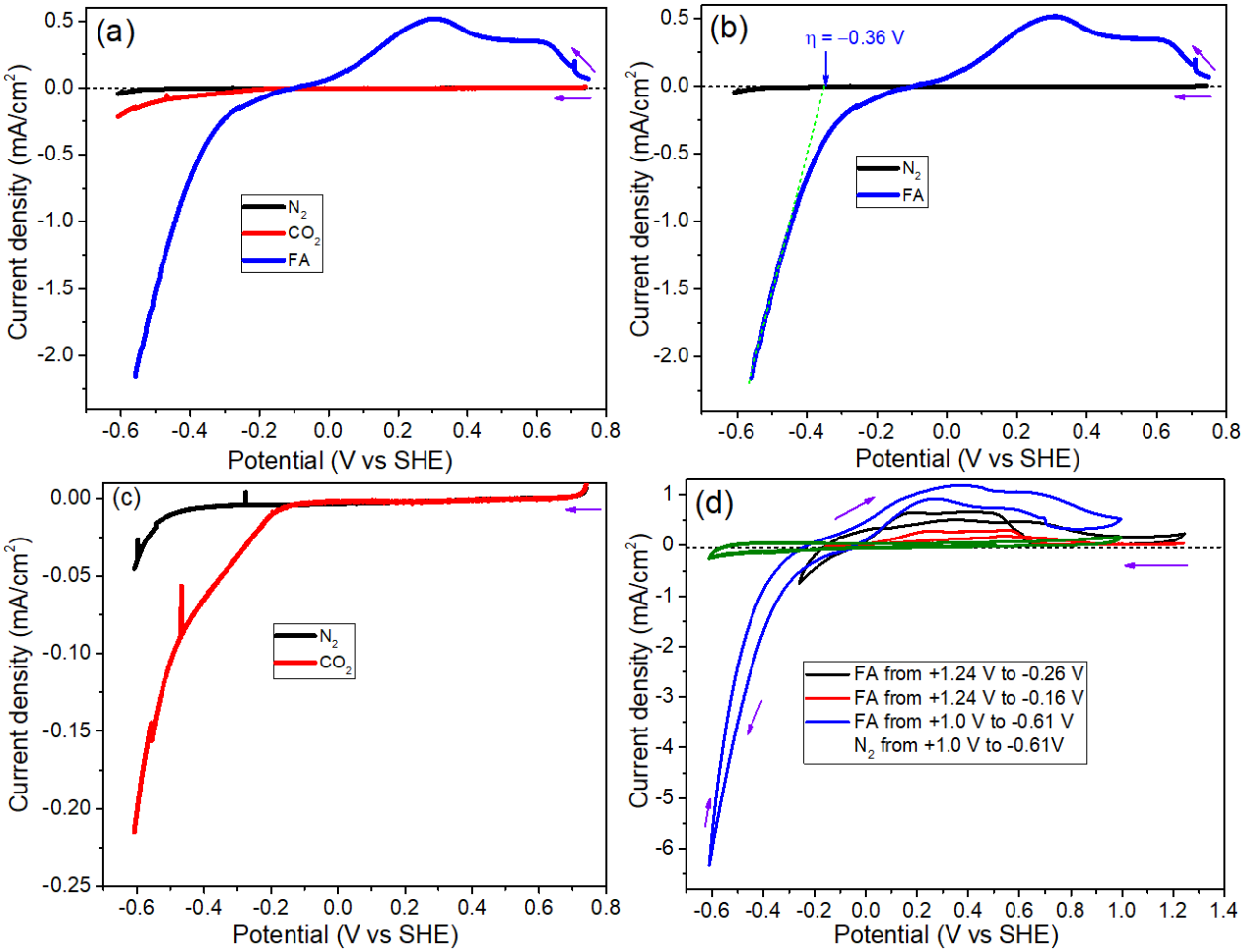

Fig. 7.1: LSV plot of (a) FARR and CO_2RR, (b) FARR, (c) CO_2RR (expanded scale) and (d) CV plot of 4.30 M FA electroreduction on In_2O_3 in the presence of 0.100 M Na_2SO_4 in the absence of any flow.

Fig. 7.1d presents the CV plot of FA at different potentials. As expected, the current-voltage curves of all the FA cases do not differ markedly in their oxidation regions. The oxidation peaks observed between +0.69 V and –0.03 V at all potentials correspond to what was observed in the LSV curves between +0.74 V and –0.03 V for FA oxidation. N_2-saturated Na_2SO_4 electrolytes are electrochemically silent. As noticed in Fig. 7.1d, the reduction peak with FA sets in at approximately –0.14 V. It can be inferred that the species being reduced could be considered mass transport limited [36,196,198,199], signifying that if an adsorption process is first necessary to occur, it may not be the rate-limiting step [36]. At the cathodic end of the CV curves, a much sharper increase in the current density can be observed under FA than with N_2 at the same conditions. The enhancement of the current must be caused by FARR. It can also be concluded here that increased current density is highly determined by means of the potential.

Fig. 7.2 relates to the chronoamperometry test recorded at different potentials. Under this individual experimental condition, good stability of all In_2O_3 electrodes was observed. Current densities of 0.062 mA/cm^2, –0.0086 mA/cm^2 and –0.090 mA/cm^2 were obtained for +0.64 V, –0.16 V, and –0.36 V respectively. Lower current density of these PTFE-free In_2O_3 electrodes could be a result of increasing inaccessibility for the reactant as noticed previously in section 5.3.

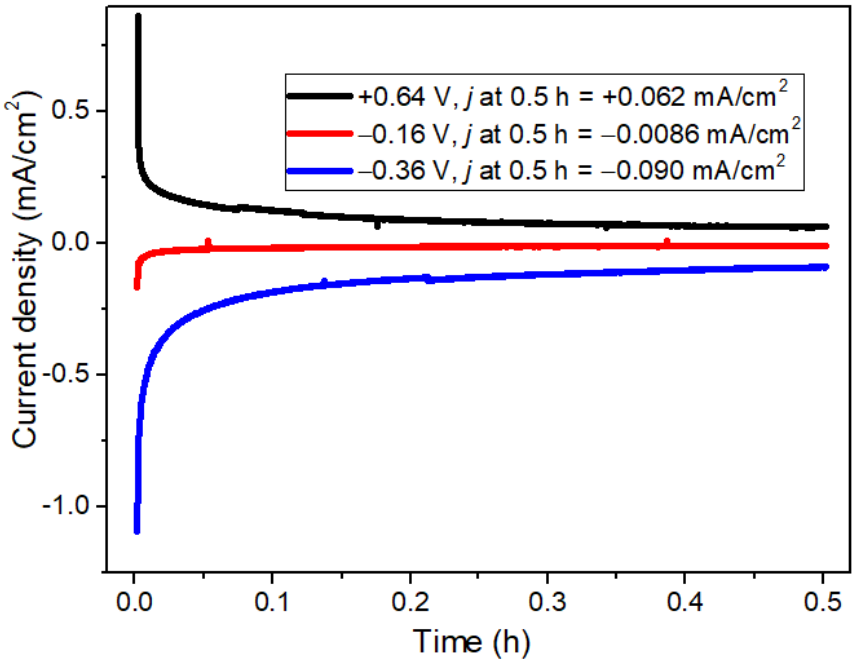

Fig. 7.2: CA plot at different potential vs SHE of 4.30 M FA on In_2O_3 in the presence of 0.100 M Na_2SO_4 in the absence of any flow or stirring.

7.3 Voltammetric studies on In_2O_3/PTFE

Fig. 7.3a presents the LSV curves of 0.15 wt% PTFE-In_2O_3 electrode in the presence of N_2 and FA. For both reactions involving N_2 and FA-saturated with Na_2SO_4 electrolytes, the onset potential was –0.16 V. The sharp current density increase noticed in the presence of 4.30 M FA-saturated with Na_2SO_4 electrolytes was due to FARR and H_2 evolution especially at the more negative potential. Notably, the linear current increase between –0.60 V to –0.76 V could be assigned mainly to the acceleration of the HER [26,282] or the reduction of formic acid to gaseous product(s). Kotoulas *et al.* [28] noticed the formation of H_2 and other gaseous products including CH_4 and C_2H_6 from FARR on a Cu(88)Sn(6)Pb(6) cathode [28]. In comparison with N_2-saturated Na_2SO_4 electrolyte, the current densities, *j*, and Ohmic resistance, R, were j = –25.6 mA/cm^2 and

R =17 Ωcm^2 for FA@ –0.76 V; while j = –0.73 mA/cm^2 and R = 143 Ωcm^2 for N_2@ –0.76 V, respectively. The significant increase in current density when the electrode is exposed to 4.30 M FA must be caused by the reduction of FA when compared with N_2. The low current density when compared with Fig. 5.23a and other 0.15 wt% PTFE-In_2O_3 samples in Table 5.5 could be attributed to the small catalyst loading [339] on the glassy carbon electrode.

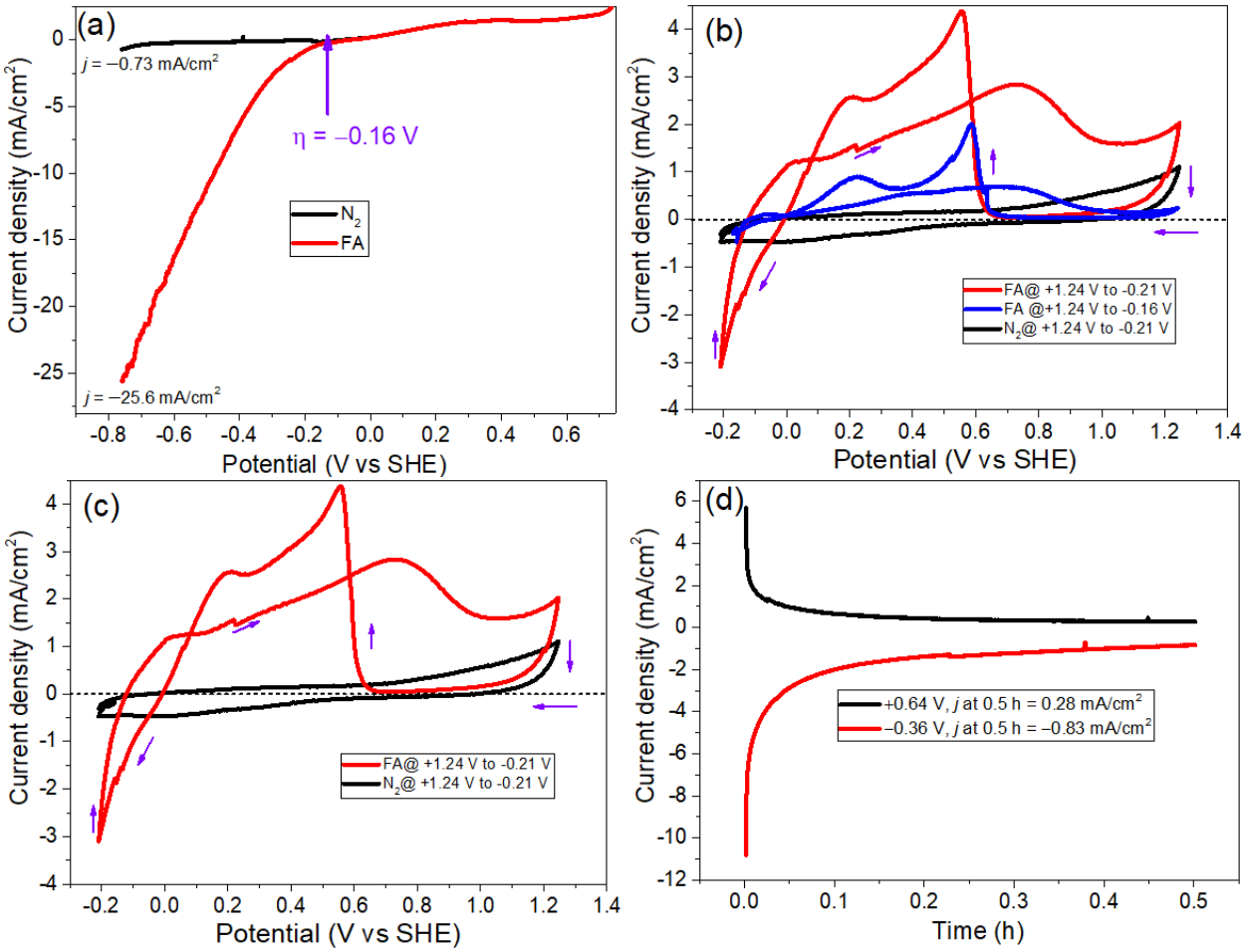

Fig. 7.3: (a) LSV (b-c) CV (4th cycle), and (d) CA experiments of 4.30 M FA electroreduction on 0.15 wt.% PTFE-In_2O_3 in the presence of 0.100 M Na_2SO_4 recorded at a scan rate of 0.05 V/s in the absence of any flow.

Furthermore, Fig. 7.3b&c present the CV plots of 0.15 wt% PTFE-In_2O_3 electrode for FA@ +1.24 V to –0.21 V (red line), FA @+1.24 V to –0.16 V (blue line), N_2@ +1.24 V to –0.21

V (black line). Under the same operating condition, a large oxidation peak is noticed for the PTFE-In_2O_3 electrode. Under the studied potentials, all signify that FA oxidation took place. In all these cases, the oxidation peak at +0.59 V may correspond to the formic oxidation while the one at +0.74 V could be attributed to the oxidation of In_2O_3 [36,196,198,199,340,341] as discussed in section 6.1. The CV experiment performed with 4.30 M FA saturated with Na_2SO_4 shows another peak at around +0.21 V that is absent in N_2-saturated Na_2SO_4, rather it is only featuring when the electrode is exposed to FA-saturated Na_2SO_4 electrolyte. This could be attributed to the surface-adsorbed intermediates on In_2O_3 [196,199,340,341]. Interestingly, looking at both LSV and CV curves (Fig. 7.3a &b), the reduction onset at around –0.16 V, confirms that the chemical feature(s) of the active centers are identical

Comparing PTFE-In_2O_3 with pristine In_2O_3 (without PTFE), in the case of the LSV experiment scanned between +0.74 V and –0.76 V in the presence of PTFE-In_2O_3, the large oxidation peaks noticed in pristine In_2O_3 disappeared. Addition of PTFE to the catalyst leads to an improvement of the current density by a factor of ca. 12 on the PTFE-In_2O_3 electrode, suggesting that FA diffusion into the electrode was enhanced. Lower overpotentials (improved kinetics) observed in PTFE-In_2O_3 (Fig. 7.3a) and low resistances were obtained, indicating that addition of PTFE improves the catalytic behavior from R = 105 Ω cm^2 (without PTFE i.e. blue line in Fig. 7.1a&b) to R = 17 Ωcm^2 (with PTFE i.e. red line in Fig. 7.3a). In the case of CV experiments (Figs. 7.1d and 7.3b&c), the anodic and cathodic current density peak heights were different, implying a different structural feature in the two electrodes which responsible for the differences in their catalytic performances. Significantly, the integrals of the reductive and oxidative parts are grossly different, demonstrating the irreversibility of the reaction. More so, in the PTFE-In_2O_3, a curve crossing in the oxidation regime is noticed which was absent in the In_2O_3 (without PTFE

(Fig. 7.1d)). The CV (having a curve crossing) noticed here is not a typical of others found in the literature. Curve-crossing was not due to the change in potentials and not due to the scan rate as the same scan rate was used. This observation could indicate multiple redox species or a multi-step parallel or consecutive mechanisms [342]. It could, therefore, be attributed to the slow formation of redox active intermediates and slow follow-up reactions occurring in the diffusion layer on the surface of the electrode [343,344]. Curve-crossings have been reported for pyrrole and interpreted as electrochemical follow-up reactions and slow kinetics of dimer-dimer coupling in the front of the electrode as the main cause [343]. The same phenomenon has been mentioned by several other studies [343,345–349]. To the best of our knowledge, curve-crossing is noticed for the first time in PTFE-In_2O_3 for FA redox reactions. It means that the GDL was optimized to show excellent electrocatalytic performance for the FA electroreduction. The appropriate amount of PTFE in the In_2O_3 catalyst layer is a significant factor for this. PTFE not only enhances the adhesion properties of the In_2O_3 catalyst layer on the carbon paper but also helps to create the hydrophobic channels in the catalytic layers. A significant advantage of even or uniform porosity structures, good mechanical strength, and ideal air permeability as well as the low fabrication cost has been found for the catalytic layer involving PTFE-GDE [293,350].

Fig. 7.3d relates the chronoamperometry measurements recorded at +0.64 V and –0.36 V at room temperature and ambient pressure. The CA tests showed good stability over 0.5 h, and current densities remained constant throughout the testing period. This indicates a stable behavior of the 0.15 wt% PTFE-In_2O_3 electrode. The current densities of 0.28 mA/cm^2 and –0.83 mA/cm^2 were observed for +0.64 V and –0.36 V respectively, which showed significant improvement by a factor of ca. 5 and ca. 9 at same potentials in comparison with the PTFE-free In_2O_3.

7.4 Fourier transform infrared spectroscopic studies

The FTIR spectroelectrochemical method allows the detection of intermediates and reaction products which consist of recording the reflectivity at 0.05 V intervals during the voltammetry scan at a sweep rate of 1 mV/s. Please note that the SPAIRS technique was recorded using LSV and CV IR-spectroelectrochemical techniques. It allows the correlation of the shifting, reduction, appearance, and disappearance of some characteristic vibration bands with potential. Prior to recording FTIR spectra for both FARR and CO_2RR, the 0.100 M Na_2SO_4 solutions were bubbled for 20 min with N_2 or CO_2, respectively.

The *in-situ* IR spectroscopic behavior of the In_2O_3 and 0.30 wt% PTFE-In_2O_3 redox reactions recorded on 4.30 M FA-saturated with Na_2SO_4 electrolytes is presented in the Figs. 7.4 & 7.5a-e. The spectra were calculated for each potential value (or time) as changes in the reflectivity (R) relative to a reference single-beam spectrum (R_{ref}). Therefore, individual spectra showed the reflectivity of FA electroreduction to products and intermediates. When the electrode is exposed to FA (Figs.7.4a-c, e-f and 7.5b-c), the formation of CO_2 was observed before the reduction process begins as a band at 2347 cm^{-1} which could be attributed to the first oxidation process of FA to CO_2 as noticed in the LSV (Fig. 7.2a&b) and CV curves (Fig. 7.2d). It has been reported that FA is thermodynamically unstable against decaying into CO_2 and H_2O [351]. Thus, this accounts for the CO_2 band growing with time in FAOR. It is clear from the IR experiments that FA (Figs. 7.4 and 7.5b-e) consumption took place as seen with or without PTFE, and a sharp loss of the absorbance band was noticed in the vibrational modes at 1000 cm^{-1} and 1500; this can be ascribed to the formation of alcohols denoted as AL in Figs 7.4 and 7.5c-e.

Previous studies have shown that the vibrational spectra of formic acid are quite variable, depending on the syn- and anti-conformation of the acid group, the formation of hydrogen-bonded

dimers, general solvation and intermolecular hydrogen bonding in aqueous environments, partial deprotonation, fast proton exchange, and even hydrophobic interactions [352–354]. In this study, the significant consumption of FA propels a decreasing absorption of up to 6 vibrational modes in the observation window (Fig. 7.4a&f and 7.6a): O–H stretching vibration at 3670 cm^{-1}, C–H stretching mode at 3037 cm^{-1}, C=O stretching mode at 2120 cm^{-1}, a double band near 1667/1589 cm^{-1} (this may be assigned to the vibrational modes with major FA C–O stretching character), and lastly one at 1225 cm^{-1}. Fig. 7.6a presents the variation of their intensities as a function of potential, implying that they belong to the same species with little or no water or ice interferences. The previous work by Susi *et al.* reported the vibrational modes of gas phase monomeric FA to be 3570 cm^{-1}, 2943 cm^{-1}, 1770 cm^{-1}, 1387 cm^{-1}, 1229 cm^{-1}, and 1033 cm^{-1} [355]. The in-plane modes of the present study are somewhat at higher frequencies than the values by Susi and co-authors [355], thus, suggesting interactions with the catalyst and the presence of the aqueous environment. The transformation reactions for FARR using SPAIRS and SPAIRS/CA, both confirm the decrease or loss in the absorbance as the FA was used up.

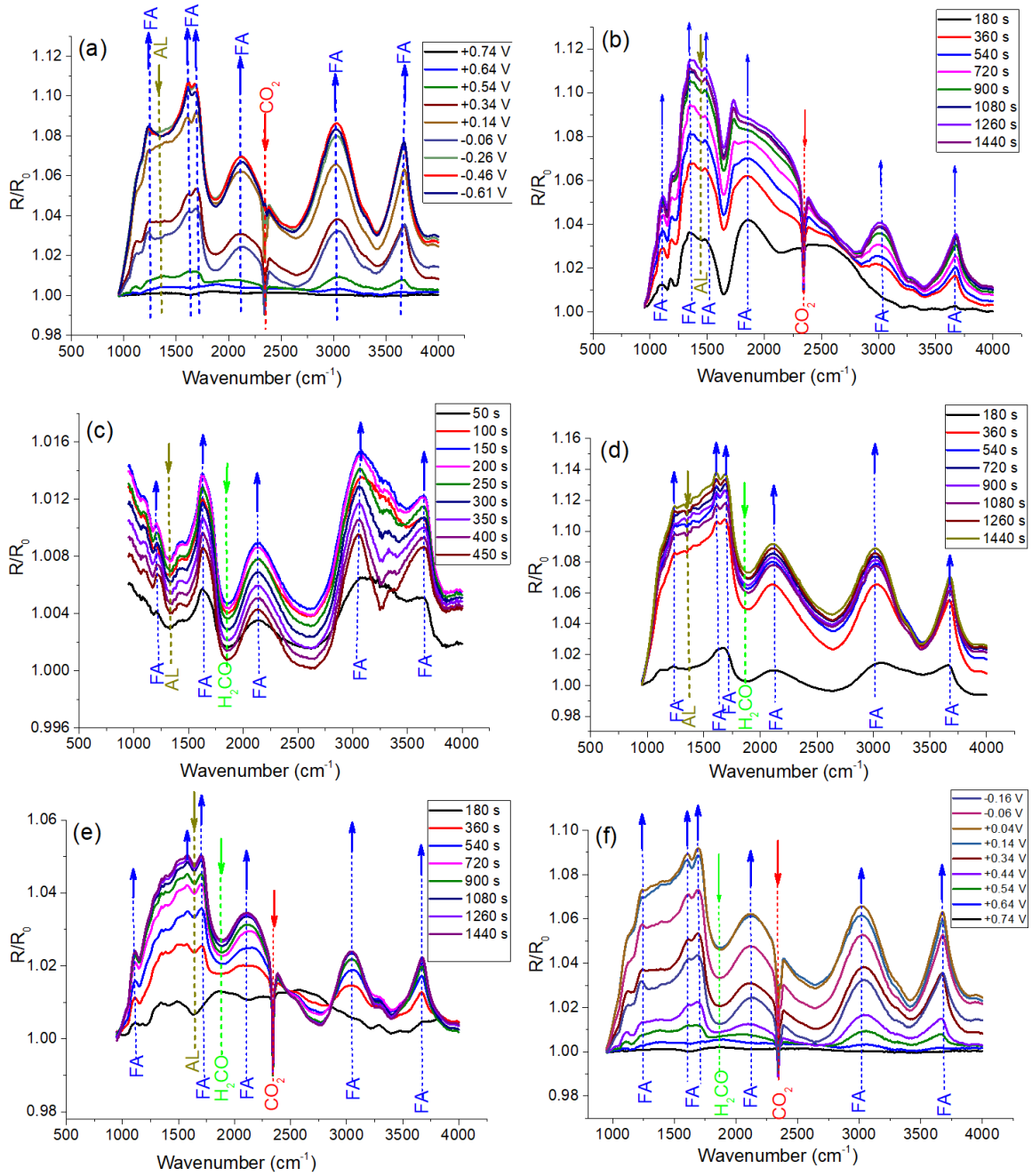

Fig. 7.4: FTIR spectra of In_2O_3 cathode: (a) SPAIR/LSV for FA at +0.74 to –0.61 V; SPAIRS/CA for FA at: (b) +0.74 V, (c) –0.16 V, (d) –0.36V, (e) +0.64 V and (f) SPAIR/CV for FA at +0.64 to –0.76 V on In_2O_3 cathode. All Potentials are relative to SHE.

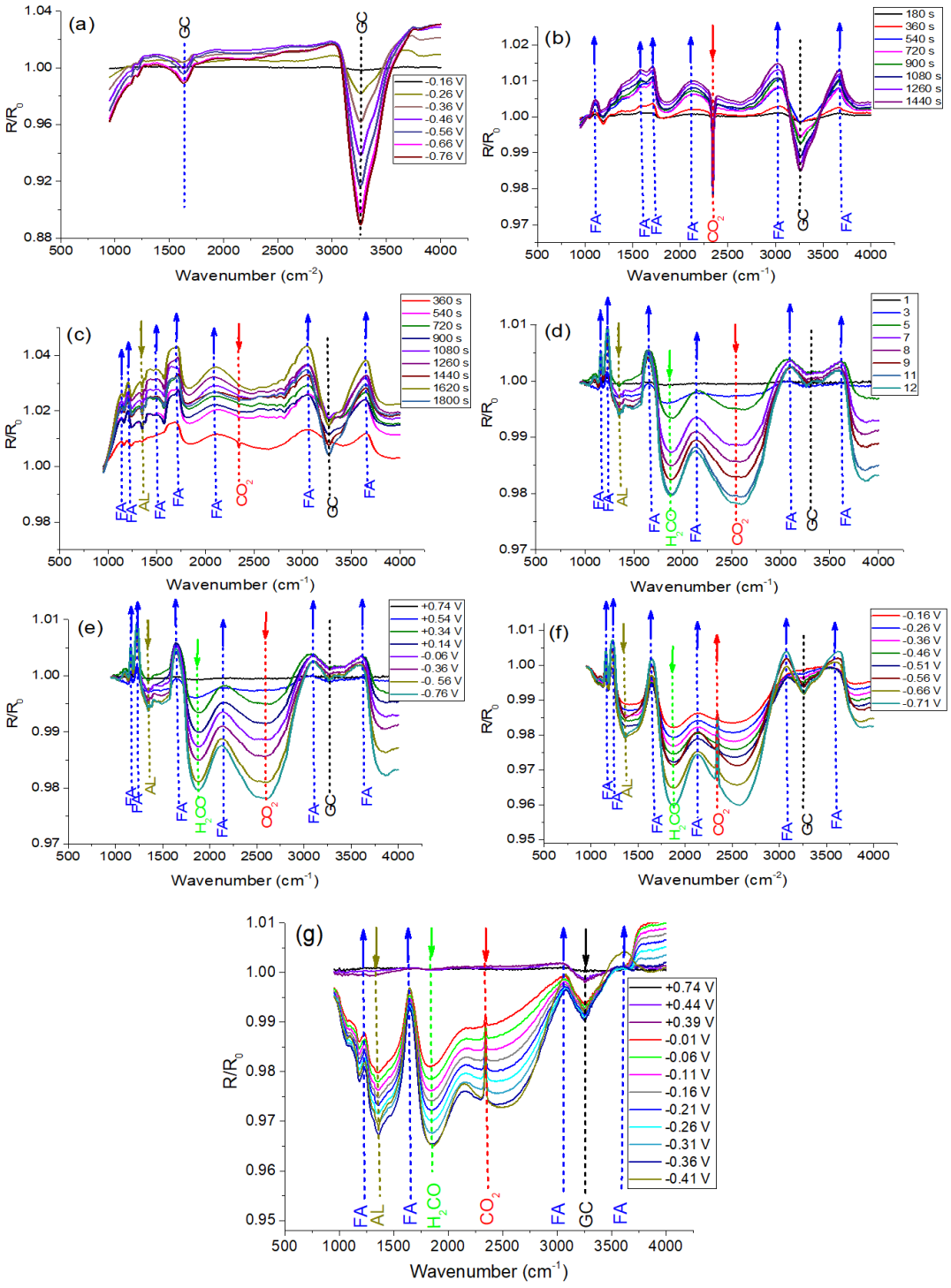

Fig. 7.5: FTIR spectra of 0.15 wt% PTFE-In_2O_3 cathode: (a) SPAIR/CV for N_2 saturated 0.100 M Na_2SO_4 catholyte at +0.64 to –0.76 V; SPAIRS/CA for FA at: (b) +0.64 V, (c) –0.36 V, (d) SPAIR/LSV for FA at +0.74 to –0.76 V; (e) SPAIR/LSV for FA at +0.74 to –0.76 V, (f) SPAIR/LSV for CO_2 saturated catholyte at +0.16 to –0.71 V; and (g) SPAIR/LSV for CO_2 saturated catholyte at +0.74 to –0.41 V. All Potentials are relative to SHE.

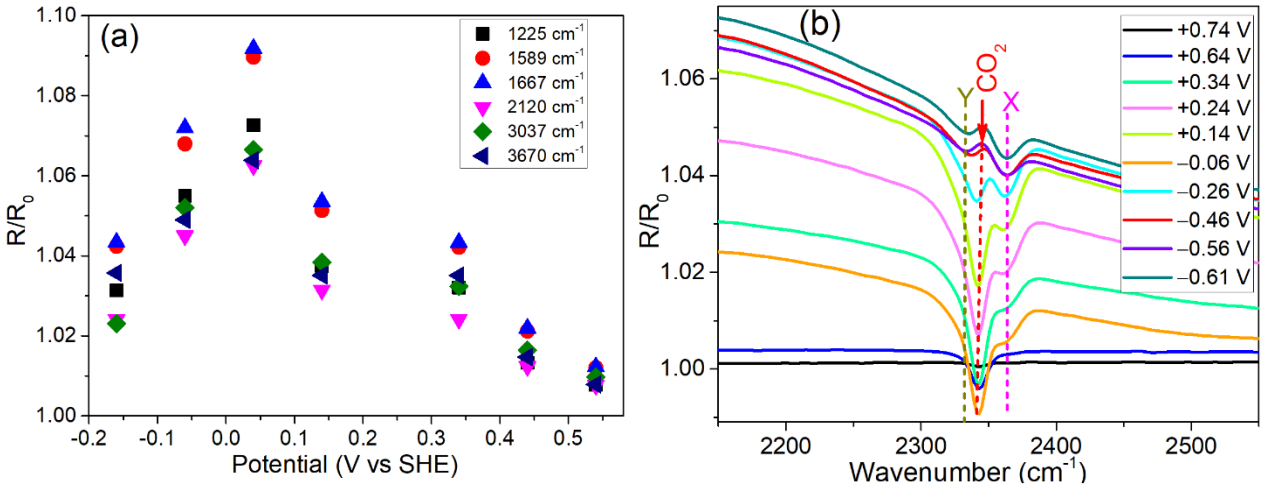

Fig. 7.6: (a) Amplitudes of IR bands assigned to FA in Fig. 7.4f as a function of potential, (b) Expanded region around the 2342 cm^{-1} CO_2 band in Fig. 7.4f [190]. All Potentials are relative to SHE.

Specifically, consideration of Fig. 7.4f (without PTFE) and 7.5f&g (with 0.15 wt% PTFE) gave some clear pictures. Fig. 7.4f collected mainly in the oxidative regime where consumption of FA and formation of H_2 and CO_2 were noticed. As expected, the distinctive asymmetric stretching mode of "free" CO_2 at 2342 cm^{-1} was noticed and this grows with time [190]. The symmetric stretching mode noticed at 1388 cm^{-1} is IR inactive, just as the H_2 stretching mode, while the CO_2 bending mode is expected at 667 cm^{-1}, well outside the observation window. An expansion of the spectra in pristine In_2O_3, Fig. 7.4a&f presented in Fig 7.6b shows the appearance of the asymmetric CO_2 stretching mode. This indeed reveals a slightly more complicated picture with two side bands appearing, suggesting that two further surface sites become accessible for CO_2 adsorption at more negative potentials. This shows that CO_2 grows in at oxidative potential (first scan at +0.74 V) and diminishes at potentials below –0.10 V. A second feature X at 2363 cm^{-1} starts to grow in at +0.34 V, and a third small feature Y at 2333 cm^{-1} is seen beyond –0.4 V. This is not the typical doublet of gas phase as reported previously [36,356] or dissolved CO_2, and it is not seen in experiments with progressing time at a constant potential. It therefore, suggests that all three bands representing the

CO_2 adsorbed on the surface of the electrocatalyst, but at more negative potentials, new surface sites become accessible.

In the experiment performed with CO_2 catholyte (Figs. 7.5f&g) on 0.15 wt% PTFE-In_2O_3 in the absence of FA, the CO_2 band disappears as expected. A convincing difference here is that while R/R_0 is >1 in Fig. 7.4a&f, dominated by the disappearance of FA, it is <1 in Fig. 7.5f&g, thus revealing the formation of intermediates and products, seen as a broad structured background. The positions of the FA bands are indicated, but the spectra show very little change at these positions, suggesting that no significant concentration of FA is built up. If FA is indeed an intermediate of CO_2 reduction, then it must be quite short-lived. The CO_2 band changes in the positive direction with the potential going more negative, suggesting that CO_2 is used up. Effects may also be masked by superposition with new intermediates that grow in. A baseline effect due to the upgoing band was noticed at around 1650 cm^{-1} corresponding to water deformation. The down going bands (Fig. 7.5f&g) between 1000 and 1510 cm^{-1} are compatible with the formation of alcohols. The OH deformation was noticed in the broad band range of 1300-1500 cm^{-1}. The sharp bands in the 1000-1150 cm^{-1} range can be assigned to the C-O stretch of different alcohols. The CO_2 band seen at 2346 cm^{-1} grows with time in FAOR and decreases at reductive potentials when the electrode is initially exposed to CO_2. The broad bands around 3250 cm^{-1} and 3679 cm^{-1} can be assigned to the O-H group. The strong band at 1878 and 1848.4 cm^{-1} (Fig. 7.5f&g respectively) can be ascribed to the formation of formaldehyde.

Comparing the samples with and without PTFE, notably, the IR of N_2 with 0.15 wt% PTFE-In_2O_3 cathode (Fig 7.5a), FA with 0.15 wt% PTFE-In_2O_3 (Fig. 7.5b-e) and CO_2 with 0.15 wt% PTFE-In_2O_3 (7.5f-g) show the appearance of the strong band at 3261 cm^{-1} ascribed O-H to stretching vibration and weak partner at 1630 cm^{-1} attributed to the O-H bending vibration. These

two bands may be due to the glassy carbon electrode (GCE) [357] and were absent in the pristine In_2O_3 (without PTFE). To ascertain the bands' assignment of 3261 cm^{-1} and 1630 cm^{-1} to GCE, as presented in Fig. 7.7, the IR of pristine In_2O_3 at −0.61 V (red) was placed in close comparison with the: (a) IR diffuse reflectance spectra of uncoated GCE in the absence of any liquid in the reaction vessel and absence of a potential (blue). The two broad bands are due to ice that condensed over time on the liquid N_2-cooled detector, (b) 0.15 wt% PTFE-In_2O_3 electrode at +0.64 V (magenta), (c) Bare GCE in 0.100 M Na_2SO_4 without any potential (olive) and (d) N_2 saturated 0.100 M Na_2SO_4 catholyte with 0.15% PTFE- In_2O_3 cathode at −0.66 V (black). In according to the literature [357], the two bands at 3261 cm^{-1} and at 1630 cm^{-1} are assigned to the –OH groups stretching and bending vibrations bound at the surface of the GCE [357].

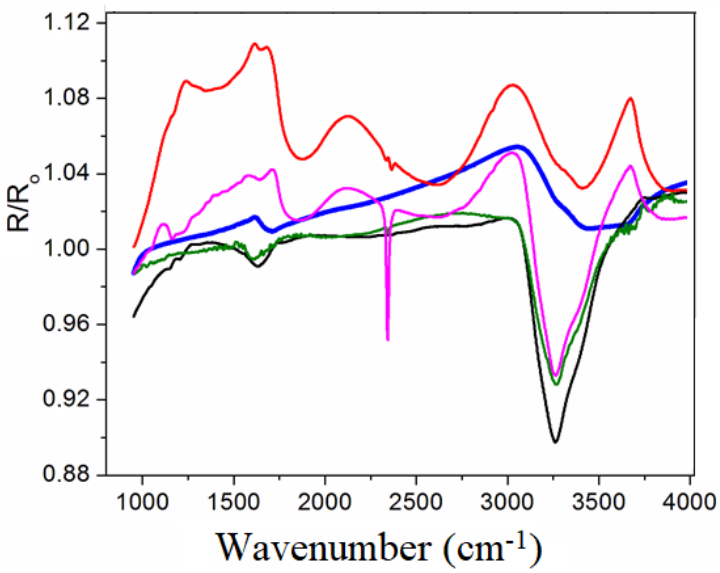

Fig. 7.7: IR spectroelectrochemistry showing the comparison of different electrodes (pristine In_2O_3 at −0.61 V (red line), uncoated GCE in the absence of any liquid in the reaction vessel and absence of a potential (blue line), 0.15 wt% PTFE-In_2O_3 electrode at +0.64 V (magenta line), bare GCE in 0.100 M Na_2SO_4 without any potential (olive line) and N_2 saturated 0.100 M Na_2SO_4 catholyte with 0.15% PTFE- In_2O_3 cathode at −0.66 V (black)) [190].

The band at 1579 cm^{-1} seen at the potential of –0.36 V chronoamperometry experiment with 0.15 wt% PTFE-In_2O_3 (Fig. 7.5c) can be assigned to the presence of vibrational modes with major FA C–O stretching character, this was not noticed at –0.36 V chronoamperometry of PTFE-free In_2O_3 (Fig. 7.4d). Also, the enhancement of products/intermediates was evident. It can be said here that the dependence of well-defined bands is due to the presence of PTFE which interacts with the In_2O_3 surface; its reduction ability. In this way, it somehow keeps the surface or the defects on the surface free for HCOOH to approach and adsorb. This further agreed with the origin of the electrocatalytic performance of PTFE on different electrodes reported in the literature [171,258,265,318].

7.5 Mechanisms of FA reduction to methanol

In agreement with the cyclic voltammetry, spectroelectrochemistry and electrolysis experiments, one may propose a plausible mechanism for FA reduction to methanol on In_2O_3 cathode (presented in the scheme 7.1). Firstly, In_2O_3 is electrochemically reduced to In^0. At the same potential, an In-H^*_{ads} surface species is formed by a 1-electron reduction of H^+. This active species can then transfer 2 electrons and a proton to FA to form the In^I species observed in cyclic voltammetry and the intermediate methanediol. This intermediate species is the hydrated form of formaldehyde that has been observed in small amounts after electrolysis experiments. In^I is readily reduced to In^0 which closes the catalytic cycle. The methanediol close to the surface can then undergo an additional reduction induced by the In-H^*_{ads} surface species and lead to methanol [190]. Then, higher alcohols (i.e. C_2 and C_3 alcohols) may be formed through the same stepwise reduction pattern involving the different intermediate species formed [190].

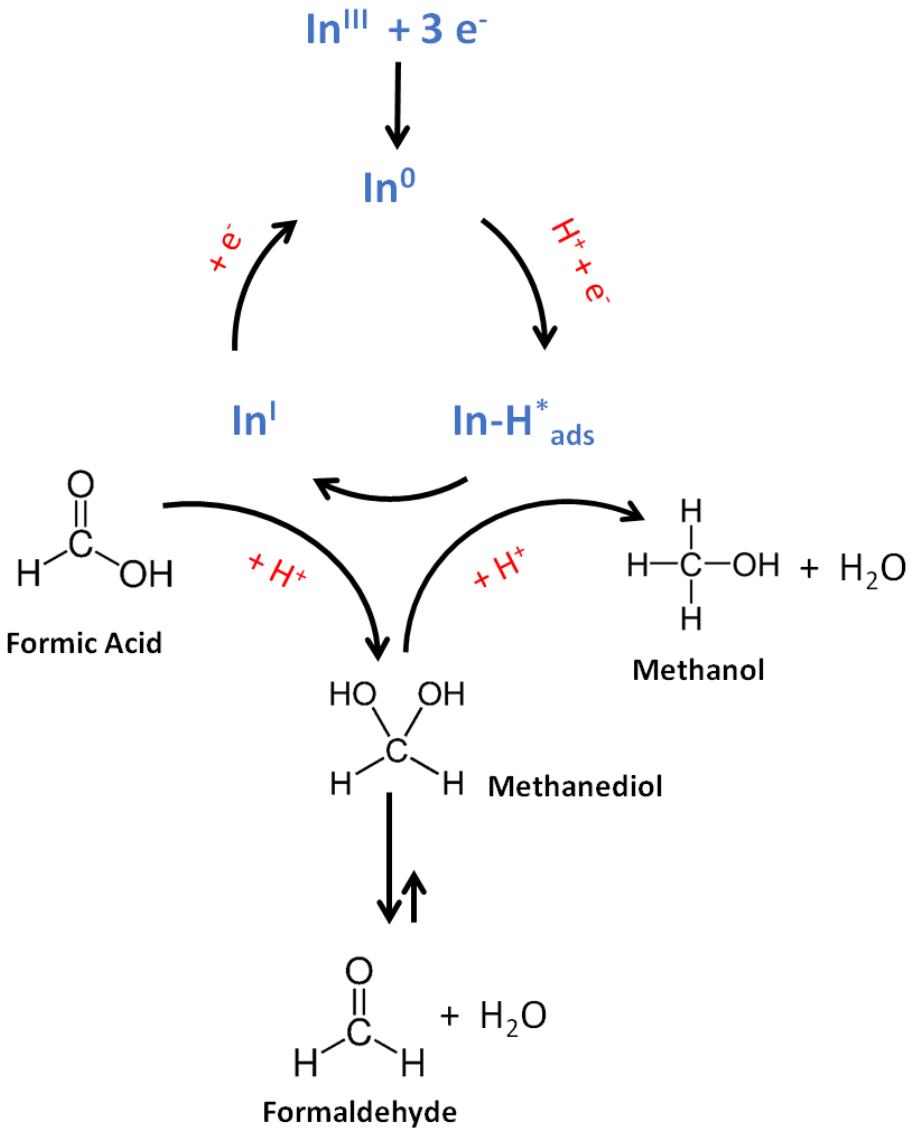

Scheme 7.1: Mechanism for FA reduction to methanol [190].

Chapter 8

CONCLUSIONS AND FUTURE PROSPECTS

8.1 Conclusions

The anodic electrocatalyst powder; IrO_2:TaC for the OER in PEM electrolyzer was successfully synthesized. This standard TaC-supported IrO_2 water-splitting electrocatalyst served as the anode. It was established that the utilization of TaC as support provides a great opportunity to reduce a large amount of expensive and scarce iridium as starting material for synthesizing iridium oxide. Three different samples of anodic electrocatalysts including 60:40 wt% IrO_2:TaC, 70:30 wt% IrO_2:TaC and 100:00 wt% IrO_2:TaC were fabricated in this study and employed for water electrolysis. From the analysis of the individual electrocatalysts for WE, the 70:30 wt% IrO_2:TaC was chosen as the best based on its superior electrochemical activities than the other samples, and therefore used for the further electrochemical studies.

Currently, indium oxide (In_2O_3) is the best thermal catalyst for methanol formation from CO_2 [1]. This study involves the synthesis of nanosized In_2O_3 catalyst that was used for the thermal conversion of CO_2 to methanol and was converted here to a cathodic electrocatalyst for the same purpose on the membrane electrode assembly with water as a proton source.

Primarily, the Nafion solution was used as the binder owing to its ability to enhance proton conduction. However, FA diffusion in the CL is insufficient since Nafion is unable to provide enough channels as revealed by the low current densities of the In_2O_3 (without PTFE) electrodes. Therefore, FA diffusion into the In_2O_3 electrocatalyst layer was enhanced by adding PTFE into the CL in addition to the Nafion solution. PTFE cannot conduct protons [258] but offers an advantage over the PTFE-free In_2O_3 electrode. As described in this thesis, it was done to overcome certain kinetics and mass transport limitations and improve the electrocatalyst performances for FARR

and CO_2RR, thus, creating a robust and unobstructed contact for FA and CO_2, catalyst and electrolytes. PTFE is hydrophobic and capable of creating abrupt reaction interfaces that can further modify the In_2O_3 electrocatalyst. Addition of PTFE to the In_2O_3 electrocatalyst layer for FARR has led to significant improvement in current density from -1.94 mA/cm^2 (without PTFE) to 66.0 mA/cm^2 (with 0.15 wt% PTFE) and 70.3 mA/cm^2 (with 0.30 wt% PTFE) which is a factor of ca. 34 and ca. 36 respectively at 2.4 V cell voltage. This further reduces the onset potential of the electroreduction by 0.4 V. Notably the Ohmic cell resistance was greatly reduced by a factor of 15, suggesting that the activation energy of the electrode and the transport resistance in the porous structure are reduced significantly. This is because of an increase in the hydrophobicity in the porous catalyst layer. This electrode structure, together with the PTFE utilization, have for the first time solved certain problems associated with the use of liquid phases, especially in the FA electroreduction. It should be noted that a preliminary experiment with higher cathode loading on 0.30 wt% PTFE-In_2O_3 electrode boosted the current density beyond 350 mA cm^{-2} using a three-electrode set-up. However, this was at the cost of Faraday's efficiency, indicating that the yield of competing hydrogen increased.

The Tafel slope was employed to investigate the performance of the electrochemical reactions involving the WE, co-electrolysis of 4.30 M formic acid and water, and CO_2. Tafel values of all the electrodes over their respective number of LSV cycles were consistent with each other. The performance of the PTFE-In_2O_3 electrode improves significantly, supported also by the lower Tafel slope compared with the PTFE-free In_2O_3 electrode. The energy efficiencies look even more promising. This underlines the dominant importance of limitation of electroreduction in aqueous solutions by transport resistance. Addition of PTFE to the In_2O_3 layer locally modified the property

of active surface areas by creating electroactive porosity on the PTFE-In_2O_3 particles which could easily be accessible by the FA species.

The CA experiment (i.e. the steady-state current density) showed excellent stability over 24 h of investigation. The CA which is a function of long-term constant current density for the electroreduction of 4.30 M FA in the absence of stirring or in the absence of any flow indicates a current density that is limited to ca. 26 mA/cm^2 at long times. Considering the initial current density of 70.3 mA/cm^2, the limitation is a result of FA transport across the diffusion layer near the electrocatalyst surface. This was further investigated using the Cottrell equation which describes the time-dependence of the current density of a convection-free, diffusion-controlled (non-activated) reaction near a planar electrode. This observation qualitatively reproduced the experimental behavior, thereby, confirming a diffusion layer that builds up, resulting in reactant depletion near the electrode surface.

FTIR spectroelectrochemistry was used to monitor the disappearance of FA and the formation or disappearance of CO_2. The significant consumption of FA propelled a remarkable decrease of IR absorption of up to 6 vibrational modes in the observation window including bands at 3670 cm^{-1} belonging to the O–H stretching vibration, 3037 cm^{-1} assigned to the C–H stretching mode, 2120 cm^{-1} attributed to a C=O stretching mode, a double band near 1667/1589 cm^{-1} assigned to the vibrational modes with major FA C–O stretching character, and finally one at 1225 cm^{-1}. The in-plane modes frequencies of the present study are somewhat higher than the corresponding literature values, suggesting interactions with the catalyst and the presence of the aqueous environment. The experiment with CO_2 catholyte showed the disappearance of the CO_2 band as expected with no FA building up, suggesting that CO_2 reacts more efficiently, and formic acid formation was bypassed as an intermediate. The spectra revealed the formation of intermediates

and products, seen as a broad structured background. The CO_2 band changes in the positive direction, implying that it is used up with the potential going more negative.

In addition to the reported literature, this study has established the ability of In_2O_3 not only to produce MeOH but also EtOH and iPrOH with a maximum combined Faraday efficiency of 82.6% and a space-time-yield of 0.431 $g_{alcohol} h^{-1} g_{cat}^{-1}$ that compares well with results from heterogeneous catalysis. $\Delta G°$ for the formation of MeOH, EtOH, and iPrOH equals +432.1 kJ/mol, +785.0 kJ/mol and +1141.0 kJ/mol, respectively. It was further discovered here that high Faraday efficiency of alcohol and current density can be achieved under a relatively low overpotential by tuning the amount of PTFE used. Interaction of appropriate amounts of PTFE with In_2O_3 is considered the major factor for improving the electrochemical performance.

Interestingly, the CV experiments with 0.15 wt% PTFE-In_2O_3 cathode established a curve-crossing oxidation peak which indicates multiple redox species or a multi-step parallel or consecutive mechanism, attributed to the slow formation of redox active intermediates and slow follow-up reaction occurring in the diffusion layer on the surface of the electrode. To the best of our knowledge, this is the first time that this is noticed in PTFE-In_2O_3 for FA redox reactions. Responsible for this was an appropriate amount of PTFE in the In_2O_3 CL. It did not only enhance the adhesion properties of the In_2O_3 CL on the carbon paper but also helped to create the hydrophobic channels in the catalytic layers. One of the novelties of this study is dealing with the formic acid reduction on the In_2O_3 electrode which is very scarce or even impossible to find in the literature. In agreement with the cyclic voltammetry, spectroelectrochemistry, and electrolysis experiments, a plausible reaction mechanism for FA reduction to methanol on In_2O_3 cathode has been proposed. Then, C_2 and C_3 alcohols may be formed through the same stepwise reduction pattern involving the different intermediate species formed.

8.2 Future prospects

Despite the promising results of the GDL used in this work, further research is required to optimize the chemical composition of the catalyst layer (e.g. distribution, pore size, binder variations, contact angle etc.), porous support (e.g. porosity, thickness, etc.), and the impacts on the FA transport and the formation of the products. On this note, it will be interesting to integrate the GDL used in this work into electrochemical dynamic flow reactor(s), hoping that limitations associated with charge and mass transfers will be minimized, and long-term stability will be achieved.

Also, *in-situ* Raman spectroscopy can be explored to provide information about interfacial reactions occurring during the FARR and CO_2RR. In addition, scanning transmission electron microscopy can be conducted with atomic resolutions. This will help to further understand In_2O_3 surface restructuring/or reaction phenomena [358] induced by the reactants, adsorbates, PTFE, and potentials.

Furthermore, computational studies should be conducted on the FARR process on In_2O_3. For example, DFT has been used over the years to provide useful information on the CO_2RR. The computational studies in addition to the advanced *in-situ* characterization studies should provide an accurate structural performance relationship that will help in further catalytic optimization.

Lastly, the influence of catalytic supports cannot be overemphasized in their electronic conducting ability, uniqueness to offer superior electrocatalytic surface areas, suitable pore structures that permit reactant and product transport and/or form electrocatalytic active sites, thereby enhancing catalyst activities. An In_2O_3/ZrO_2 thermal catalyst was reported for a remarkable 100% methanol yield and stability over 1000 h^{-1}. It will be interesting to use ZrO_2 as support for In_2O_3 by simply preparing a cathode with In_2O_3/ZrO_2 electrocatalysts that can do the

FA and CO_2 conversion near room temperature. Such a system is recommended to use for water electrolysis, giving hydrogen as the second starting compound. In line with that, dynamic electrochemical measurements (cyclo-voltammetry and impedance spectroscopy) should be carried out on such a cathode to determine the kinetics of individual reaction steps. Similarly, FTIR spectroelectrochemical experiments on In_2O_3/ZrO_2 cathode without and with exposure to CO_2 and before and after electrochemical use should be carried out to develop an understanding of CO_2 surface binding on a molecular level. The effect of electrocatalyst loadings and the influence of In_2O_3-support interaction in addition to the bonding stability between In_2O_3 electrocatalyst and ZrO_2 support material should be studied in detail. This understanding is expected to provide more insight into the electrocatalyst modifications and novel electrocatalytic designs from wider perspectives.

REFERENCES

1. Martin, O. *et al.* Indium Oxide as a Superior Catalyst for Methanol Synthesis by CO_2 Hydrogenation. *Angew. Chemie Int. Ed.* **55**, 6261–6265 (2016).
2. Zhu, D. D., Liu, J. L. & Qiao, S. Z. Recent Advances in Inorganic Heterogeneous Electrocatalysts for Reduction of Carbon Dioxide. *Adv. Mater.* **28**, 3423–3452 (2016).
3. Jiang, Z., Xiao, T., Kuznetsov, V. L. & Edwards, P. P. Turning carbon dioxide into fuel. *Philos. Trans. R. Soc. A Math. Phys. Eng. Sci.* **368**, 3343–3364 (2010).
4. Gauvillé, P., Foucher, J. C. & Moreau, D. Achievable combustion efficiency with Alstom CFB boilers for burning discarded coal. *J. South. African Inst. Min. Metall.* **112**, 437–447 (2012).
5. Boosari, S. S. H., Aybar, U. & Eshkalak, M. O. Carbon Dioxide Storage and Sequestration in Unconventional Shale Reservoirs. *J. Geosci. Environ. Prot.* **03**, 7–15 (2015).
6. Maginn, E. J. What to do with CO_2. *J. Phys. Chem. Lett.* **1**, 3478–3479 (2010).
7. Metz, B., Davidson, O. & Bosch, P. Climate Change 2007 University of Sierra Leone. *Waste Manag.* 8 (2007).
8. Toftegaard, M. B., Brix, J., Jensen, P. A., Glarborg, P. & Jensen, A. D. Oxy-fuel combustion of solid fuels. *Prog. Energy Combust. Sci.* **36**, 581–625 (2010).
9. Shih, C. F., Zhang, T., Li, J. & Bai, C. Powering the Future with Liquid Sunshine. *Joule* **2**, 1925–1949 (2018).
10. Ilson, T. O. M. W. *et al.* SPECIAL S q SECTION : **1020423006**, 148–149 (2010).
11. Michael, K. *et al.* Geological storage of CO_2 in saline aquifers-A review of the experience from existing storage operations. *Int. J. Greenh. Gas Control* **4**, 659–667 (2010).
12. Olajire, A. A. CO_2 capture and separation technologies for end-of-pipe applications - A

review. *Energy* **35**, 2610–2628 (2010).

13. Thambimuthu, K. (Kailai) *et al.* Capture of CO_2. *IPCC Spec. Rep. Carbon dioxide Capture Storage* 105–178 (2005).

14. MacDowell, N. *et al.* An overview of CO_2 capture technologies. *Energy Environ. Sci.* **3**, 1645 (2010).

15. Adegoke, K. A. *et al.* Photocatalytic conversion of CO_2 using ZnO semiconductor by hydrothermal method. *Pakistan J. Anal. Environ. Chem.* **19**, 1–27 (2018).

16. Wang, W., Wang, S., Ma, X. & Gong, J. Recent advances in catalytic hydrogenation of carbon dioxide. *Chem. Soc. Rev.* **40**, 3703–3727 (2011).

17. Olah, G. A., Goeppert, A. & Prakash, G. K. S. Chemical Recycling of Carbon Dioxide to Methanol and Dimethyl Ether : From Greenhouse Gas to Renewable , Environmentally Carbon Neutral Fuels and Synthetic Hydrocarbons Chemical Recycling of Carbon Dioxide to Methanol and Dimethyl Ether : From Greenhouse. *J. Org. Chem.* **74**, 487–498 (2009).

18. Olah, G. A., Prakash, G. K. S. & Goeppert, A. Anthropogenic chemical carbon cycle for a sustainable future. *J. Am. Chem. Soc.* **133**, 12881–12898 (2011).

19. Mikkelsen, M., Jørgensen, M. & Krebs, F. C. The teraton challenge. A review of fixation and transformation of carbon dioxide. *Energy Environ. Sci.* **3**, 43–81 (2010).

20. Graves, C., Ebbesen, S. D., Mogensen, M. & Lackner, K. S. Sustainable hydrocarbon fuels by recycling CO_2 and H_2O with renewable or nuclear energy. *Renew. Sustain. Energy Rev.* **15**, 1–23 (2011).

21. Yu, K. M. K., Curcic, I., Gabriel, J. & Tsang, S. C. E. Recent advances in CO_2 capture and utilization. *ChemSusChem* **1**, 893–899 (2008).

22. Quadrelli, E. A., Centi, G., Duplan, J. L. & Perathoner, S. Carbon dioxide recycling: Emerging large-scale technologies with industrial potential. *ChemSusChem* **4**, 1194–1215 (2011).

23. Jitaru, M., Lowy, D. A., Toma, M., Toma, B. C. & Oniciu, L. Electrochemical reduction of carbon dioxide on flat metallic cathodes. *Journal of Applied Electrochemistry* **27**, 875–889 (1997).

24. Kuhl, K. P. *et al.* Electrocatalytic conversion of carbon dioxide to methane and methanol on transition metal surfaces. *J. Am. Chem. Soc.* **136**, 14107–14113 (2014).

25. Ming, M. Selective Electrocatalytic CO_2 Conversion on Metal Surfaces. (China University of Petroleum, 2017). doi:10.4233/uuid:8b16b984-197d-4486-a139-02cbf9b80e69

26. Kapusta, S. & Hackerman, N. The Electroreduction of Carbon Dioxide and Formic Acid on Tin and Indium Electrodes. *J. Electrochem. Soc.* **130**, 607–613 (1983).

27. Russell, P. G., Kovac, N., Srinivasan, S. & Steinberg, M. The Electrochemical Reduction of Carbon Dioxide, Formic Acid, and Formaldehyde. *J. Electrochem. Soc.* **124**, 1329–1338 (1977).

28. Kotoulas, I., Schizodimou, A. & Kyriacou, G. Electrochemical Reduction of Formic Acid on a Copper-Tin-Lead Cathode. *Bentham Sci.* **4**, 8–12 (2013).

29. Jin, F. *et al.* Hydrothermal conversion of carbohydrate biomass into formic acid at mild temperatures. *Green Chem.* **10**, 612–615 (2008).

30. Zhou, Z. B. *et al.* Preparation of indium tin oxide films and doped tin oxide films by an ultrasonic spray CVD process. *Appl. Surf. Sci.* **172**, 245–252 (2001).

31. Liang, Y. X., Li, S. Q., Nie, L., Wang, Y. G. & Wang, T. H. In situ synthesis of In_2O_3 nanowires with different diameters from indium film. *Appl. Phys. Lett.* **88**, 1–3 (2006).

32. Chandradass, J., Bae, D. S. & Kim, K. H. A simple method to prepare indium oxide nanoparticles: Structural, microstructural and magnetic properties. *Adv. Powder Technol.* **22**, 370–374 (2011).

33. Hoch, L. B. *et al.* The rational design of a single-component photocatalyst for gas-phase CO_2 reduction using both UV and visible light. *Adv. Sci.* **1**, 1–10 (2014).

34. Rameshan, C. *et al.* CO_2-selective methanol steam reforming on In-doped Pd studied by in situ X-ray photoelectron spectroscopy. *J. Catal.* **295**, 186–194 (2012).

35. Iwasa, N., Mayanagi, T., Ogawa, N., Sakata, K. & Takezawa, N. New catalytic functions of Pd-Zn, Pd-Ga, Pd-In, Pt-Zn, Pt-Ga and Pt-in alloys in the conversions of methanol. *Catal. Letters* **54**, 119–123 (1998).

36. Detweiler, Z. M., White, J. L., Bernasek, S. L. & Bocarsly, A. B. Anodized indium metal electrodes for enhanced carbon dioxide reduction in aqueous electrolyte. *Langmuir* **30**, 7593–7600 (2014).

37. Ye, J., Liu, C., Mei, D. & Ge, Q. Active oxygen vacancy site for methanol synthesis from CO_2 hydrogenation on In_2O_3(110): A DFT study. *ACS Catal.* **3**, 1296–1306 (2013).

38. Ye, J., Liu, C. & Ge, Q. DFT Study of CO_2 Adsorption and Hydrogenation on the In_2O_3 Surface. *J. Phys. Chem. C* **116**, 7817–7825 (2012).

39. Bielz, T. *et al.* Hydrogen on In_2O_3: Reducibility, bonding, defect formation, and reactivity. *J. Phys. Chem. C* **114**, 9022–9029 (2010).

40. Sun, K. *et al.* Hydrogenation of CO_2 to methanol over In_2O_3 catalyst. *J. CO_2 Util.* **12**, 1–6 (2015).

41. Frei, M. S. *et al.* Atomic-scale engineering of indium oxide promotion by palladium for methanol production via CO_2 hydrogenation. *Nat. Commun.* **10**, 1–11 (2019).

42. Sun, L., Ran, R., Wang, G. & Shao, Z. Fabrication and performance test of a catalyst-coated membrane from direct spray deposition. *Solid State Ionics* **179**, 960–965 (2008).

43. Klingele, M., Breitwieser, M., Zengerle, R. & Thiele, S. Direct deposition of proton exchange membranes enabling high performance hydrogen fuel cells. *J. Mater. Chem. A* **3**, 11239–11245 (2015).

44. Klingele, M. *et al.* A completely spray-coated membrane electrode assembly. *Electrochem. commun.* **70**, 65–68 (2016).

45. Armaroli, N. & Balzani, V. The future of energy supply: Challenges and opportunities. *Angewandte Chemie - International Edition* (2007). doi:10.1002/anie.200602373

46. Chu, S. & Majumdar, A. Opportunities and challenges for a sustainable energy future. *Nature* (2012). doi:10.1038/nature11475

47. Solomon, S., Plattner, G. K., Knutti, R. & Friedlingstein, P. Irreversible climate change due to carbon dioxide emissions. *Proc. Natl. Acad. Sci. U. S. A.* **106**, 1704–1709 (2009).

48. Hartmann, D. L. *et al.* Observations: Atmosphere and surface. in *Climate Change 2013 the Physical Science Basis: Working Group I Contribution to the Fifth Assessment Report of the Intergovernmental Panel on Climate Change* (2013). doi:10.1017/CBO9781107415324.008

49. Key World Energy Statistics 2009. *Key World Energy Stat. 2009* (2009). doi:10.1787/9789264039537-en

50. BP. *BP Energy Outlook 2019 edition*. *BP Energy Outlook 2019* (2019).

51. Intergovernmental Panel on Climate Change. *Climate Change 2013 - The Physical Science Basis*. *Climate Change 2013 - The Physical Science Basis* (2014). doi:10.1017/cbo9781107415324

52. BP. Energy in Focus - BP Statistical Review of World Energy June 2004. *BP Stat. Rev. World Energy* (2004).

53. Olah, G. A. & Prakash, G. K. S. Recycling of Carbon Dioxide Into Methyl Alcohol and Related Oxygenates for Hydrocarbons. in 1235–1242 (2003). doi:10.1142/9789812791405_0239

54. Goeppert, A., Czaun, M., Jones, J. P., Surya Prakash, G. K. & Olah, G. A. Recycling of carbon dioxide to methanol and derived products-closing the loop. *Chem. Soc. Rev.* **43**, 7995–8048 (2014).

55. Sánchez-Sánchez, C. M., Montiel, V., Tryk, D. a., Aldaz, a. & Fujishima, a. Electrochemical approaches to alleviation of the problem of carbon dioxide accumulation*. *Pure Appl. Chem.* **73**, 1917–1927 (2001).

56. Chaplin, R. P. S. & Wragg, A. A. Effects of process conditions and electrode material on reaction pathways for carbon dioxide electroreduction with particular reference to formate formation. *J. Appl. Electrochem.* **33**, 1107–1123 (2003).

57. Gattrell, M., Gupta, N. & Co, A. A review of the aqueous electrochemical reduction of CO_2 to hydrocarbons at copper. *J. Electroanal. Chem.* **594**, 1–19 (2006).

58. Weidner, J. W., Sethuraman, V.A. & Van Zee, J. W. Engineering a Membrane Electrode, Electrochem. Society Interf. 40-43 (2003).

59. Whipple, D. T. & Kenis, P. J. A. Prospects of CO_2 utilization via direct heterogeneous electrochemical reduction. *J. Phys. Chem. Lett.* **1**, 3451–3458 (2010).

60. Spinner, N. S., Vega, J. A. & Mustain, W. E. Recent progress in the electrochemical conversion and utilization of CO_2. *Catal. Sci. Technol.* **2**, 19–28 (2012).

61. Lee, J., Kwon, Y., Machunda, R. L. & Lee, H. J. Electrocatalytic Recycling of CO_2 and

Small Organic Molecules. *Chem. An Asian J.* **4**, 1516–1523 (2009).

62. Jhong, H. R. M., Ma, S. & Kenis, P. J. Electrochemical conversion of CO_2 to useful chemicals: Current status, remaining challenges, and future opportunities. *Curr. Opin. Chem. Eng.* **2**, 191–199 (2013).

63. Jiang, K. *et al.* Transition-Metal Single Atoms in a Graphene Shell as Active Centers for Highly Efficient Artificial Photosynthesis. *Chem* **3**, 950–960 (2017).

64. De Luna, P. *et al.* What would it take for renewably powered electrosynthesis to displace petrochemical processes? *Science* **364**, (2019).

65. Greenblatt, J. B., Miller, D. J., Ager, J. W., Houle, F. A. & Sharp, I. D. The Technical and Energetic Challenges of Separating (Photo)Electrochemical Carbon Dioxide Reduction Products. *Joule* **2**, 381–420 (2018).

66. Bushuyev, O. S. *et al.* What Should We Make with CO_2 and How Can We Make It? *Joule* **2**, 825–832 (2018).

67. Agarwal, A. S., Zhai, Y., Hill, D. & Sridhar, N. The electrochemical reduction of carbon dioxide to formate/formic acid: Engineering and economic feasibility. *ChemSusChem* **4**, 1301–1310 (2011).

68. Hori, Y., Wakebe, H., Tsukamoto, T. & Koga, O. Electrocatalytic process of CO selectivity in electrochemical reduction of CO_2 at metal electrodes in aqueous media. *Electrochim. Acta* **39**, 1833–1839 (1994).

69. Oloman, C. & Li, H. Electrochemical processing of carbon dioxide. *ChemSusChem* **1**, 385–391 (2008).

70. Sheet, S. D. Formic acid Formic acid. *ICIS Chem. Bus.* **1**, 1–12 (2017).

71. Innocent, B. *et al.* Electro-reduction of carbon dioxide to formate on lead electrode in

aqueous medium. *J. Appl. Electrochem.* **39**, 227–232 (2009).

72. Rees, N. V. & Compton, R. G. Sustainable energy: A review of formic acid electrochemical fuel cells. *J. Solid State Electrochem.* **15**, 2095–2100 (2011).

73. Li, H. & Oloman, C. Development of a continuous reactor for the electro-reduction of carbon dioxide to formate - Part 2: Scale-up. *J. Appl. Electrochem.* **37**, 1107–1117 (2007).

74. Ganesh, I. Conversion of carbon dioxide into methanol - A potential liquid fuel: Fundamental challenges and opportunities (a review). *Renew. Sustain. Energy Rev.* **31**, 221–257 (2014).

75. Martin, O. & Pérez-Ramírez, J. New and revisited insights into the promotion of methanol synthesis catalysts by CO_2. *Catal. Sci. Technol.* **3**, 3343–3352 (2013).

76. Bevilacqua, M. *et al.* Energy Savings in the Conversion of CO_2 to Fuels using an Electrolytic Device. *Energy Technol.* **2**, 522–525 (2014).

77. Qiao, J., Liu, Y., Hong, F. & Zhang, J. *A review of catalysts for the electroreduction of carbon dioxide to produce low-carbon fuels*. *Chemical Society Reviews* **43**, (2014).

78. Centi, G., Quadrelli, E. A. & Perathoner, S. Catalysis for CO_2 conversion: a key technology for rapid introduction of renewable energy in the value chain of chemical industries. *Energy Environ. Sci.* **6**, 1711–173 (2013).

79. Wang, W. H., Himeda, Y., Muckerman, J. T., Manbeck, G. F. & Fujita, E. CO_2 Hydrogenation to Formate and Methanol as an Alternative to Photo- and Electrochemical CO_2 Reduction. *Chem. Rev.* **115**, 12936–12973 (2015).

80. Behrens, M. *et al.* The Active Site of Methanol Synthesis over $Cu/ZnO/Al_2O_3$ Industrial Catalysts. *Science (80-.).* **336**, 893–897 (2012).

81. Peterson, A. A. & Nørskov, J. K. Activity descriptors for CO_2 electroreduction to methane

on transition-metal catalysts. *J. Phys. Chem. Lett.* **3**, 251–258 (2012).

82. Peterson, A. A., Abild-Pedersen, F., Studt, F., Rossmeisl, J. & Nørskov, J. K. How copper catalyzes the electroreduction of carbon dioxide into hydrocarbon fuels. *Energy Environ. Sci.* **3**, 1311–1315 (2010).

83. Shi, C., O'Grady, C. P., Peterson, A. A., Hansen, H. A. & Nørskov, J. K. Modeling CO_2 reduction on Pt(111). *Phys. Chem. Chem. Phys.* **15**, 7114 (2013).

84. Fashedemi, O. O. & Ozoemena, K. I. Oxygen reduction reaction at MWCNT-modified nanoscale iron(ii) tetrasulfophthalocyanine: Remarkable performance over platinum and tolerance toward methanol in alkaline medium. *RSC Adv.* **5**, 22869–22878 (2015).

85. Li, Y.-N., Ma, R., He, L.-N. & Diao, Z.-F. Homogeneous hydrogenation of carbon dioxide to methanol. *Catal. Sci. Technol.* **4**, 1498–1512 (2014).

86. Merino-Garcia, I., Alvarez-Guerra, E., Albo, J. & Irabien, A. Electrochemical membrane reactors for the utilisation of carbon dioxide. *Chemical Engineering Journal* **305**, 104–120 (2016).

87. Durst, J., Herranz, J. S., Paratcha, Y., Permyakova, A. A. & Schmidt, T. J. Co-Electrolysis Cell Configurations for CO_2 Electrochemical Reduction. *Meet. Abstr.* **MA2015-02**, 1741 (2015).

88. Albo, J., Alvarez-Guerra, M., Castaño, P. & Irabien, A. Towards the electrochemical conversion of carbon dioxide into methanol. *Green Chem.* **17**, 2304–2324 (2015).

89. Basile, A., Liguori, S. & Iulianelli, A. Membrane reactors for methane steam reforming (MSR). in *Membrane Reactors for Energy Applications and Basic Chemical Production* 31–59 (2015). doi:10.1016/B978-1-78242-223-5.00002-9

90. Solomon, S., Plattner, G. K., Knutti, R. & Friedlingstein, P. Irreversible climate change

due to carbon dioxide emissions. *Proc. Natl. Acad. Sci. U. S. A.* **106**, 1704–1709 (2009).

91. Kalamaras, C. M. & Efstathiou, A. M. Hydrogen Production Technologies: Current State and Future Developments. *Conf. Pap. Energy* **2013**, 1–9 (2013).

92. Zeng, K. & Zhang, D. Recent progress in alkaline water electrolysis for hydrogen production and applications. *Prog. Energy Combust. Sci.* **36**, 307–326 (2010).

93. Marcinkoski, J. *et al.* Fuel Cell System Cost -2015. *DOE Hydrog. Fuel Cells Progr. Rec. Rec.* 15015 (2015).

94. Barreto, L., Makihira, A. & Riahi, K. The hydrogen economy in the 21st century: A sustainable development scenario. *Int. J. Hydrogen Energy* **28**, 267–284 (2003).

95. Ball, M. & Wietschel, M. The future of hydrogen - opportunities and challenges. *Int. J. Hydrogen Energy* **34**, 615–627 (2009).

96. Simons, A. & Bauer, C. Life cycle assessment of hydrogen production. in *Transition to Hydrogen: Pathways Toward Clean Transportation* 13–57 (2011). doi:10.1017/CBO9781139018036.006

97. Forner-Cuenca, A. Novel Gas Diffusion Layers with Patterned Wettability for Advanced Water Management Strategies in Polymer Electrolyte Fuel Cells - Research Collection. (ETH ZURICH, 2016). doi:https://doi.org/10.3929/ethz-a-010811344

98. Ridjan, I., Mathiesen, B. V., Connolly, D. & Duić, N. The feasibility of synthetic fuels in renewable energy systems. *Energy* **57**, 76–84 (2013).

99. Melek, Y. & Aytun, O. U. An energy benchmarking model based on artificial neural network method utilizing US Commercial Buildings Energy Consumption Survey (CBECS) database. *Int. J. energy Res.* **31**, 135–147 (2007).

100. Costentin, C., Robert, M. & Savéant, J.-M. M. Catalysis of the electrochemical reduction

of carbon dioxide. *Chem. Soc. Rev.* **42**, 2423–2436 (2013).

101. Kumar, B. *et al.* Photochemical and Photoelectrochemical Reduction of CO_2. *Annu. Rev. Phys. Chem.* **63**, 541–569 (2012).

102. García, M. *et al.* Electro and photoelectrochemical reduction of carbon dioxide on multimetallic porphyrins/polyoxotungstate modified electrodes. *Electrochim. Acta* **115**, 146–154 (2014).

103. Ren, X., Springer, T. E., Zawodzinski, T. A. & Gottesfeld, S. Methanol Transport Through Nation Membranes. Electro-osmotic Drag Effects on Potential Step Measurements. *J. Electrochem. Soc.* (2002). doi:10.1149/1.1393219

104. Centi, G. & Perathoner, S. Catalysis: Role and challenges for a sustainable energy. in *Topics in Catalysis* (2009). doi:10.1007/s11244-009-9245-x

105. Song, C. Global challenges and strategies for control, conversion and utilization of CO_2 for sustainable development involving energy, catalysis, adsorption and chemical processing. *Catal. Today* **115**, 2–32 (2006).

106. Song, C. & Pan, W. Tri-reforming of methane: A novel concept for catalytic production of industrially useful synthesis gas with desired H_2/CO ratios. in *Catalysis Today* **98**, 463–484 (2004).

107. Liu, C., Colón, B. C., Ziesack, M., Silver, P. A. & Nocera, D. G. Water splitting-biosynthetic system with CO_2 reduction efficiencies exceeding photosynthesis. *Science (80-.).* **352**, 1210–1213 (2016).

108. Walter, M. G. *et al.* Solar water splitting cells. *Chem. Rev.* **110**, 6446–6473 (2010).

109. Soriaga, M. P. *et al.* Electrochemical surface science twenty years later: Expeditions into the electrocatalysis of reactions at the core of artificial photosynthesis. *Surf. Sci.* **631**, 285–

294 (2015).

110. Li, X., Wen, J., Low, J., Fang, Y. & Yu, J. Design and fabrication of semiconductor photocatalyst for photocatalytic reduction of CO_2 to solar fuel. *Sci. China Mater.* **57**, 70–100 (2014).

111. Simakov, D. S. A. Chapter 2 Electrocatalytic Reduction of CO_2 Renewable. *Renew. Synth. Fuels Chem. from Carbon Dioxide* 27–43 (2017). doi:10.1007/978-3-319-61112-9

112. Taifan, W., Boily, J. F. & Baltrusaitis, J. Surface chemistry of carbon dioxide revisited. *Surface Science Reports* **71**, 595–671 (2016).

113. Tyczka, J., Eberling, S. & Baljer, G. Immunization experiments with recombinant Coxiella burnetii proteins in a murine infection model. *Ann. N. Y. Acad. Sci.* **1063**, 143–148 (2005).

114. Lu, X., Leung, D. Y. C. C., Wang, H., Leung, M. K. H. H. & Xuan, J. Electrochemical Reduction of Carbon Dioxide to Formic Acid. *ChemElectroChem* **1**, 836–849 (2014).

115. Udupa, K. S., Subramanian, G. S. & Udupa, H. V. K. The electrolytic reduction of carbon dioxide to formic acid. *Electrochim. Acta* **16**, 1593–1598 (1971).

116. Paik, W., Andersen, T. N. & Eyring, H. Kinetic studies of the electrolytic reduction of carbon dioxide on the mercury electrode. *Electrochim. Acta* **14**, 1217–1232 (1969).

117. Ryu, J. Y., Andersen, T. N. & Erying, H. Electrode Reduction Kinetics of Carbon Dioxide in Aqueous Solution. *J. Phys. Chem.* **76**, 3278–3286 (1972).

118. Whipple, D. T., Finke, E. C. & Kenis, P. J. A. Microfluidic reactor for the electrochemical reduction of carbon dioxide: The effect of pH. *Electrochem. Solid-State Lett.* **13**, B109–B111 (2010).

119. Marshall, R. J. & Walsh, F. C. A review of some recent electrolytic cell designs. *Surf.*

Technol. **24**, 45–77 (1985).

120. Suffredini, H. B., Cerne, J. L., Crnkovic, F. C., MacHado, S. A. S. & Avaca, L. A. Recent developments in electrode materials for water electrolysis. *Int. J. Hydrogen Energy* **25**, 415–423 (2000).

121. Omae, I. Aspects of carbon dioxide utilization. *Catal. Today* **115**, 33–52 (2006).

122. Jessop, P. G., Hsiao, Y., Ikariya, T. & Noyori, R. Homogeneous Catalysis in Supercritical Fluids: Hydrogenation of Supercritical Carbon Dioxide to Formic Acid, Alkyl Formates, and Formamides. *J. Am. Chem. Soc.* **118**, 344–355 (1996).

123. Furuya, N. & Matsui, K. Electroreduction of carbon dioxide on gas-diffusion electrodes modified by metal phthalocyanines. *J. Electroanal. Chem.* **271**, 181–191 (1989).

124. Yamamoto, T., Tryk, D. A., Fujishimal, A. & Ohata, H. Production of syngas plus oxygen from CO_2 in a gas-diffusion electrode-based electrolytic cell. *Electrochim. Acta* (2002). doi:10.1016/S0013-4686(02)00253-0

125. Cook, R. L., MacDuff, R. C. & Sammells, A. F. High Rate Gas Phase CO_2 Reduction to Ethylene and Methane Using Gas Diffusion Electrodes. *J. Electrochem. Soc.* **137**, 607–608 (1990).

126. Han, L., Zhou, W. & Xiang, C. High-Rate Electrochemical Reduction of Carbon Monoxide to Ethylene Using Cu-Nanoparticle-Based Gas Diffusion Electrodes. *ACS Energy Lett.* **3**, 855–860 (2018).

127. Kaneco, S., Katsumata, H., Suzuki, T. & Ohta, K. Electrochemical reduction of CO_2 to methane at the Cu electrode in methanol with sodium supporting salts and its comparison with other alkaline salts. *Energy and Fuels* **20**, 409–414 (2006).

128. Summers, D. P., Leach, S. & Frese, K. W. The electrochemical reduction of aqueous

carbon dioxide to methanol at molybdenum electrodes with low overpotentials. *J. Electroanal. Chem.* **205**, 219–232 (1986).

129. Giesbrecht, P. K. & Herbert, D. E. Electrochemical reduction of carbon dioxide to methanol in the presence of benzannulated dihydropyridine additives. *ACS Energy Lett.* **2**, 549–555 (2017).

130. Barton Cole, E. *et al.* Using a one-electron shuttle for the multielectron reduction of CO_2 to methanol: Kinetic, mechanistic, and structural insights. *J. Am. Chem. Soc.* **132**, 11539–11551 (2010).

131. Barton Cole, E. *et al.* Using a one-electron shuttle for the multielectron reduction of CO_2 to methanol: Kinetic, mechanistic, and structural insights. *J. Am. Chem. Soc.* **132**, 11539–11551 (2010).

132. Kortlever, R., Balemans, C., Kwon, Y. & Koper, M. T. M. Electrochemical CO_2 reduction to formic acid on a Pd-based formic acid oxidation catalyst. *Catal. Today* **244**, 58–62 (2015).

133. Prakash, G. K. S., Viva, F. A. & Olah, G. A. Electrochemical reduction of CO_2 over Sn-Nafion®coated electrode for a fuel-cell-like device. *J. Power Sources* **223**, 68–73 (2013).

134. Kwon, Y. & Lee, J. Formic Acid from Carbon Dioxide on Nanolayered Electrocatalyst. *Electrocatalysis* **1**, 108–115 (2010).

135. Saeki, T., Hashimoto, K., Kimura, N., Omata, K. & Fujishima, A. Electrochemical reduction of CO_2 with high current density in a CO_2 + methanol medium at various metal electrodes. *J. Electroanal. Chem.* **404**, 299–302 (1996).

136. Yuan, D. *et al.* Electrochemical activation of carbon dioxide for synthesis of dimethyl carbonate in an ionic liquid. *Electrochim. Acta* **54**, 2912–2915 (2009).

137. Lu, B. *et al.* Electrochemical conversion of CO_2 into dimethyl carbonate in a functionalized ionic liquid. *J.* CO_2 *Util.* **3**–**4**, 98–101 (2013).

138. Kaneco, S., Katsumata, H., Suzuki, T. & Ohta, K. Photoelectrocatalytic reduction of CO_2 in LiOH/methanol at metal-modified p-InP electrodes. *Appl. Catal. B Environ.* **64**, 139–145 (2006).

139. Zhu, W. *et al.* Monodisperse Au nanoparticles for selective electrocatalytic reduction of CO_2 to CO. *J. Am. Chem. Soc.* **135**, 16833–16836 (2013).

140. Rumayor, M., Dominguez-Ramos, A. & Irabien, A. Formic Acid manufacture: Carbon dioxide utilization alternatives. *Appl. Sci.* **8**, 914 (2018).

141. Laitar, D. S., Müller, P. & Sadighi, J. P. Efficient homogeneous catalysis in the reduction of CO_2 to CO. *J. Am. Chem. Soc.* **127**, 17196–17197 (2005).

142. Barton, E. E., Rampulla, D. M. & Bocarsly, A. B. Selective solar-driven reduction of CO_2 to methanol using a catalyzed p-GaP based photoelectrochemical cell. *J. Am. Chem. Soc.* **130**, 6342–6344 (2008).

143. Oh, K. H. *et al.* Interlocking membrane/catalyst layer interface for high mechanical robustness of hydrocarbon-membrane-based polymer electrolyte membrane fuel cells. *Adv. Mater.* **27**, 2974–2980 (2015).

144. Gubler, L., Gürsel, S. A. & Scherer, G. G. Radiation grafted membranes for polymer electrolyte fuel cells. *Fuel Cells* **5**, 317–335 (2005).

145. Taheri Najafabadi, A. CO_2 chemical conversion to useful products: An engineering insight to the latest advances toward sustainability. *Int. J. Energy Res.* **37**, 485–499 (2013).

146. Delacourt, C., Ridgway, P. L., Kerr, J. B. & Newman, J. Design of an electrochemical cell making syngas (CO+ H_2) from CO_2 and H_2O reduction at room temperature. *J.*

Electrochem. Soc. **155**, (2008).

147. Li, Y. C. *et al.* Electrolysis of CO_2 to Syngas in Bipolar Membrane-Based Electrochemical Cells. *ACS Energy Lett.* **1**, 1149–1153 (2016).

148. Revankar, S. T. & Majumdar, P. *Fuel cells: Principles, design, and analysis*. *Fuel Cells: Principles, Design, and Analysis* (2016).

149. Oberholzer, P. *et al.* Simultaneous neutron imaging of six operating PEFCs: Experimental set-up and study of the MPL effect. *Electrochem. commun.* **20**, 67–70 (2012).

150. Weber, A. Z. & Newman, J. Effects of microporous layers in polymer electrolyte fuel cells. *J. Electrochem. Soc.* **152**, A677–A688 (2005).

151. Andisheh-Tadbir, M., Orfino, F. P. & Kjeang, E. Three-dimensional phase segregation of micro-porous layers for fuel cells by nano-scale X-ray computed tomography. *J. Power Sources* **310**, 61–69 (2016).

152. Wang, X. L. *et al.* Micro-porous layer with composite carbon black for PEM fuel cells. *Electrochim. Acta* **51**, 4909–4915 (2006).

153. Wang, X. *et al.* A bi-functional micro-porous layer with composite carbon black for PEM fuel cells. *J. Power Sources* **162**, 474–479 (2006).

154. Li, X. & Sabir, I. Review of bipolar plates in PEM fuel cells: Flow-field designs. *Int. J. Hydrogen Energy* **30**, 359–371 (2005).

155. Forner-Cuenca, A. *et al.* Advanced water management in PEFCs: Diffusion layers with patterned wettability: III. Operando characterization with neutron imaging. *J. Electrochem. Soc.* **163**, F1389–F1398 (2016).

156. Yano, H., Shirai, F., Nakayama, M. & Ogura, K. Electrochemical reduction of CO_2 at three-phase (gas | liquid | solid) and two-phase (liquid | solid) interfaces on Ag electrodes.

J. Electroanal. Chem. **533**, 113–118 (2002).

157. Bockris, J. O. & Cahan, B. D. Effect of a Finite-Contact-Angle Meniscus on Kinetics in Porous Electrode Systems. *J. Chem. Phys.* **50**, 1307–1324 (1969).

158. Ogura, K. & Watanabe, H. Reduction of carbon monoxide on a mediated and partially immersed electrode. *J. Chem. Soc. Faraday Trans. 1 Phys. Chem. Condens. Phases* **81**, 1569–1576 (1985).

159. Yano, H., Tanaka, T., Nakayama, M. & Ogura, K. Selective electrochemical reduction of CO_2 to ethylene at a three-phase interface on copper(I) halide-confined Cu-mesh electrodes in acidic solutions of potassium halides. *J. Electroanal. Chem.* **565**, 287–293 (2004).

160. Mathias, M. F., Roth, J., Fleming, J. & Lehnert, W. Diffusion media materials and characterisation. in *Handbook of Fuel Cells* (2010). doi:10.1002/9780470974001.f303046

161. Sousa, T., Mamlouk, M. & Scott, K. A non-isothermal model of a laboratory intermediate temperature fuel cell using PBI doped phosphoric acid membranes. *Fuel Cells* **10**, 993–1012 (2010).

162. Cheng, H. & Scott, K. Carbon-supported manganese oxide nanocatalysts for rechargeable lithium-air batteries. *J. Power Sources* (2010). doi:10.1016/j.jpowsour.2009.09.030

163. Soehn, M., Lebert, M., Wirth, T., Hofmann, S. & Nicoloso, N. Design of gas diffusion electrodes using nanocarbon. *J. Power Sources* **176**, 494–498 (2008).

164. Gostick, J. T., Ioannidis, M. A., Fowler, M. W. & Pritzker, M. D. On the role of the microporous layer in PEMFC operation. *Electrochem. Commun.* (2009). doi:10.1016/j.elecom.2008.12.053

165. Kang, J. H. *et al.* Visualization of invasion-percolation drainage process in porous media

using density-matched immiscible fluids and refractive-index-matched solid structures. *J. Power Sources* **195**, 2608–2612 (2010).

166. Chen, H. H. & Chang, M. H. Effect of cathode microporous layer composition on proton exchange membrane fuel cell performance under different air inlet relative humidity. *J. Power Sources* **232**, 306–309 (2013).

167. Li, A., Wang, H., Han, J. & Liu, L. Preparation of a Pb loaded gas diffusion electrode and its application to CO_2 electroreduction. *Front. Chem. Sci. Eng.* **6**, 381–388 (2012).

168. Su, H., Pasupathi, S., Bladergroen, B., Linkov, V. & Pollet, B. G. Optimization of gas diffusion electrode for polybenzimidazole-based high temperature proton exchange membrane fuel cell: Evaluation of polymer binders in catalyst layer. *Int. J. Hydrogen Energy* **38**, 11370–11378 (2013).

169. Jhong, H. R. Q., Brushett, F. R. & Kenis, P. J. A. The effects of catalyst layer deposition methodology on electrode performance. *Adv. Energy Mater.* **3**, 589–599 (2013).

170. Mahmood, M. N., Masheder, D. & Harty, C. J. Use of gas-diffusion electrodes for high-rate electrochemical reduction of carbon dioxide. I. Reduction at lead, indium- and tin-impregnated electrodes. *J. Appl. Electrochem.* **17**, 1159–1170 (1987).

171. Mahmood, M. N., Masheder, D. & Harty, C. J. Use of gas-diffusion electrodes for high-rate electrochemical reduction of carbon dioxide. II. Reduction at metal phthalocyanine-impregnated electrodes. *J. Appl. Electrochem.* **17**, 1223–1227 (1987).

172. Perathoner, S., Gangeri, M., Lanzafame, P. & Centi, G. Nanostructured electrocatalytic Pt-carbon materials for fuel cells and CO_2 conversion. *Kinet. Catal.* **48**, 877–883 (2007).

173. Centi, G. & Perathoner, S. Nanostructured Electrodes and Devices for Converting Carbon Dioxide Back to Fuels: Advances and Perspectives. *Green Energy Technol.* **33**, 561–583

(2011).

174. Centi, G. & Perathoner, S. Opportunities and prospects in the chemical recycling of carbon dioxide to fuels. *Catal. Today* **148**, 191–205 (2009).

175. Zhao, H., Zhang, Y., Zhao, B., Chang, Y. & Li, Z. Electrochemical reduction of carbon dioxide in an MFC-MEC system with a layer-by-layer self-assembly carbon nanotube/cobalt phthalocyanine modified electrode. *Environ. Sci. Technol.* **46**, 5198–5204 (2012).

176. Sapountzi, F. M., Gracia, J. M., Weststrate, C. J. (Kee. J., Fredriksson, H. O. A. & Niemantsverdriet, J. W. (Hans. Electrocatalysts for the generation of hydrogen, oxygen and synthesis gas. *Progress in Energy and Combustion Science* **58**, 1–35 (2017).

177. Fabbri, E., Habereder, A., Waltar, K., Kötz, R. & Schmidt, T. J. Developments and perspectives of oxide-based catalysts for the oxygen evolution reaction. *Catalysis Science and Technology* **4**, 3800–3821 (2014).

178. Damjanovic, A., Dey, A. & Bockris, J. O. Electrode Kinetics of Oxygen Evolution and Dissolution on Rh, Ir, and Pt-Rh Alloy Electrodes. *J. Electrochem. Soc.* **113**, 739 (1966).

179. Miles, M. H. Periodic Variations of Overvoltages for Water Electrolysis in Acid Solutions from Cyclic Voltammetric Studies. *J. Electrochem. Soc.* **123**, 1459 (1976).

180. Park, S., Shao, Y., Liu, J. & Wang, Y. Oxygen electrocatalysts for water electrolyzers and reversible fuel cells: Status and perspective. *Energy and Environmental Science* (2012). doi:10.1039/c2ee22554a

181. Miles, M. H. *et al.* The oxygen evolution reaction on platinum, iridium, ruthenium and their alloys at 80°C in acid solutions. *Electrochim. Acta* **23**, 521–526 (1978).

182. Carmo, M., Fritz, D. L., Mergel, J. & Stolten, D. A comprehensive review on PEM water

electrolysis. *Int. J. Hydrogen Energy* **38**, 4901–4934 (2013).

183. Trasatti, S. & Buzzanca, G. Ruthenium dioxide: A new interesting electrode material. Solid state structure and electrochemical behaviour. *J. Electroanal. Chem.* **29**, (1971).

184. Kötz, R. XPS Studies of Oxygen Evolution on Ru and RuO[sub 2] Anodes. *J. Electrochem. Soc.* **130**, 825 (1983).

185. Hackwood, S., Schiavone, L. M. & Beni, G. Anodic Evolution of Oxygen on Sputtered Iridium Oxide Films. in *Proceedings - The Electrochemical Society* 198–208 (1982).

186. Slavcheva, E. *et al.* Sputtered iridium oxide films as electrocatalysts for water splitting via PEM electrolysis. *Electrochim. Acta* (2007). doi:10.1016/j.electacta.2006.11.005

187. Polonský, J. *et al.* Tantalum carbide as a novel support material for anode electrocatalysts in polymer electrolyte membrane water electrolysers. *Int. J. Hydrogen Energy* **37**, 2173–2181 (2012).

188. Butler, J. N., Giner, J. & Parry, J. M. Some topics in electrocatalysis. *Surf. Sci.* (1969). doi:10.1016/0039-6028(69)90272-6

189. <I>"Fuel Cell Today Industry Review 2011"</I>. *Platin. Met. Rev.* **55**, 268–270 (2011).

190. Adegoke, K. A. *et al.* Highly efficient formic acid and carbon dioxide electro-reduction to alcohols on indium oxide electrodes. *Sustain. Energy Fuels* (2020). doi:10.1039/d0se00623h

191. Comninellis, C. & Vercesi, G. P. Characterization of DSA®-type oxygen evolving electrodes: Choice of a coating. *J. Appl. Electrochem.* **21**, 335–345 (1991).

192. Ma, L., Sui, S. & Zhai, Y. Preparation and characterization of Ir/TiC catalyst for oxygen evolution. *J. Power Sources* **177**, 470–477 (2008).

193. Nikiforov, A. V., Tomás García, A. L., Petrushina, I. M., Christensen, E. & Bjerrum, N. J.

Preparation and study of IrO_2/SiC-Si supported anode catalyst for high temperature PEM steam electrolysers. *Int. J. Hydrogen Energy* **36**, 5797–5805 (2011).

194. Puthiyapura, V. K. *et al.* Investigation of supported IrO_2 as electrocatalyst for the oxygen evolution reaction in proton exchange membrane water electrolyser. *Int. J. Hydrogen Energy* **39**, 1905–1913 (2014).

195. Puthiyapura, V. K., Mamlouk, M., Pasupathi, S., Pollet, B. G. & Scott, K. Physical and electrochemical evaluation of ATO supported IrO_2 catalyst for proton exchange membrane water electrolyser. *J. Power Sources* **269**, 451–460 (2014).

196. Shaughnessy, C. I., Jantz, D. T. & Leonard, K. C. Selective electrochemical CO_2 reduction to CO using: In situ reduced In_2O_3 nanocatalysts. *J. Mater. Chem. A* **5**, 22743–22749 (2017).

197. Lefèvre, G. In situ Fourier-transform infrared spectroscopy studies of inorganic ions adsorption on metal oxides and hydroxides. *Advances in Colloid and Interface Science* **107**, 109–123 (2004).

198. Pander, J. E., Baruch, M. F. & Bocarsly, A. B. Probing the Mechanism of Aqueous CO_2 Reduction on Post-Transition-Metal Electrodes using ATR-IR Spectroelectrochemistry. *ACS Catal.* **6**, 7824–7833 (2016).

199. White, J. L. & Bocarsly, A. B. Enhanced Carbon Dioxide Reduction Activity on Indium-Based Nanoparticles. *J. Electrochem. Soc.* **163**, H410–H416 (2016).

200. Rosen, J. *et al.* Electrodeposited Zn Dendrites with Enhanced CO Selectivity for Electrocatalytic CO_2 Reduction. *ACS Catal.* (2015). doi:10.1021/acscatal.5b00922

201. Pan, Y. X. *et al.* Photocatalytic CO_2 Reduction by Carbon-Coated Indium-Oxide Nanobelts. *J. Am. Chem. Soc.* **139**, 4123–4129 (2017).

202. Xie, H. *et al.* Boosting Tunable Syngas Formation via Electrochemical CO_2 Reduction on Cu/In2O3 Core/Shell Nanoparticles. *ACS Appl. Mater. Interfaces* (2018). doi:10.1021/acsami.8b12747

203. Rasul, S. *et al.* A highly selective copper-indium bimetallic electrocatalyst for the electrochemical reduction of aqueous CO_2 to CO. *Angew. Chemie - Int. Ed.* **54**, 2146–2150 (2015).

204. Jedidi, A., Rasul, S., Masih, D., Cavallo, L. & Takanabe, K. Generation of Cu-In alloy surfaces from $CuInO_2$ as selective catalytic sites for CO_2 electroreduction. *J. Mater. Chem. A* (2015). doi:10.1039/c5ta05669a

205. Larrazábal, G. O., Martín, A. J., Mitchell, S., Hauert, R. & Pérez-Ramírez, J. Enhanced Reduction of CO_2 to CO over Cu-In Electrocatalysts: Catalyst Evolution Is the Key. *ACS Catal.* **6**, 6265–6274 (2016).

206. Larrazábal, G. O., Martín, A. J., Mitchell, S., Hauert, R. & Pérez-Ramírez, J. Synergistic effects in silver–indium electrocatalysts for carbon dioxide reduction. *J. Catal.* **343**, 266–277 (2016).

207. Hori, Y., Wakebe, H., Tsukamoto, T. & Koga, O. Electrocatalytic process of CO selectivity in electrochemical reduction of CO_2 at metal electrodes in aqueous media. *Electrochim. Acta* **39**, 1833–1839 (1994).

208. Ikeda, S., Takagi, T. & Ito, K. Selective formation of formic acid, oxalic acid, and carbon monoxide by electrochemical reduction of carbon dioxide. *Bull. Chem. Soc. Jpn.* **60**, 2517–2522 (1987).

209. Hori, Y. Electrochemical CO_2 Reduction on Metal Electrodes. in *Modern Aspects of Electrochemistry* 89–189 (2008). doi:10.1007/978-0-387-49489-0_3

210. Todoroki, M., Hara, K., Kudo, A. & Sakata, T. Electrochemical reduction of high pressure CO_2 at Pb, Hg and In electrodes in an aqueous $KHCO_3$ solution. *J. Electroanal. Chem.* (1995). doi:10.1016/0022-0728(95)04010-L

211. Hernández, S. *et al.* Syngas production from electrochemical reduction of CO_2 : Current status and prospective implementation. *Green Chem.* **19**, 2326–2346 (2017).

212. Brajter-Toth, A. Electrochemistry for Chemists, 2nd ed By Donald Sawyer (Texas A&M University), Andrzej Sobkowiak (Rzeszow University of Technology), and Julian L. Roberts, Jr. (University of Redlands). Wiley: New York. 1995. xv + 505 pp. ISBN 0-471-59468-7. *J. Am. Chem. Soc.* (2002). doi:10.1021/ja955400e

213. Sawyer, D. T. T. A. M. U. & Roberts, J. L. J. U. O. R. ELECTROCHEMISTRY FOR CHEMISTS Second Edition. *JOHN WILEY SONS INC* (1994).

214. Pan, X. *et al.* Enhanced ethanol production inside carbon-nanotube reactors containing catalytic particles. *Nat. Mater.* **6**, 507–511 (2007).

215. Speiser, B. Molecular electrochemistry. *Analytical and Bioanalytical Chemistry* **372**, (THE UNIVERSITY OF HULL Molecular, 2002).

216. Meijer, E. W. Jacobus Henricus van 't Hoff; Hundred Years of Impact on Stereochemistry in the Netherlands. *Angew. Chemie Int. Ed.* **40**, 3783–3789 (2002).

217. Van Houten, J. A Century of Chemical Dynamics Traced through the Nobel Prizes. 1909: Wilhelm Ostwald. *J. Chem. Educ.* **79**, 146 (2009).

218. Chen, Y., Li, C. W. & Kanan, M. W. Aqueous CO_2 reduction at very low overpotential on oxide-derived au nanoparticles. *J. Am. Chem. Soc.* **134**, 19969–19972 (2012).

219. Hori, Y. CO_2 reduction, catalyzed by metal electrodes . *Handb. Fuel Cells* (2010). doi:10.1002/9780470974001.f207055

220. Manthiram, K., Beberwyck, B. J. & Alivisatos, A. P. Enhanced electrochemical methanation of carbon dioxide with a dispersible nanoscale copper catalyst. *J. Am. Chem. Soc.* **136**, 13319–13325 (2014).

221. Rosen, J. *et al.* Mechanistic Insights into the Electrochemical Reduction of CO_2 to CO on Nanostructured Ag Surfaces. *ACS Catal.* **5**, 4293–4299 (2015).

222. Lu, Q. & Jiao, F. Electrochemical CO_2 reduction: Electrocatalyst, reaction mechanism, and process engineering. *Nano Energy* **29**, 439–456 (2016).

223. Allen J. Bard and Larry R. Faulkner. *A Electrochemical Methods: Fundamentals and Applications, New York: Wiley, 2001, 2nd ed. Russian Journal of Electrochemistry* (2002). doi:10.1023/A:1021637209564

224. Heusler, K. E. E. Gileadi; electrode kinetics for chemists, chemical engineers and material scientists. VCH, Weinheim, New York, Basel, Cambridge, Tokyo 1993, ISBN 3-527-89561-2, 597 S., *Berichte der Bunsengesellschaft für Phys. Chemie* **98**, 644–645 (1994).

225. Liu, Z. *et al.* Thickness controllable and mass produced WC@C@Pt hybrid for efficient hydrogen production. *Energy Storage Mater.* **10**, 268–274 (2018).

226. Zsigmondy, R. Kolloidchemie Ein Lehrbuch. *Kolloidchem. Ein Lehrb.* (1912). doi:10.1007/978-3-662-33915-2

227. Patterson, A. L. The scherrer formula for X-ray particle size determination. *Phys. Rev.* (1939). doi:10.1103/PhysRev.56.978

228. Park, G. G. *et al.* Effect of PTFE contents in the gas diffusion media on the performance of PEMFC. *J. Power Sources* **131**, 182–187 (2004).

229. Chi, B. *et al.* Tuning hydrophobic-hydrophilic balance of cathode catalyst layer to improve cell performance of proton exchange membrane fuel cell (PEMFC) by mixing

polytetrafluoroethylene (PTFE). *Electrochim. Acta* **277**, 110–115 (2018).

230. Velayutham, G., Kaushik, J., Rajalakshmi, N. & Dhathathreyan, K. S. Effect of PTFE content in gas diffusion media and microlayer on the performance of PEMFC tested under ambient pressure. *Fuel Cells* **7**, 314–318 (2007).

231. Dufek, E. J., Lister, T. E. & McIlwain, M. E. Influence of Electrolytes and Membranes on Cell Operation for Syn-Gas Production. *Electrochem. Solid-State Lett.* **15**, B48 (2012).

232. Nicholson, R. S. & Shain, I. Theory of Stationary Electrode Polarography: Single Scan and Cyclic Methods Applied to Reversible, Irreversible, and Kinetic Systems. *Anal. Chem.* **36**, 706–723 (1964).

233. Bard, A. & Faulkner, L. Allen J. Bard and Larry R. Faulkner, Electrochemical Methods: Fundamentals and Applications, New York: Wiley, 2001. *Russ. J. Electrochem.* (2002). doi:10.1023/A:1021637209564

234. Bewick, A. & Kunimatsu, K. Infra red spectroscopy of the electrode-electrolyte interphase. *Surf. Sci.* **101**, 131–138 (1980).

235. Ye, J. Y., Jiang, Y. X., Sheng, T. & Sun, S. G. In-situ FTIR spectroscopic studies of electrocatalytic reactions and processes. *Nano Energy* **29**, 414–427 (2016).

236. Zhou, Z. Y., Lin, S. C., Chen, S. P. & Sun, S. G. In situ step-scan time-resolved microscope FTIR spectroscopy working with a thin-layer cell. *Electrochem. commun.* **7**, 490–495 (2005).

237. Mojet, B. L., Ebbesen, S. D. & Lefferts, L. Light at the interface: The potential of attenuated total reflection infrared spectroscopy for understanding heterogeneous catalysis in water. *Chemical Society Reviews* **39**, 4643–4655 (2010).

238. Yajima, T., Uchida, H. & Watanabe, M. In-situ ATR-FTIR spectroscopic study of electro-

oxidation of methanol and adsorbed CO at Pt-Ru alloy. *J. Phys. Chem. B* **108**, 2654–2659 (2004).

239. Wang, Y., Jiang, K. & Cai, W. Bin. Enhanced electrocatalysis of ethanol on dealloyed Pd-Ni-P film in alkaline media: An infrared spectroelectrochemical investigation. *Electrochim. Acta* **162**, 100–107 (2015).

240. Yan, Y. G. *et al.* Study of CO oxidation on polycrystalline Pt electrodes in acidic solution by ATR-SEIRAS. *J. Phys. Chem. C* **115**, 16378–16388 (2011).

241. Kunimatsu, K., Uchida, H., Osawa, M. & Watanabe, M. In situ infrared spectroscopic and electrochemical study of hydrogen electro-oxidation on Pt electrode in sulfuric acid. *J. Electroanal. Chem.* **587**, 299–307 (2006).

242. Kunimatsu, K., Yoda, T., Tryk, D. A., Uchida, H. & Watanabe, M. In situ ATR-FTIR study of oxygen reduction at the Pt/Nafion interface. *Phys. Chem. Chem. Phys.* **12**, 621–629 (2010).

243. Faguy, P. W. & Fawcett, W. R. Infrared reflection-absorption spectroscopy of the electrode/electrolyte solution interface. Optical considerations. *Appl. Spectrosc.* **44**, 1309–1316 (1990).

244. Pons, S. The use of fourier transform infrared spectroscopy for in situ recording of species in the electrode-electrolyte solution interphase. *J. Electroanal. Chem.* **150**, 495–504 (1983).

245. Pons, S., Davidson, T. & Bewick, A. Vibrational spectroscopy of the electrode-electrolyte interface. Part IV. Fourier transform infrared spectroscopy: Experimental considerations. *J. Electroanal. Chem.* **160**, 63–71 (1984).

246. Corrigan, D. S., Leung, L. W. H. & Weaver, M. J. Single Potential-Alteration Surface

Infrared Spectroscopy: Examination of Adsorbed Species Involved in Irreversible Electrode Reactions. *Anal. Chem.* **59**, 2252–2256 (1987).

247. Lin, W. F. & Sun, S. G. In situ FTIRS investigations of surface processes of Rh electrode - Novel observation of geminal adsorbates of carbon monoxide on Rh electrode in acid solution. *Electrochim. Acta* **41**, 803–809 (1996).

248. Nahir, T. M., Clark, R. A. & Bowden, E. F. Linear-Sweep Voltammetry of Irreversible Electron Transfer in Surface-Confined Species Using the Marcus Theory. *Anal. Chem.* **66**, 2595–2598 (1994).

249. Adams, R. & Shriner, R. L. Platinum oxide as a catalyst in the reduction of organic compounds. III. Preparation and properties of the oxide of platinum obtained by the fusion of chloroplatinic acid with sodium nitrate. *J. Am. Chem. Soc.* **45**, 2171–2179 (1923).

250. Song, S. *et al.* Electrochemical investigation of electrocatalysts for the oxygen evolution reaction in PEM water electrolyzers. *Int. J. Hydrogen Energy* **33**, 4955–4961 (2008).

251. Marshall, A., Børresen, B., Hagen, G., Tsypkin, M. & Tunold, R. Electrochemical characterisation of $Ir_xSn_{1-x}O_2$ powders as oxygen evolution electrocatalysts. *Electrochim. Acta* **51**, 3161–3167 (2006).

252. Cheng, J., Zhang, H., Ma, H., Zhong, H. & Zou, Y. Preparation of $Ir_{0.4}Ru_{0.6}Mo_xO_y$ for oxygen evolution by modified Adams' fusion method. *Int. J. Hydrogen Energy* **34**, 6609–6613 (2009).

253. Cheng, J., Zhang, H., Ma, H., Zhong, H. & Zou, Y. Study of carbon-supported IrO_2 and RuO_2 for use in the hydrogen evolution reaction in a solid polymer electrolyte electrolyzer. *Electrochim. Acta* **55**, 1855–1861 (2010).

254. Polonský, J., Mazúr, P., Paidar, M., Christensen, E. & Bouzek, K. Performance of a PEM

water electrolyser using a TaC-supported iridium oxide electrocatalyst. *Int. J. Hydrogen Energy* **39**, 3072–3078 (2014).

255. Karimi, F. & Peppley, B. A. Metal Carbide and Oxide Supports for Iridium-Based Oxygen Evolution Reaction Electrocatalysts for Polymer-Electrolyte-Membrane Water Electrolysis. *Electrochim. Acta* **246**, 654–670 (2017).

256. Wu, J., Sharma, P. P., Harris, B. H. & Zhou, X. D. Electrochemical reduction of carbon dioxide: IV dependence of the Faradaic efficiency and current density on the microstructure and thickness of tin electrode. *J. Power Sources* **258**, 189–194 (2014).

257. Wilson, M. S. & Gottesfeld, S. Thin-film catalyst layers for polymer electrolyte fuel cell electrodes. *J. Appl. Electrochem.* **22**, 1–7 (1992).

258. Wang, Q., Dong, H., Yu, H. H. & Yu, H. H. Enhanced performance of gas diffusion electrode for electrochemical reduction of carbon dioxide to formate by adding polytetrafluoroethylene into catalyst layer. *J. Power Sources* **279**, 1–5 (2015).

259. Dridi, H. *et al.* Catalysis and inhibition in the electrochemical reduction of CO_2 on platinum in the presence of protonated pyridine. New insights into mechanisms and products. *J. Am. Chem. Soc.* **139**, 13922–13928 (2017).

260. Polonský, J. *et al.* Tantalum carbide as a novel support material for anode electrocatalysts in polymer electrolyte membrane water electrolysers. *Int. J. Hydrogen Energy* **37**, 2173–2181 (2012).

261. Felix, C., Maiyalagan, T., Pasupathi, S., Bladergroen, B. & Linkov, V. Synthesis and Optimisation of IrO_2 Electrocatalysts by Adams Fusion Method for Solid Polymer Electrolyte Electrolysers. *Micro Nanosyst.* **4**, 186–191 (2012).

262. Al-Resheedi, A., Alhokbany, N. S. & Mahfouz, R. M. Radiation induced synthesis of

In_2O_3 nanoparticles - Part 1: Synthesis of In_2O_3 nanoparticles by sol-gel method using un-irradiated and γ-irradiated indium acetate. *Mater. Res.* **17**, 346–351 (2014).

263. Mazúr, P., Polonský, J., Paidar, M. & Bouzek, K. Non-conductive TiO_2 as the anode catalyst support for PEM water electrolysis. *Int. J. Hydrogen Energy* **37**, 12081–12088 (2012).

264. Nikiforov, A. V., Petrushina, I. M., Christensen, E., Tomás-García, A. L. & Bjerrum, N. J. Corrosion behaviour of construction materials for high temperature steam electrolysers. *Int. J. Hydrogen Energy* **36**, 111–119 (2011).

265. Wang, Q., Dong, H. & Yu, H. Development of rolling tin gas diffusion electrode for carbon dioxide electrochemical reduction to produce formate in aqueous electrolyte. *J. Power Sources* **271**, 278–284 (2014).

266. Albo, J., Sáez, A., Solla-Gullón, J., Montiel, V. & Irabien, A. Production of methanol from CO_2 electroreduction at Cu_2O and Cu_2O/ZnO-based electrodes in aqueous solution. *Appl. Catal. B Environ.* **4**, 59970–59976 (2014).

267. Lee, S. *et al.* Electrocatalytic reduction of gas-phased CO_2 on nano-sized Sn electrode surface. *ECS Trans.* **53**, 41–47 (2013).

268. MacHunda, R. L., Ju, H. & Lee, J. Electrocatalytic reduction of CO_2 gas at Sn based gas diffusion electrode. *Curr. Appl. Phys.* **11**, 986–988 (2011).

269. Eggins, B. R. B. R. & McNeill, J. Voltammetry of carbon dioxide. Part I. A general survey of voltammetry at different electrode materials in different solvents. *J. Electroanal. Chem.* (1983). doi:10.1016/S0022-0728(83)80127-2

270. Eggins, B. R., Bennett, E. M. & McMullan, E. A. A. Voltammetry of carbon dioxide. Part 2. Voltammetry in aqueous solutions on glassy carbon. *J. Electroanal. Chem.* **408**, 165–

171 (1996).

271. Albo, J., Beobide, G., Castaño, P. & Irabien, A. Methanol electrosynthesis from CO_2 at Cu_2O/ZnO prompted by pyridine-based aqueous solutions. *J. CO_2 Util.* **18**, 164–172 (2017).

272. Albo, J. & Irabien, A. Cu_2O-loaded gas diffusion electrodes for the continuous electrochemical reduction of CO_2 to methanol. *J. Catal.* **343**, 232–239 (2016).

273. Wang, Q., Dong, H. & Yu, H. Fabrication of a novel tin gas diffusion electrode for electrochemical reduction of carbon dioxide to formic acid. *RSC Adv.* **4**, 59970–59976 (2014).

274. Wang, Q. *et al.* Electrodeposition of tin on Nafion-bonded carbon black as an active catalyst layer for efficient electroreduction of CO_2 to formic acid. *Sci. Rep.* **7**, (2017).

275. Wang, Q., Dong, H. & Yu, H. Development of rolling tin gas diffusion electrode for carbon dioxide electrochemical reduction to produce formate in aqueous electrolyte. *J. Power Sources* **271**, 278–284 (2014).

276. Ma, C., Zhang, L., Mukerjee, S., Ofer, D. & Nair, B. An investigation of proton conduction in select PEM's and reaction layer interfaces-designed for elevated temperature operation. *J. Memb. Sci.* **219**, 123–136 (2003).

277. Čejka, J., Corma, A. & Zones, S. *Zeolites and Catalysis: Synthesis, Reactions and Applications*. *Zeolites and Catalysis: Synthesis, Reactions and Applications* **1**–**2**, (2010).

278. Cruz, J. C. *et al.* Nanosized IrO_2 electrocatalysts for oxygen evolution reaction in an SPE electrolyzer. *J. Nanoparticle Res.* **13**, 1639–1646 (2011).

279. Polonský, J., Mazúr, P., Paidar, M. & Bouzek, K. Investigation of β-SiC as an anode catalyst support for PEM water electrolysis. *J. Solid State Electrochem.* **18**, 2325–2332

(2014).

280. Bitar, Z., Fecant, A., Trela-Baudot, E., Chardon-Noblat, S. & Pasquier, D. Electrocatalytic reduction of carbon dioxide on indium coated gas diffusion electrodes-Comparison with indium foil. *Appl. Catal. B Environ.* **189**, 172–180 (2016).

281. Kaneco, S. *et al.* Electrochemical Reduction of Carbon Dioxide on an Indium Wire in a KOH/Methanol-Based Electrolyte at Ambient Temperature and Pressure. *Environ. Eng. Sci.* **16**, 131–137 (1999).

282. Schizodimou, A., Kotoulas, I. & Kyriacou, G. Electrochemical reduction of formic acid through its decarbonylation in phosphoric acid solution. *Electrochim. Acta* **210**, 236–239 (2016).

283. Qiu, Y. L. *et al.* Selective Electrochemical Reduction of Carbon Dioxide Using Cu Based Metal Organic Framework for CO_2 Capture. *ACS Appl. Mater. Interfaces* **10**, 2480–2489 (2018).

284. Lee, S. *et al.* Sustainable production of formic acid by electrolytic reduction of gaseous carbon dioxide. *J. Mater. Chem. A* **3**, 3029–3034 (2015).

285. Choi, S. Y., Jeong, S. K., Kim, H. J., Baek, I. H. & Park, K. T. Electrochemical Reduction of Carbon Dioxide to Formate on Tin-Lead Alloys. *ACS Sustain. Chem. Eng.* **4**, 1311–1318 (2016).

286. Kim, B., Hillman, F., Ariyoshi, M., Fujikawa, S. & Kenis, P. J. A. Effects of composition of the micro porous layer and the substrate on performance in the electrochemical reduction of CO_2 to CO. *J. Power Sources* **312**, 192–198 (2016).

287. Wu, J. *et al.* A metal-free electrocatalyst for carbon dioxide reduction to multi-carbon hydrocarbons and oxygenates. *Nat. Commun.* **7**, 1–6 (2016).

288. Lu, Q. *et al.* A selective and efficient electrocatalyst for carbon dioxide reduction. *Nat. Commun.* **5**, 1–6 (2014).

289. Schrebler, R., Cury, P., Herrera, F., Gómez, H. & Córdova, R. Study of the electrochemical reduction of CO_2 on electrodeposited rhenium electrodes in methanol media. *J. Electroanal. Chem.* **516**, 23–30 (2001).

290. Kim, J. J., Summers, D. P. & Frese, K. W. Reduction of CO_2 and CO to methane on Cu foil electrodes. *J. Electroanal. Chem.* **245**, 223–244 (1988).

291. Wu, J., Risalvato, F. G., Ma, S. & Zhou, X.-D. D. Electrochemical reduction of carbon dioxide III. the role of oxide layer thickness on the performance of Sn electrode in a full electrochemical cell. *J. Mater. Chem. A* **2**, 1647–1651 (2014).

292. Wang, Q., Dong, H. & Yu, H. Development of rolling tin gas diffusion electrode for carbon dioxide electrochemical reduction to produce formate in aqueous electrolyte. *J. Power Sources* **271**, 278–284 (2014).

293. Wang, Q., Dong, H. & Yu, H. Fabrication of a novel tin gas diffusion electrode for electrochemical reduction of carbon dioxide to formic acid. *RSC Adv.* **4**, 59970–59976 (2014).

294. Wang, X. *et al.* High catalytic activity of ultrafine nanoporous palladium for electro-oxidation of methanol, ethanol, and formic acid. *Electrochem. commun.* **11**, 1896–1899 (2009).

295. Huang, X. *et al.* Freestanding palladium nanosheets with plasmonic and catalytic properties. *Nat. Nanotechnol.* **6**, 28–32 (2011).

296. Shinagawa, T., Garcia-Esparza, A. T. & Takanabe, K. Insight on Tafel slopes from a microkinetic analysis of aqueous electrocatalysis for energy conversion. *Sci. Rep.* **5**,

(2015).

297. Ryu, J., Andersen, T. N. & Eyring, H. The electrode reduction kinetics of carbon dioxide in aqueous solution. *J. Phys. Chem.* **76**, 3278–3286 (1972).

298. Buchholz, D. B. *et al.* The structure and properties of amorphous indium oxide. *Chem. Mater.* **26**, 5401–5411 (2014).

299. Thomele, D., Bourret, G. R., Bernardi, J., Bockstedte, M. & Diwald, O. Hydroxylation Induced Alignment of Metal Oxide Nanocubes. *Angew. Chemie - Int. Ed.* **56**, 1407–1410 (2017).

300. Thomele, D. *et al.* Thin water films and particle morphology evolution in nanocrystalline MgO. *J. Am. Ceram. Soc.* **101**, 4994–5003 (2018).

301. Grassian, V. H. Surface science of complex environmental interfaces: Oxide and carbonate surfaces in dynamic equilibrium with water vapor. *Surface Science* **602**, 2955–2962 (2008).

302. Bourret, G. R. & Diwald, O. Thin water films covering oxide nanomaterials: Stability issues and influences on materials processing. *J. Mater. Res.* (2019). doi:10.1557/jmr.2018.429

303. Cottrell, F. G. Der Reststrom bei galvanischer Polarisation, betrachtet als ein Diffusionsproblem. *Zeitschrift für Phys. Chemie* **42U**, 385–431 (1903).

304. Kumar, R., Agrawal, A., Bhuvana, T. & Sharma, A. Porous indium oxide hollow spheres (PIOHS) for asymmetric electrochemical supercapacitor with excellent cycling stability. *Electrochim. Acta* **270**, 87–95 (2018).

305. Dam, D. T. & Lee, J. M. Capacitive behavior of mesoporous manganese dioxide on indium-tin oxide nanowires. *Nano Energy* **2**, 933–942 (2013).

306. Vargas, A. M. M., Cazetta, A. L., Kunita, M. H., Silva, T. L. & Almeida, V. C. Adsorption of methylene blue on activated carbon produced from flamboyant pods (Delonix regia): Study of adsorption isotherms and kinetic models. *Chem. Eng. J.* (2011). doi:10.1016/j.cej.2011.01.067

307. Chang, J., Lee, W., Mane, R. S., Cho, B. W. & Han, S. H. Morphology-dependent electrochemical supercapacitor properties of indium oxide. *Electrochem. Solid-State Lett.* **11**, A9–A11 (2008).

308. Fabregat-Santiago, F., Mora-Seró, I., Garcia-Belmonte, G. & Bisquert, J. Cyclic voltammetry studies of nanoporous semiconductors. Capacitive and reactive properties of nanocrystalline TiO_2 electrodes in aqueous electrolyte. *J. Phys. Chem. B* **107**, 758–768 (2003).

309. Bockris, J. Electrochemical methods — Fundamentals and applications Allen J. Bard and Larry R. Faulkner, Wiley, New York, 1980, xviii + 718 pp., *J. Electroanal. Chem.* (1981). doi:10.1016/0368-1874(81)87163-8

310. Portenkirchner, E. *et al.* Electrocatalytic reduction of carbon dioxide to carbon monoxide by a polymerized film of an alkynyl-substituted Rhenium(I) complex. *ChemCatChem* **5**, 1790–1796 (2013).

311. Holze, R. Elektrochemie. C. H. Hamann, W. Vielstich Wiley-VCH Verlagsgesellschaft mbH, Weinheim 1998, 602 S., 301 Abb., 35 Tab., brosch., ISBN 3-527-27894-X. *Chemie Ing. Tech. - CIT* (2004). doi:10.1002/cite.330711024

312. Miles, M. H., Fletcher, A. N., McManis, G. E. & Spreer, L. O. The electrochemical conversion of carbon dioxide into methanol. The formic acid reduction step in acidic solutions. *J. Electroanal. Chem.* **190**, 157–170 (1985).

313. Bohlen, B., Wastl, D., Radomski, J., Sieber, V. & Vieira, L. Electrochemical CO_2 reduction to formate on indium catalysts prepared by electrodeposition in deep eutectic solvents. *Electrochem. commun.* **110**, 1–13 (2019).

314. Laviron, E. General expression of the linear potential sweep voltammogram in the case of diffusionless electrochemical systems. *J. Electroanal. Chem.* **101**, 19–28 (1979).

315. Wang, L. *et al.* Room-Temperature Activation of H_2 by a Surface Frustrated Lewis Pair. *Angew. Chemie - Int. Ed.* **58**, 9501–9505 (2019).

316. Wu, J. *et al.* Electrochemical Reduction of Carbon Dioxide: II. Design, Assembly, and Performance of Low Temperature Full Electrochemical Cells. *J. Electrochem. Soc.* **160**, F953–F957 (2013).

317. Fu, Y. *et al.* Novel hierarchical SnO_2 microsphere catalyst coated on gas diffusion electrode for enhancing energy efficiency of CO_2 reduction to formate fuel. *Appl. Energy* **175**, 536–544 (2016).

318. Kitahara, T., Nakajima, H. & Okamura, K. Gas diffusion layers coated with a microporous layer containing hydrophilic carbon nanotubes for performance enhancement of polymer electrolyte fuel cells under both low and high humidity conditions. *J. Power Sources* **283**, 115–124 (2015).

319. Kitahara, T., Nakajima, H., Inamoto, M. & Morishita, M. Novel hydrophilic and hydrophobic double microporous layer coated gas diffusion layer to enhance performance of polymer electrolyte fuel cells under both low and high humidity. *J. Power Sources* **234**, 129–138 (2013).

320. Avcioglu, G. S., Ficicilar, B. & Eroglu, I. Influence of FEP nanoparticles in catalyst layer on water management and performance of PEM fuel cell with high Pt loading. *Int. J.*

Hydrogen Energy **42**, 496–506 (2017).

321. Xiong, Z. *et al.* Enhanced water management in the cathode of an air-breathing PEMFC using a dual catalyst layer and optimizing the gas diffusion and microporous layers. *Int. J. Hydrogen Energy* **40**, 3961–3967 (2015).

322. Li, A., Han, M., Chan, S. H. & Nguyen, N. Effects of hydrophobicity of the cathode catalyst layer on the performance of a PEM fuel cell. *Electrochim. Acta* **55**, 2706–2711 (2010).

323. Choun, M., Nauryzbayev, D., Shin, D. & Lee, J. Polydimethylsiloxane treated cathode catalyst layer to prolong hydrogen fuel cell lifetime. *Catal. Today* **262**, 155–160 (2016).

324. Öztürk, A., Fıçıcılar, B., Eroğlu, İ. & Bayrakçeken Yurtcan, A. Facilitation of water management in low Pt loaded PEM fuel cell by creating hydrophobic microporous layer with PTFE, FEP and PDMS polymers: Effect of polymer and carbon amounts. *Int. J. Hydrogen Energy* **42**, 21226–21249 (2017).

325. Wang, Y., Wang, L., Advani, S. G. & Prasad, A. K. Double-layer gas diffusion media for improved water management in polymer electrolyte membrane fuel cells. *J. Power Sources* **292**, 39–48 (2015).

326. Kuhl, K. P., Cave, E. R., Abram, D. N. & Jaramillo, T. F. New insights into the electrochemical reduction of carbon dioxide on metallic copper surfaces. *Energy Environ. Sci.* **5**, 7050–7059 (2012).

327. Liao, F. *et al.* Morphology-dependent interactions of ZnO with Cu nanoparticles at the materials' interface in selective hydrogenation of CO_2 to CH_3OH. *Angew. Chemie - Int. Ed.* **50**, 2162–2165 (2011).

328. Narayanan, R. & El-Sayed, M. A. Catalysis with transition metal nanoparticles in

colloidal solution: Nanoparticle shape dependence and stability. *J. Phys. Chem. B* **109**, 12663–12676 (2005).

329. Gao, J. *et al.* Highly Selective and Efficient Electroreduction of Carbon Dioxide to Carbon Monoxide with Phosphate Silver-Derived Coral-like Silver. *ACS Sustain. Chem. Eng.* **7**, 3536–3543 (2019).

330. Li, A., Chan, S. H. & Nguyen, N. Anti-flooding cathode catalyst layer for high performance PEM fuel cell. *Electrochem. commun.* **11**, 897–900 (2009).

331. Ohta, K., Kawamoto, M., Mizuno, T. & Lowy, D. A. Electrochemical reduction of carbon dioxide in methanol at ambient temperature and pressure. *J. Appl. Electrochem.* **28**, 717–724 (1998).

332. Hori, Y., Kikuchi, K. & Suzuki, S. Production of CO and CH_4 in Electrochemical Reduction of CO_2 At Metal Electrodes in Aqueous Hydrogencarbonate Solution . *Chem. Lett.* **14**, 1695–1698 (1985).

333. Hori, Y., Takahashi, I., Koga, O. & Hoshi, N. Electrochemical reduction of carbon dioxide at various series of copper single crystal electrodes. *J. Mol. Catal. A Chem.* **199**, 39–47 (2003).

334. Hori, Y., Takahashi, I., Koga, O. & Hoshi, N. Selective formation of C_2 compounds from electrochemical reduction of CO_2 at a series of copper single crystal electrodes. *J. Phys. Chem. B* **106**, 15–17 (2002).

335. Khezri, B., Fisher, A. C. & Pumera, M. CO_2 reduction: The quest for electrocatalytic materials. *Journal of Materials Chemistry A* **5**, 8230–8246 (2017).

336. Weng, Z. *et al.* Electrochemical CO_2 Reduction to Hydrocarbons on a Heterogeneous Molecular Cu Catalyst in Aqueous Solution. *J. Am. Chem. Soc.* **138**, 8076–8079 (2016).

337. Bewick, A. In-situ infrared spectroscopy of the electrode/electrolyte solution interphase. *J. Electroanal. Chem.* **150**, 481–493 (1983).

338. Wang, H., Zhou, Y. W. & Cai, W. Bin. Recent applications of in situ ATR-IR spectroscopy in interfacial electrochemistry. *Current Opinion in Electrochemistry* **1**, 73–79 (2017).

339. Li, X., Zhang, H. J., Li, H., Deng, C. & Yang, J. Evaluation of loading influence on catalytic performance of co-based catalyst for oxygen reduction. *ECS Electrochem. Lett.* **3**, (2014).

340. Luo, W., Xie, W., Li, M., Zhang, J. & Züttel, A. 3D hierarchical porous indium catalyst for highly efficient electroreduction of CO_2. *J. Mater. Chem. A* **7**, 4505–4515 (2019).

341. Xia, Z. *et al.* Highly Selective Electrochemical Conversion of CO_2 to HCOOH on Dendritic Indium Foams. *ChemElectroChem* **5**, 215 (2018).

342. Zhao, F., Slade, R. C. T. & Varcoe, J. R. Techniques for the study and development of microbial fuel cells: An electrochemical perspective. *Chem. Soc. Rev.* **38**, 1926–1939 (2009).

343. Zhou, M. & Heinze, J. Electropolymerization of pyrrole and electrochemical study of polypyrrole: 1. Evidence for structural diversity of polypyrrole. *Electrochim. Acta* **44**, 1733–1748 (1999).

344. West, R., Josowicz, M., Janata, J., Minet, I. & Hevesi, L. Controlled Electropolymerization of 1-Pyrrolyl-10-decanephosphonic Acid: An Anion Barrier Layer. *J. Electrochem. Soc.* **156**, F55 (2009).

345. Dequaire, M., Limoges, B., Moiroux, J. & Savéant, J. M. Mediated electrochemistry of horseradish peroxidase. Catalysis and inhibition. *J. Am. Chem. Soc.* **124**, 240–253 (2002).

346. Limoges, B., Savéant, J. M. & Yazidi, D. Quantitative analysis of catalysis and inhibition at horseradish peroxidase monolayers immobilized on an electrode surface. *J. Am. Chem. Soc.* **125**, 9192–9203 (2003).

347. Fox, M. A. & Akaba, R. Curve Crossing in the Cyclic Voltammetric Oxidation of 2-Phenylnorbornene. Evidence for an ECE Reaction Pathway. *J. Am. Chem. Soc.* **105**, 3460–3463 (1983).

348. Feldberg, S. W. Nuances of the ECE mechanism. III. Effects of homogeneous redox equilibrium in cyclic voltammetry. *J. Phys. Chem.* **75**, 2377–2380 (1971).

349. Houmam, A., Hamed, E. M. & Still, I. W. J. A unique autocatalytic process and evidence for a concerted-stepwise mechanism transition in the dissociative electron-transfer reduction of aryl thiocyanates. *J. Am. Chem. Soc.* **125**, 7258–7265 (2003).

350. Cindrella, L. *et al.* Gas diffusion layer for proton exchange membrane fuel cells-A review. *Journal of Power Sources* **194**, 146–160 (2009).

351. Roduner, E. Understanding catalysis. *Chemical Society Reviews* **43**, 8226–8239 (2014).

352. Giubertoni, G., Sofronov, O. O. & Bakker, H. J. Observation of Distinct Carboxylic Acid Conformers in Aqueous Solution. *J. Phys. Chem. Lett.* **10**, 3217–3222 (2019).

353. Chen, J., Brooks, C. L. & Scheraga, H. A. Revisiting the carboxylic acid dimers in aqueous solution: Interplay of hydrogen bonding, hydrophobic interactions and entropy. *J. Phys. Chem. B* **112**, 242–249 (2008).

354. Zhang, Y. *et al.* Structural analysis of transient reaction intermediate in formic acid dehydrogenation catalysis using two-dimensional IR spectroscopy. *Proc. Natl. Acad. Sci. U. S. A.* **115**, 12395–12400 (2018).

355. Susi, H. & Scheker, J. R. The normal vibrations of formic acid and methyl formate.

Spectrochim. Acta Part A Mol. Spectrosc. **25**, 1243–1263 (1969).

356. Baruch, M. F., Pander, J. E., White, J. L. & Bocarsly, A. B. Mechanistic Insights into the Reduction of CO_2 on Tin Electrodes using in Situ ATR-IR Spectroscopy. *ACS Catal.* **5**, 3148–3156 (2015).

357. Kautek, W., Conradi, A., Fabjan, C. & Bauer, G. In situ FTIR spectroscopy of the Zn-Br battery bromine storage complex at glassy carbon electrodes. *Electrochim. Acta* **47**, 815–823 (2001).

358. Huang, J. *et al.* Potential-induced nanoclustering of metallic catalysts during electrochemical CO_2 reduction. *Nat. Commun.* **9**, 1–9 (2018).

APPENDICES

Appendix A: List of other Figures and Tables

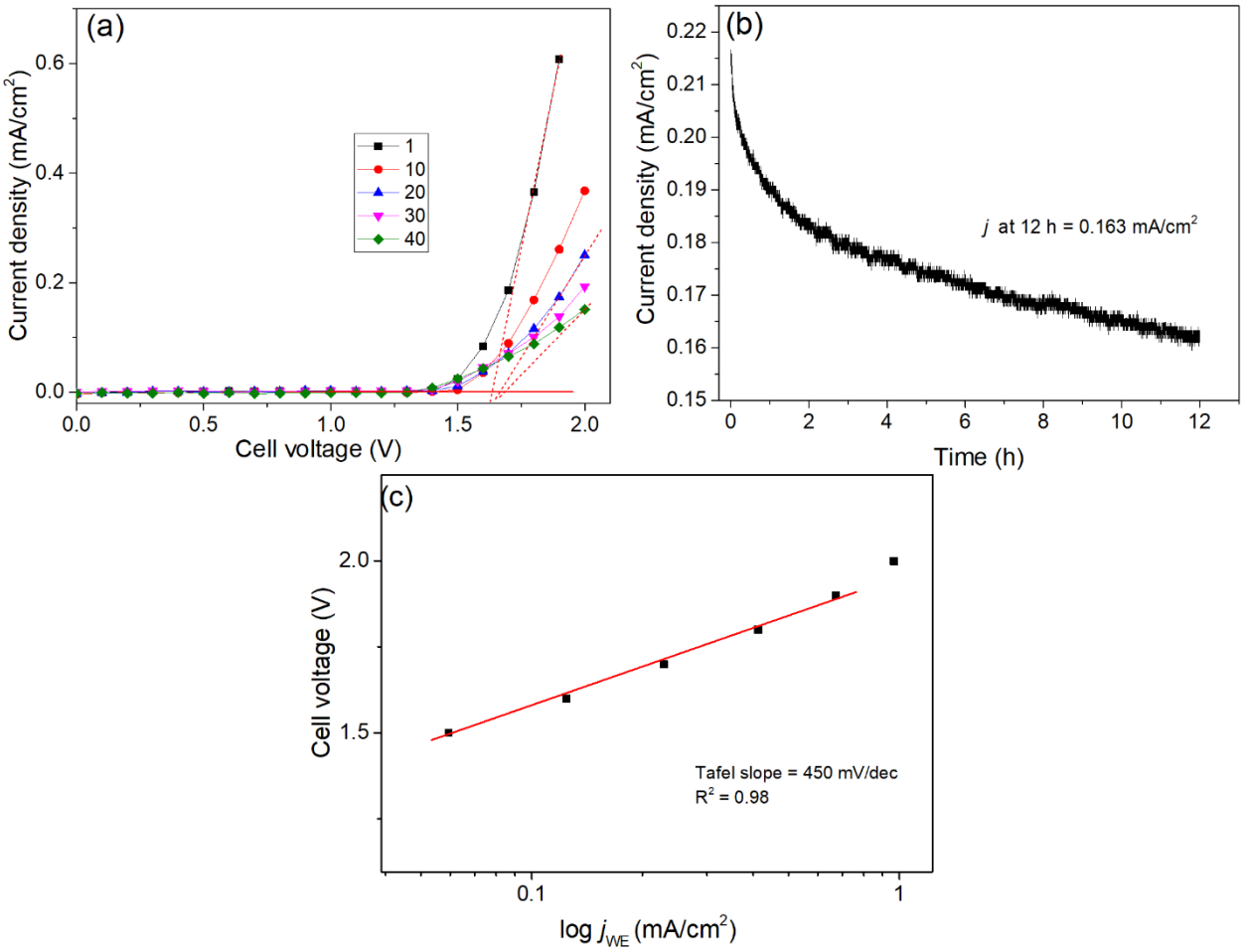

Fig. SI 1: (a) LSV for WE, (b) chronoamperometry of 60:40wt% IrO_2:TaC at 1.9 V, and (c) Tafel plot.

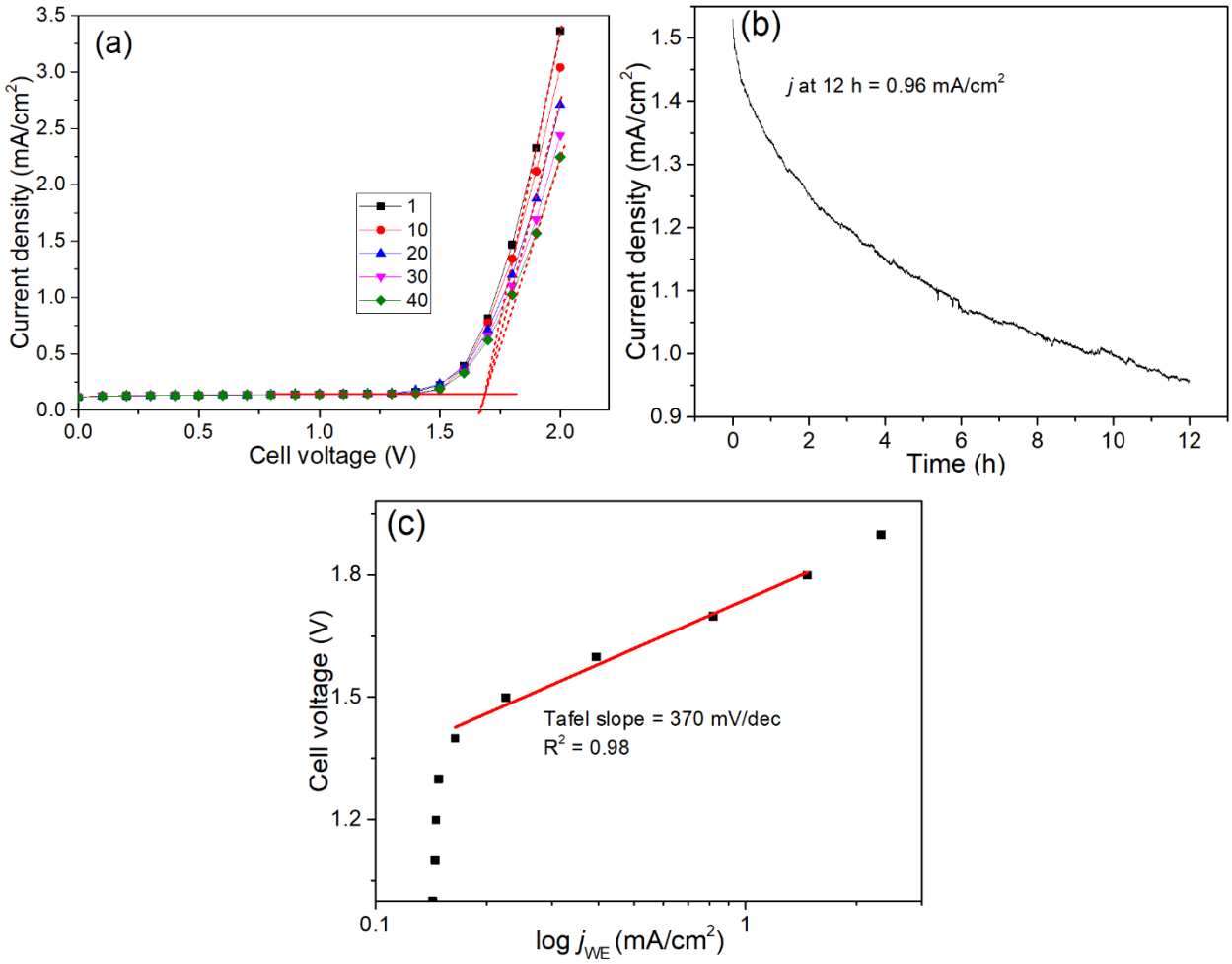

Fig. SI 2: (a) LSV for WE showing selected cycles, (b) chronoamperometry of 70:30 wt% IrO_2:TaC at 1.9 V with quoted end current density, and (c) Tafel plot.

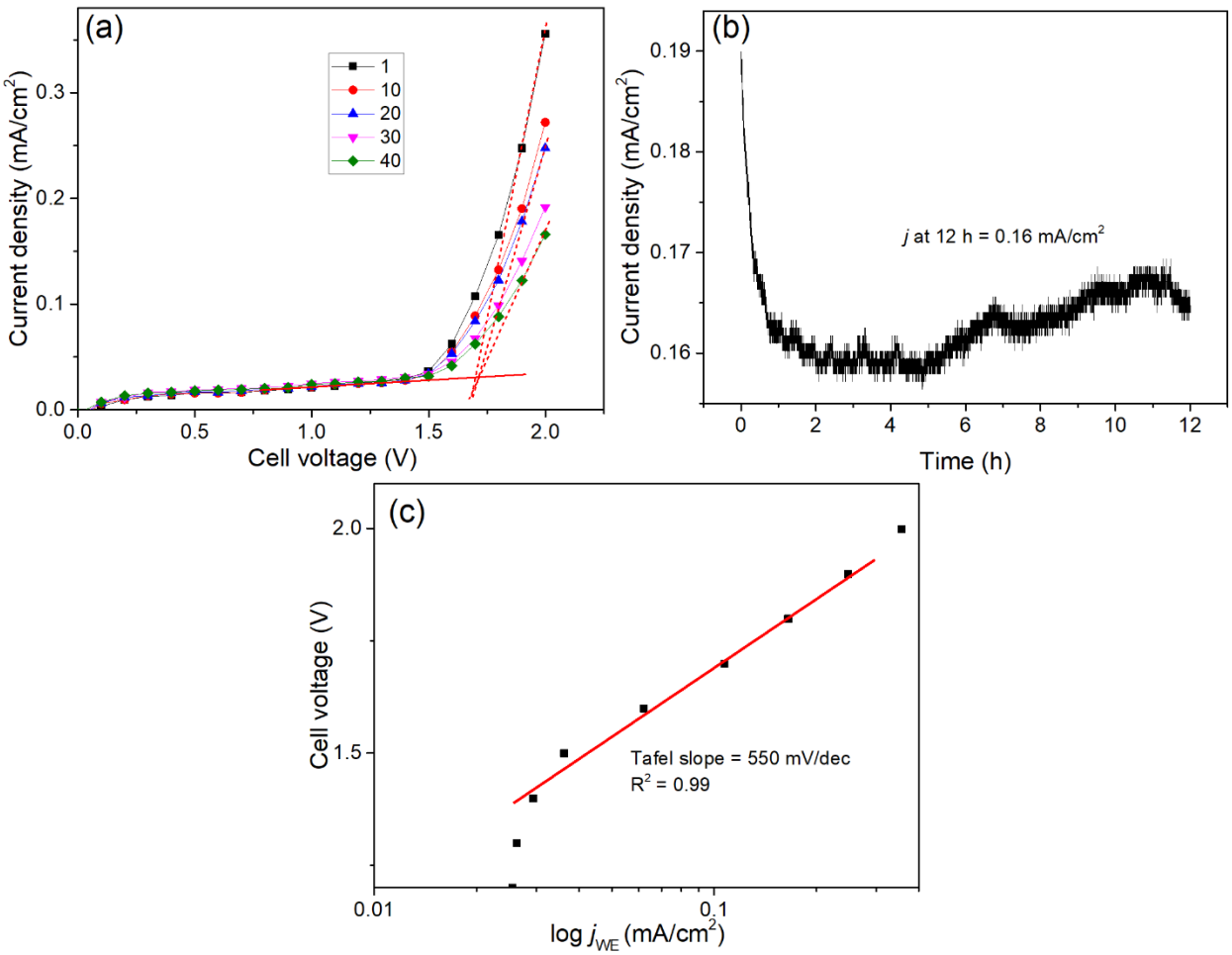

Fig. SI 3: (a) LSV for WE, (b) chronoamperometry of 100:00 wt% IrO_2:TaC at 1.9 V, and (c) Tafel plot.

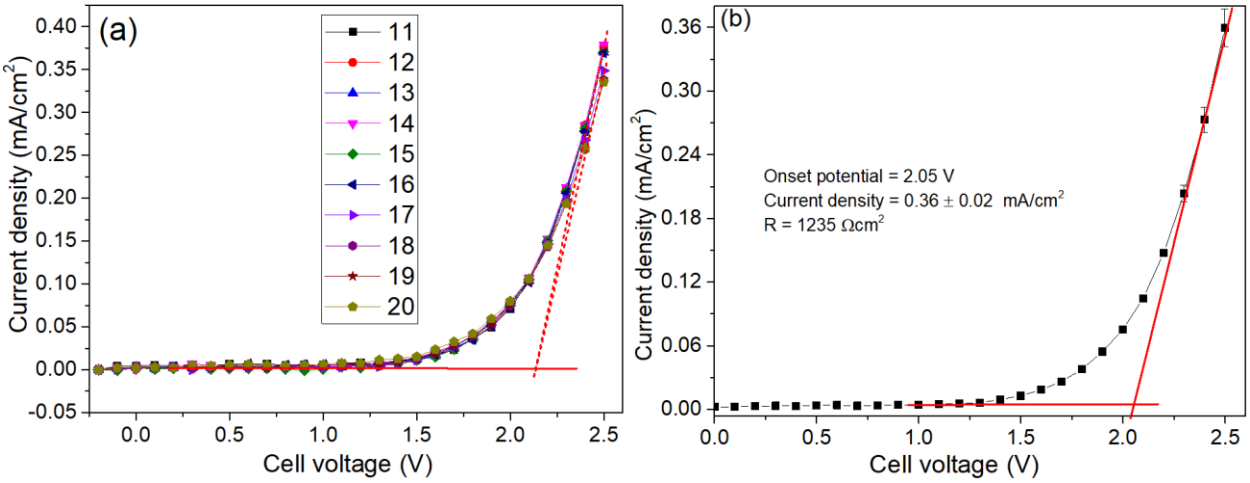

Fig. SI 4: LSV of FARR showing the fair stability of sample A between 9 and 16 cycles, (a) Current density picked at random and (b) averaged current density curve.

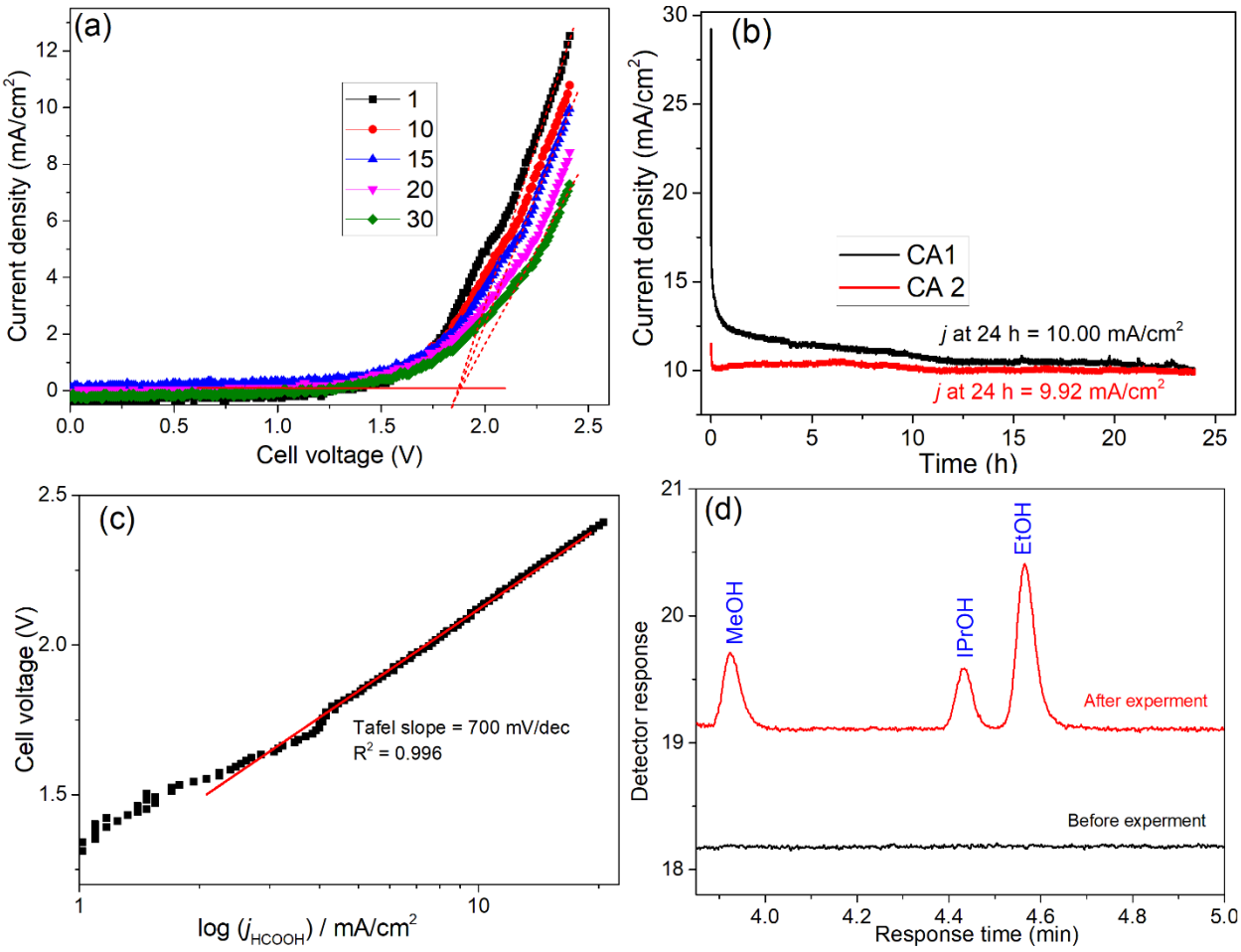

Fig. SI 5: LSV of FA reduction on 0.15 wt% PTFE-In_2O_3 cathode (anode: 60:40 wt% IrO_2:TaC catalyst loading of 2.5 mg/cm^2) for sample M: (a) Current density picked at random, (b) chronoamperometry at 2.4 V in the absence of any flow, (c) Tafel plot, and (d) liquid injected GC-FID chromatogram.

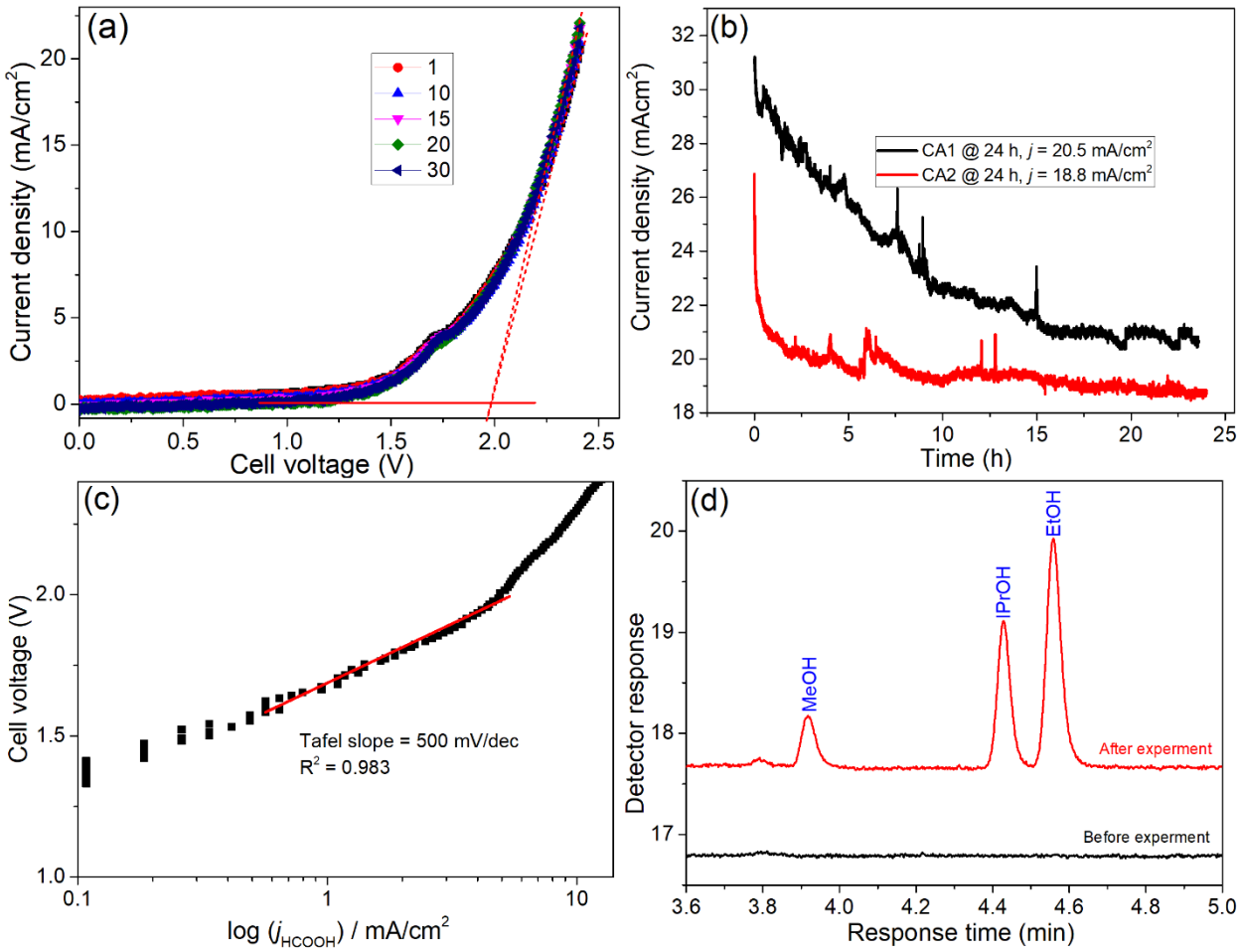

Fig. SI 6: LSV of FA reduction on 0.15 wt% PTFE-In_2O_3 cathode (anode: 70:30 wt IrO_2:TaC (catalyst loading of 2 mg/cm^2) for sample M: (a) Current density picked at random, (b) chronoamperometry at 2.4 V in the absence of any flow, (c) Tafel plot, and (d) liquid injected GC-FID chromatogram.

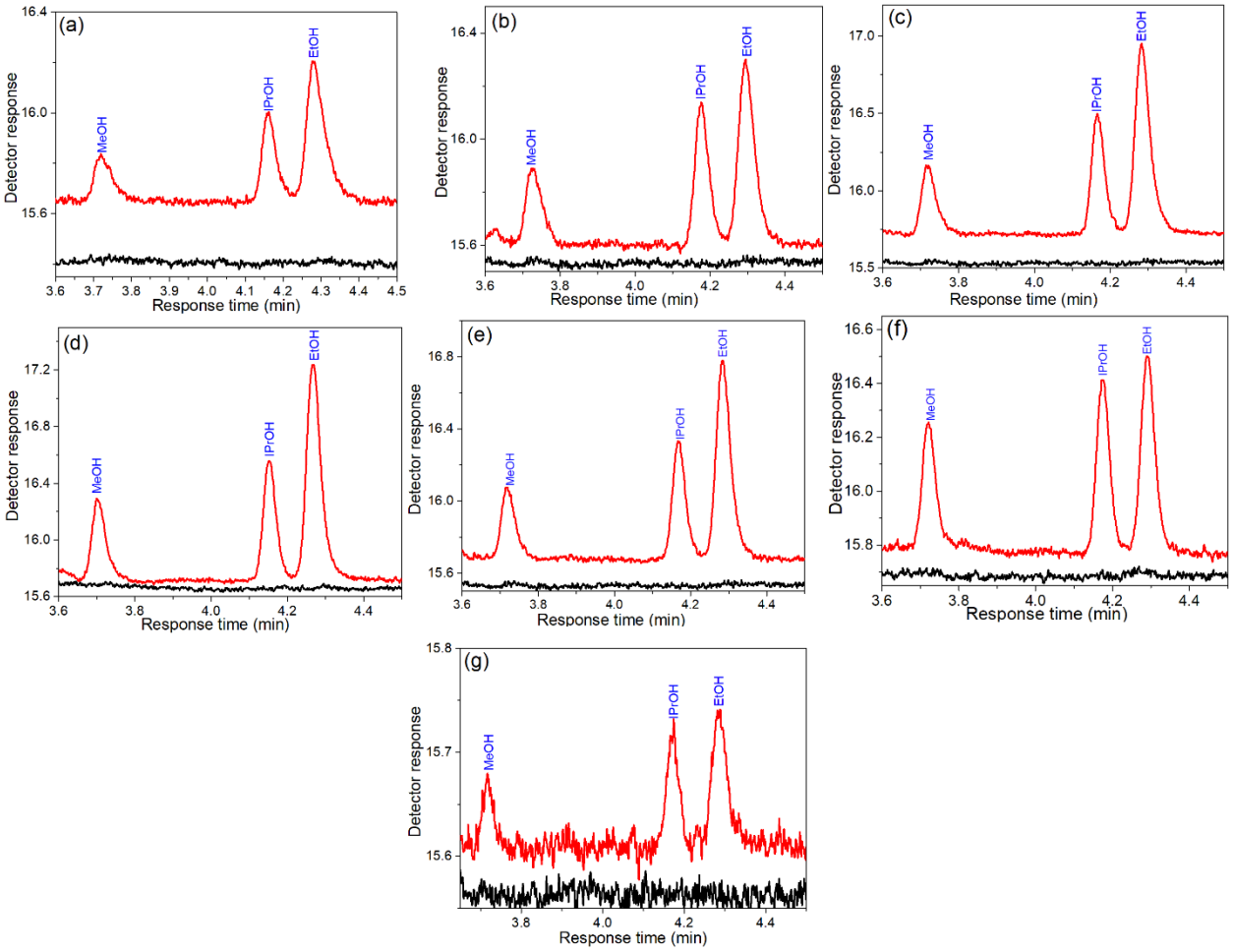

Fig. SI 7: Liquid injected GC-FID chromatogram at: (a) –2.0 V, (b) –2.5 V, (c) –3.0 V, (d) –3.5 V, (e) –4.0 V, (f) –4.5 V, and (g) –5.0 V [black and red lines are before and after the experiments].

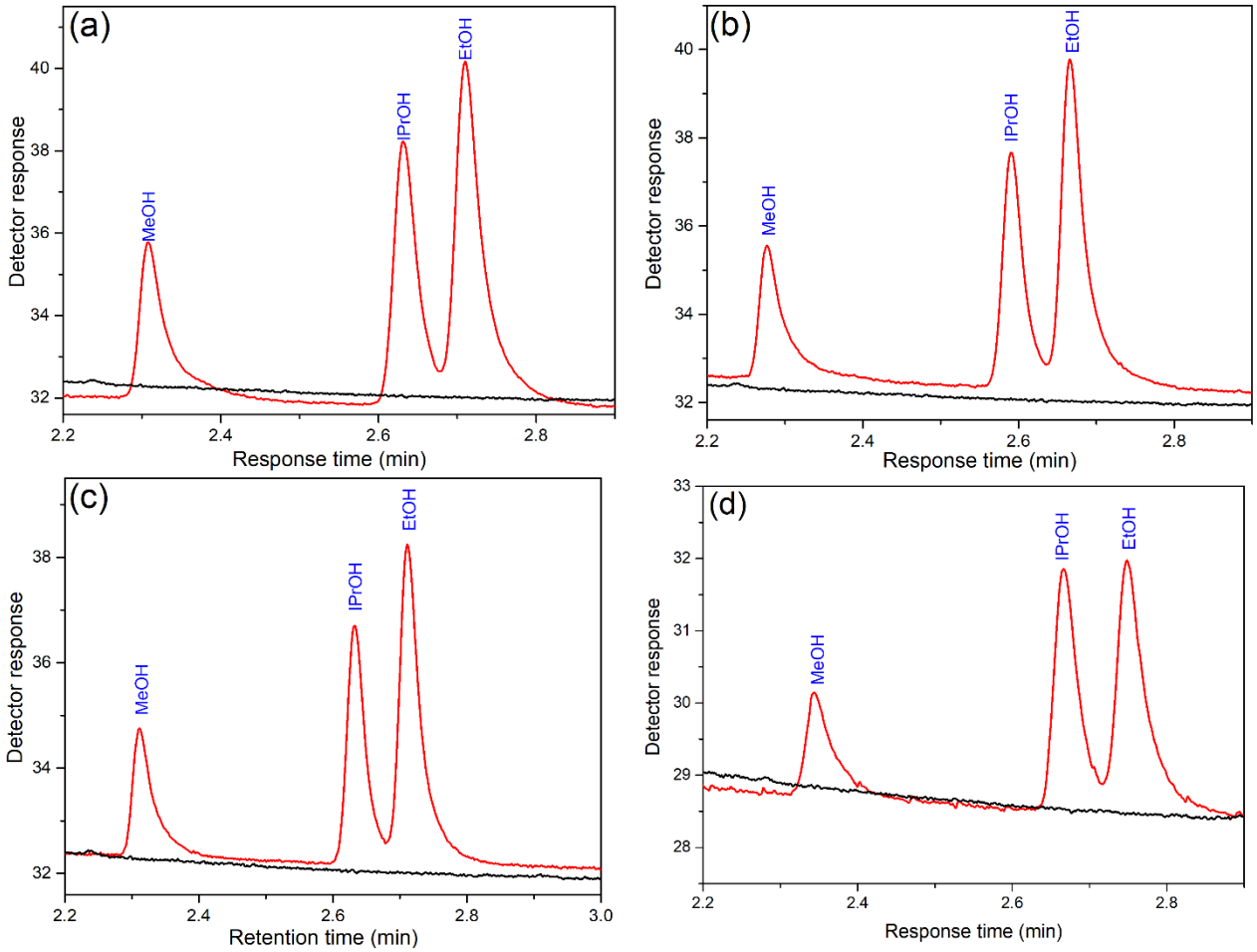

Fig. SI 8: Liquid injected GC-FID chromatogram at: (a) –0.60 V, (b) –0.65 V, (c) –0.70 V and (d) –0.75 V [black and red lines are before and after the experiments].

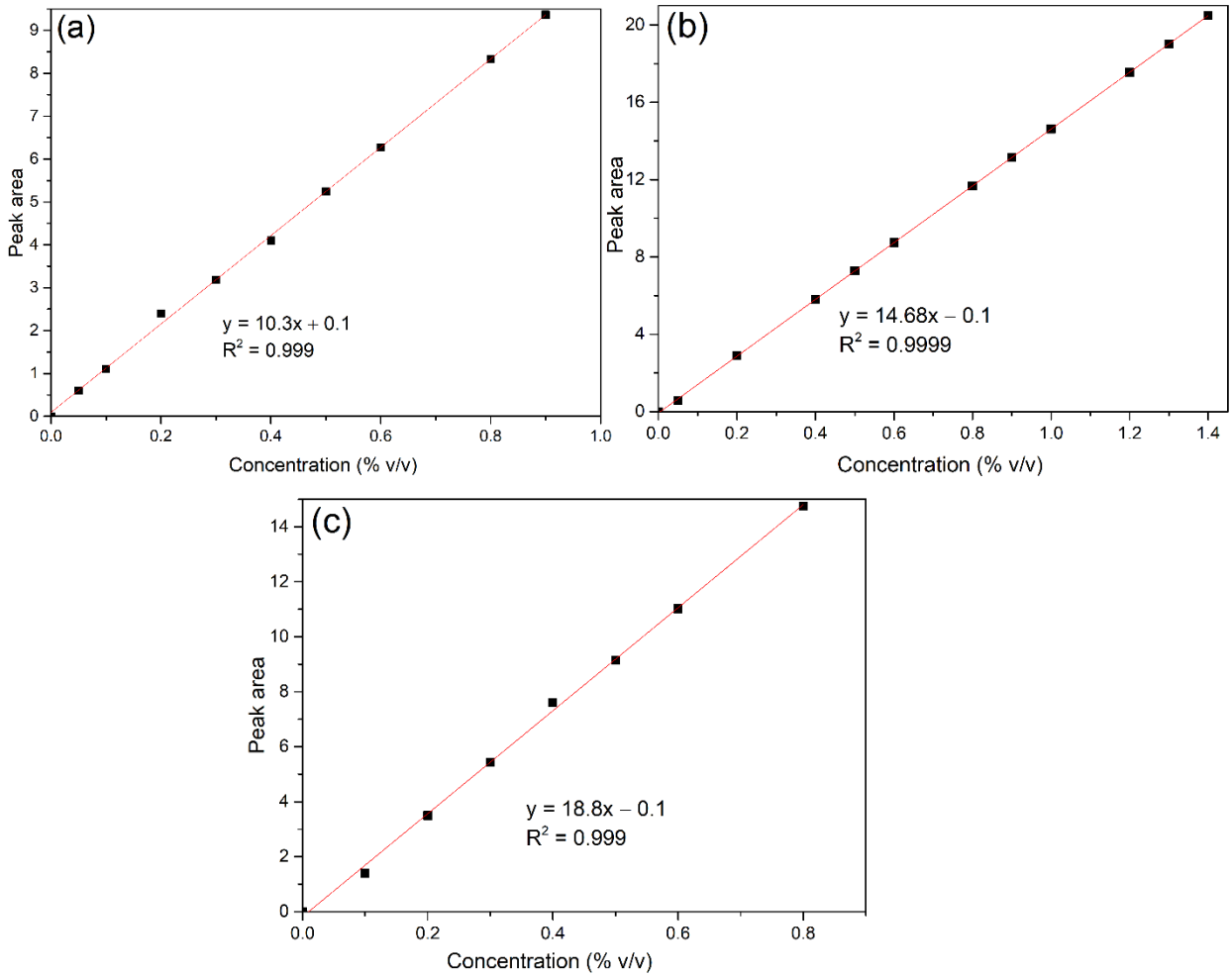

Fig. SI 9: GC-FID Calibration curves of (a) MeOH, (b) EtOH and (c) iPrOH, demonstrating good reproducibility with negligible scatter.

Calculation of the space-time yield (STY)

Space-time yield (STY) of Alcohol (*in $g_{alcohol}\, h^{-1} g_{cat}^{-1}$*)

According to Oliver Martin Angew. Chem. Int. Ed. 2016, 55, 6261 –6265

$$STY_{MeOH} = \frac{g_{alcohol}}{t(h) \times g_{cat}}$$

where

$g_{alcohol}$ is the mass (g) of the alcohol produced, t = time (h) and g_{cat} is the mass (g) of the catalyst.

Mass of the catalyst loaded is 50 mg = 0.05 g (for chapter 6) and time t =24 h

Potential (V vs SHE)	Mass of MeOH in the sample (g)	STY (MeOH)	Mass of iPOH in the sample (g)	STY (iPrOH)	Mass of EtOH in the sample (g)	STY (EtOH)	Total STY
–0.80	0.05	0.04	0.04	0.03	0.09	0.07	0.15
–0.85	0.07	0.06	0.07	0.06	0.14	0.11	0.23
–0.90	0.11	0.10	0.11	0.09	0.21	0.17	0.36
–0.95	0.04	0.03	0.05	0.04	0.07	0.06	0.13

Appendix B: List of publication, scientific conferences, symposium and workshops

(i). **Kayode Adesina Adegoke,** Shankara Gayathri Radhakrishnan, Clarissa L. Gray, Barbara Sowa, Claudia Morais, Paul Rayess, Egmont R. Rohwer, Clément Comminges, K. Boniface Kokoh and Emil Roduner; Highly efficient formic acid and carbon dioxide electro-reduction to alcohols on indium oxide electrodes, Sustainable Energy & Fuels 2020, https://doi.org/10.1039/D0SE00623H

(ii). **K.A. Adegoke**, S.G. Radhakrishnan, E. Roduner; Formic acid electro-reduction to alcohols on indium oxide cathode under ambient conditions; *Cell Symposium (Elsevier): Next-Generation Materials for Energy Applications*, November 16-19, 2019, University of Xiamen, China.

(iii). Shankara G. Radhakrishna, **Kayode Adesina Adegoke**, Emil Roduner Electrochemical Reduction of formic Acid at a metal oxide Cathode, *the 70th Annual Meeting of the International Society of Electrochemistry ((ISE), Electrochemistry: Linking Resources to Sustainable Development*, 4th – 9th August 2019, Durban, South Africa.

(iv). **Kayode Adesina, Adegoke:** Liquid fuels synthesis from Formic Acid on Membrane-Electrode-Assembly (MEA) under ambient conditions; *CO_2 conversion to value chemicals South Africa/France Science and Technology Research Collaboration (Protea) Kickstart Workshop*, 8th April, 2019, University of Pretoria South Africa.

(v). **Kayode Adesina Adegoke**, Shankara G Radhakrishnan and Emil Roduner Electrochemical reduction of formic acid at indium oxide cathode, *4th International Symposium on Electrochemistry organized by ElectrochemSA*, 3rd to 5th April 2018, University of Johannesburg, South Africa.